"La Sapienza" università di Roma. Dottorato di Ricerca in Scienze della Terra, XXXVI ciclo.

PhotoMonitoring: A new low-cost technique for landslide monitoring using multispectral data

Ph.D. thesis in Engineering Geology (GEO/05)

Antonio Cosentino

Ph.D. University Tutor:
   Prof. Carlo Esposito

Ph.D. Company Tutor:
   Prof. Paolo Mazzanti

Academic Year 2023 – 2024

Revised by:

Prof. Andrea Manconi [1,2]

Affiliation:
1) WSL Institute for Snow and Avalanche Research SLF
2) ETH Zurich, Department of Earth Sciences

Prof. Alessandro Corsini [3]

Affiliation:
3) Università di Modena e Reggio Emilia

Preface

This PhD is one of 25 projects of Innovative & Industrial PhD for the cycle XXXVI co-funded by the Lazio Region Call " Intervento per il rafforzamento della ricerca nel Lazio- incentivi per i dottorati di innovazione per le imprese " and performed in collaboration with NHAZCA S.r.l., Startup Sapienza.

The activities in this Innovative and industrial PhD were carried out using IRIS, a software developed by Nhazca dedicated to PhtoMonitoring applications.

This thesis is a collection of articles and the main chapters (Chapters 2-5) have to be considered as separate manuscripts. I worked on each manuscript in collaboration with the other co-authors.

Chapter 2 has been published with the following citation:

Romeo, S.; Cosentino, A.; Giani, F.; Mastrantoni, G.; Mazzanti, P. Combining Ground Based Remote Sensing Tools for Rockfalls Assessment and Monitoring: The Poggio Baldi Landslide Natural Laboratory. Sensors 2021, 21, 2632.

Chapter 3 has been published with the following citation:

Mazza, D.; Cosentino, A.; Romeo, S.; Mazzanti, P.; Guadagno, F.M.; Revellino, P. Remote Sensing Monitoring of the Pietrafitta Earth Flows in Southern Italy: An Integrated Approach Based on Multi-Sensor Data. Remote Sens. 2023, 15, 1138.

Chapter 4 has been published with the following citation:

Mazza, D.; Romeo, S.; Cosentino, A.; Mazzanti, P.; Guadagno, F.M.; Revellino, P. The Contribution of Digital Image Correlation for the Knowledge, Control and Emergency Monitoring of Earth Flows. Geosciences 2023, 13, 364.

Chapter 5 has been published with the following citation:

Cosentino, A.; Marmoni, G.M.; Fiorucci, M.; Mazzanti, P.; Scarascia Mugnozza, G.; Esposito, C. Optical and Thermal Image Processing for Monitoring Rainfall Triggered Shallow Landslides: Insights from Analogue Laboratory Experiments. Remote Sens. 2023, 15, 5577.

Table of Contents

Abstract

Landslides are widespread Natural hazards with significant social and economic impact, needing advanced monitoring and analysis technologies. In recent years, innovative and non-intrusive PhotoMonitoring (PM) techniques have attracted attention for their potential in landslide monitoring. These techniques offer the opportunity to enhance our understanding of landslide processes, contribute to risk mitigation, and provide new perspectives for geotechnical asset management. The research questions guiding this study include the applicability of non-invasive techniques like Digital Image Correlation (DIC) and Change Detection (CD) in monitoring rapid landslides, the additional information that PM techniques can offer compared to conventional methods, and the accuracy and reliability of measurements obtained through PM techniques, along with the development of new analysis methodologies to further enhance their potential. Throughout the thesis, the research explores PM techniques, focusing on specific case studies.

Chapter 2 illustrates the application of PM in combining various ground-based remote sensing tools for rockfall monitoring. The results show that PM techniques, particularly Gigapixel images combined with PM analysis, provide a unique view of deformations preceding rockfalls, thus improving the rockfall risk assessment.

Chapter 3 extends this investigation to the Pietrafitta Earth Flow, examining the integration of PM techniques using satellite images with other monitoring techniques such as T-InSAR, R-TS, and TLS. The results expose the suitability of PM techniques for improving the understanding of Earth Flow processes, bridging knowledge gaps left by conventional methods.

Chapter 4 delves deeper into the potential of PM techniques, expanding the discussion of DIC techniques to assess knowledge, control, and emergency monitoring of Earth Flows. The results suggest that PM analyses can be used in a range of ways and offer a huge amount of information for a variety of monitoring purposes.

In Chapter 5, the focus shifts to optical and thermal image processing for monitoring shallow landslides triggered by rainfall. The experimental application of PM techniques reveals their sensitivity in observing precursor signals of slope failure, highlighting their potential for Early Warning Systems.

Overall, all these sections demonstrate the high potential of PM techniques in various contexts, with different objectives, and using various data acquisition platforms, all aimed at

monitoring rapid geological phenomena such as Rockfall and slow but impulsive processes such as Earth Flow and Shallow landslide.

The concluding section of this thesis addresses the research questions introduced in the introduction, providing answers based on the study's findings. It is evident that non-invasive PM techniques contribute significantly to the monitoring of rapid or slow but impulsive landslides and offer unique information not obtainable through conventional methods. The accuracy and reliability of PM measurements are highlighted, particularly when using high-resolution images. However, some limitations still exist, and these are thoroughly discussed.

Furthermore, the broader implications and prospects are explored, emphasizing the adaptability, cost-effectiveness, and versatility of PM techniques, particularly in understanding and monitoring landslide processes. This opens new opportunities for research and practical implementation. Finally, the increasing use of optical sensors and smartphones is discussed, further expanding the potential scope of data collection. These implications have led to the creation of "IntelligEarth," a start-up of Sapienza aimed at realizing the vision outlined in this thesis.

Riassunto

Le frane sono fenomeni naturali diffusi con significative implicazioni sociali ed economiche, che richiedono avanzate tecnologie di monitoraggio ed analisi. Negli ultimi anni, tecniche di PhotoMonitoring (PM) innovative e non intrusive, hanno attirato l'attenzione per il loro potenziale nel monitoraggio di fenomeni franosi. Queste tecniche offrono l'opportunità di migliorare la comprensione dei processi di frana, di contribuire alla mitigazione dei rischi e di offrire nuove prospettive per la gestione degli asset geotecnici. Le domande di ricerca che guidano questo studio includono l'applicabilità di tecniche non invasive come la Digital Image Correlation (DIC) e la Change Detection (CD) nel monitoraggio di frane rapide; l'aggiunta di informazioni che le tecniche di PM possono fornire rispetto ai metodi convenzionali; l'accuratezza e l'affidabilità delle misure ottenute attraverso le tecniche di PM e lo sviluppo di nuove metodologie di analisi per incrementale ulteriormente il potenziale di tali tecniche. Nel corso della tesi, la ricerca esplora le tecniche di PM, concentrandosi su casi di studio specifici.

Il capitolo 2 illustra l'applicazione delle PM nella combinazione di vari strumenti di telerilevamento a terra per monitorare la caduta di massi. I risultati dimostrano che le tecniche di PM, in particolare le immagini Gigapixel combinate con l'analisi di PM, offrono una visione unica delle deformazioni che precedono le cadute di massi, migliorando così la valutazione dei rischi di caduta massi.

Il capitolo 3 estende questa indagine al flusso di terra di Pietrafitta, esaminando l'integrazione delle tecniche di DIC utilizzando immagini satellitari con altre tecniche di monitoraggio come T-InSAR, R-TS e TLS. I risultati rivelano l'idoneità delle tecniche PM a migliorare la comprensione dei processi di flusso terrestre, colmando le lacune di conoscenza lasciate dai metodi convenzionali.

Il capitolo 4 approfondisce il potenziale delle tecniche PM, ampliando la discussione sulle tecniche DIC per valutare la conoscenza, il controllo e il monitoraggio di emergenza dei flussi terrestri. I risultati sottolineano che le analisi PM possono essere utilizzate in vari modi e sono preziose per ottenere una grande quantità di informazioni per diversi scopi di monitoraggio.

Nel capitolo 5, l'attenzione si sposta sull'elaborazione di immagini ottiche e termiche per il monitoraggio di frane poco profonde innescate da precipitazioni. L'applicazione sperimentale delle tecniche di PM rivela la loro sensibilità nell'osservare i segnali precursori del cedimento del versante, evidenziando il loro potenziale per i sistemi di allerta precoce.

Nel complesso, questi capitoli dimostrano l'elevato potenziale delle tecniche di PM in vari contesti, con diversi obiettivi e con varie piattaforme di acquisizione dei dati, tutti finalizzati al monitoraggio di fenomeni geologici rapidi come la caduta di massi, e/o fenomeni lenti ed impulsivi come le colate di terra e le frane poco profonde.

La parte conclusiva affronta le domande di ricerca introdotte nell'introduzione, fornendo risposte basate sui risultati dello studio. È evidente che le tecniche non invasive di PM contribuiscono in modo significativo al monitoraggio sia delle frane rapide sia delle frane lente con attività impulsive impulsive offrendo informazioni uniche non ottenibili con i metodi convenzionali. Vengono sottolineate l'accuratezza e l'affidabilità delle misure di PM, in particolare quando si utilizzano immagini ad alta risoluzione. Tuttavia, esistono ancora alcune limitazioni che vengono ampiamente discusse. Inoltre, vengono esplorate le implicazioni più ampie e le prospettive future, sottolineando l'adattabilità, l'economicità e la versatilità delle tecniche di PM soprattutto per la comprensione ed il monitoraggio dei processi di frana, aprendo nuove opportunità per la ricerca e l'implementazione pratica. Infine, si discute dell'uso crescente di sensori ottici e smartphone che amplia ulteriormente la portata potenziale della raccolta dati. Queste implicazioni hanno portato alla creazione di "IntelligEarth", una start-up Sapienza che mira a realizzare la visione delineata in questa tesi.

Chapter 1

Introduction

1.1 General Context

Landslide is a type of mass wasting process that acts on natural and engineered slopes, and it is the movement of a mass of rock, debris, or earth down a slope, under the influence of gravity [1,2]. Landslides involve flowing, sliding, toppling, falling, or spreading, and many landslides exhibit a combination of different types of movements, at the same time or during their lifetime. This natural process is present on all continents and plays a significant role in the evolution of landscapes, but it also poses a serious hazard to the population in many areas of [3]. Different factors can affect the stability of slopes and cause landslides, such as precipitation, snow melting, temperature changes, earthquake shaking, volcanic activity, and human actions [4]. Climate and its variations control or influence some of these factors, chiefly precipitation and temperature [5,6] (Figure 1.1).
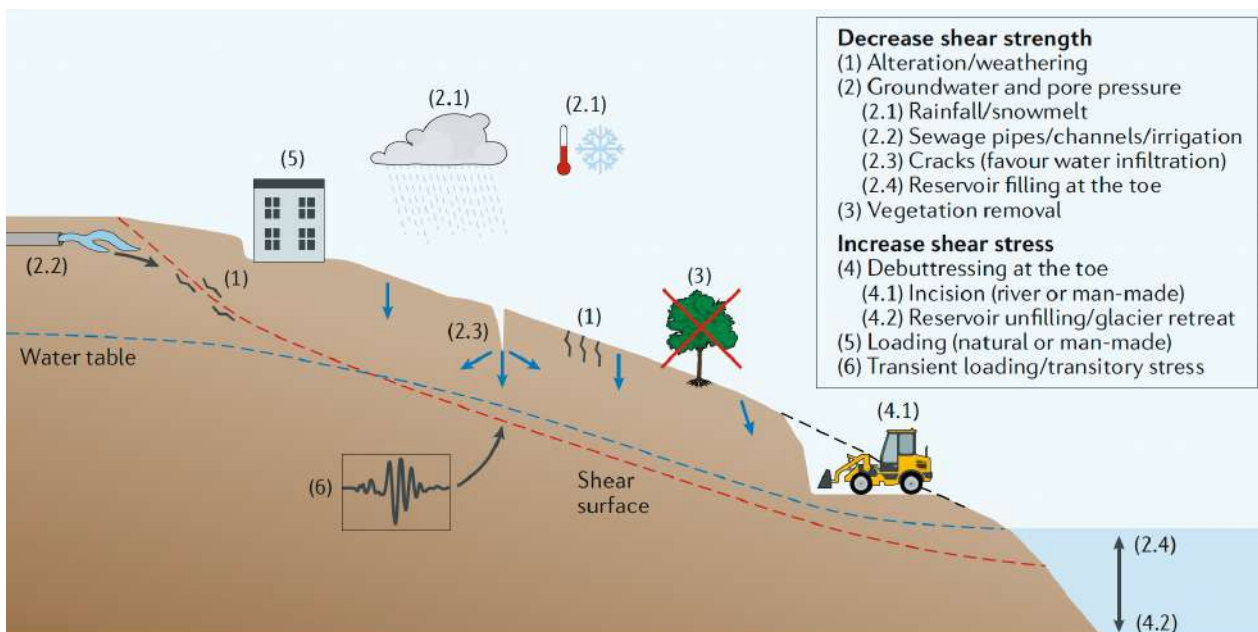
Figure 1.1. Schematic demonstrating the possible forcings of landslides. Forcings that may lead to a decrease in the shear strength of the landslide material, including alteration and/or weathering, removal of vegetation and hydrological processes from rainfall infiltration, lake infill or material property changes during earthquakes. Alternative forcings might lead to increased shear stress acting on the landslide material, including debuttressing at the toe, anthropogenic loading or natural material deposition, and short-term loading (for example, earthquakes) [7].

Between 2004 and 2016 alone, an estimated 55,997 people were killed worldwide in 4,862 distinct landslide events (not counting those caused by earthquakes) [8].

As shown by [9] countries such as Colombia, Peru, Brazil, Nicaragua, El Salvador, Italy, Nepal, India, China and New Zealand have a high number of landslides, with a total number of 37,946 landslides and 185,753 victims recorded between 1903 and 2020 (Figure 1.2).
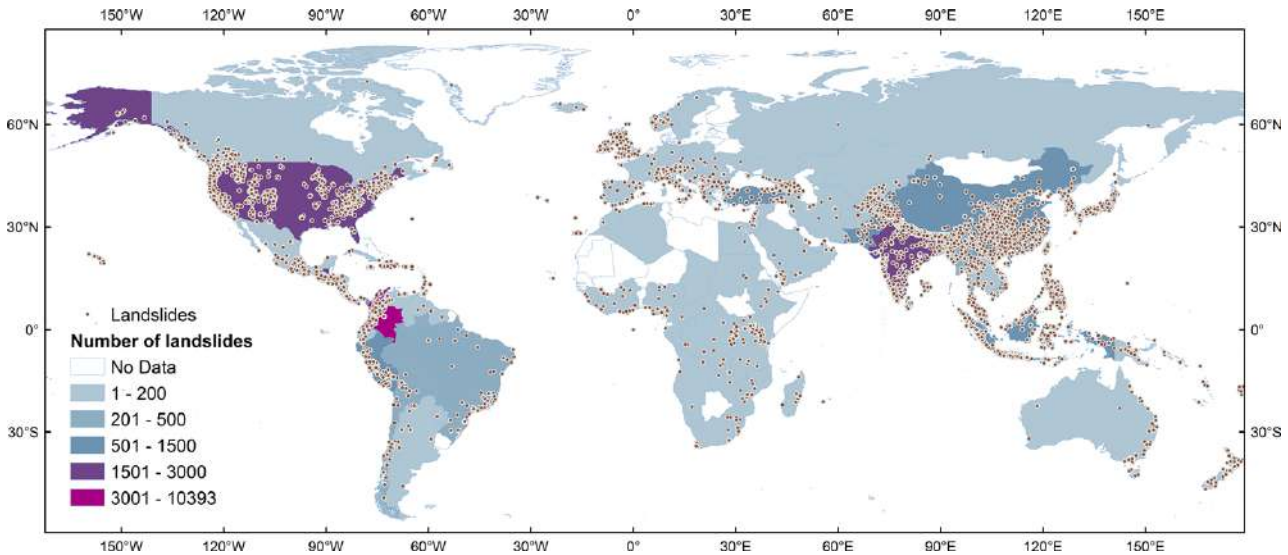
Figure 1.2. Spatial distribution of landslides worldwide registered between 1903 and 2020 in the UGLD database [9]

Specifically, over the last 20 years, 1370 fatalities and 784 casualties have been recorded in 27 European countries due to 476 landslide events (an increasing trend in recent years), with an average of 108 ± 82 fatalities each year. In addition, landslides cause billions of Euros of damage to infrastructure such as roads, railways, pipelines, structures, embankments, and buildings, and have a relevant "indirect" cost for the society, encompassing loss of productivity, reduction of real estate value, loss of tax revenue, and other induced economic effects [10]. In Europe, the average economic loss per year is 4.7 billion Euros, and in Italy, the total annual losses caused by landslides are 3.9 billion Euros [11] (Figure 1.3). In the world, the nations that suffer the greatest economic impact due to landslides are Italy, the United States, Japan and India, with a loss of about 0.19% of their Gross Domestic Product (GDP) (From International Monetary) [12].
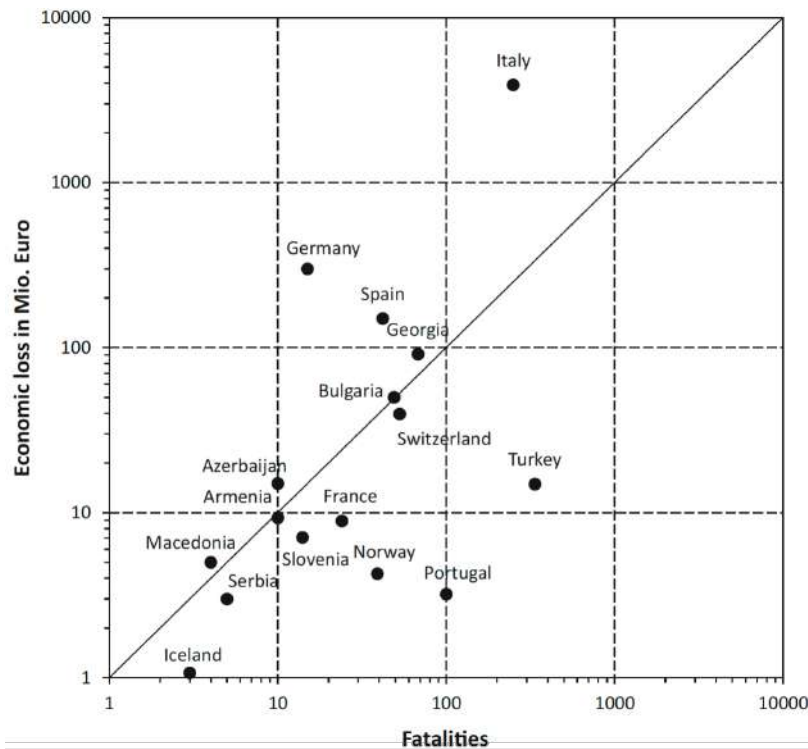
Figure 1.3. *Fatalities and economic losses due to fatal landslides in Europe [12].*

The Landslide risks could be exacerbated by global changes such as increases in the frequency or magnitude of rainfall and permafrost degradation. This issue was considered in the IPCC's special report "Managing the Risks of Extreme Events and Disasters to Advance Climate Change Adaptation" [13], reads that "There is high confidence that changes in heat waves, glacial retreat, and/or permafrost degradation will affect slope instabilities in high mountains, and medium confidence that temperature-related changes will influence bedrock stability. There is also high confidence that changes in heavy precipitation will affect landslides in some regions" [14].

International organisations and agencies actively support policies that aim to mitigate the risk of landslides, with the goal of deepening understanding of these phenomena and improving disaster preparation and response [15]. The 2020 Landslide Kyoto Commitment aimed to provide the information, platforms, and technical expertise to promote landslide risk assessment on a global scale also because it has been confirmed, in several cases, that the cost of risk mitigation is significantly less than the economic impact of failure (five times the cost of mitigation and prevention) [16].

To achieve these goals, both landslide detection and monitoring are crucial, as integral parts of the general goal of landslide prevention [15,17].

Landslide detection consists of the collection of data and information on the presence, distribution, and intensity of landslides and the identification of the elements affected by the deformative process. The detection is strategic to plan immediate disaster response; moreover,

historical landslide inventories are also needed to prepare landslide susceptibility and hazard maps. Following its identification, it is fundamental to measure and monitor the key parameters in real landslide conditions, most notably its surface displacement over time [15], which is a mandatory step in the final landslide risk assessment.

Monitoring instruments can be classified into two main categories, i.e. ''contact'' and ''remote''. Contact systems require physical contact between instruments and the ground, but remote instruments do not because they are primarily based on sensors that receive and emit electromagnetic waves. Contact methods are today the most common in monitoring practice because of their longer history and the capability to measure all the key geotechnical parameters. But in most cases, the measurement of a single parameter is not enough for a complete understanding of the behaviours of the slope, and these tools are generally not suitable for wide area monitoring, as every single sensor provides information for a specific location and not for surrounding areas, and in many cases can require the operators to enter hazardous or inaccessible areas [18].

Given the large number of landslides with contact methods, full monitorability of landslides results in an optimistic mirage, as well as only some of the broad spectrum of failure mechanisms can be adequately monitored for early warning purposes [19].

During the past 30 years, there have been rapid developments in remote sensing methods for monitoring deformation, creating significant applications in the geotechnical field. Remote-sensing techniques (RSTs) have therefore become an indispensable tool in landslide investigation, as they offer a systematic and synoptic view of the ground surface at various scales. The use of RSTs has enabled a greater understanding of the complex interaction between different geological and geomorphological phenomena behind instability processes [15].

The RSTs are possible to categorise based on three key features: the type of platform (whether it's ground-based, aerial-based on an aeroplane, or satellite-based), the type of wave they collect (visible, infrared, or microwaves), and the type of sensor they use (active or passive). Based on these categories, a variety of different sensors are available today, which can be implemented on ground-based, airborne and satellite platforms. Given the huge availability of platforms and sensors for each specific monitoring objective, several factors must be considered to assess which RST is most suitable. These include precision (measurement repeatability), temporal resolution (data collection frequency), spatial resolution (pixel size on the ground/structure), information density (number and distribution of pixels), deformation geometry (measurement characteristics), interaction level with the ground/structure (from fully remote to high sensor installation), monitored size area (maximum

coverage per sensor), data reliability and validity, maximum operability range, sensitivity to atmospheric noise, and budgetary considerations (a qualitative assessment of the characteristics described above is shown in Figure 1.4) [20].

	Precision	Temporal resolution	Spatial resolution	Density	Deformation geometry	Interaction	Size monitored area	Operability range	Data reliability	Atmospheric noise	Costs
TLS	Medium	Medium	High	Ext. High	Ext. High	Ext. High	High	Medium	High	Low	Low
TInSAR	Ext. High	Ext. High	Medium	High	Low	Ext. High	High	High	High	High	Low
RTS	Ext. High	High	High	Medium	Ext. High	Medium	Medium	Ext. High	Medium	Medium	Medium
RRTS	High	High	High	High	Medium	Medium	Low	Ext. Low	Medium	Low	High
SInSAR	Medium	Ext. Low	Low	High	Ext. Low	Ext. High	Ext. High	Ext. High	Medium	Low	Low
DP	Low	Medium	Medium	Medium	Medium	Ext. High	Ext. High	Ext. High	Low	Ext. Low	Ext. High
D-GPS	High	High	Ext. Low	Ext. Low	Ext. Low	Ext. Low	Ext. High	Ext. High	High	High	Medium

Ext. Low	Low	Medium	High	Ext. High

Figure 1.4. Qualitative evaluation of remote techniques based on the features described in this article. From red colour to green colour (see the scale bar) there is an increasing performance of the technique (e.g. increasing precision, temporal resolution, spatial resolution, density, geometric information, monitoring area, operability range, data reliability) and decreasing (e.g. atmospheric noise, cost, and interaction) [20].

However, in landslide monitoring and management, it is crucial to ensure a suitable balance between the cost of implementing monitoring systems in an area and the benefits linked to using them. For example, if an extensive and expensive monitoring network is installed to address a large landslide that has recently exhibited signs of reactivation, the high cost involved may limit the life of the system due to the high maintenance costs. Employing less expensive instruments for a long-term monitoring campaign on one or more landslides could enhance the likelihood of effectively monitoring any potential activation. This is also important to maintain a good cost-benefit ratio of monitoring [15]. For this reason, more and more attempts are being made to experiment with and test monitoring techniques that are non-invasive but at the same time able to provide important feedback for the three main steps required in the management of landslide hazards (detection, monitoring and prediction) [15]. Therefore, future challenges in the field of landslide research are focusing on enhancing tools, aiming to acquire precise data at high frequencies and on a broader scale. Moreover, special attention will be given to cost reduction in monitoring programs through the utilization of innovative sensors and techniques [7].

In recent years, the evaluation of an innovative method known as Digital Image Processing (DIP) also known as PhotoMonitoring (PM), has been applied to various fields of engineering geology, as evidenced by the increasing number of publications on this topic [21–24].

In general, PM techniques are based on extracting information about changes in the terrain by comparing different types of digital images (e.g., satellite, aerial or terrestrial images) collected at

different times over the same area and scene [23,25]. Results are quantitative and expressed as the amount of change or displacement of the target objects in the scene: PM algorithms can return displacement field maps made up of pixel-based vectors of displacement (application called Digital Image Correlation- DIC) and changes field maps (application called Change Detection- CD) with an accuracy that is a function of the intrinsic spatial, temporal and radiometric resolution of the images and whole dataset. In detail DIC, also known as feature-tracking or subpixel offset [26,27], is an image processing technique that identifies and quantifies ground displacement occurring orthogonal to the line-of-sight (LOS) of the camera. While DIC can be applied to various types of input data from different platforms, its primary potential for slope instability detection and monitoring lies in the utilization of high-resolution optical imagery, acquired by satellites [28] and manned or unmanned aerial vehicles (UAVs) [29]. Before failure, the deformation of a slope's surface is one of the main parameters that allow for describing and observing the temporal evolution of slope instabilities, to understand their behaviour, and predict their potential failure. In particular, a landslide's velocity is a fundamental parameter because it will determine the intensity of the damage. However, the degree of the damage also depends on other factors, such as the internal distortion of the displaced mass, the type of landslide and the vulnerability of the exposed elements. The slow and continuous displacement of slopes over long periods can also be utilized to detect previously unknown instabilities and assess their hazard potential [30]. However, when referring to extremely rapid movements like Rockfalls or movements from extremely slow to extremely rapid like Earth Flow and Shallow landslides, which are characterised by extended periods of relative quiescence interspersed with faster "surges," it can be challenging, if not impossible, to measure the speed of mass movement [1,2]. For this aim and this specific landslide process, the use of DIC with optical images to track Earth's surface displacement is a potential alternative or complementary system to SAR interferometry that has no limitations in terms of maximum detectable velocity and has the potential to be used in several deformation scenarios [22]. PM analysis could provide key information on the spatial and temporal evolution of surface displacements at slope instabilities; however, its potential and accuracy have not yet been fully evaluated and exploited by [30]. Obstacles to the full exploitation of potential are of a technical nature on the one hand, but also due to the lack of dissemination of specific skills on the other [31].

1.2 Research Objective

This research strives to extract the maximum amount of information from the PhotoMonitoring (PM) technique, developing new methods for using the results obtained and evaluating their reliability. Also, the overall objective is to use the PM technique in different ways, coupled with different RTSs, in order to estimate, quantify and validate its potential and accuracy in the monitoring of rapid processes such as Rockfall and slow but impulsive processes such as Earth Flow and Shallow landslide, which act at slope scale. In addition, the aim is to investigate the substantial effects that the PM technique, which uses data from satellite, aerial, and ground-based platforms, can have on our understanding of the scientific processes involved in rapid (Rockfall) or slow but impulsive landslides (Earth flow, and shallow landslides), as well as the evaluation of the risk of landslides.

This work proposes some monitoring case studies of different landslides, exploiting remote sensing techniques.

The specific research questions are the following:

I. Can non-invasive monitoring techniques that utilize digital image processing, such as Digital Image Correlation (DIC) and Change Detection (CD), contribute to the monitoring of rapid landslides such as Rockfall and slow but impulsive processes such as Earth Flow?

II. What additional information can PhotoMonitoring techniques provide compared to more conventional monitoring methods?

III. How accurate and reliable are measurements obtained through PhotoMonitoring techniques, including their ability to detect and quantify movement with high precision and sensitivity?

IV. What are the main limitations of PhotoMonitoring techniques, and how may they be overcome to improve digital image analysis techniques?

V. How can the understanding of shallow landslides be improved using thermal infrared data, analysed with PhotoMonitoring techniques?

VI. Could DIC and CD techniques contribute to the development of early warning systems (EWS) for landslides?

VII. Can PhotoMonitoring techniques be used to mitigate the risk of landslides and help to manage high-risk areas in a safe and sustainable way?

1.3 Outline of the Thesis

After this general introduction (Chapter 1), the outline of the thesis is structured as a collection of papers:

Chapter 2 (Combining Ground Based Remote Sensing Tools for Rockfalls Assessment and Monitoring: The Poggio Baldi Landslide Natural Laboratory) focuses on research questions I, II, III, IV and VII, through an intensive field survey at the Poggio Baldi Landslide Natural Laboratory.

This chapter conducts a comprehensive evaluation of the effectiveness of Gigapixel imaging and the PhotoMonitoring technique in the field of rockfall characterization and monitoring. Furthermore, it explores the simultaneous application of different types of Remote Sensing technology (HYDRA-G ArcSAR, Gigapan robotic systems equipped with DSLR cameras, and the DUO Smart Noise Monitor) during a continuous three-day monitoring campaign in a natural laboratory. The objective is to assess each sensor's capability to identify rockfall events by comparing the results obtained from all sensors for the same area and at the same time. Finally, this chapter proposes a multi-sensor approach that could contribute to the sustainable and safe management of areas at high risk of rockfalls, exploiting the full potential of gigapixel images and digital image processing techniques.

This chapter was published in *Sensors* Journal and in the Special Issue *Sensors and Measurements in Geotechnical Engineering* in April 2021 (DOI: https://doi.org/10.3390/s21082632). The additional authors who contributed to this manuscript are Saverio Romeo, Giandomenico Mastrantoni, Francesco Giani and Paolo Mazzanti.

Chapter 3 (Remote Sensing Monitoring of the Pietrafitta Earth Flows in Southern Italy: An Integrated Approach Based on Multi-Sensor Data) focuses on research questions I, II, IV, V and VII, through a field survey at the Pietrafitta Earth Flow.

The present chapter aims to assess the capabilities, peculiarities, and limitations of various remote sensing techniques for earth flow monitoring through the case study of the Pietrafitta landslide in Southern Italy. The research compared and combined data collected during the main landslide reactivations from different ground-based remote sensors, including Robotic Total Station (R-TS), Terrestrial Synthetic Aperture Radar Interferometry (T-InSAR), and Terrestrial Laser Scanner (TLS), with data derived from satellite-based Digital Image Correlation (DIC) analysis. The objective is to understand whether, in the face of complex events, the use of a single monitoring technique might be sufficient to fully observe and comprehend the ongoing processes and to determine the suitability

of satellite-based DIC compared to ground-based techniques. An additional aspect of this chapter is that analysis was performed using IRIS software, developed by NHAZCA S.r.l., a start-up of the 'Sapienza' University of Rome, which enables Change Detection (CD) and Digital Image Correlation (DIC), using various algorithms from the relevant literature and new algorithms developed specifically for this purpose. Finally, this chapter focuses on PhotoMonitoring techniques and their contribution to the understanding of complex land sliding phenomena, with possible implications for landslide risk mitigation and sustainable management in high-risk areas.

This chapter has been published in the *Remote Sensing* Journal and in the Special Issue *Ground and Structural Deformations Monitoring Systems Integrating Remote Sensing and Ground-Based Data* in February 2023 (DOI: https://doi.org/10.3390/rs15041138). The additional authors that contributed to this manuscript are Davide Mazza, Saverio Romeo, Paolo Mazzanti, Francesco M. Guadagno and Paola Revellino.

Chapter 4 (The Contribution of Digital Image Correlation for the Knowledge, Control, and Emergency Monitoring of Earth Flows) focuses on research questions I, III, IV, V and VII, through a field survey at the Pietrafitta and Grillo Earth Flows.

This chapter focuses on evaluating modern DIC (Digital Image Correlation) techniques using data acquired from low-cost ground cameras and UAV (Unmanned Aerial Vehicle) imagery at two different landslide sites. The data obtained through these sensors were compared with more conventional monitoring methods, such as GNSS (Global Navigation Satellite System) and Robotic Total Stations (R-TS). The objective was to establish the most effective methodology and present the potential advantages and limitations of employing DIC techniques for sustainable landslide monitoring near linear infrastructure. Finally, this chapter provides valuable insights into quantifying the accuracy and sensitivity of displacement measurements using PhotoMonitoring techniques, which are essential for understanding the contribution that this method can make in the development of Early Warning Systems (EWS) for landslide events."

This chapter has been published in the *Geosciences* Journal and a Special Issue, *Remote Sensing Monitoring of Geomorphological Hazards* in September 2023, in November 2023 (DOI: https://doi.org/10.3390/geosciences13120364). The additional authors that contributed to this manuscript are Davide Mazza, Saverio Romeo, Paolo Mazzanti, Francesco M. Guadagno and Paola Revellino.

Chapter 5 (*Optical and Thermal Image Processing for monitoring rainfall triggered shallow landslides: insights from analogue laboratory experiments*) focuses on research questions I, III, V, VI, VII and VIII, through a flume analogue laboratory experiment.

This chapter explores the practical application of innovative monitoring techniques in the context of rainfall-triggered landslides. It examines the integration of Digital Image Processing (DIP) techniques, including Digital Image Correlation (DIC) and Change Detection (CD), with Infrared Thermography (IRT) in laboratory experiments. These experiments aim to replicate and monitor the initiation of shallow landslides due to precipitation. The chapter analyzes deformation behaviour and tests the reliability of PhotoMonitoring analyses using IRT images, to identify possible precursor signals, useful for the possible development of early warning systems (EWS). Finally, this work aims to advance the field of digital image analysis methods, particularly enhancing landslide monitoring through these methods by surpassing the limitations of optical images and utilizing thermal imagery.

This chapter has been published in the *Remote Sensing* Journal and in Special Issue A*dvances in Multisensor Applications for Remote Sensing in the Engineering Geology and the Environment*, in November 2023 (DOI: https://doi.org/10.3390/rs15235577). The additional authors that contributed to this manuscript are Gian Marco Marmoni, Matteo Fiorucci, Paolo Mazzanti, Gabriele Scarascia Mugnozza and Carlo Esposito.

Chapter 6 corresponds to the Conclusions of the thesis. This chapter summarizes the main findings, answering the research questions of this thesis and presents possibilities for future development of the work presented.

References

1.   LANDSLIDE TYPES AND PROCESSES.

2.   Hungr, O.; Leroueil, S.; Picarelli, L. The Varnes Classification of Landslide Types, an Update. *Landslides* 2014, *11*, 167–194, doi:10.1007/s10346-013-0436-y.

3.   Petley, D. Global Patterns of Loss of Life from Landslides. *Geology* 2012, *40*, 927–930, doi:10.1130/G33217.1.

4.   Gariano, S.L.; Guzzetti, F. Landslides in a Changing Climate. *Earth-Science Reviews* 2016, *162*, 227–252, doi:10.1016/j.earscirev.2016.08.011.

5.   Dhakal, A.S.; Sidle, R.C. Distributed Simulations of Landslides for Different Rainfall Conditions. *Hydrological Processes* 2004, *18*, 757–776, doi:10.1002/hyp.1365.

6.   Crozier, M.J. Deciphering the Effect of Climate Change on Landslide Activity: A Review. *Geomorphology* 2010, *124*, 260–267, doi:10.1016/j.geomorph.2010.04.009.

7.   Lacroix, P.; Handwerger, A.L.; Bièvre, G. Life and Death of Slow-Moving Landslides. *Nat Rev Earth Environ* 2020, *1*, 404–419, doi:10.1038/s43017-020-0072-8.

8.   Froude, M.J.; Petley, D.N. Global Fatal Landslide Occurrence from 2004 to 2016. *Nat. Hazards Earth Syst. Sci.* 2018, *18*, 2161–2181, doi:10.5194/nhess-18-2161-2018.

9.   Gómez, D.; García, E.F.; Aristizábal, E. Spatial and Temporal Landslide Distributions Using Global and Open Landslide Databases. *Nat Hazards* 2023, *117*, 25–55, doi:10.1007/s11069-023-05848-8.

10.   Scaioni, M.; Longoni, L.; Melillo, V.; Papini, M. Remote Sensing for Landslide Investigations: An Overview of Recent Achievements and Perspectives. *Remote Sensing* 2014, *6*, 9600–9652, doi:10.3390/rs6109600.

11.   Klose, M.; Maurischat, P.; Damm, B. Landslide Impacts in Germany: A Historical and Socioeconomic Perspective. *Landslides* 2016, *13*, 183–199, doi:10.1007/s10346-015-0643-9.

12.   Haque, U.; Blum, P.; Da Silva, P.F.; Andersen, P.; Pilz, J.; Chalov, S.R.; Malet, J.-P.; Auflič, M.J.; Andres, N.; Poyiadji, E.; et al. Fatal Landslides in Europe. *Landslides* 2016, *13*, 1545–1554, doi:10.1007/s10346-016-0689-3.

13.   Seneviratne, S.I.; Nicholls, N.; Easterling, D.; Goodess, C.M.; Kanae, S.; Kossin, J.; Luo, Y.; Marengo, J.; McInnes, K.; Rahimi, M.; et al. Changes in Climate Extremes and Their Impacts on the Natural Physical Environment. In *Managing the Risks of Extreme Events and Disasters to Advance Climate Change Adaptation*; Field, C.B., Barros, V., Stocker, T.F., Dahe, Q., Eds.; Cambridge University

Press, 2012; pp. 109–230 ISBN 978-1-107-02506-6.

14.   Gariano, S.L.; Guzzetti, F. Landslides in a Changing Climate. *Earth-Science Reviews* 2016, *162*, 227–252, doi:10.1016/j.earscirev.2016.08.011.

15.   Casagli, N.; Intrieri, E.; Tofani, V.; Gigli, G.; Raspini, F. Landslide Detection, Monitoring and Prediction with Remote-Sensing Techniques. *Nat Rev Earth Environ* 2023, *4*, 51–64, doi:10.1038/s43017-022-00373-x.

16.   Mazzanti, P. Toward Transportation Asset Management: What Is the Role of Geotechnical Monitoring? *J Civil Struct Health Monit* 2017, *7*, 645–656, doi:10.1007/s13349-017-0249-0.

17.   Yordanov, V.; Biagi, L.; Truong, X.Q.; Tran, V.A.; Brovelli, M.A. AN OVERVIEW OF GEOINFORMATICS STATE-OF-THE-ART TECHNIQUES FOR LANDSLIDE MONITORING AND MAPPING. *Int. Arch. Photogramm. Remote Sens. Spatial Inf. Sci.* 2021, *XLVI-4/W2-2021*, 205–212, doi:10.5194/isprs-archives-XLVI-4-W2-2021-205-2021.

18.   Mazzanti, P. Toward Transportation Asset Management: What Is the Role of Geotechnical Monitoring? *J Civil Struct Health Monit* 2017, *7*, 645–656, doi:10.1007/s13349-017-0249-0.

19.   Canuti, P.; Casagli, N.; Ermini, L.; Fanti, R.; Farina, P. Landslide Activity as a Geoindicator in Italy: Significance and New Perspectives from Remote Sensing.

20.   Mazzanti, P. Remote Monitoring of Deformation. An Overview of the Seven Methods Described in Previous GINs.

21.   Mazzanti, P.; Caporossi, P.; Muzi, R. Sliding Time Master Digital Image Correlation Analyses of CubeSat Images for Landslide Monitoring: The Rattlesnake Hills Landslide (USA). *Remote Sensing* 2020, *12*, 592, doi:10.3390/rs12040592.

22.   Guerriero, L.; Di Martire, D.; Calcaterra, D.; Francioni, M. Digital Image Correlation of Google Earth Images for Earth's Surface Displacement Estimation. *Remote Sensing* 2020, *12*, 3518, doi:10.3390/rs12213518.

23.   Caporossi, P.; Mazzanti, P.; Bozzano, F. Digital Image Correlation (DIC) Analysis of the 3 December 2013 Montescaglioso Landslide (Basilicata, Southern Italy): Results from a Multi-Dataset Investigation. *IJGI* 2018, *7*, 372, doi:10.3390/ijgi7090372.

24.   Manconi, A.; Kourkouli, P.; Caduff, R.; Strozzi, T.; Loew, S. Monitoring Surface Deformation over a Failing Rock Slope with the ESA Sentinels: Insights from Moosfluh Instability, Swiss Alps. *Remote Sensing* 2018, *10*, 672, doi:10.3390/rs10050672.

25.   Walter, T.R.; Legrand, D.; Granados, H.D.; Reyes, G.; Arámbula, R. Volcanic Eruption Monitoring by Thermal Image Correlation: Pixel Offsets Show Episodic Dome Growth of the Colima

Volcano. *JGR Solid Earth* 2013, *118*, 1408–1419, doi:10.1002/jgrb.50066.

26.   Cai, J.; Wang, C.; Mao, X.; Wang, Q. An Adaptive Offset Tracking Method with SAR Images for Landslide Displacement Monitoring. *Remote Sensing* 2017, *9*, 830, doi:10.3390/rs9080830.

27.   Walter, T.R. Low Cost Volcano Deformation Monitoring: Optical Strain Measurement and Application to Mount St. Helens Data. *Geophysical Journal International* 2011, *186*, 699–705, doi:10.1111/j.1365-246X.2011.05051.x.

28.   Heid, T.; Kääb, A. Evaluation of Existing Image Matching Methods for Deriving Glacier Surface Displacements Globally from Optical Satellite Imagery. *Remote Sensing of Environment* 2012, *118*, 339–355, doi:10.1016/j.rse.2011.11.024.

29.   Mugnai, F.; Masiero, A.; Angelini, R.; Cortesi, I. High-Resolution Monitoring of Landslides with UAS Photogrammetry and Digital Image Correlation. *European Journal of Remote Sensing* 2023, *56*, 2216361, doi:10.1080/22797254.2023.2216361.

30.   Bickel, V.; Manconi, A.; Amann, F. Quantitative Assessment of Digital Image Correlation Methods to Detect and Monitor Surface Displacements of Large Slope Instabilities. *Remote Sensing* 2018, *10*, 865, doi:10.3390/rs10060865.

31.   Kääb, A.; Huggel, C.; Fischer, L.; Guex, S.; Paul, F.; Roer, I.; Salzmann, N.; Schlaefli, S.; Schmutz, K.; Schneider, D.; et al. Remote Sensing of Glacier- and Permafrost-Related Hazards in High Mountains: An Overview. *Natural Hazards and Earth System Sciences* 2005, *5*, 527–554, doi:10.5194/nhess-5-527-2005.

Chapter 2

Combining Ground Based Remote Sensing Tools for Rockfalls Assessment and Monitoring: The Poggio Baldi Landslide Natural Laboratory

Authors: Saverio Romeo [1,2], Antonio Cosentino [1], Francesco Giani [1], Giandomenico Mastrantoni [1,*] and Paolo Mazzanti[1,2]

[1] Department of Earth Sciences, University of Rome "Sapienza", Piazzale Aldo Moro 5, 00185 Rome, Italy; saverio.romeo@uniroma1.it (S.R.); cosentino.1666074@studenti.uniroma1.it (A.C.); giani.1658368@studenti.uniroma1.it (F.G.); paolo.mazzanti@uniroma1.it (P.M.)

[2] NHAZCA S.r.l., Via Vittorio Bachelet 12, 00185 Rome, Italy

* Correspondence: mastrantoni.1651807@studenti.uniroma1.it.

2.1 Abstract

Nowadays the use of remote monitoring sensors is a standard practice in landslide characterization and monitoring. In the last decades, technologies such as LiDAR, terrestrial and satellite SAR interferometry (InSAR) and photogrammetry demonstrated a great potential for rock slope assessment while limited studies and applications are still available for ArcSAR Interferometry, Gigapixel imaging and Acoustic sensing. Taking advantage of the facilities located at the Poggio Baldi Landslide Natural Laboratory, an intensive monitoring campaign was carried out on May 2019 using simultaneously the HYDRA-G ArcSAR for radar monitoring, the Gigapan robotic system equipped with a DSLR camera for photo-monitoring purposes and the DUO Smart Noise Monitor for acoustic measurements. The aim of this study was to evaluate the potential of each monitoring sensor and to investigate the ongoing gravitational processes at the Poggio Baldi landslide. Analysis of multi-temporal Gigapixel-images revealed the occurrence of 84 failures of various sizes between 14–17 May 2019. This allowed us to understand the short-term evolution of the rock cliff that is characterized by several impulsive rockfall events and continuous debris production. Radar displacement maps

revealed a constant movement of the debris talus at the toe of the main rock scarp, while acoustic records proved the capability of this technique to identify rockfall events as well as their spectral content in a narrow range of frequencies between 200 Hz to 1000 Hz. This work demonstrates the great potential of the combined use of a variety of remote sensors to achieve high spatial and temporal resolution data in the field of landslide characterization and monitoring.

2.2 Introduction

Varnes in 1978 described the rockfall process as "a detached fragment of rock that falls along a vertical or sub-vertical cliff, proceeds down slope by bouncing and flying along ballistic trajectories or by rolling on talus or debris slopes" [1]. Rockfalls are the most frequent and widespread instabilities affecting steep slopes in mountain regions and sea cliffs [2–6]. Therefore, their impact energy and the associated hazard can reach very high values [7–13]. According to [14], along the Italian mountain ranges (Alps and Apennines), fast moving landslides such as rockfalls caused the largest number of deaths. As demonstrated in recent studies [15–23], surveying and monitoring activities play a key role in rockfall hazard assessment and are therefore of paramount importance for the preservation of human life. As rockfalls occur in very steep slopes sometimes showing limited precursor signals [24–29], their investigations, as well as their prediction and stabilisation, could face many difficulties [30]. Conventional geotechnical instrumentations like extensometers, inclinometers and piezo-electric transducers recording acoustic emissions (AE) caused by rock fracturing are currently used in rock slope monitoring with positive results [31–37]. In detail, acoustic emissions have the potential to identify ongoing deformations affecting the slope, representing a key component in the development of early-warning systems [33,38]. AE is generated during slope movements and acoustic monitoring is often capable of detecting pre-failure deformations [39]. However, the installation of contact sensors on steep and unstable slopes may be expensive and hazardous. Hence, rockfall assessment and monitoring can be carried out using remote sensing techniques. Techniques like Terrestrial Laser Scanning (TLS) and Aerial Photogrammetry [4,40–43] are becoming more and more used for volumetric analyses of rock falls [44–47], geomechanical characterization [21,48–51] and long-term monitoring of slow movements [52,53]. However, such technologies suffer some limitations for real time monitoring implementation (e.g., automated data processing, measurement repeatability, reliability, etc.). Therefore, their implementation in early warning systems has not been fully achieved [54,55].

In this context, this work shows the field activities performed at the Poggio Baldi Landslide Natural Laboratory (hereafter referred as PBL) with the aim to combine data acquired from different ground-based remote sensing sensors for rockfalls assessment and monitoring. The PBL, developed since 2015 by the joint effort of the Department of Earth Sciences of "Sapienza" University of Rome" and NHAZCA Srl [56], is today an ideal environment for testing the potential of different remote sensing technologies thanks to the frequent rockfall activity of its scarp.

The paper discusses the results of a three-day intensive monitoring campaign (14–17 May 2019) based on continuous Terrestrial Interferometric SAR (TInSAR) data (i.e., every 30 s for 72 h), multi-temporal Gigapixel images and acoustic records. Real-time analysis was carried out for TInSAR data, while optical Gigapixel images and acoustics data were subsequently processed by means of change detection and frequency analysis respectively. These monitoring activities were performed at PBL with the purpose of assessing the potential gains from the combined use of ground-based remote sensors and improving the knowledge of the ongoing gravitational processes.

In addition to the Introduction Section, the paper is organized in five main chapters. The Materials and Methods Section describes the employed methodology and equipment used. In Section 3 the geological and geo-morphological setting of PBL is described as well as its recent rockfall activity. Section 4 shows the main results of this field-work and the results are analysed in Section 5. Finally, the main conclusions are presented in Section 6.

2.3 Materials and Methods

In this section, the monitoring techniques used during the three-day monitoring campaign at PBL are presented including their technical specifications, settings and location on-field (Figure 2.1). It is worth highlighting that innovative tools, at the disposal of the research team, were used for the first time in an integrated way for an intensive monitoring campaign.
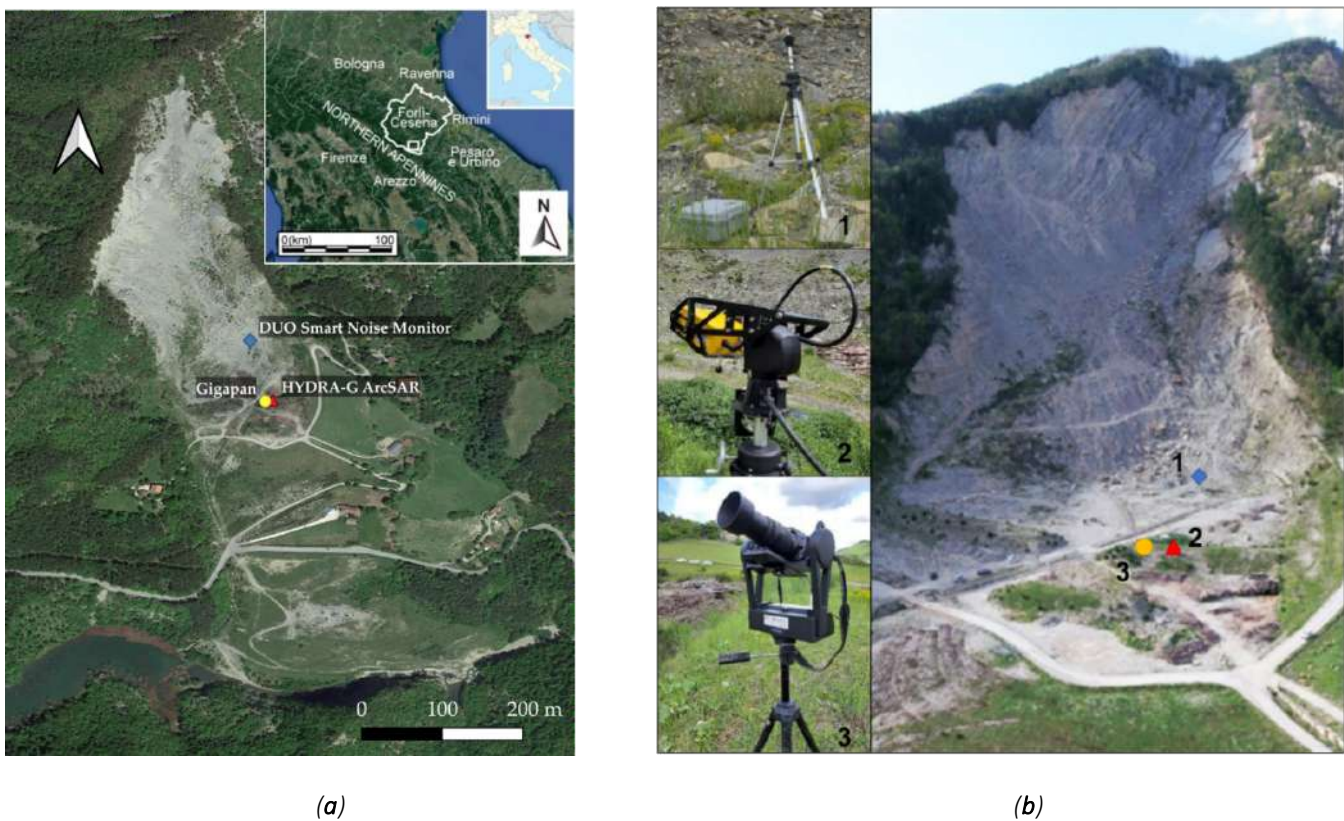
(a)   (b)

Figure 2.1. *Operational ground-based remote sensing tools during the intensive monitoring campaign at Poggio Baldi*
*Landslide Natural Laboratory (PBL): (**a**) Top view of the slope including the location of monitoring instruments. Upper right*
*inset with enclose the geographical frame of the Forlì-Cesena province in the Northern Apennines; (**b**) UAV picture of the*
Poggio Baldi landslide upper slope and the corresponding positions of 01dB DUO Smart Noise Monitor (1), HYDRA-G ArcSAR
(2) and GigaPan Epic Pro V system (3) about the rock cliff under study.

Regarding the methods used, before the field activities (i.e., data acquisition stage) a
reasonable amount of time was dedicated to the designing of monitoring activities to be carried out,
taking into account the specific conditions of the landslide process, previous studies and evidence
from past field surveys. In detail, the definition of the main parameters to be monitored, the
identification of the most appropriate technological solutions and the setting of measurement
procedures with their on-field operational activities were carried out.

In this way, a systematic approach to planning the monitoring network was applied [57]. The
planning activity started by analyzing and defining the project conditions which included the analysis
of existing documents, data and literature describing the recent history of the landslide process. Focus
was on physical parameters such as those which were objects of the intensive monitoring campaign:
surface movements, sounds produced by cracks/joints opening and rockfalls. All these conditions
were integrated with available geological and geotechnical information to provide for a

comprehensive picture of the situation to deal with. In addition, given the remote location of the landslide, particular focus was paid to logistics aspects (e.g., power supply, telecommunications, safety of workers, etc.).

2.3.1 GigaPan

Gigapixel identifies a digital image achieved by stitching technique, i.e., by merging several images acquired from the same position covering the whole view of interest. These digital images can be composed of billions of pixels or more (equal to or greater than 1000 Megapixels) [58–60]. As commercial DSLR cameras generally use sensors with more than 20 million pixels (20 Megapixels), to create a Gigapixel image it is required the use of tool like GigaPan EPIC PRO, produced by GigaPan Systems LLC [61]. GigaPan was created in 2008 by a research collaboration between NASA and Carnegie Mellon University to develop a high-resolution imaging technique for use in the Mars Exploration Rover mission. In short, the GigaPan system allows the sequential acquisition, using a robotic head (Figure 2.2), of hundreds of partially overlapped (40–80%) images, thus avoiding parallax errors. This result is achieved thanks to a robotic head mounted on a tripod that allows the rotation of the camera around the point of no parallax (NPP) [62,63]. The overlapping areas are exploited by the stitching software to determine the points of correspondence, from which starts the reconstruction of the image and the rearrangement of the pixels' number. To date, this technique saw its greatest use in geosciences as a qualitative way for the representation and interpretation of high-resolution scenarios [64]. The use of Gigapixel images as raw data processed by innovative PhotoMonitoring techniques (e.g., using Change Detection algorithms) may represent an effective starting point for quantitative analysis for assessing and monitoring purposes. That means capturing high-resolution images over time from a fixed position and comparing them, thus performing a 2D Change Detection (2D-CD) [65–67].

(a)   (b)

Figure 2.2. GigaPan acquisition system used at PBL: (**a**) GigaPan robotic head with screen and controls; (**b**) GigaPan system equipped with a Nikon D5000 camera and 300mm telephoto lens.

For the present case study, the high-resolution images in RGB colors have been acquired by the GigaPan Epic Pro V system [68] (produced by GigaPan Systems LLC), equipped with:

- Digital camera Nikon D5000 with 23.6 × 15.8 mm CMOS sensor (12.3 Megapixel).
- Telephoto lens with variable focal length up to 300 mm.

The single shots, acquired up to a maximum distance of 700 m from the cliff, were processed through the stitching software Image Composite Editor (ICE, Microsoft) [69]. The stitched images were represented by an original resolution of 2.2 gigapixel. However, in order to facilitate further processing operations, the images have been resampled to a lower resolution (572.28 megapixels) and finally exported. Once the stitching phase was completed, the images were imported into the free software QGIS to carry out the 2D-CD through the co-registration made by the georeferencing and the raster alignment tools. Within the 2D-CD, rockfall areas were detected and measured, and finally enclosed into a unique vector file. For such analysis, the GigaPan system was used from the same position with a time interval of two hours during the monitoring campaign (daytime only).

2.3.2 Terrestrial ArcSAR Interferometry

In the last decades, one of the most effective technologies among landslide monitoring systems has been Terrestrial SAR Interferometry, which exploits the interferometric technique (i.e., by comparing the phase signal difference between two or more images collected at different times) measuring the displacement along the Line of Sight (LOS). This technology has several advantages, including the capability to collect data under any weather and lighting conditions, a high data sampling

rate (up to few seconds), and does not require direct interaction with the investigated area (e.g., targets are not mandatory) [70–73]. The first applications of SAR interferometry (InSAR) appeared in the early 1990s, using radar images taken from satellites to measure displacements on the ground [74–79]. Terrestrial SAR interferometry (TInSAR) also referred as Ground-Based Interferometric Synthetic Aperture Radar (GB-InSAR), is a technique for displacement monitoring based on the same principles of satellite-based InSAR [78–84]. TInSAR is an active microwave acquisition system operating in the Ku-band (12–18 GHz) which uses phase measurements of the radar signal to detect displacements of targets; therefore, it is able to acquire images in any weather conditions during both day and night, and for each pixel of a SAR image, a phase value is measured along the LOS of the radar [85–89].

Differently from conventional SAR systems for landslide monitoring, consisting of radar antennas that move along a linear scanner, Terrestrial ArcSAR Interferometry uses sensor motion along a circular trajectory (e.g., along an arc) to create the synthetic aperture [88,90]. The ArcSAR configuration (i.e., radar antenna placed on a tripod which follows a circular movement) has solved many drawbacks of conventional TInSAR, such as large sizes, heavy weights, and significant on site infrastructure requirements [91]. Basically, ArcSAR allows to retrieve better resolution with smaller antenna [92,93].

In the framework of the present study, a compact ArcSAR called HYDRA-G designed and manufactured by IDS GeoRadar (part of Hexagon) was used (Figure 2.3). Such an instrument is able to provide displacement measures with a sub-millimetre accuracy, by combining a very high phase measurement accuracy (<0.1 radians) and a short wavelength (4 mm) [55]. Its maximum range is about 800 m with a field of view up to 120° (horizontal) and 30° (vertical) and its operating temperature is −20°C to +55 °C. The image resolution is 0.2 m in range and 14 mrad in cross-range. The maximum sampling interval is of about 30 s. The instrument is also equipped with an optical and infrared HD camera and with a short-range laser scanner in order to provide real-time images and to autonomously reconstruct the geometry of the monitored scenario.

(a) (b)

Figure 2.3. (a) HYDRA-G equipment; *(b)* Terrestrial ArcsSAR Interferometry installed at PBL.

The equipment was deployed within the monitoring site of PBL in the vicinity of the other instruments used. The selection of the radar location represented a crucial factor for the monitoring activities and data interpretation as the radar measurements are computed only along the LOS. In detail, the radar with its tripod was placed in a stable and safe area about 400 m away from the scarp in order to obtain a field of view including both the vertical rock cliff and the debris talus at its toe (Figure 2.1). The radar measurements started on 14 May 2019 from 11:00 (UTC+ 01:00) and ended on 17 May 2019 at 11:15 (UTC+ 01:00) for a total of 72 h of monitoring.

2.3.3 Acoustic Measurements

The acoustic signal measurements were carried out on the sound level meter DUO Smart Noise Monitor (FW 2.45, class 1 IEC-61672 certification) produced by 01dB company (part of ACOEM Group, Limonest, Rhône, France) and combined with an outdoor microphone unit of type DMK01, especially designed to split the microphone from the instrument body. This unit is made of a stainless-steel body, a dedicated preamplifier (PRE22) connected to the external output, a noise cone and a specific windscreen (Figure 2.4). The 01dB DUO can measure one-third octave band noise levels down to 6.3 Hz together with recording audio samples up to 180 dB at set intervals.

(a)   (b)
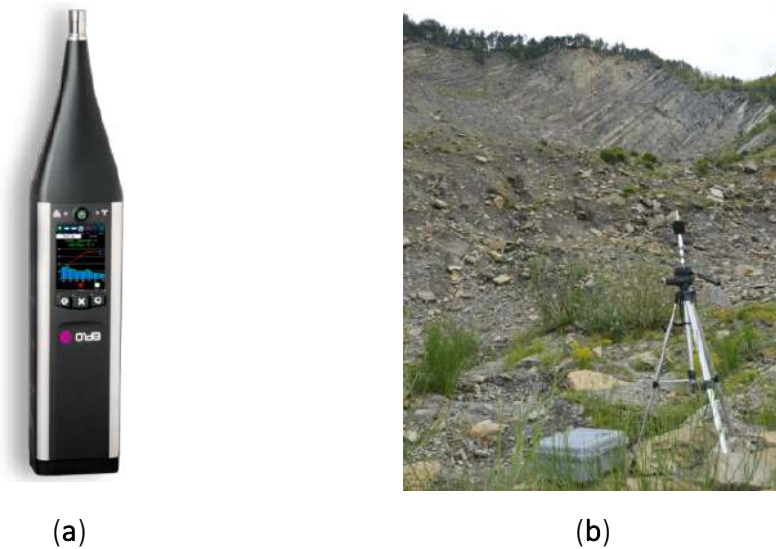
Figure 2.4. *Overview of the 01dB DUO Smart Noise Monitor: (a) DUO instrument body in LOG mode; (b) Outdoor microphone unit DMK01 and the waterproof case DSC01 containing the instrument body during the rockfall monitoring campaign carried out at the PBL.*

Regarding acoustic landslide monitoring, instantaneous sound pressure levels (dB) and spectra (Hz) have been recorded [94,95]. In this way we could analyse and classify them by using the proprietary software dBTrait 6 in post-processing LOG mode (Integrating Logging sound level meter), a kind of signal capture which includes the storage of time histories.

According to the aim of identifying rockfall occurrence and its spectral signatures, we recorded both sound pressure levels and frequencies on 15 May 2019 from 18:00 to 19:00 (UTC+ 01:00) and on 16 May from 12:40 to 15:10 (UTC +01:00), installing the microphone unit on the lower part of the debris generated by the rock cliff (Figure 2.4b). These activities were allowed thanks to the waterproof DSC01 case which provide complete protection to the DUO instrument also for mid- and long-term environmental sound measurements. With this configuration, the external microphone DMK01 with its tripod was the only outdoor instrument.

Once rockfall events were recognized and classified using the dBTrait software, we were able to visualize their spectra with frequency-weightings of type "Lin", and compare them with each other and with environmental sounds like birds, water runoff and aircraft noise, with the aim of defining the spectral contents of rockfalls arising from the Poggio Baldi rock cliff. Audio tracks of rockfall events and other environmental noises are available as supplementary materials.

## 2.4 Test Site of Poggio Baldi Landslide

2.4.1 General Framework

The PBL is located in the municipality of Santa Sofia (northern Apennines, Emilia Romagna Region, Italy), close to the Corniolo village, and it is reported in Sheet no. 265 "S. Piero in Bagno "scale 1:50000 of the geological map of Italy [96]. The Poggio Baldi landslide develops from the slopes of the homonymous mountain (43.910538° N, 11.807625° E), on the hydrographic left of the Bidente river, to the stream below, and it represents one the most prominent geomorphological features of the Bidente Valley. The first activation dates to 25 March 1914, whereas the last reactivation of the landslide deposit took place on 18 March 2010, and it was triggered due to the increase of water pressure in the pores of the paleo-landslide's body following the melting of the snow blanket caused by a sudden increase in temperatures. The landslide has an estimated volume of about 4×10^6 m^3 [56], and it is currently active in its upper scarp due to frequent rockfall events [47].

Thanks to its distinctive features, which are representative of many landslides worldwide in terms of material involved, type of movement and triggering factors, the PBL was established in 2015 [56] with the aim of testing innovative remote sensing technologies in such a characteristic environment [47,97].

2.4.2 Geological and Geomorphological Setting

The slope involved in the Poggio Baldi landslide is a part of the hanging-wall of a major thrust system (i.e., San Benedetto in Alpe) and is composed by the Marnoso-Arenacea Formation (Miocene), involving an alternation of claystone, siltstone and sandstone, arranged in a monoclinal dip slope sequence (Figure 2.5) [56,97–101]. Landslides involving Flysch sequences, which are characterized by geo-lithological complexity and heterogeneity, are widely diffused in the northern Apennines as well as in other mountain chains [102–105]. A slight bending of the strata occurs in the lower part of the slope: the bedding attitude, dipping at about 45° upslope, progressively decreases reaching dip angles of about 15–20° downstream. A set of high angle, normal faults oriented roughly perpendicular to the main thrust geared NW-SE complete the structural frame [56,97,99,106]. The geomorphology of this sector is strongly controlled by the structural setting and the recent tectonic activity. Thanks to the progressive erosion of the Bidente river, gravitational processes, featured by different landslide

types with a very wide range of dimensions, are one of the most significant morpho-genetic factors of the area.
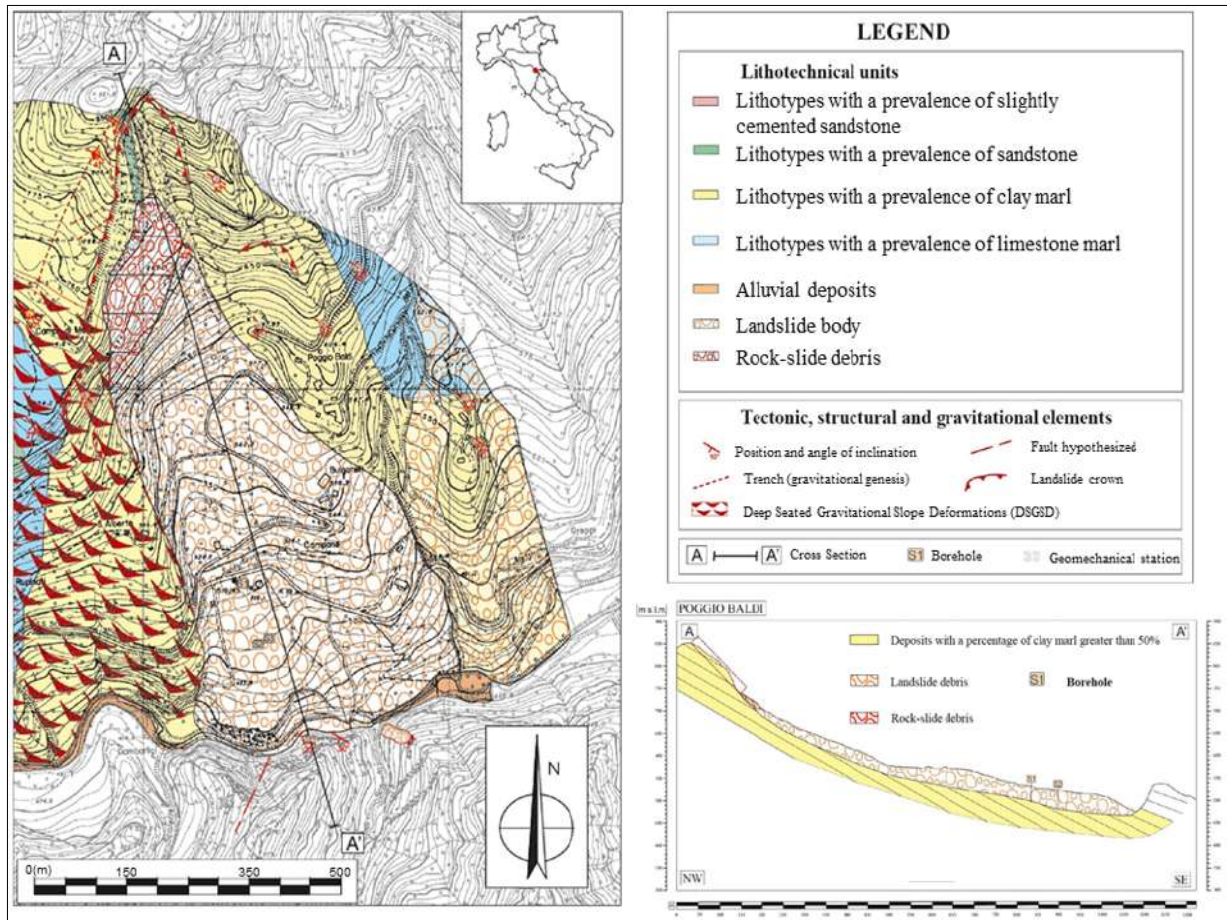
Figure 2.5. *Geological map of the Poggio Baldi landslide area with a related cross-section along its body. The investigated rockfalls arise from the rock cliff outlined by the red dashed line and by the red box in the cross-section; modified from [47].*

According to [47,56,97], the landslide can be classified as a complex process initially set as a rock wedge slide (1914) followed by rockfall processes arising from the resulting head scarp. Following a long period (about a century) of rock debris accumulation on top of the landslide deposit, a critical overload, combined with intense and prolonged rainfall and snow melting, led to reactivation of the landslide deposit (2010) which evolved into a composite movement presenting rotational debris, earth slide [1,107] and flow slide-like movement [56,97,108,109]. The landslide was also favoured by the structure dip out of the outcropping rocks. The main rock slope, the target of this study, is a sub-vertical scarp with a rise of about 100 m and a width of 250 m and it is characterized by high-frequency rockfall processes.

2.4.3 The Occurrence of Recent Rockfall Events

Since the first activation in 1914, despite the following steady state of the main landslide body, the newly formed vertical rock cliff has always been frequently affected by rockfalls, which accumulate at the base of the scarp generating a debris talus which continuously increases its volume [47]. The instability is predisposed by geologic, geomorphologic and structural factors, such as the alternance of arenaceous and clayey strata and the presence of several discontinuities. In [97] it is demonstrated that the bedding is the main discontinuity system on the slope face and the joint set N108/73° (here called JS 1), is the prevalent joint system. Using the Markland method [110] different failure mechanisms like translational sliding movements of rock wedges, translational planar sliding and direct toppling were detected. Moreover, considering the progressive erosion of the clay strata, which gradually increases the overhang of the arenaceous strata, rockfalls are mainly triggered by: (i) the breaking of the arenaceous mass due to shear strength exceedance (Figure 2.6a) and, (ii) the intersection of a JS 1 joint with the exposed surface of the cliff (Figure 2.6b). The detached debris and blocks often find deposition surfaces over the underlying arenaceous strata. Over time, the volume of fallen material increases on the overhanging strata till the debris friction angle ($\phi = 15°$) is exceeded, with the consequent remobilisation, or the strata collapsing. These conditioning factors, combined with each other, are the main cause of the widespread instability throughout the vertical rock cliff. As a matter of fact, [47] estimates the general loss of volume from the vertical rock cliff to be in the range of 2.0 to 2.8 × 10^3 m^3 per year.

(a)   (b)
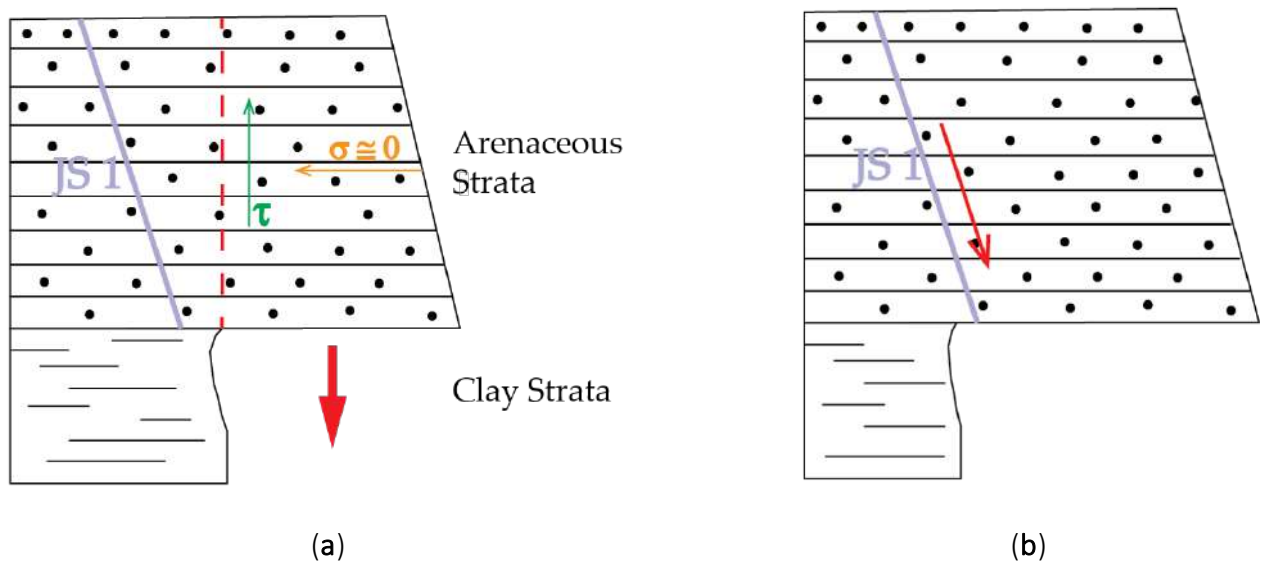
Figure 2.6. Conceptual model related to the two main triggering mechanisms of rockfall phenomena on the Poggio Baldi rock cliff: (*a*) Breaking of the arenaceous mass due to shear strength (τ) exceedance; (*b*) Failures due to planar sliding along the JS 1 discontinuity set.

2.5 Results

3.5.1 GigaPan

The 2D-CD from GigaPan images allowed us to identify and map a total number of 84 rockfalls, developed in the three days of monitoring, with 32 rockfalls occurring on the first day, 9 rockfalls on the second day and 43 on the third day of monitoring. The most active portion of the rock cliff between 14 and 17 May 2019 was the central one, and it is pointed out in Figure 2.7.

Using the different Gigapixel images, rockfalls were dated with an accuracy of two hours. For example, the rockfall depicted in Figure 2.8, having a surface of about 0.5 m2, occurred on 16 May 2019 between 11:50 and 13:50. To calculate the surface of the rockfall and its size, it was necessary to define the Ground Pixel Size (GPS) using the 3DM CalibCam software and an object distance calculation spreadsheet tool, knowing the exact distance between the GigaPan station and the rockfall source zone. From the analysis of the Gigapixel images, acquired every two hours, it was possible to identify both the debris movements on the cliff and at the base of the cliff. The detailed analysis of such images allowed us to also observe some precursory movements of the rock blocks, which later collapsed. An example is given in Figure 2.9, where it shown the evolution of the same rock block which moved two days before its collapse, progressively changing its dip angle.

(a)
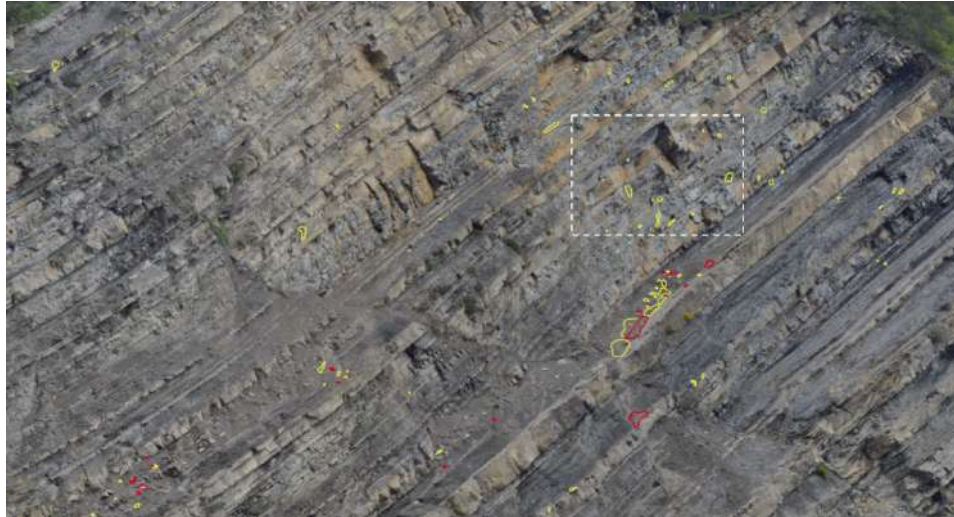
(b)

Figure 2.7. Gigapixel image with all rockfalls detected during the three days monitoring campaign: (**a**) 2D Change
Detection (2D-CD) along the Poggio Baldi cliff with detached rock falls (yellow) and debris removal (red); (**b**) Zoom of the
most active sector during the monitoring campaign.

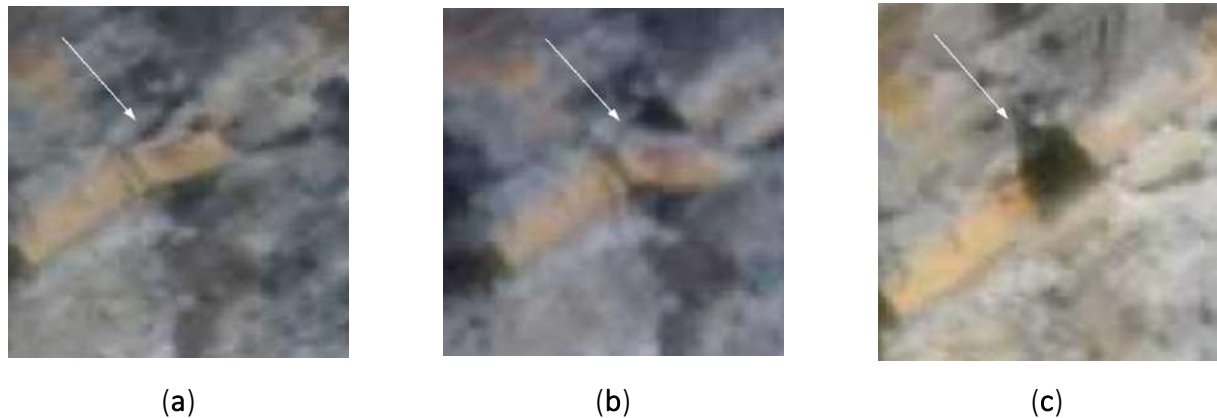(a)   (b)   (c)

Figure 2.8. Example of a rockfall which occurred on 16 May 2019 between 11:50 and 13:50 local time: (**a**) Image of 11:50;
(**b**) Image of 13:50; (**c**) Location of the rockfall event in the cliff (white-dashed box in Figure 7b).

(a)　　　　　　　　　　　　(b)　　　　　　　　　　　　(c)

Figure 2.9. *Evidence of precursory movements before the rockfall event as indicated by the withe arrow: (**a**) Zoomed Gigapixel image of 14 May 2019; (**b**) Zoomed Gigapixel image of 15 May 2019 with the tilted rock block; (**c**) Zoomed Gigapixel image of 17 May 2019 after the failure.*

3.5.2 Terrestrial ArcSAR Interferometry

The radar monitoring by using the HYDRA-G equipment was carried out with continuous acquisition for 72 h. Data were processed directly on-field by the Guardian software provided by IDS GeoRadar. Thanks to a rugged tablet it was possible to continuously check on-site the evolution of the monitoring parameters (e.g., displacement map and time series, reflectivity map, etc.) and the status of the system during all phases of the work.

Following the data processing, all pixels containing the measurement information along the LOS (Radar-slope) were overlaid to a 3D model of the slope, generated by the instrument itself. Each pixel contains the cumulative displacement data of the 72 h of acquisition. As shown in Figure 2.10, the maximum cumulative displacement recorded during the 3-days monitoring by the ArcSAR instrument was about 5 mm (along LOS, approaching the sensor). The most active sector detected by the radar, displayed in red, was the debris talus located at the toe of the rock scarp with some portions bordering the scarp itself. In addition to the displacements recorded on the debris talus, a significant cumulative displacement of approximately 5 mm was identified in the central sector of the slope (Figure 2.11). According to the radar measurements, such areas (D1 and D2) suddenly moved between 14 and 15 May 2019.
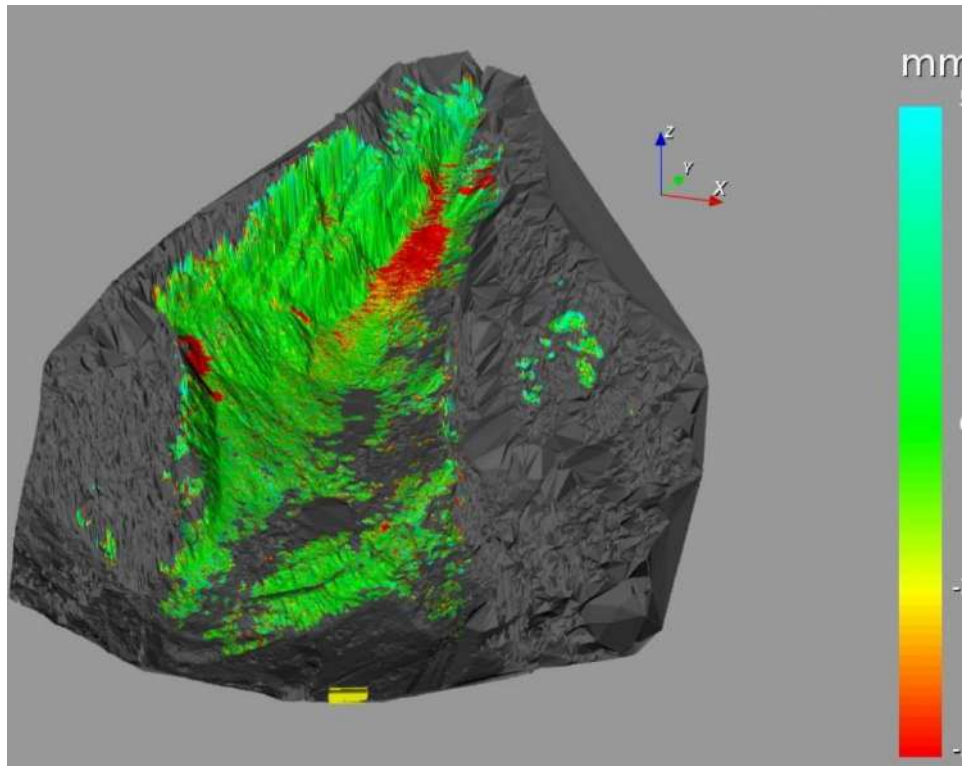
(a)
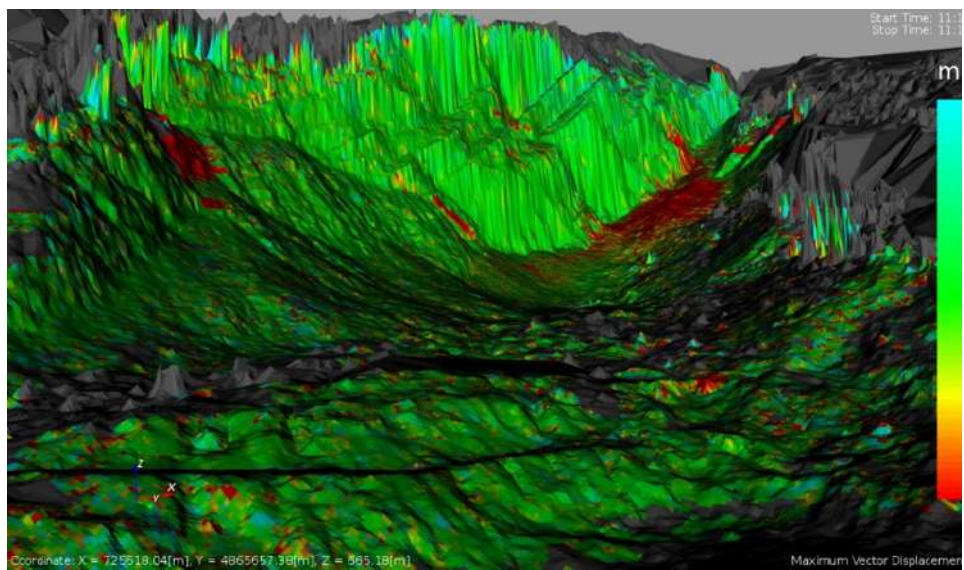
(b)

Figure 2.10. Line Of Sight (LOS) displacement map as result of 72 h monitoring of the Poggio Baldi landslide by HYDRA-G ArcSAR: *(a)* Landslide top view with the cumulative LOS displacement map overlaid on the 3D model of the slope; *(b)* The same LOS displacement map from the viewpoint of HYDRA-G.
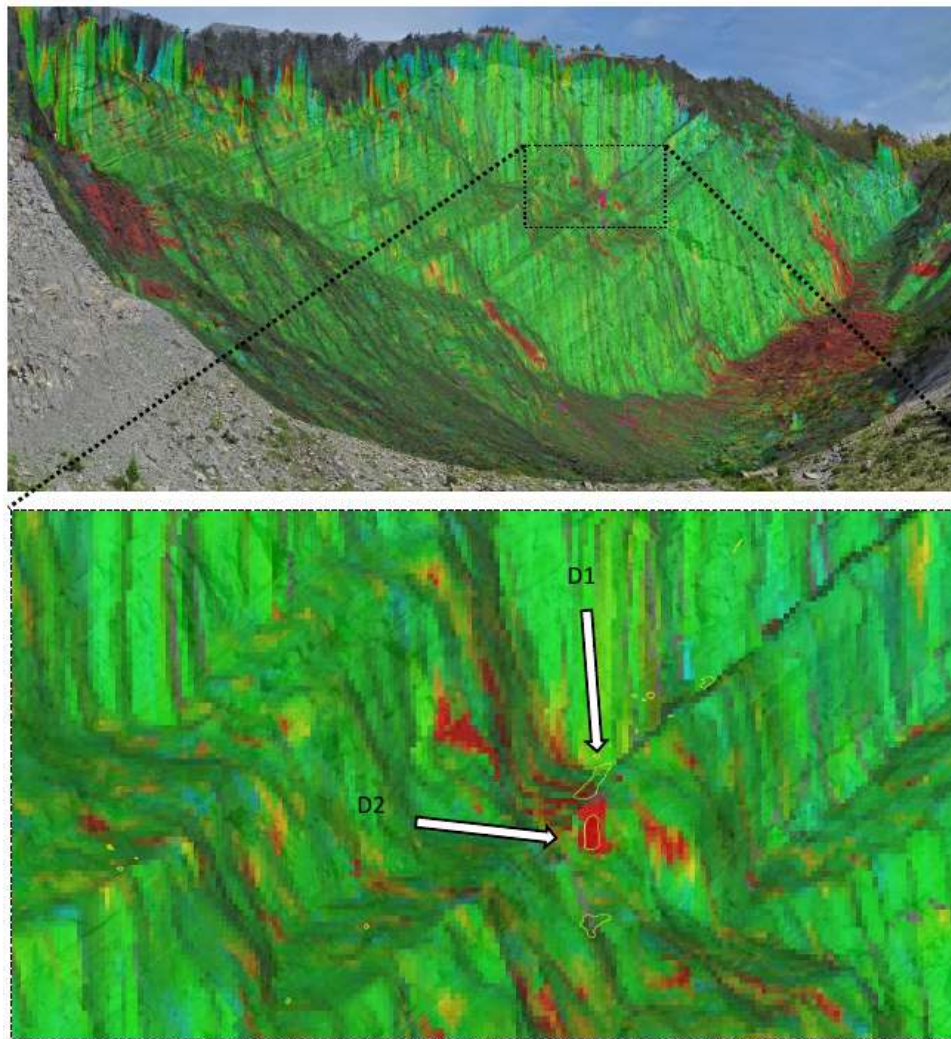
Figure 2.11. *Central sector of the slope with correspondence between changes detected by radar measurements (green-red pixels) and GigaPan image analysis (yellow polygons); D1 and D2 polygons indicate areas that suddenly moved between 14 and 15 May 2019.*

3.5.3 Acoustic Measurements

The collected acoustic signals allowed us to identify both the exact time of rockfall events and their signal characteristics in terms of sound pressure levels and spectral contents with a period of 100 ms. During the monitoring time span, three rockfall events were registered. The first one was artificially triggered by an operator by scaling a boulder in the middle part of the debris lying on the slope. This rock block felt for about ten metres before stopping at the bottom of the debris. By analysing the acoustic signal produced by the fallen rock block (Figure 2.12a), the final impact is clearly detectable (i.e., 15 May 2019, 18:28:09:000 UTC +01:00). Its noise peak reaches 64.7 dB at the frequency of 315 Hz (Figure 2.12a). The corresponding frequency histogram shows values above 60

dB with frequencies ranging between 250 and 500 Hz. Thanks to the sonogram, it was possible to investigate the amount of dBs for different frequencies and time steps (Figure 2.12b). In Figure 2.12b, three peaks at 315 Hz corresponding to different impacts occurred during the fall, can be observed (i_1, i_2, i_3). Focusing on peak i_3, its frequencies with the highest sound values (greater than 50 dB) range between 200 and 630 Hz, with relevant contributions up to 1 kHz (49 dB) and 2 kHz (47.4 dB). For all the three impacts, sound values above 40 dB are also reported for frequencies ranging from 16 Hz to 80 Hz. In detail, those values were recorded with a time delay of 0.1 to 0.6 s from the block impact time.

Based on the results of the experimental rockfall, two different natural rockfalls detached from the rock cliff on 16 May 2019 at 13:28:00:400 and 13:59:40:700 (UTC + 01:00) were detected. Figures 2.13 and 2.14 show the acoustic signal of the first and second rockfall, respectively. For the first one, significant noise from birds, water runoff and aircraft was recorded. However, among acoustic records, birdsong, water runoff and aircraft noise are depicted by frequencies of about 4–5 kHz, 8–100 Hz and 6.3–250 Hz respectively (Figure 2.15) allowing us to separate them from the rockfalls related spectra.

The 13:28 rockfall event was a long event with a total duration of 10.3 s including the detachment of the rock block from the cliff and the subsequent downfall marked by several impacts before stopping on the debris. Figure 2.13a shows in red the soundtrack section classified as rockfall and its frequencies histogram, which records the highest values of dBs between 630 Hz and 800 Hz (45.1 dB and 46.5 dB respectively), considering lower frequencies as introduced by the aircraft noise. The related sonogram confirms those values. At 800 Hz of frequency, different peaks relating to impacts occurred during the collapse are clearly evident (Figure 2.13b).

The 13:59 rockfall event was quite different from the previous one. It was recorded only the detachment phase without clear evidence related to its eventual impacts along the cliff and on the debris. Therefore, as shown by the classified soundtrack (Figure 2.14a), its total duration was about 2 s. This event produced the highest sound values between 630 Hz and 1.25 kHz, with its peak at 1 kHz (45.7 dB). The sonogram confirms the absence of subsequent impacts of the block and made it possible to distinguish bird noise (4–5 kHz) from the noise produced by the rockfall itself (Figure 2.14b).
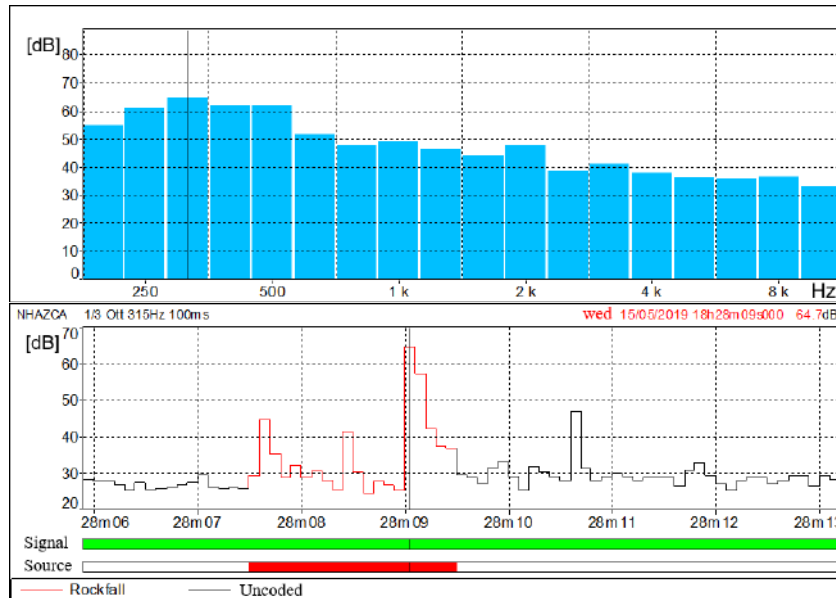
(a)
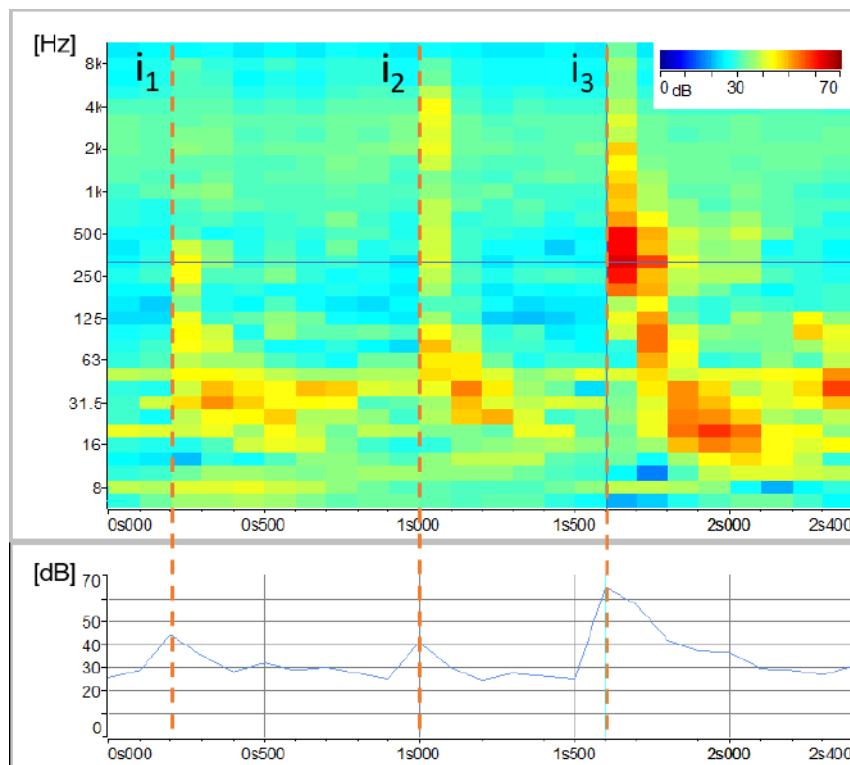
(b)

*Figure 2.12. Overall representation of the acoustic signal emitted by the rockfall event on 15 May 2019 at 18:28 (UTC +
01:00) with its related impacts (i_1, i_2 and i_3): (**a**) Spectral time history of the rockfall event with the classified soundtrack
(lower plot) and frequencies histogram (upper plot); (**b**) Focus on the audio track classified as rockfall by means of the
sonogram showing the amount of sound pressure levels expressed in dB as a function of time and signal frequency. The
plot at the bottom shows the amount of sound pressure level over time at the frequency of 315 Hz. Temporal resolution is
0.1s.*

(a)
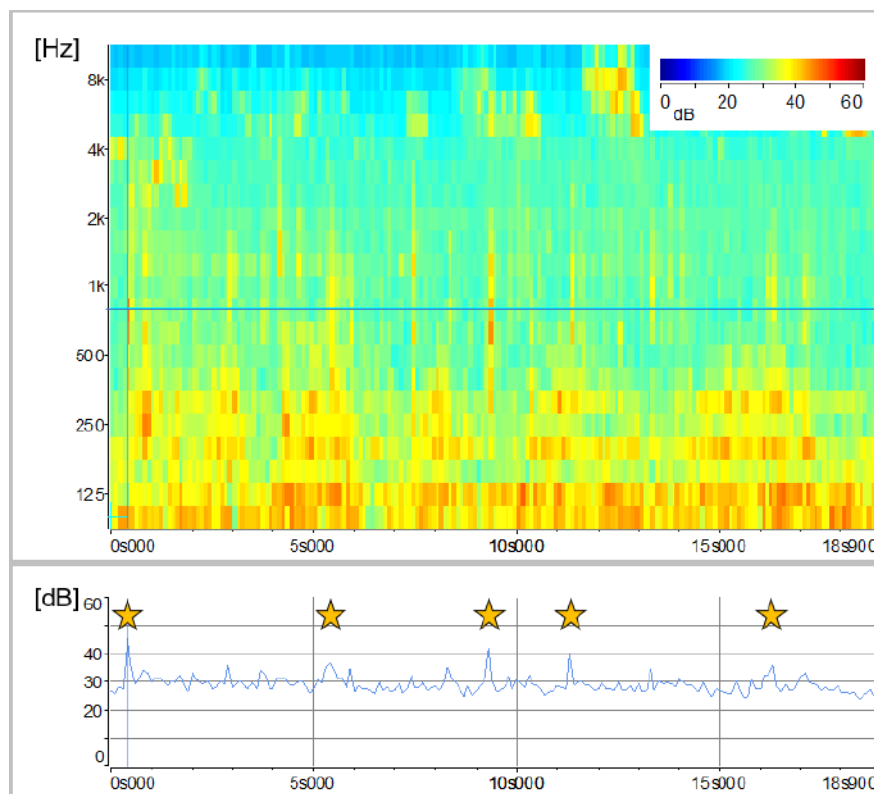
(b)

Figure 2.13. Overall representation of the acoustic signal emitted by the rockfall event on 16 May 2019 at 13:28 (UTC +
01:00): (**a**) Spectral time history of the rockfall event with the classified audio track (lower plot) and frequencies histogram
(upper plot); (**b**) Focus on the audio track classified as rockfall by means of the sonogram showing the amount of sound
pressure levels expressed in dB as a function of time and signal frequency. The plot at the bottom shows the amount of

sound pressure levels over time at the frequency of 800 Hz. Yellow stars refer to different impacts recorded during the collapse. Temporal resolution is 0.1s.
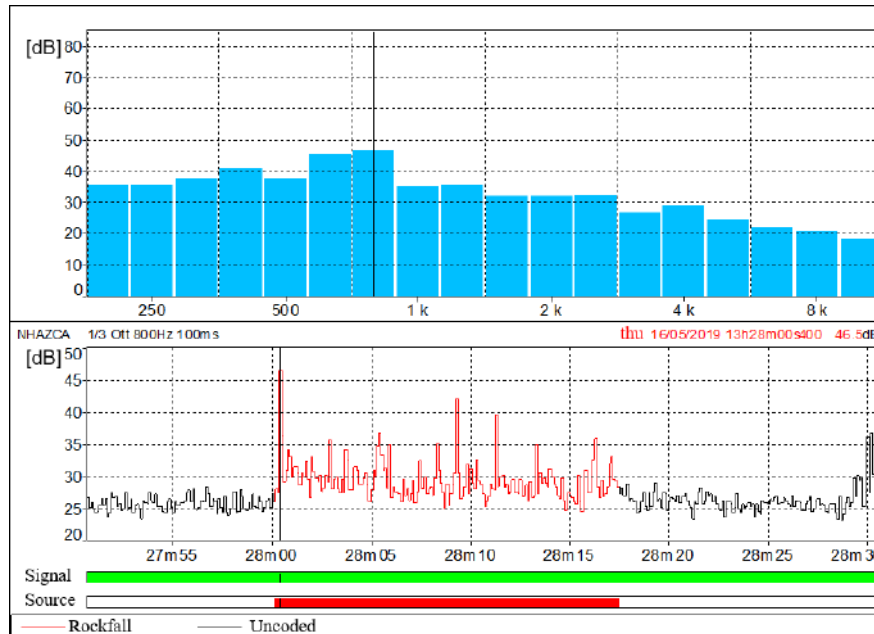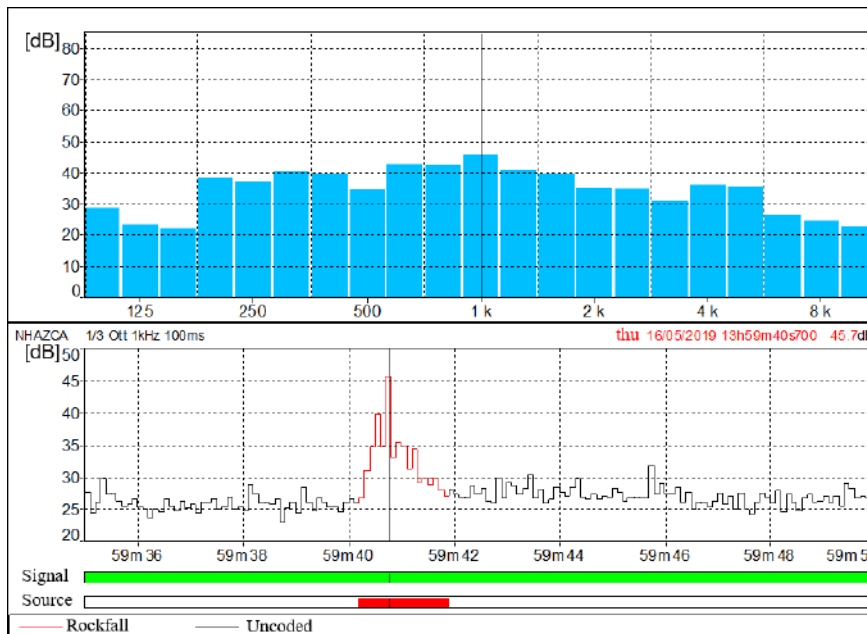

(a)
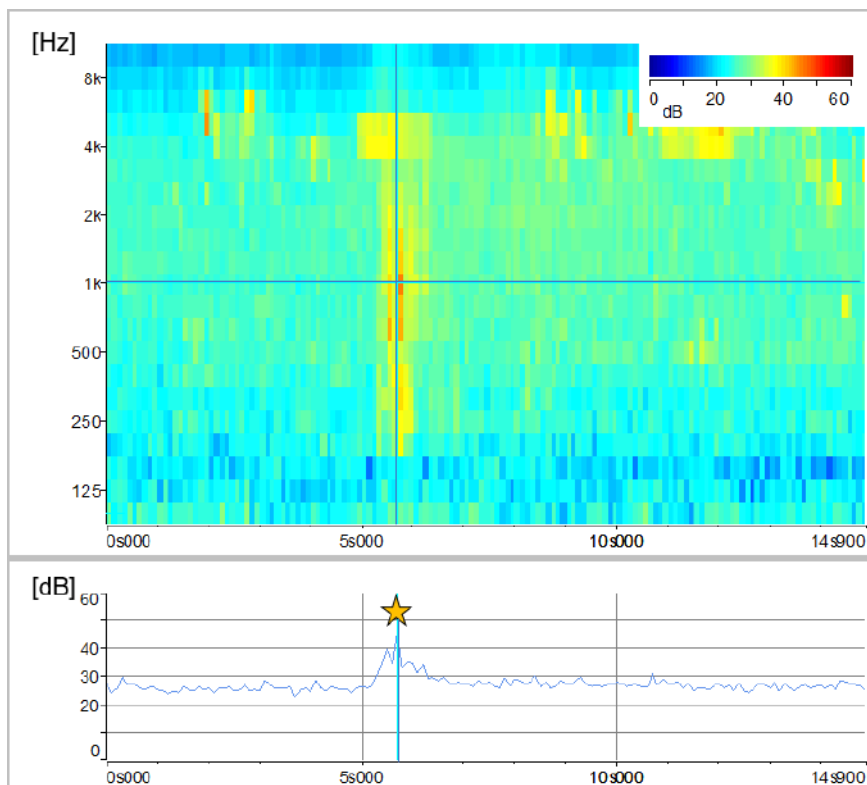
(b)

Figure 2.14. *Overall representation of the acoustic signal emitted by the rockfall event on 16 May 2019 at 13:59 (UTC + 01:00): (a) Spectral time history of the rockfall event with the classified audio track (lower plot) and frequencies histogram (upper plot); (b) Focus on the audio track classified as rockfall by means of the sonogram showing the amount of sound*

pressure levels expressed in dB as a function of time and signal frequency. The plot at the bottom shows the amount of sound pressure levels over time at the frequency of 1 kHz. Yellow star refers to the time of the rock block detachment. Temporal resolution is 0.1s.

(a)

(b)

(c)
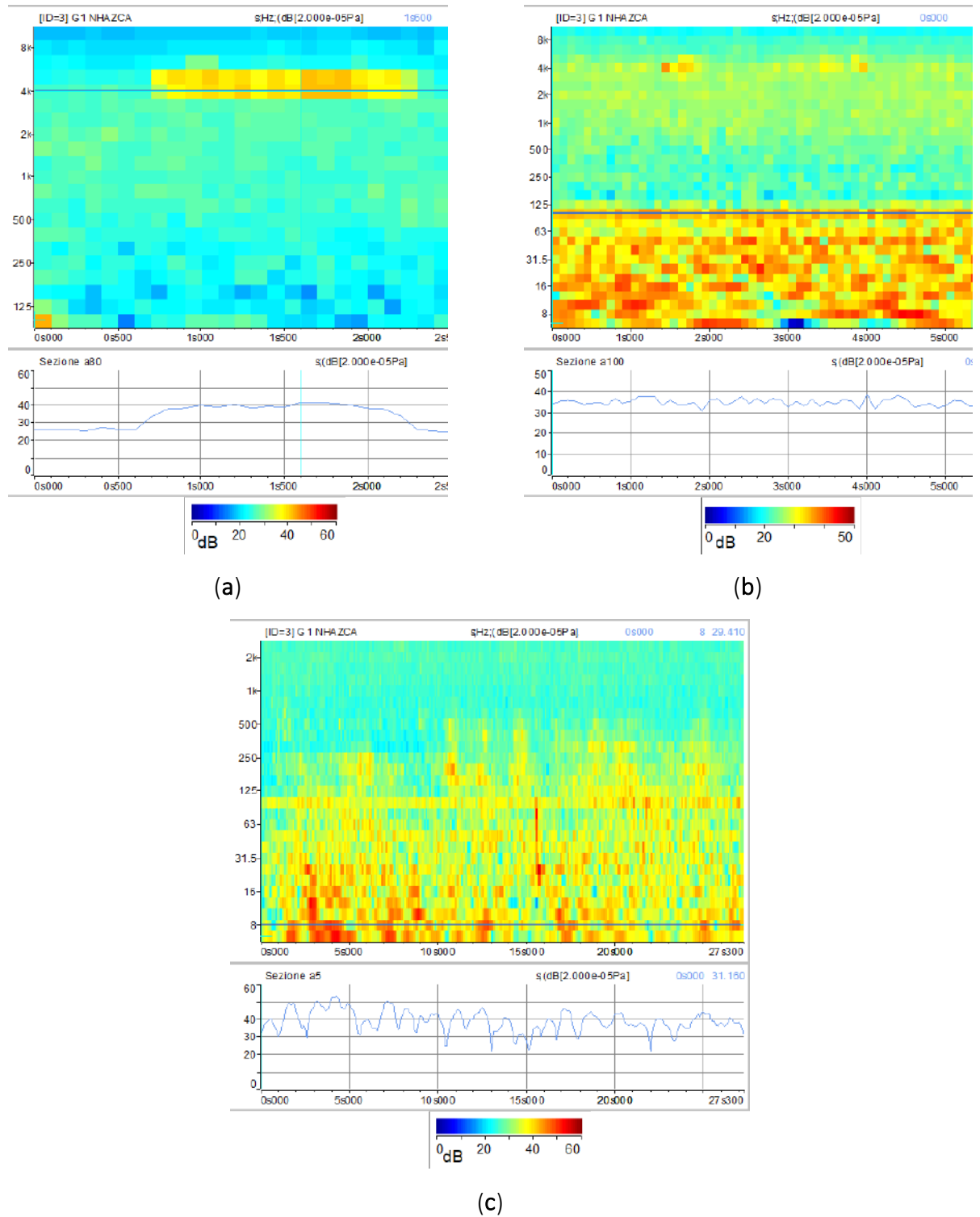
Figure 2.15. *Sonograms referring to specific noise sources recorded during the acoustic monitoring campaign: (a) Birdsong; (b) Water runoff; (c) Aircraft noise. Line plots underlying each sonogram show the amount of sound level expressed in dBs over time at a fixed frequency (dark blue line).*

5. Discussion

In the present study, the Gigapixel technique results in a high-performance tool, able to achieve images with a millimetric Ground Pixel Size (in the present case study up to 5 mm) from a sensing distance of several hundred meters (700 m). At the same time, it allows the capturing of RGB information useful in monitoring rockfalls and for the identification of lithological heterogeneities.

The 2D-CD allowed us to identify several rockfall events that occurred during the three-day monitoring campaign, precisely between 14–17 May 2019. Thanks to this technique, 84 failures along the rock cliff were identified and measured, many of which were attributed to rockfall phenomena even smaller than 1 m^2 (down to 0.06 m^2 at 500 m). The analysis of Figure 2.7 suggests that rockfalls mainly involved arenaceous mass and subordinately clayey strata. As noted by [47], they are clustered in the upper central portion of the rock cliff and accumulate at its toe. Furthermore, by means of several Gigapixel acquisitions within the same day, we were able to date rockfalls that occurred during the time span of two contiguous acquisitions (i.e., every two hours). Since only one rockfall event was detected through the 2D-CD performed with the pair of Gigapixel images acquired at 11:50 and 13:50 on 16 May 2019, it was possible to localise the source zone related to noise recorded at 13:28 by the 01dB DUO Smart Noise Monitor. Furthermore, knowing the exact Ground Pixel Size at that distance from the camera, we evaluated the areal dimensions of the collapsed rock mass in approximately 0.5 m^2.

As the acquisition and analysis of Gigapixel images is time consuming, the synchronous use of the acoustic and optical sensor allowed a more efficient selection of Gigapixel images. These images were then processed for change detection purposes in order to localize the source area of the collapsed rock block.

As showed in Figure 2.9, major rockfalls might be preceded by precursory movements (i.e., pre-failure deformation) highlighting the proneness of certain rock slopes to have deforming areas and associated opening fractures that precede the main failure event [111,112]. Gigapixel techniques can also be combined with LiDAR products for further analysis aimed at three-dimensional characterisation and monitoring of rock slopes [113–117]. In [62,115] the Gigapixel images have been used to identify unweathered rock surfaces in order to map recent rockfall source zones. Another approach achieved by [113] consists of using such a technique to perform granulometric analysis of talus in rock slopes. In the case of PBL, we tested the application of 2D-CD to take the process one

step further and present the use of Gigapixel images as a standalone tool to detect and date recent rockfall events as well as their geometrical features.

The use of Terrestrial ArcSAR Interferometry allowed us to perform a fully remote sensing monitoring of the Poggio Baldi landslide, without the need to place targets directly on the slope. Radar measurements were continuously carried out for 72 h (during both day and night) with acquisitions performed every 30 s. Thanks to its high temporal resolution and the integrated LiDAR, the radar was able to accurately date and locate the unstable processes occurred during the intensive monitoring campaign. In detail, between 14–15 May a sudden displacement of the D1 and D2 areas within the central sector of the slope was clearly detected. Such process was also confirmed by comparing the results from Gigapixel image analysis with the displacement time series recorded by the radar (Figure 2.16). In fact, D1 and D2 areas in Figure 2.16, were detected by the 2D-CD and interpreted as debris movements. However, radar system was not able to detect pre-failure deformations as observed with Gigapixel image analysis for the failure depicted in Figure 2.9. This could likely be due to the magnitude of deformation being above the level of detection (related to the wavelength of the radar system) or being shorter than the monitoring interval or due to monitoring geometry (e.g., no displacement along the LOS) or to the small size of the blocks, much smaller than the pixel size. Nevertheless, unlike the Gigapixel image analysis, radar data allowed to detect and quantify the displacement of debris talus at the toe of the scarp which reached a maximum displacement of 5 mm. Previous radar monitoring campaigns have been carried out at PBL using linear scanner TInSAR [56]. Thanks to the new monitoring campaign, through the use of HYDRA-G ArcSAR it was possible to focus the measurements within the unstable debris talus.

The complementary and combined use of sonograms relating to experimental and natural rockfalls together with sonograms relating to external noise sources, such as birdsongs, water runoff and aircraft noises, allowed us to study sound pressure levels of rockfall phenomena as well as their spectral contents. According to the results, we can state that features of acoustic signals vary with the volume and distance of the rockfalls from the microphone unit, as observed by [95]. This is also confirmed by [118], who affirms that landslide volumes are directly proportional to the spectral magnitude. Hence, a unique spectral signature of rock blocks falling from the Poggio Baldi landslide scarp is barely discernible. A further factor is the different sound attenuation level, which depends on the amount of atmosphere through which the sound waves travel. However, a narrow range of frequencies (200 Hz to 1000 Hz) can be designated as those most representative of rockfall signals. The assumption is validated by the experimental rockfall we triggered, which was both the least-

affected by other noise sources and the closest to the microphone unit DMK01. In addition, according to [95], significant acoustic waves in the range of infrasonic frequencies (<20 Hz) up to 80 Hz were produced by the artificially triggered rockfall. However, as the other rockfalls recorded excessive noises in that frequency range, this spectral content can not be confirmed.

By comparing the three acoustic measurements we can also deduce different degrees in rockfalls fragmentation. Often, the detached mass breaks up on impact [107,119]. Rockfall fragmentation is the process by which the detached mass loses its integrity as it drops down a steep slope and shatters into smaller pieces [120]. Hence, the sonogram would show a series of minor randomly distributed peaks instead of a single well-defined impact.

As a result, for the artificially triggered rockfall (Figure 2.12), which did not exhibit fragmentation, the highest sound value is recorded at its third impact. Whereas we can assume a progressive and an instantaneous fragmentation respectively for the second and the third recorded rockfall (Figures 2.13 and 14). For the second one, fragmentation is suggested by the gradual reduction in the acoustic waves power as the number of impacts increases; while for the third one, it is indicated by the absence of audible impacts during the collapse. In our opinion, these different behaviours in fragmentation are due to lithological composition (i.e., sandstone or marl) and/or various fracture intensities of the rock mass. However, further studies are needed to confirm this hypothesis.

14/05/2019 at 18:45 (UTC +01:00)   15/05/2019 at 19:58 (UTC +01:00)

(a)

(b)
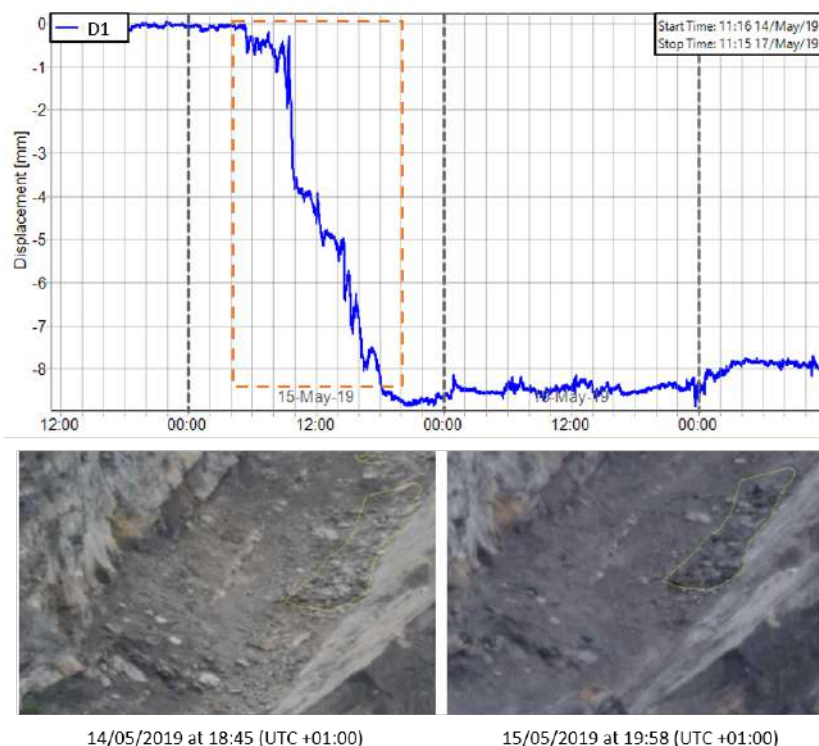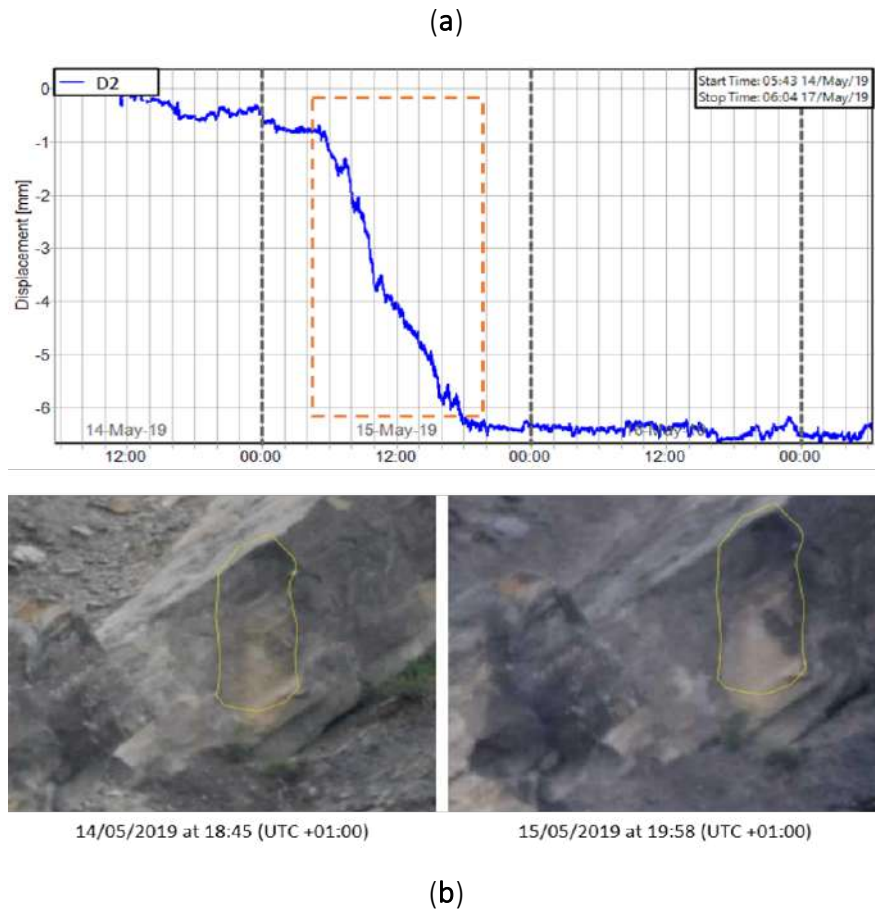
Figure 2.16. Comparison between radar measurements and Gigapixel analysis for D1 and D2 areas: (*a*) Displacement time series of D1 area measured by radar (above) and pre/post event images taken by GigaPan (below); (*b*) Displacement time series of D2 area measured by radar (above) and pre/post event images by GigaPan (below).

6. Conclusions

The aim of this study was to evaluate the potential of innovative remote sensing rockfall monitoring systems and to characterize the very short-term gravitational processes ongoing at the Poggio Baldi landslide, with a specific focus in its upper part. For the first time, in-depth studies combining Terrestrial Interferometric ArcSAR, Gigapixel imagery and acoustic signals related to slope stability were carried out. The results of the monitoring campaign revealed the capabilities and limitations of each used tool: ArcSAR provided displacements of debris accumulated both at the toe of the scarp and on the arenaceous strata after the detachment. Gigapixel images have been analysed carrying out a 2D-CD in order to investigate the short-term evolution of the vertical rock cliff. This approach allowed us to detect and isolate several rockfalls events consisting of both sandstones and marls. Moreover, thanks to the short time interval of GigaPan acquisitions, pre-failure deformations prior to rock fall were observed. As well as ArcSAR data, Gigapixel image analysis was able to identify small deformations of the accumulated debris on the bulging strata surfaces that evolved into debris avalanches. Further, acoustic measurements were analysed in both acoustic decibel curves and time-frequency spectrum, revealing the ability of such sensors to detect failure occurrences and dominant frequencies affected by rockfall related signals. These unique properties could be used to automate the detection of future events.

Despite these capabilities, some open points in the assessment of PBL rockfall activity are still present. For instance, the obtained results could be combined with three-dimensional data such as point clouds, in order to achieve rockfalls frequency-volume relationships.

With reference to the integration of acoustic measurements and Gigapixel 2D-CD, we argued that the combination of these techniques should be intended as an integrated monitoring method aimed at improving the dating as well as the characterization—in terms of source zones, sizes, and lithology—of rockfall events. Following this approach, both high-resolution spatial and temporal distribution of rockfalls can be obtained.

In this perspective, future developments will be aimed at using both optical Gigapixel images and acoustic records for the automatic detection and distribution of rockfall events as well as the development of Digital Image Correlation (DIC) algorithms tailored for Gigapixel images, in order to detect and track slow deforming areas.

References

1. Varnes, D.J. Slope Movement Types and Processes. *Spec. Rep.* 1978, *176*, 11–33.

2. Abellán, A.; Vilaplana, J.M.; Martínez, J. Application of a Long-Range Terrestrial Laser Scanner to a Detailed Rockfall Study at Vall de Núria (Eastern Pyrenees, Spain). *Eng. Geol.* 2006, *88*, 136–148, doi:10.1016/j.enggeo.2006.09.012.

3. Abellán, A.; Calvet, J.; Vilaplana, J.M.; Blanchard, J. Detection and Spatial Prediction of Rockfalls by Means of Terrestrial Laser Scanner Monitoring. *Geomorphology* 2010, *119*, 162–171, doi:10.1016/j.geomorph.2010.03.016.

4. Abellán, A.; Vilaplana, J.M.; Calvet, J.; García-Sellés, D.; Asensio, E. Rockfall Monitoring by Terrestrial Laser Scanning—Case Study of the Basaltic Rock Face at Castellfollit de La Roca (Catalonia, Spain). *Nat. Hazards Earth Syst. Sci.* 2011, *11*, 829–841, doi:10.5194/nhess-11-829-2011.

5. Mineo, S.; Pappalardo, G.; Mangiameli, M.; Campolo, S.; Mussumeci, G. Rockfall Analysis for Preliminary Hazard Assessment of the Cliff of Taormina Saracen Castle (Sicily). *Sustainability* 2018, *10*, 417, doi:10.3390/su10020417.

6. Paranunzio, R.; Laio, F.; Chiarle, M.; Nigrelli, G.; Guzzetti, F. Climate Anomalies Associated with the Occurrence of Rockfalls at High-Elevation in the Italian Alps. *Nat. Hazards Earth Syst. Sci.* 2016, *16*, 2085–2106, doi:10.5194/nhess-16-2085-2016.

7. Crosta, G.B.; Agliardi, F. A Methodology for Physically Based Rockfall Hazard Assessment. *Nat. Hazards Earth Syst. Sci.* 2003, *3*, 407–422, doi:10.5194/nhess-3-407-2003.

8. Michoud, C.; Derron, M.-H.; Horton, P.; Jaboyedoff, M.; Baillifard, F.-J.; Loye, A.; Nicolet, P.; Pedrazzini, A.; Queyrel, A. Rockfall Hazard and Risk Assessments along Roads at a Regional Scale: Example in Swiss Alps. *Nat. Hazards Earth Syst. Sci.* 2012, *12*, 615–629, doi:10.5194/nhess-12-615-2012.

9. Baillifard, F.; Jaboyedoff, M.; Sartori, M. Rockfall Hazard Mapping along a Mountainous Road in Switzerland Using a GIS-Based Parameter Rating Approach. *Nat. Hazards Earth Syst. Sci.* 2003, *3*, 435–442, doi:10.5194/nhess-3-435-2003.

10. Budetta, P. Assessment of Rockfall Risk along Roads. *Nat. Hazards Earth Syst. Sci.* 2004, *4*, 71–81, doi:10.5194/nhess-4-71-2004.

11. Budetta, P.; De Luca, C.; Nappi, M. Quantitative Rockfall Risk Assessment for an Important Road by Means of the Rockfall Risk Management (RO.MA.) Method. *Bull. Eng. Geol. Environ.* 2016, *75*, 1377–1397, doi:10.1007/s10064-015-0798-6.

12. Frattini, P.; Crosta, G.; Carrara, A.; Agliardi, F. Assessment of Rockfall Susceptibility by Integrating Statistical and Physically-Based Approaches. *Geomorphology* 2008, *94*, 419–437, doi:10.1016/j.geomorph.2006.10.037.

13. Guzzetti, F.; Reichenbach, P.; Ghigi, S. Rockfall Hazard and Risk Assessment Along a Transportation Corridor in the Nera Valley, Central Italy. *Environ. Manag.* 2004, *34*, 191–208, doi:10.1007/s00267-003-0021-6.

14. Guzzetti, F. Landslide Fatalities and the Evaluation of Landslide Risk in Italy. *Eng. Geol.* 2000, *58*, 89–107, doi:10.1016/S0013-7952(00)00047-8.

15. Guzzetti, F.; Reichenbach, P.; Wieczorek, G.F. Rockfall Hazard and Risk Assessment in the Yosemite Valley, California, USA. *Nat. Hazards Earth Syst. Sci.* 2003, *3*, 491–503, doi:10.5194/nhess-3-491-2003.

16. Mazzanti, P.; Brunetti, A. Assessing Rockfall Susceptibility by Terrestrial SAR Interferometry. In Proceedings of the Mountain Risks International Conference, Firenze, Italy, 24–26 November *2010*; pp 24–26.

17. Abellán, A.; Oppikofer, T.; Jaboyedoff, M.; Rosser, N.J.; Lim, M.; Lato, M.J. Terrestrial Laser Scanning of Rock Slope Instabilities. *Earth Surf. Process. Landf.* 2014, *39*, 80–97, doi:10.1002/esp.3493.

18. Mazzanti, P.; Brunetti, A.; Bretschneider, A. A New Approach Based on Terrestrial Remote-Sensing Techniques for Rock Fall Hazard Assessment. In *Modern Technologies for Landslide Monitoring and Prediction*; Scaioni, M., Ed.; Springer Natural Hazards; Springer: Berlin/Heidelberg, Germany, 2015; pp 69–87, doi:10.1007/978-3-662-45931-7_4.

19. Janeras, M.; Jara, J.-A.; Royán, M.J.; Vilaplana, J.-M.; Aguasca, A.; Fàbregas, X.; Gili, J.A.; Buxó, P. Multi-Technique Approach to Rockfall Monitoring in the Montserrat Massif (Catalonia, NE Spain). *Eng. Geol.* 2017, *219*, 4–20, doi:10.1016/j.enggeo.2016.12.010.

20. Bonneau, D.; DiFrancesco, P.-M.; Hutchinson, D.J. Surface Reconstruction for Three-Dimensional Rockfall Volumetric Analysis. *ISPRS Int. J. Geo-Inf.* 2019, *8*, 548, doi:10.3390/ijgi8120548.

21. Farmakis, I.; Marinos, V.; Papathanassiou, G.; Karantanellis, E. Automated 3D Jointed Rock Mass Structural Analysis and Characterization Using LiDAR Terrestrial Laser Scanner for Rockfall Susceptibility Assessment: Perissa Area Case (Santorini). *Geotech. Geol. Eng.* 2020, *38*, 3007–3024, doi:10.1007/s10706-020-01203-x.

22. Manconi, A.; Picozzi, M.; Coviello, V.; Santis, F.D.; Elia, L. Real-Time Detection, Location, and Characterization of Rockslides Using Broadband Regional Seismic Networks. *Geophys. Res. Lett.* 2016, *43*, 6960–6967, doi:10.1002/2016GL069572.

23. Fiorucci, M.; Marmoni, G.M.; Martino, S.; Mazzanti, P. Thermal Response of Jointed Rock Masses Inferred from Infrared Thermographic Surveying (Acuto Test-Site, Italy). *Sensors* 2018, *18*, 2221, doi:10.3390/s18072221.

24. Abellán, A.; Jaboyedoff, M.; Oppikofer, T.; Vilaplana, J.M. Detection of Millimetric Deformation Using a Terrestrial Laser Scanner: Experiment and Application to a Rockfall Event. *Nat. Hazards Earth Syst. Sci.* 2009, *9*, 365–372.

25. Royán, M.J.; Abellán, A.; Jaboyedoff, M.; Vilaplana, J.M.; Calvet, J. Spatio-Temporal Analysis of Rockfall Pre-Failure Deformation Using Terrestrial LiDAR. *Landslides* 2014, *11*, 697–709, doi:10.1007/s10346-013-0442-0.

26. Kromer, R.; Lato, M.; Hutchinson, D.J.; Gauthier, D.; Edwards, T. Managing Rockfall Risk through Baseline Monitoring of Precursors Using a Terrestrial Laser Scanner. *Can. Geotech. J.* 2017, *54*, 953–967, doi:10.1139/cgj-2016-0178.

27. Kromer, R.A.; Rowe, E.; Hutchinson, J.; Lato, M.; Abellán, A. Rockfall Risk Management Using a Pre-Failure Deformation Database. *Landslides* 2018, *15*, 847–858, doi:10.1007/s10346-017-0921-9.

28. D'Angiò, D.; Fantini, A.; Fiorucci, M.; Grechi, G.; Iannucci, R.; Marmoni, G.M.; Martino, S.; Lenti, L. *Multisensor Monitoring for Detecting Rock Wall Instabilities from Precursors to Failures: The Acuto Test-Site (Central Italy)*; ISRM International Symposium – EUROCK 2020; OnePetro: 2020.

29. Fantini, A.; Fiorucci, M.; Martino, S.; Paciello, A. Investigating Rock Mass Failure Precursors Using a Multi-Sensor Monitoring System: Preliminary Results From a Test-Site (Acuto, Italy). *Procedia Eng.* 2017, *191*, 188–195, doi:10.1016/j.proeng.2017.05.171.

30. Scavia, C.; Barbero, M.; Castelli, M.; Marchelli, M.; Peila, D.; Torsello, G.; Vallero, G. Evaluating Rockfall Risk: Some Critical Aspects. *Geosciences* 2020, *10*, 98, doi:10.3390/geosciences10030098.

31. Hardy Jr, H.R. *Acoustic Emission/Microseismic Activity: Principle*; Taylor and Francis: Abingdon, UK, 2003.

32. Corominas, J.; Moya, J.; Lloret, A.; Gili, J.A.; Angeli, M.G.; Pasuto, A.; Silvano, S. Measurement of Landslide Displacements Using a Wire Extensometer. *Eng. Geol.* 2000, *55*, 149–166, doi:10.1016/S0013-7952(99)00086-1.

33. Dixon, N.D.; Spriggs, M.S. Quantification of Slope Displacement Rates Using Acoustic Emission Monitoring. *Can. Geotech. J.* 2007, doi:10.1139/T07-046.

34. Codeglia, D.; Dixon, N.; Fowmes, G.J.; Marcato, G. Strategies for Rock Slope Failure Early Warning Using Acoustic Emission Monitoring. In *IOP Conference Series: Earth and Environmental Science*; IOP Publishing: Bristol, UK, 2015; Volume 26, p. 012028, doi:10.1088/1755-1315/26/1/012028.

35. Arosio, D.; Longoni, L.; Papini, M.; Scaioni, M.; Zanzi, L.; Alba, M. Towards Rockfall Forecasting through Observing Deformations and Listening to Microseismic Emissions. *Nat. Hazards Earth Syst. Sci.* 2009, *9*, 1119–1131, doi:10.5194/nhess-9-1119-2009.

36. Wasowski, J.; Pisano, L. Long-Term InSAR, Borehole Inclinometer, and Rainfall Records Provide Insight into the Mechanism and Activity Patterns of an Extremely Slow Urbanized Landslide. *Landslides* 2020, *17*, 445–457, doi:10.1007/s10346-019-01276-7.

37. Dixon, N.; Spriggs, M.P.; Marcato, G.; Pasuto, A. Landslide Hazard Evaluation by Means of Several Monitoring Techniques, Including an Acoustic Emission Sensor; Loughborough University: Loughborough, UK, 2012.

38. Smith, A.; Dixon, N. Quantification of Landslide Velocity from Active Waveguide–Generated Acoustic Emission. *Can. Geotech. J.* 2014, doi:10.1139/cgj-2014-0226.

39. Dixon, N.; Hill, R.; Kavanagh, J. Acoustic Emission Monitoring of Slope Instability: Development of an Active Waveguide System. *Proc. Inst. Civ. Eng.-Geotech. Eng.* 2003, *156*, 83–95, doi:10.1680/geng.2003.156.2.83.

40. Petrie, G.; Toth, C.K. Introduction to Laser Ranging, Profiling, and Scanning. *Topogr. Laser Ranging Scanning Princ. Process.* 2008, 1–28.

41. Abellan, A.; Derron, M.-H.; Jaboyedoff, M. "Use of 3D Point Clouds in Geohazards" Special Issue: Current Challenges and Future Trends. *Remote Sens.* 2016, *8*, 130, doi:10.3390/rs8020130.

42. Lato, M.J.; Hutchinson, D.J.; Gauthier, D.; Edwards, T.; Ondercin, M. Comparison of Airborne Laser Scanning, Terrestrial Laser Scanning, and Terrestrial Photogrammetry for Mapping Differential Slope Change in Mountainous Terrain. *Can. Geotech. J.* 2014, doi:10.1139/cgj-2014-0051.

43. Lato, M.J.; Gauthier, D.; Hutchinson, D.J. Rock Slopes Asset Management: Selecting the Optimal Three-Dimensional Remote Sensing Technology. *Transp. Res. Rec.* 2015, *2510*, 7–14, doi:10.3141/2510-02.

44. Jaboyedoff, M.; Oppikofer, T.; Abellán, A.; Derron, M.-H.; Loye, A.; Metzger, R.; Pedrazzini, A. Use of LIDAR in Landslide Investigations: A Review. *Nat. Hazards* 2012, *61*, 5–28.

45. Carrea, D.; Abellan, A.; Derron, M.-H.; Jaboyedoff, M. Automatic Rockfalls Volume Estimation Based on Terrestrial Laser Scanning Data. In *Engineering Geology for Society and Territory-Volume 2*; Springer: Berlin/Heidelberg, Germany, 2015; pp 425–428.

46. van Veen, M.; Hutchinson, D.J.; Kromer, R.; Lato, M.; Edwards, T. Effects of Sampling Interval on the Frequency-Magnitude Relationship of Rockfalls Detected from Terrestrial Laser Scanning Using Semi-Automated Methods. *Landslides* 2017, *14*, 1579–1592.

47. Mazzanti, P.; Caporossi, P.; Brunetti, A.; Mohammadi, F.I.; Bozzano, F. Short-Term Geomorphological Evolution of the Poggio Baldi Landslide Upper Scarp via 3D Change Detection. *Landslides* 2021, 1–15, doi:10.1007/s10346-021-01647-z.

48. Sturzenegger, M.; Stead, D. Close-Range Terrestrial Digital Photogrammetry and Terrestrial Laser Scanning for Discontinuity Characterization on Rock Cuts. *Eng. Geol.* 2009, *106*, 163–182.

49. Slob, S. Automated Rock Mass Characterisation Using 3-D Terrestrial Laser Scanning; 2010.

50. Gigli, G.; Casagli, N. Semi-Automatic Extraction of Rock Mass Structural Data from High Resolution LIDAR Point Clouds. *Int. J. Rock Mech. Min. Sci.* 2011, *48*, 187–198.

51. Di Luzio, E.; Mazzanti, P.; Brunetti, A.; Baleani, M. Assessment of Tectonic-Controlled Rock Fall Processes Threatening the Ancient Appia Route at the Aurunci Mountain Pass (Central Italy). *Nat. Hazards* 2020, *102*, 909–937.

52. Prokop, A.; Panholzer, H. Assessing the Capability of Terrestrial Laser Scanning for Monitoring Slow Moving Landslides. *Nat. Hazards Earth Syst. Sci.* 2009, *9*, 1921–1928, doi:10.5194/nhess-9-1921-2009.

53. Corsini, A.; Castagnetti, C.; Bertacchini, E.; Rivola, R.; Ronchetti, F.; Capra, A. Integrating Airborne and Multi-Temporal Long-Range Terrestrial Laser Scanning with Total Station Measurements for Mapping and Monitoring a Compound Slow Moving Rock Slide. *Earth Surf. Process. Landf.* 2013, *38*, 1330–1338, doi:10.1002/esp.3445.

54. Kukutsch, R.; Kajzar, V.; Konicek, P.; Waclawik, P.; Ptacek, J. Possibility of Convergence Measurement of Gates in Coal Mining Using Terrestrial 3D Laser Scanner. *J. Sustain. Min.* 2015, *14*, 30–37, doi:10.1016/j.jsm.2015.08.005.

55. Cecchetti, M.; Rossi, M.; Coppi, F.; Bicci, A.; Coli, N.; Boldrini, N.; Preston, C. *A Novel Radar-Based System for Underground Mine Wall Stability Monitoring*; Australian Centre for Geomechanics: Perth, Australia, 2017; pp 431–443, doi:10.36487/ACG_rep/1710_34_Cecchetti.

56. Mazzanti, P.; Bozzano, F.; Brunetti, A.; Caporossi, P.; Esposito, C.; Mugnozza, G.S. Experimental Landslide Monitoring Site of Poggio Baldi Landslide (Santa Sofia, N-Apennine, Italy). In *Advancing*

Culture of Living with Landslides; Mikoš, M., Arbanas, Ž., Yin, Y., Sassa, K., Eds.; Springer International Publishing: Cham, Switzerland, 2017; pp 259–266, doi:10.1007/978-3-319-53487-9_29.

57. Dunnicliff, J. Geotechnical Instrumentation for Monitoring Field Performance; John Wiley & Sons: Hoboken, NJ, USA, 1993.

58. Kopf, J.; Uyttendaele, M.; Deussen, O.; Cohen, M.F. Capturing and Viewing Gigapixel Images. *ACM Trans. Graph.* 2007, 26, 93-es, doi:10.1145/1276377.1276494.

59. Brady, D.J.; Gehm, M.E.; Stack, R.A.; Marks, D.L.; Kittle, D.S.; Golish, D.R.; Vera, E.M.; Feller, S.D. Multiscale Gigapixel Photography. *Nature* 2012, *486*, 386–389, doi:10.1038/nature11150.

60. Cossairt, O.S.; Miau, D.; Nayar, S.K. Gigapixel Computational Imaging. In Proceedings of the 2011 IEEE International Conference on Computational Photography (ICCP); Pittsburgh, PA, USA, 8–10 April 2011; pp 1–8, doi:10.1109/ICCPHOT.2011.5753115.

61. Sargent, R.; Bartley, C.; Dille, P.; Keller, J.; Nourbakhsh, I.; LeGrand, R. Timelapse GigaPan: Capturing, Sharing, and Exploring Timelapse Gigapixel Imagery. In *Proceedings of the Fine International Conference on Gigapixel Imaging for Science*; November 11-13 2010; Volume 1, Carnegie Mellon University (ed.).

62. Lato, M.; Smebye, H.; Kveldsvik, V. Mapping the Inaccessible with LiDAR and Gigapixel Photography: A Case Study from Norway.

63. Lato, M.J.; Bevan, G.; Fergusson, M. Gigapixel Imaging and Photogrammetry: Development of a New Long Range Remote Imaging Technique. *Remote Sens.* 2012, *4*, 3006–3021, doi:10.3390/rs4103006.

64. Romeo, S.; Di Matteo, L.; Kieffer, D.S.; Tosi, G.; Stoppini, A.; Radicioni, F. The Use of Gigapixel Photogrammetry for the Understanding of Landslide Processes in Alpine Terrain. Geosciences 2019, 9, 99, doi:10.3390/geosciences9020099.

65. Lu, D.; Mausel, P.; Brondízio, E.; Moran, E. Change Detection Techniques. *Int. J. Remote Sens.* 2004, *25*, 2365–2401, doi:10.1080/0143116031000139863.

66. Lu, P.; Stumpf, A.; Kerle, N.; Casagli, N. Object-Oriented Change Detection for Landslide Rapid Mapping. *IEEE Geosci. Remote Sens. Lett.* 2011, *8*, 701–705, doi:10.1109/LGRS.2010.2101045.

67. Tewkesbury, A.P.; Comber, A.J.; Tate, N.J.; Lamb, A.; Fisher, P.F. A Critical Synthesis of Remotely Sensed Optical Image Change Detection Techniques. *Remote Sens. Environ.* 2015, *160*, 1–14, doi:10.1016/j.rse.2015.01.006.

68. GigaPan | High-Resolution Images | Panoramic Photography|GigaPixel Images http://gigapan.com/ (accessed on 22 March 2021).

69. Wójcicka, A.; Wróbel, Z. The Panoramic Visualization of Metallic Materials in Macro- and Microstructure of Surface Analysis Using Microsoft Image Composite Editor (ICE). In *Information Technologies in Biomedicine*; Piętka, E., Kawa, J., Eds.; Lecture Notes in Computer Science; Springer: Berlin/Heidelberg, Germany, 2012; pp 358–368, doi:10.1007/978-3-642-31196-3_36.

70. Antonello, G.; Casagli, N.; Farina, P.; Leva, D.; Nico, G.; Sieber, A.J.; Tarchi, D. Ground-Based SAR Interferometry for Monitoring Mass Movements. *Landslides* 2004, *1*, 21–28, doi:10.1007/s10346-003-0009-6.

71. Corsini, A.; Farina, P.; Antonello, G.; Barbieri, M.; Casagli, N.; Coren, F.; Guerri, L.; Ronchetti, F.; Sterzai, P.; Tarchi, D. Space-borne and Ground-based SAR Interferometry as Tools for Landslide Hazard Management in Civil Protection. *Int. J. Remote Sens.* 2006, *27*, 2351–2369, doi:10.1080/01431160600554405.

72. Bozzano, F.; Cipriani, I.; Mazzanti, P.; Prestininzi, A. Displacement Patterns of a Landslide Affected by Human Activities: Insights from Ground-Based InSAR Monitoring. *Nat. Hazards* 2011, *59*, 1377–1396, doi:10.1007/s11069-011-9840-6.

73. Romeo, S.; Tran, Q.C.; Mastrantoni, G.; Dominh, D.; Minh, D.; Nguyen, H.T.; Mazzanti, P. Remote Monitoring Of Natural Slopes: Insights From The First Terrestrial Insar Campaign In Vietnam. *Ital. J. Eng. Geol. Environ.* 2020, 55–63, doi:10.4408/IJEGE.2020-01.O-05.

74. Gabriel, A.K.; Goldstein, R.M.; Zebker, H.A. Mapping Small Elevation Changes over Large Areas: Differential Radar Interferometry. *J. Geophys. Res. Solid Earth* 1989, 94, 9183–9191, doi:10.1029/JB094iB07p09183.

75. Goldstein, R.M.; Engelhardt, H.; Kamb, B.; Frolich, R.M. Satellite Radar Interferometry for Monitoring Ice Sheet Motion: Application to an Antarctic Ice Stream. *Science* 1993, *262*, 1525–1530, doi:10.1126/science.262.5139.1525.

76. Allen, C.T. Interferometric Synthetic Aperture Radar. *IEEE Geosci. Remote Sens. Soc. Newsl.* 1995, *96*, 6–13.

77. Dixon, T. SAR Interferometry and Surface Change Detection: Workshop Held. *Eos Trans. Am. Geophys. Union* 1994, *75*, 269–270, doi:10.1029/94EO00943.

78. Massonnet, D.; Feigl, K.L. Radar Interferometry and Its Application to Changes in the Earth's Surface. *Rev. Geophys.* 1998, *36*, 441–500, doi:10.1029/97RG03139.

79. Klees, R.; Massonnet, D. Deformation Measurements Using SAR Interferometry: Potential and Limitations. *Geol. En Mijnb.* 1998, *77*, 161–176, doi:10.1023/A:1003594502801.

80. Luzi, G. Ground Based SAR Interferometry: A Novel Tool for Geoscience. In Geoscience and Remote Sensing New Achievements; 2010, doi:10.5772/9090.

81. Barra, A.; Monserrat, O.; Mazzanti, P.; Esposito, C.; Crosetto, M.; Mugnozza, G.S. First Insights on the Potential of Sentinel-1 for Landslides Detection. *Geomat. Nat. Hazards Risk* 2016, *7*, 1874–1883, doi:10.1080/19475705.2016.1171258.

82. Moretto, S.; Bozzano, F.; Esposito, C.; Mazzanti, P.; Rocca, A. Assessment of Landslide Pre-Failure Monitoring and Forecasting Using Satellite SAR Interferometry. *Geosciences* 2017, *7*, 36, doi:10.3390/geosciences7020036.

83. Bozzano, F.; Mazzanti, P.; Perissin, D.; Rocca, A.; De Pari, P.; Discenza, M.E. Basin Scale Assessment of Landslides Geomorphological Setting by Advanced InSAR Analysis. *Remote Sens.* 2017, *9*, 267, doi:10.3390/rs9030267.

84. Bozzano, F.; Esposito, C.; Mazzanti, P.; Patti, M.; Scancella, S. Imaging Multi-Age Construction Settlement Behaviour by Advanced SAR Interferometry. *Remote Sens.* 2018, *10*, 1137, doi:10.3390/rs10071137.

85. Tarchi, D.; Casagli, N.; Fanti, R.; Leva, D.D.; Luzi, G.; Pasuto, A.; Pieraccini, M.; Silvano, S. Landslide Monitoring by Using Ground-Based SAR Interferometry: An Example of Application to the Tessina Landslide in Italy. *Eng. Geol.* 2003, *68*, 15–30, doi:10.1016/S0013-7952(02)00196-5.

86. Bozzano, F.; Mazzanti, P.; Prestininzi, A.; Scarascia Mugnozza, G. Research and Development of Advanced Technologies for Landslide Hazard Analysis in Italy. *Landslides* 2010, *7*, 381–385, doi:10.1007/s10346-010-0208-x.

87. Mazzanti, P.; Bozzano, F.; Brunetti, A.; Esposito, C.; Martino, S.; Prestininzi, A.; Rocca, A.; Scarascia Mugnozza, G. Terrestrial SAR Interferometry Monitoring of Natural Slopes and Man-Made Structures. In *Engineering Geology for Society and Territory—Volume 5*; Lollino, G., Manconi, A., Guzzetti, F., Culshaw, M., Bobrowsky, P., Luino, F., Eds.; Springer International Publishing: Cham, Switzerland, 2015; pp 189–194, doi:10.1007/978-3-319-09048-1_37.

88. Bar, N.; Ryan, C.; Yacoub, T.; McQuillan, A.; Coli, N.; Leoni, L.; Harries, N.; Rea, S.; Pano, K.; Bu, J. Integration of 3D Limit Equilibrium Models with Live Deformation Monitoring from Interferometric Radar to Identify and Manage Slope Hazards; Rock Mechanics for Natural Resources and Infrastructure Developmen; Fontoura, Rocca & Pavòn Mendoza (Eds); 2019.

89. Lombardi, L.; Nocentini, M.; Frodella, W.; Nolesini, T.; Bardi, F.; Intrieri, E.; Carlà, T.; Solari, L.; Dotta, G.; Ferrigno, F. The Calatabiano Landslide (Southern Italy): Preliminary GB-InSAR Monitoring Data and Remote 3D Mapping. *Landslides* 2017, *14*, 685–696.

90. Cecchetti, M.; Rossi, M.; Coppi, F. Performance Evaluation of a New MMW Arc SAR System for Underground Deformation Monitoring. In *Active and Passive Microwave Remote Sensing for Environmental Monitoring II*; International Society for Optics and Photonics: 2018, Berlin, Germany; Vol. 10788, p 107880B, doi:10.1117/12.2323828.

91. Zambanini, C.; Kieffer, D.S.; Galler, R. HYDRA ArcSAR: Applications of a Portable InSAR System for Monitoring Geo-Constructions. In *Geomechanik-Kolloquium*; 2018, Austria.

92. Chen, L.; Jiang, X.; Li, Z.; Liu, X.; Zhou, Z. Feature-Enhanced Speckle Reduction via Low-Rank and Space-Angle Continuity for Circular SAR Target Recognition. *IEEE Trans. Geosci. Remote Sens.* 2020, *58*, 7734–7752, doi:10.1109/TGRS.2020.2983420.

93. Pieraccini, M.; Miccinesi, L. Ground-Based Radar Interferometry: A Bibliographic Review. *Remote Sens.* 2019, *11*, 1029, doi:10.3390/rs11091029.

94. Hübl, J.; Schimmel, A.; Kogelnig, A.; Suriñach, E.; Vilajosana, I.; Mcardell, B.W. A Review on Acoustic Monitoring of Debris Flow. *Int. J. Saf. Secur. Eng.* 2013, *3*, 105–115, doi:10.2495/SAFE-V3-N2-105-115.

95. Ulivieri, G.; Vezzosi, S.; Farina, P.; Meier, L. *On the Use of Acoustic Records for the Automatic Detection and Early Warning of Rockfalls*; Australian Centre for Geomechanics: Perth,Australia, 2020; doi:10.36487/ACG_repo/2025_80.

96. Benini, A.; Farabegoli, E.; Martelli, L.; Severi, P. Stratigrafia e Paleogeografia Del Gruppo Di S. Sofia (Alto Appennino Forlivese). *Mem. Descr. Della Carta Geol. Ditalia* 1992, *46*, 231–243.

97. Esposito, C.; Di Luzio, E.; Baleani, M.; Troiani, F.; Della Seta, M.; Bozzano, F.; Mazzanti, P. Fold Architecture Predisposing Deep-Seated Gravitational Slope Deformations Within A Flysch Sequence in the Northern Apennines (Italy). *Geomorphology* 2021, 380, 107629.

98. Ricci Lucchi, F. The Miocene Marnoso-Arenacea Turbidites, Romagna and Umbria Apennines. Excursion N 7, Excursion Guidebook. In *2nd European Regional Meeting IAS*; Pascal and Francis; 1981.

99. Ricci-Lucchi, F. Depositional Cycles in Two Turbidite Formations of Northern Apennines. *J. Sediment. Res.* 1975, *45*, 3–43, doi:10.1306/212F6CB7-2B24-11D7-8648000102C1865D.

100. Martelli, L.; Camassi, R.; Catanzariti, R.; Fornaciari, L.; Spadafora, E. Explanatory Notes of the Geological Map of Italy, Scale 1:50,000, Sheet 265 "Bagno Di Romagna."; 2002.

101.   Conti, P.; Pieruccini, P.; Bonciani, F.; Callegari, I. Explanatory Notes of the Geological Map of Italy, Scale 1:50.000, Sheet 266 "Mercato Saraceno"; 2009.

102.   Dugonjić Jovančević, S.; Rubinić, J.; Arbanas, Ž. Conditions and Triggers of Landslides on Flysch Slopes in Istria, Croatia. *Eng. Rev.* 2020, *40*, 77–87, doi:10.30765/er.40.2.09.

103.   Cano, M.; Tomás, R. Characterization of the Instability Mechanisms Affecting Slopes on Carbonatic Flysch: Alicante (SE Spain), Case Study. *Eng. Geol.* 2013, *156*, 68–91, doi:10.1016/j.enggeo.2013.01.009.

104.   Arbanas, Ž.; Jovančević, S.D.; Vivoda, M.; Arbanas, S.M. Study of Landslides in Flysch Deposits of North Istria, Croatia: Landslide Data Collection and Recent Landslide Occurrences. In *Landslide Science for a Safer Geoenvironment*; Sassa, K., Canuti, P., Yin, Y., Eds.; Springer International Publishing: Cham, Switzerland, 2014; pp 89–94, doi:10.1007/978-3-319-04999-1_7.

105.   Akgun, A.; Gorum, T.; Nefeslioglu, H.A. Landslide Size Distribution Characteristics of Cretaceous and Eocene Flysch Assemblages in the Western Black Sea Region of Turkey. In *Understanding and Reducing Landslide Disaster Risk: Volume 2 From Mapping to Hazard and Risk Zonation*; Guzzetti, F., Mihalić Arbanas, S., Reichenbach, P., Sassa, K., Bobrowsky, P.T., Takara, K., Eds.; ICL Contribution to Landslide Disaster Risk Reduction; Springer International Publishing: Cham, Switzerland, 2021; pp 299–303, doi:10.1007/978-3-030-60227-7_33.

106.   Feroni, A.C.; Leoni, L.; Martelli, L.; Martinelli, P.; Ottria, G.; Sarti, G. The Romagna Apennines, Italy: An Eroded Duplex. *Geol. J.* 2001, *36*, 39–54, doi:10.1002/gj.874.

107.   Hungr, O.; Leroueil, S.; Picarelli, L. The Varnes Classification of Landslide Types, an Update. *Landslides* 2014, *11*, 167–194, doi:10.1007/s10346-013-0436-y.

108.   Hutchinson, J.N. General Report : Morphological and Geotechnical Parameters of Landslides in Relation to Geology and Hydrogeology; International symposium on landslides. 5 (1988-07-05); pp 3–35.

109.   Benini, A.; Biavati, G.; Generali, M.; Pizziolo, M. The Poggio Baldi Landslide (High Bidente Valley): Event and Post-Event Analysis and Geological Characterization. Proc. 7th EUREGEO – European Congress on Regional GEOscientific Cartography and Information Systems. Bologna Italy 2012; pp. 64-65.

110.   Markland, J.T. A Useful Technique for Estimating the Stability of Rock Slopes When the Rigid Wedge Slide Type of Failure Is Expected; Interdepartmental Rock Mechanics Project, Imperial College of Science and Technology; 1972; p 10.

111.   Kromer, R.A.; Hutchinson, D.J.; Lato, M.J.; Gauthier, D.; Edwards, T. Identifying Rock Slope Failure Precursors Using LiDAR for Transportation Corridor Hazard Management. *Eng. Geol.* 2015, *195*, 93–103, doi:10.1016/j.enggeo.2015.05.012.

112.   Kromer, R.; Hutchinson, D.; Lato, M.; Abellan, A. Rock Slope Pre-Failure Deformation Database for Improved Transportation Corridor Risk Management. In *Landslides and Engineered Slopes. Experience, Theory and Practice*; CRC Press: Boca Raton, FL, USA, 2016.

113.   Kromer, R.; Hutchinson, D.; Gauthier, D.; Lato, M.; Ondercin, M.; Macgowan, T. Characterization and Monitoring of Talus in Rock Slope Gullies Using High Temporal Resolution Terrestrial LiDAR and Gigapixel Photography. In Proceedings of the Vertical Geology Conference 2014, Lausanne, Switzerland, 5–7 February 2014.

114.   Sala, Z.; Hutchinson, D.J.; Harrap, R. Simulation of Fragmental Rockfalls Detected Using Terrestrial Laser Scans from Rock Slopes in South-Central British Columbia, Canada. *Nat. Hazards Earth Syst. Sci.* 2019, *19*, 2385–2404, doi:10.5194/nhess-19-2385-2019.

115.   Smebye, H.; Latob, M.J.; Kveldsvikc, V. Using Gigapan and LiDAR as Supporting Tools When Analyzing Rockfall Hazard in Norway. In *Information Technology in Geo-Engineering: Proceedings of the 2nd International Conference (ICITG) Durham, UK*; IOS Press: *Amsterdam,* The Netherlands, 2014; Volume 3, p 139, doi:10.3233/978-1-61499-417-6-139.

116.   Ondercin, M.; Kromer, R.; Hutchinson, D.J. A Comparison of Rockfall Models Calibrated Using Rockfall Trajectories Inferred from LiDAR Change Detection and Inspection of Gigapixel Photographs. In Proceedings of the 6th Canadian Geohazards Conference, Kingston, ON, Canada, 15–18 June *2014*.

117.   Rowe, E.; Hutchinson, D.J.; Kromer, R.A. An Analysis of Failure Mechanism Constraints on Pre-Failure Rock Block Deformation Using TLS and Roto-Translation Methods. *Landslides* 2018, *15*, 409–421, doi:10.1007/s10346-017-0886-8.

118.   Feng, Z.-Y.; Huang, H.-Y.; Chen, S.-C. Analysis of the Characteristics of Seismic and Acoustic Signals Produced by a Dam Failure and Slope Erosion Test. *Landslides* 2020, *17*, 1605–1618, doi:10.1007/s10346-020-01390-x.

119.   Cruden, D.M.; Varnes, D.J. Landslides Investigation and Mitigation. Landslide Types and Processes. *Spec. Rep.* 1996, *247*.

120.   Corominas, J.; Mavrouli, O.; Ruiz-Carulla, R. Rockfall Occurrence and Fragmentation. In *Advancing Culture of Living with Landslides*; Sassa, K., Mikoš, M., Yin, Y., Eds.; Springer International Publishing: Cham, Switzerland, 2017; pp 75–97, doi:10.1007/978-3-319-59469-9_4.

Chapter 3

Remote Sensing Monitoring of the Pietrafitta Earth Flows in Southern Italy: An Integrated Approach Based on Multi-Sensor Data

Authors: Davide Mazza [1,2], Antonio Cosentino [2,3,*], Saverio Romeo [4], Paolo Mazzanti [2,3], Francesco M. Guadagno [1] and Paola Revellino [1]

[1] Department of Sciences and Technologies, University of Sannio, 82100 Benevento, Italy; dmazza@unisannio.it (D.M.); guadagno@unisannio.it (F.M.G.); paola.revellino@unisannio.it (P.R.)

[2] NHAZCA S.r.l., Via V. Bachelet 12, 00185 Rome, Italy; paolo.mazzanti@uniroma1.it

[3] Earth Sciences Department, Sapienza University of Rome, Piazzale Aldo Moro 5, 00185 Rome, Italy

[4] ISPRA—Geological Survey of Italy, Via V. Brancati 48, 00144 Roma, Italy; saverio.romeo@isprambiente.it

* Correspondence: antonio.cosentino@uniroma1.it

3.1 Abstract

Earth flows are complex gravitational events characterised by a heterogeneous displacement pattern in terms of scale, style, and orientation. As a result, their monitoring, for both knowledge and emergency purposes, represents a relevant challenge in the field of engineering geology. This paper aims to assess the capabilities, peculiarities, and limitations of different remote sensing monitoring techniques through their application to the Pietrafitta earth flow (Southern Italy). The research compared and combined data collected during the main landslide reactivations by different ground-based remote sensors such as Robotic Total Station (R-TS), Terrestrial Synthetic Aperture Radar Interferometry (T-InSAR), and Terrestrial Laser Scanner (TLS), with data being derived by satellite-based Digital Image Correlation (DIC) analysis. The comparison between R-TS and T-InSAR measurements showed that, despite their different spatial and temporal resolutions, the observed deformation trends remain approximately coherent. On the other hand, DIC analysis was able to

detect a kinematic process, such as the expansion of the landslide channel, which was not detected by the other techniques used. The results suggest that, when faced with complex events, the use of a single monitoring technique may not be enough to fully observe and understand the processes taking place. Therefore, the limitations of each different technique alone can be solved by a multi-sensor monitoring approach.

3.2 Introduction

Earth flows can be dominant mass movements in hilly areas characterised by lithologically and structurally complex sequences [1,2]. Bulging toes, teardrop-shaped forms and smooth surface profiles are the most common features which identify this kind of intermittent landslide. In addition, the presences of discrete shear surfaces; viscous, finer grained material; and long periods of relative dormancy alternating with more rapid "surge" differ earth flows from other flow-like landslides [3].

Their activity is controlled by hydrologic forcing, the geometry of the basal slip surface, and the transmission of sediment pulses along the length of the flow.

These types of landslides are generally characterised by slow and persistent surface movements alternating between periods of rapid evolution, with the rates of displacement ranging between a few millimetres per day to more than one metre per day [4]. Accelerations or decelerations in surface displacement rates are mainly linked to the variation of the pore water pressure. However, the combination of prolonged rainfall, loss of efficient drainage pathways, and new sediment availability in the source area can cause earth flow surges. Under these conditions, the movement velocity can reach several metres per day. Moreover, during surge events, earth flow material can locally fluidise and fail catastrophically, involving life-line infrastructures (such as roadways and railways) and causing emergency phases in terms of civil protection [3,5–9].

The combination of slow (millimetres per day), long-term (over years) and localised (contained within five square meters or less) movements with surge events is a fundamental feature of earth flow activity [3]. Therefore, landslide monitoring, for knowledge, control or emergency purposes, requires the integration of different remote sensing and in situ techniques [10–18]. Where earth flows show the outcropping of shear surfaces, wire extensometers are one of the most common geotechnical tools used for continuous superficial displacement monitoring. This method is a cost-effective solution for slow and persistent movement, ensuring sub-millimetre accuracy [19–21]. However, wire extensometers allow one to detect only 1D deformation. In this case, the

implementation of physical or optical benchmarks, for the use of Global Navigation Satellite System (GNSS) and Robotic Total Station (R-TS) technology, is necessary to measure earth flow movements. GNSS and R-TS enable the detection of 3D deformation with millimetric precision [10,19,22–24]. Although the potential high frequency of data collection (from seconds to hours) makes these methods suitable for near-real-time monitoring, the difficulty of installing distance targets on sloped surfaces during earth flow surges represents a great disadvantage. Terrestrial Synthetic Aperture Radar Interferometry (T-InSAR) allows one to overcome this drawback and, at the same time, ensures high temporal resolution and measurement accuracy ($\sim 10^{-3}$ m). Depending on the acquisition configuration, T-InSAR is able to detect several deformation rates, ranging from m/day to mm/day. These features make this technology an essential support as an early warning system in landslide risk management [25–29]. Nevertheless, T-InSAR is not particularly suited to investigating the 3D kinematics of earth flows due to its limitation of only measuring displacements along the Line of Sight (LOS). Instead, 3D models generated by Terrestrial Laser Scanner (TLS), Unmanned Aerial Vehicle (UAV) or Structure from Motion Photogrammetry (SfM-P) can detect deformation in all directions. Comparing between multi-temporal Point Clouds (PCs) or Digital Elevation Models (DEMs) (elaborated from PCs) allows us to reconstruct the topographic evolution and estimate the sediment and volumetric balance along the earth flows [22,30,31]. However, although SfM-P from TLS and UAV ensures high-density information covering large areas, it is unsuitable for near-real-time monitoring. Furthermore, the multi-temporal approach for earth flow monitoring (knowledge-control) can also be performed thanks to the application of Digital Image Correlation (DIC) algorithms for satellite images or TLS imagery analysis [32–37]. DIC algorithms can return displacement field maps with an accuracy that is a function of the spatial and temporal resolution of the dataset.

This paper presents the results of the integrated monitoring activity performed at the site of the Pietrafitta earth flow (southern Italy) during the surge event of April–May 2016 that affected the SS87 national road. The study exploits the displacement data recorded and derived from continuous T-InSAR and R-TS and multi-temporal TLS surveys during the landslide paroxysm. It also analyses the deformational processes through a DIC analysis of multispectral satellite imagery. Unfortunately, in then literature, only few works combined and critically evaluated different remote sensing techniques specifically focused on earth flows over the same time period. This represents a serious gap considering that such phenomena can generate damage to human settlements and assets. In this context, starting from this case study, following a bottom-up approach, the outcomes of various

sensors and methodologies are thus integrated and compared to highlight advantages and limitations that are valuable for other earth flow sites.

3.3 Study Area and Landslide Features

The Pietrafitta earth flow (Lat = 41°13'12.83"N, Long = 14°44'32.51"E) affects the national road SS87 in Benevento Province (Campania Region, southern Italy), resulting in the occurrence of a typical slow-moving and intermittent event in the clay-rich flysch sequences of the Southern Apennines [1] (Figure 3.1A). It develops along the north-western slope of the Torre Palazzo hill on the southern side of the Reventa river valley from 200 to 250 m above sea level.
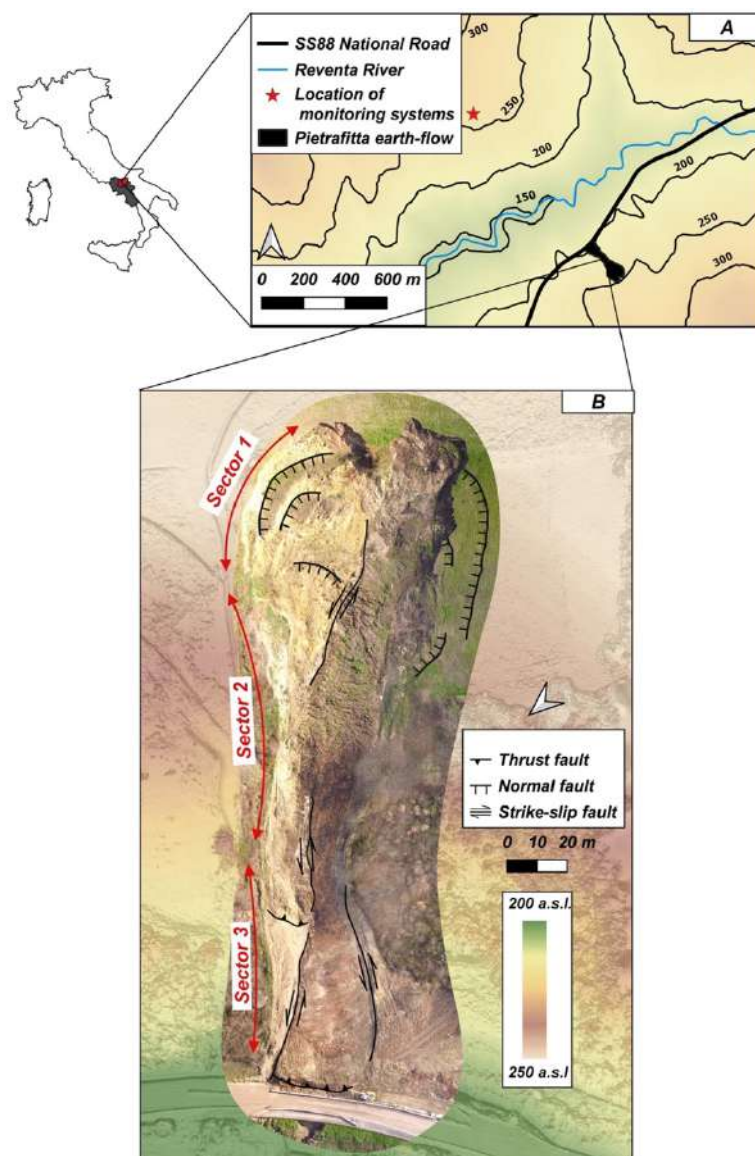
Figure 3.1. (**A**) *Location of the Pietrafitta earth flow within the Reventa river valley.* (**B**) *Distribution of the main kinematic elements along the slope. Basemap: orthophoto and Digital Surface Model (DSM) acquired during a UAV survey in February 2016.*

From a geological viewpoint, the Pietrafitta earth flow is located at an overthrust fault between (i) the Flysch Rosso formation (FYR) outcropping in the upper part of the slope, where the main scarp of the source area is located, and (ii) the Fragneto Monforte formation (UFM) at the middle and lower parts of the slope [38,39]. Lithological and structural complexity is the distinctive characteristic of these sequences, which consist of a chaotic alternation of clay, sandstone and calcareous marl levels.

The earth flow is placed across the main flow drainage axis of the slope. This position plays a key role in the movement direction and magnitude. The source area is complex and characterised by rotational–translational movements on the right side and by a flow-like zone on the left; downslope of the source area, the sliding of viscous–elastic materials is dominant above all when significant rainfalls occur. Soil softening and fluidification are favoured by local geomorphological and hydrogeological conditions [40] that lead superficial and shallow-circulating rainwater to be collected along the landslide axis.

The landslide was about 250 m long from the source area to the active bulging toe, covering an area of about 10×10^3 m^2: its width ranged from ~30 m (middle channel) to ~100 m (source and depositional area). The landslide body had an average slope angle, including the head scarp, of about 16°, and involved an approximate volume of $3 \times 10^5 \times 10$ m^3. Landslide thickness ranged between 2 and 4–5 m.

The compound kinematic of the upper part of the source area, where grabens, scarps and back-tilted surfaces were present, together with the whole deformational pattern (normal, thrust and strike slip faults (Figure 3.1B)) have some similarities with those characterising other earth flows composed of multiple kinematic zones in similar geo-structural settings [41,42] and are related to the longitudinal geometry of the basal slip surface. In particular, a slip surface can be composed of an alternation between risers and treads controlled by the geologic complexity of the slope's higher velocities occurring at steep traits (risers), with lower velocities occurring at gentle ones (treads).

Due to the landslide, since 2014, only one lane of the SS87 has allowed the passage of the motor vehicles, in an alternating manner; the other lane is occupied by part of the landslide toe. In October 2015, two intense and consecutive rainfall events affected Benevento Province, causing multiple effects such as floods, landslides and extensive soil erosion in a wide area [43,44]. The rainy events reactivated the landslide body, leading to the total closure of the road.

3.4 Materials and Methods

In order mitigate the risk of the deposit of landslide material on the transit lane, an integrated monitoring system of the earth flow displacement was installed in an emergency in March 2016 (Figure 3.2A). It consisted of (i) a Robotic Total Station (R-TS, Figure 3.2B), located on the opposite slope, looking at 16 reflectors (Figure 3.2C); (ii) a Terrestrial Synthetic Aperture Radar Interferometry (T-InSAR, Figure 3.2D) device, located in front of the landslide on the opposite slope; (iii) a Terrestrial Laser Scanner (TLS, Figure 3.2E) conducting multi-temporal scans; (iv) a video surveillance system, installed at the toe and working for 24 h; and (v) some experimental, low-cost sensors [20].

The joint use of different accurate monitoring techniques allowed safety countermeasures to be undertaken and alert procedures to be used in order to stop the traffic at the right time on the road. From July 2016, the landslide activity decreased, but by June, T-InSAR monitoring had been removed, and between November 2016 and July 2017, the TS monitoring was also temporarily stopped, in order to allow provisional works to be carried out.
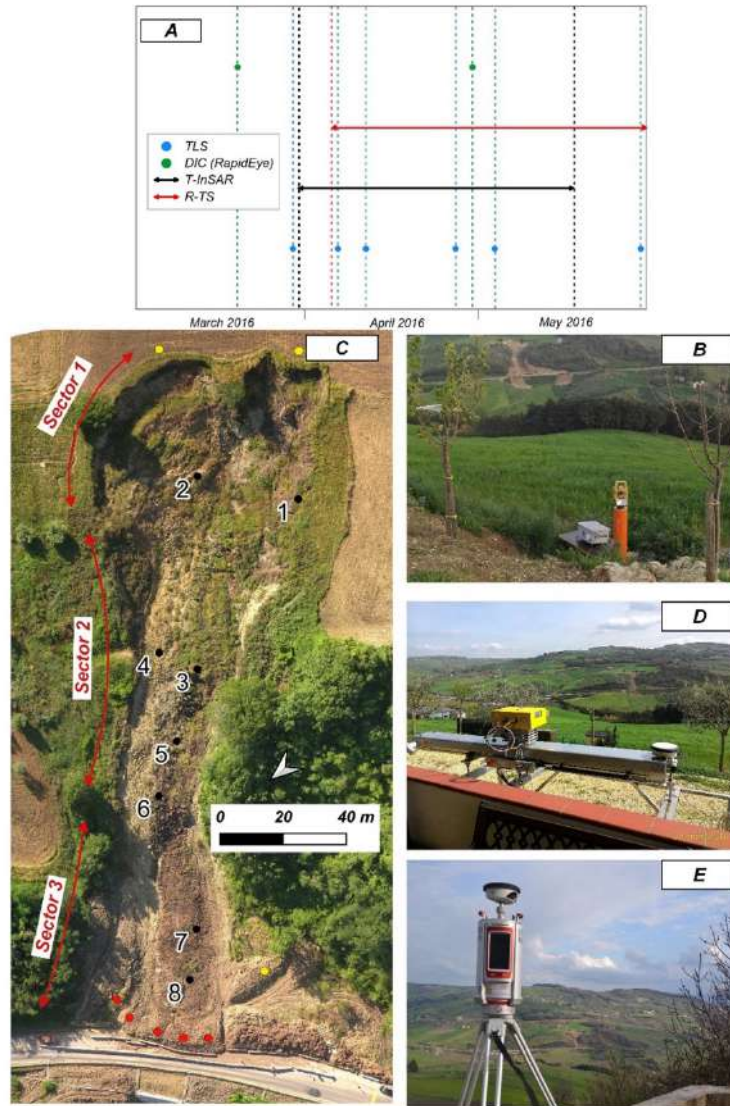
Figure 3.2. (*A*) *Dataset temporal distribution.* (*B*) *TOPCON 101 Robotic Total Station.* (*C*) *distribution of R-TS optical prisms along the slope. Basemap: orthophoto acquired during UAV survey in June 2016. The yellow dots represent the reference points installed in areas considered stable. The red dots represent the optical prisms relocated.* (*D*) *Position of the IBIS-FL/FM radar device.* (*E*) *Riegl Scan VZ-4000 Terrestrial Laser Scanner on the slope opposite the Pietrafitta earth flow*

3.4.1 Ground-Based Monitoring

### 3.4.1.1 Robotic Total Station (R-TS) Data

The R-TS represents the evolution of the common Total Station survey. It is equipped with a servomechanism and an automatic target recognition device, which locks onto a specific target and follows its movement [45]. This instrument allows the operator to work remotely, as it is able to move and orientate autonomously, and to measure the direction and magnitude of the displacement of a series of points with a maximum precision of up to a millimetre (depending on various factors such as type of instrumentation and the configuration of the monitoring network) at high sampling rates.

The measurements acquired during this study and presented here were recorded by a TOPCON 101 Robotic Total Station. The station was remote-controlled via 3G connection, and installed on the slope opposite the monitored slope, where 16 reflective prisms were installed at an average distance of 800 metres from the R-TS. For the analysis, we used the data recorded from 8 prisms (see Figure 3.2C for location) for the time span of 5 April 2016–31 May 2016, with an acquisition frequency of 1 h. Because of the continuous relocation, no completed time series were available for the remaining targets, and consequently, they were not considered for analysis. Moreover, it is worth noting that 3 optical prisms were installed in areas considered stable, and these were thus assumed as a reference. However, more than 1350 acquisitions were performed in less than 2 months.

3.4.1.2. Terrestrial Interferometric Synthetic Aperture Radar (T-InSAR) Data

T-InSAR is a ground-based radar which uses microwaves to remotely detect the displacement of natural targets through the measurement of the phase shift between two or more images collected at different times [26,27]. Radar signals are acquired by emitting and receiving antennas mounted in the radar head. This technology has several advantages, including (i) the ability to collect data with high temporal resolution (e.g., up to a few seconds) under any weather and lighting conditions, and (ii) the ability to remotely monitor an entire area, rather than single points. The main limitations are (i) that only the displacement component parallel to the Line of Sight (LOS) can be measured, and (ii) the risk of displacement underestimation for rapid processes due to the cyclical behaviour of the phase [26]. The main results which can be achieved by exploiting this technique involve the creation of both coloured maps and displacement time series from each pixel, when continuous monitoring is available.

The equipment used in the present study is the IBIS-FL/FM radar device produced by IDS Georadar S.r.l. (Figure 3.2D). The SAR device consists of a sensor module, a linear track (2 metres), a control PC, a power supply and data processing software (Figure 3.3). The sensor module transmits an electromagnetic signal at a central frequency of 17.2 GHz (Ku band) with a maximum bandwidth of 200 MHz and an accuracy of up to 0.1 mm. The main characteristics of the sensor are shown in Table 3.1.
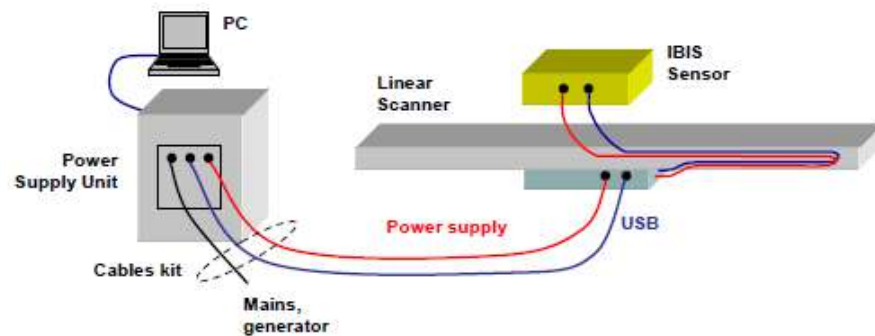
Figure 3.3. *T-InSAR System: schematisation of the system and its components (image from IBIS Guardian User Manual).*

T-InSAR continuous monitoring started on 30 March 2016 and ended on 18 May 2016, with a temporal frequency of 5 min and more than 13,000 acquisitions recorded. Although the radar footprint covered an area larger than the extent of the landslide, the data analysis focused on Sector 3 of the landslide (see Figure 3.1B), which represented the most critical sector in terms of damages and risk to the road. Moreover, due to the presence of vegetation and shadow areas within the more distant sectors (1 and 2) causing continuous phase noise and a low correlation index, reliable displacement analyses in these areas could not be performed.

The analysis and monitoring were carried out using the IBIS Guardian software, a powerful tool for managing the SAR images acquired by the ground-based radar which enables the user to quickly interpret the information processed. The software is able to store long-term datasets within a single monitoring project. Furthermore, displacement data are provided to the user in real time by employing advanced automatic atmospheric correction techniques. The interpretation of radar data is made via the visualisation of fully georeferenced 3D data.

Table 3.1. *Characteristics of radar sensor IBIS-FL/FM installed on the Pietrafitta earth flow.*

Operating Frequency	17.2 GHz (Ku Band)
Max. Operational Distance	1000 m
Max. Range Resolution	0.5 m

Operating Frequency	17.2 GHz (Ku Band)
Nominal Displacement Accuracy	10^{-5} m
Max. Acquisition Rate	200 Hz
Cross-range Resolution	4.4 mrad in Ku band

3.4.1.3 Terrestrial Laser Scanner (TLS) Data

TLS is an instrument based on laser technology capable of measuring the distance, with a high level of accuracy, between the instrument and the object being measured [16]. Thanks to mechanical systems and rotating and oscillating mirrors, it is able to direct laser pulses to different positions in space, thereby 'scanning' the objects in front of it. Among the suitable techniques for landslide monitoring, the TLS is one of the most generally applicable [46,47]. Moreover, it is characterised by lower instrumental accuracy compared to R-TS, but its surveys are very fast, efficient and precise.

The high-density Point Clouds provided (per cm^2) can be processed to distinguish vegetation from soil [16]. The three-dimensional modelling of complex areas is also possible, combining surveys from different scanning positions [48].

The data used for this study were acquired by a Riegl Scan VZ-4000 Terrestrial Laser Scanner (TLS), positioned on the opposite slope at an average distance of approximately 800 metres (Figure 3.2E). The high-speed, high-resolution 3D Laser Scanner RIEGL VZ-4000 has a range of over 4000 m and a field of view of 60° vertically and 360° horizontally. It uses an invisible laser beam for eye-safe operation within Laser Class 1. The main characteristics of the sensor are shown in Table 3.2. Seven main scans were carried out from 29 March 2016 to 16 June 2016, as listed in Table 3.3.

Table 3.2. Characteristics of Laser Scanner RIEGL VZ-4000.

| Accuracy	Precision	Laser Wavelength	Minimum Range	Maximum Range	Laser Beam Divergence	Laser Beam Footprint
15 mm	10 mm	Near infrared	5 m	4000 m	0.15 mrad	150 mm @ 1000 m

Table 3.3. Scans carried out at the site of the Pietrafitta landslide during the period of interest.

Month	Number of Scans	Dates
March	1	29 March 2016
April	3	6 April 2016
		11 April 2016
		27 April 2016
May	2	4 May 2016
		30 May 2016

The data obtained from the TLS scanning were used for the 3D modelling of the unstable slope surface and for the assessment of the volumetric differences related to the earth flow process by comparing several Point Clouds [49]. The analysis was carried out using the M3C2 plugin [50], which represents one of the main algorithms capable of producing distances directly between two Point Clouds implemented on Cloud Compare. Prior to the analysis using the M3C2 comparison algorithm, the Point Clouds were filtered by the presence of vegetation and aligned semi-automatically using the alignment tool on Cloud Compare (RMS error: 0.17).

3.4.2 Satellite PhotoMonitoring Data and Analysis

PhotoMonitoring is a new monitoring solution based on advanced digital image-processing algorithms that exploits the widespread use of optical/multispectral, hyperspectral and radar sensors worldwide to obtain information on changes or displacements in the terrain [51]. Analyses can be carried out on datasets of images acquired from the same type of platform, over the same area of interest and at different times, evaluating any variations in radiometric characteristics (Change Detection) and/or displacements occurring in the time interval covered by the image acquisition. Generally, the Digital Image Correlation (DIC) technique, which is an optical–numerical measurement technique, can provide full-field 2D and 3D displacements of any type of object surface (Figure 3.4) [32].
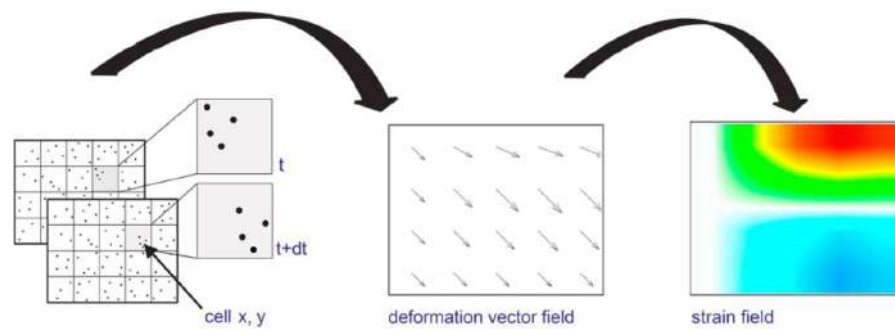
Figure 3.4. *Schematisation of the DIC process.*

Recently, analyses based on DIC algorithms have been recognised as a powerful tool not only for measuring landslide displacements [52–54], but also for other monitoring applications, such as assessing the stability of flanks of active volcanos [55], tracking the flow of a glacier [56] or assessing earthquake-induced displacement [57]. DIC displacement measurements can theoretically provide a sub-pixel accuracy of approximately 1/50th of a pixel [58] under optimal conditions, although problems linked to image orientation, co-registration, topographical distortion, instrumental and atmospheric noise, temporal and spatial decorrelations and co-registration errors represent limitations that do not always allow these accuracy values to be achieved [59]. Algorithms available to date allow analysis between two images as well as between several consecutive images (multi-master analysis).

3.4.3 IRIS Software Analysis

Satellite PhotoMonitoring analysis was performed using IRIS software, developed by NHAZCA S.r.l., a start-up of the 'Sapienza' University of Rome, which enables Change Detection (CD) and Digital Image Correlation (DIC), using various algorithms from the relevant literature and new algorithms developed specifically for this purpose. The Change Detection method implemented in the software makes use of the Structural Similarity Index, an algorithm in which the measurement of image quality is based on an initial image taken as a reference. The method is used on a local scale, iteratively assessing image similarity over a small subset of image pixels using a sliding window approach, which allows the automatic identification of portions of the scene where changes have occurred. The displacement analysis method implemented uses different types of algorithms that exploit different analysis techniques (feature tracking, template matching, phase correlation algorithm). Displacement maps can be created through a single pair of images (single analysis approach) or through a stack of

images depicting the same area (multi-master approach), which also permits the extrapolation of displacement time series for areas or pixels.

The analyses shown in this paper are based on high-resolution RapidEye satellite images, a constellation of five identical satellites owned and operated by Planet, launched on 29 August, 2008 (https://earth.esa.int/eogateway/catalog/rapideye-full-archive (accessed on 20 September 2022)). The sensors on the satellite platforms of this constellation produce images in five spectral bands (red, green, blue, red edge and near infrared), with a geometric resolution of 5 metres/pixel on orthorectified products.

A synopsis of the dataset used is shown in Table 3.4, which provides a description of the characteristics and dates of image collection.

Table 3.4. *Image used for DIC analysis.*

Name Images	Date
3358114_2016-03-19_RE4_3A_Analytic_SR_5	19 March, 2016
3358114_2016-04-30_RE3_3A_Analytic_SR_5	30 April, 2016

In this case, the analysis was performed using the phase correlation algorithm [60], which is based on a frequency domain representation of the data, usually calculated by means of fast Fourier transforms (FT), with a moving variable window that, in this case, was 8 pixels. This algorithm, the most commonly used, is based on the FT translation property, which states that a shift of two relevant images in the spatial domain is transformed in the frequency domain as phase differences. In the following equation, the functions $F(u,v)$ and $G(u,v)$ are the corresponding FT of $f(x,y)$ and $g(x,y)$, which we assume are two image functions, and F^{-1} denotes the inverse FT.

$$PC = F^{-1}\left\{\frac{F(u,v)*G(u,v)}{|F(u,v)*G(u,v)|}\right\} = F^{-1}\{exp\,(-i(u\Delta x + \, v\Delta y))\}$$

$$1)$$

The images, after being downloaded, were imported in the IRIS processing software. After the co-registration step, a landslide Region of Interest (ROI) was selected, and the analysis was started.

3.5 Results

3.5.1 R-TS Analysis

Figure 3.5 shows the cumulative planimetric displacements of the benchmarks selected for the analysis at each sector during the observation period.
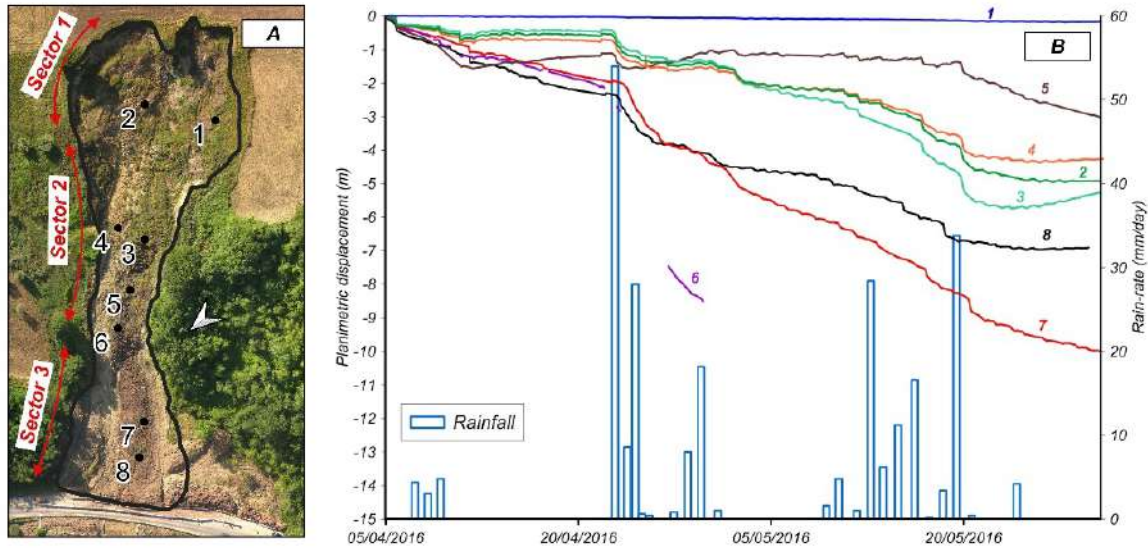
Figure 3.5. *(**A**) Distribution of the benchmarks along the slope. Basemap: orthophoto acquired during UAV survey in June 2016. (**B**) Correlation between planimetric displacement for selected targets and rainfall events: coloured lines represent the displacement cumulative time series while vertical bars represent the daily rain data.*

Despite having different magnitudes, a common displacement trend was found for all benchmarks. The only exception is represented by benchmark 1, which is located on the left side of the source area, close to the landslide boundary. This difference could be due to the different kinematic behaviours of this area, where rotational sliding (i.e., retrogressive movements) is generally prevalent, unlike in the translational areas.

The maximum displacements recorded between 5 April 2016 and 31 May 2016 were ~4.5 m in Sector 2 and ~10 m in Sector 3, albeit with variable velocities. Significant accelerations were recorded after rainfall events. Figure 3.6B compares the cumulative displacement of the monitoring points, with rainfall data collected at the "San Lupo" rain gauge, managed by the Agrometeorological Center (Centro Agrometeorologico Regionale, C.A.R.) of the Campania Region, and located 9 km west at an elevation of 343 m a.s.l. The main accelerations occurred following the main rainy events of 23–25 April 2016 (85.6 mm) and 14–20 May 2016 (96.2 mm). Table 3.5 summarises the variation in the average displacement rate measured in a 5-day range from 23 April 2016 for each benchmark (except

for benchmarks No. 1 and No. 5, as explained below), which contains continuous recordings for the whole period.

Table 3.5. *Displacement rates measured between 18–22 April (T1) and 23–27 April (T2).*

Benchmark	Displacement Rate T1 (m/day)	Displacement Rate T2 (m/day)
2	<0.01	~0.019
3	<0.01	~0.018
4	<0.01	~0.018
6	~0.01	~0.011
7	~0.07	~0.035
8	~0.06	~0.028
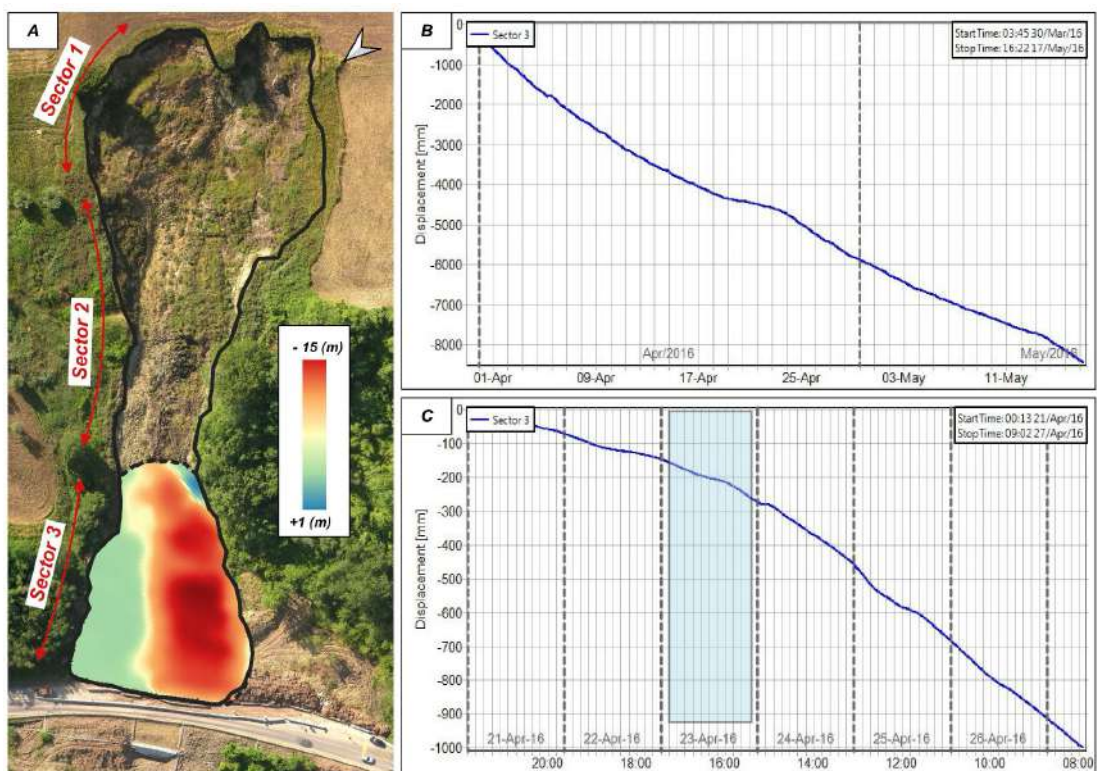
Figure 3.6. (**A**) *LOS displacement map. The raster raw data (3 m/pixel) were resampled (1 m/pixel) only for visualisation purposes. Each pixel of the image shows the cumulative displacement recorded in 48 days of observation. Negative and positive values indicate movement towards and away from the instrument, respectively. The black line represents the landslide boundary. The dashed black line represents the Sector 3 boundary. Basemap: orthophoto acquired during UAV survey in June 2016. (**B**) Average displacement time series for Sector 3 from 30 March 2016 to 17 May 2016. (**C**) Average*

displacement time series for Sector 3 from 21 April 2016 to 27 April 2016. The light-blue box represents the 23 April rainfall event.

However, it should be noted that the irregular surface deformations caused the tilting of some optical prisms, affecting the measurements and resulting in a temporary rising-like trend of the time series. This is evident from the curve's tail at benchmark 3 and parts of the benchmark 5 curve before and after the 23–25 April rainfall event. Because of the high displacement rate, benchmark 6 was not visible for several days and, subsequently, was completely lost.

3.5.2 T-InSAR Analysis

As shown in Figure 3.6A, the LOS cumulative displacement map obtained from the interferometric device highlights displacements of up to a maximum of 15 m on the left side of Sector 3 between 30 March 2016 and 18 May 2016. However, the average displacement of the entire Sector 3 was approximately 10 m. This value was computed from the average of the cumulative displacement recorded on each pixel of the map. The displacements mainly occurred along shear surfaces which border this area. No significant activity was identified at the left side of the toe and outside the landslide perimeter. The average displacement time series (Figure 3.6B) of the whole sector indicates a constant progression of the landslide toe, with sudden accelerations in connection with rainfall events (e.g., 23 April rainfall event (Figure 3.6C)). The average displacement rate recorded was ~0.1 m/day, whereas the maximum velocity was ~0.2 m/day on 25 April 2016.

3.5.3 TLS Analysis

Figure 3.7 shows the results of TLS scans (29 March 2016–27 April 2016) performed at the site of the Pietrafitta earth flow. Considering that the vertical lowering and raising of the topographic surface are interpreted as the loss or gain and material, respectively, the colour map of Figure 3.7 indicates a prevalent loss of material along the left flank of the landslide, specifically at the border between Sectors 2 and 3, where the maximum variation reaches about −1 m. Despite having lower values, negative variations in elevation were also detected at the landslide head, connected with the retrogressive kinematics of this zone.
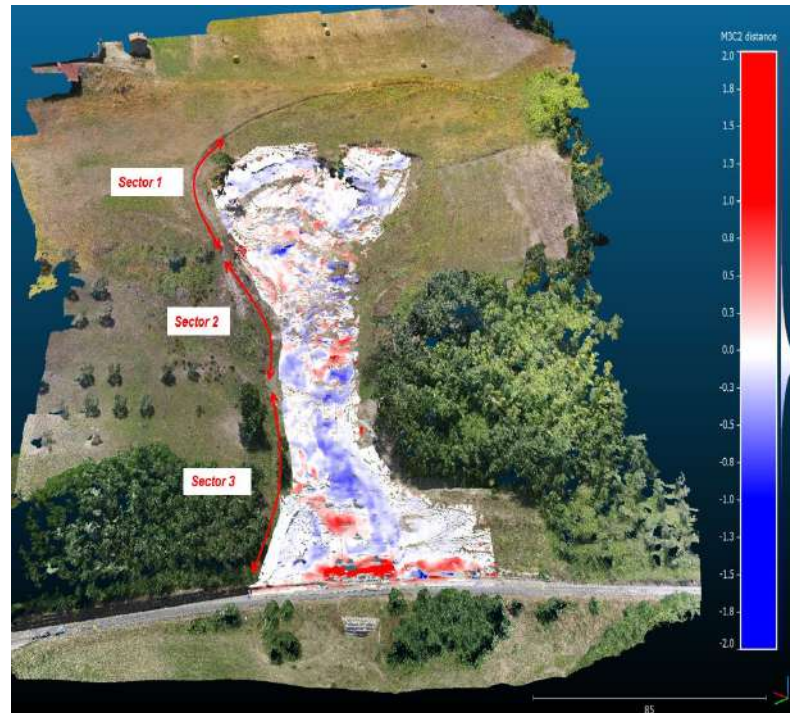
Figure 3.7. *Vertical displacement map computed through 29 March 2016 and 27 April 2016 scans. The results are overlaid on the June 2018 3D model of the slope. Raising and lowering of the topographic surface are indicated with red and blue colours, respectively.*

Conversely, an increase in elevation of up to 2 m was assessed at the toe of the earth flow. It should be noted that this part of the landslide suffered significant material removals to maintain road circulation. Therefore, the value gained of the increase in elevation is not fully representative of the natural evolution of the phenomenon and is underestimated. This underestimation is confirmed by the volumetric analysis performed, which indicates a total mobilised volume deficit (negative surface variation) of about 853 m^3, between 29 March 2016 and 27 April 2016, and a total mobilised volume surplus (positive surface variation) of about ~621 m^3, providing a negative volume balance of about −232 m^3. This result can be explained by the removal of material from the toe.

3.5.4 DIC Analysis

As mentioned above, the deformation process of the Pietrafitta landslide that occurred between March and April 2016 was studied using the DIC analysis of high-resolution RapidEye satellite images. Figure 3.8 presents the displacement map obtained, which shows that the most active areas during the period of interest were the transport zone and the toe of the landslide, located in Sectors 2 and 3, respectively. The maximum measured displacement was about 4 metres. In contrast, no significant movements were detected in Sector 1. The prevailing direction of movement was along

the line of greatest slope, from north to south, corresponding to the strike–slip fault direction. The results obtained also identify two zones—named "A" and "B"—which present different behaviours to the rest of the landslide body.
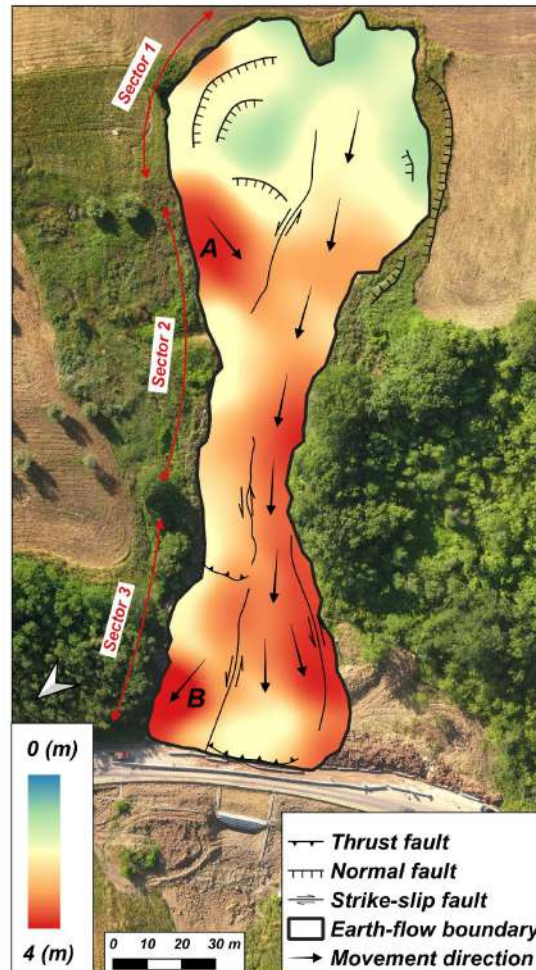
Figure 3.8. Results obtained from Digital Image Correlation (DIC) analysis. Displacement map projected on June 2016 orthophoto. The raster raw data (5 m/pixel) were resampled (1 m/pixel) only for visualisation purposes. Each pixel of the image shows the displacement computed on variable window comparing master (19 March 2016) and slave image (30 April 2016).

5. Discussion

The analysis performed shows that the countless differences in terms of spatial and temporal resolution of the employed sensors and the variability in magnitude and geometry of the displacements produce outcomes that are not always easy to compare, as shown in Figure 3.9.
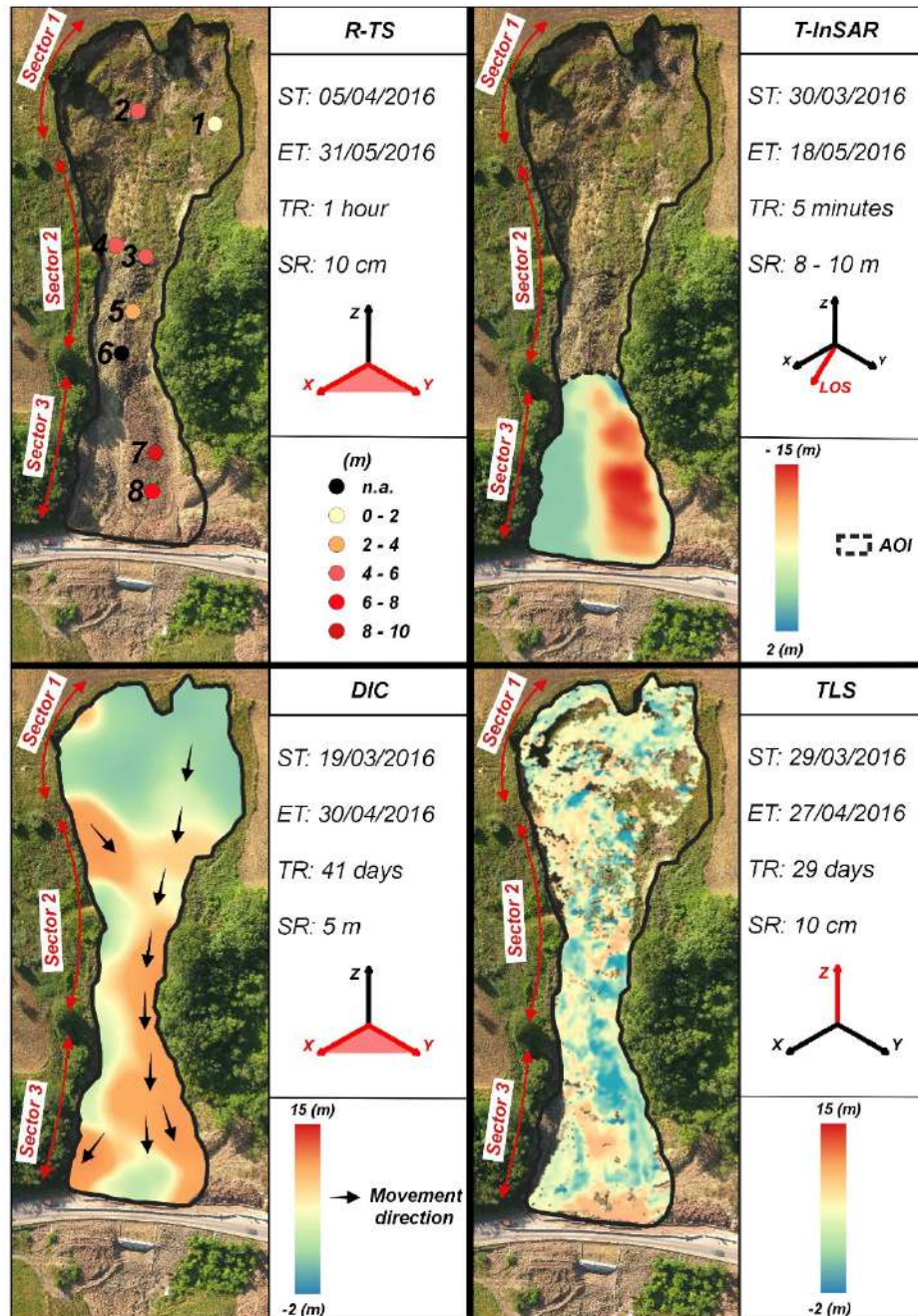
Figure 3.9. *Summary and comparison of the monitoring results. ST: start-time; ET: end-time; TR: temporal resolution; SR: spatial resolution. The R-TS spatial resolution refers to the optical prisms dimension. The red, right-handed Cartesian axes and planes represent the direction and the field of displacements, respectively, to which the results refer.*

The R-TS and T-InSAR monitoring allowed us to obtain high-frequency and accurate data to be used for both the understanding of middle- to long-term behaviour and the short-term emergency management and risk reduction of the landslide. They returned comparable displacement data within certain movement velocities. The average displacement computed from T-InSAR data for the whole of Sector 3 was about 10 m, with the maximum pixel-based values being measured up to 15 m. On the other hand, the cumulative displacements reached at R-TS benchmarks 7 and 8, located in the same sector, were about 10 m and 7 m, respectively (Figure 3.9).

A qualitative comparison between R-TS and T-InSAR outputs was made, similar to that reported in [61], re-projecting R-TS data recorded at benchmark 7 alongside T-InSAR LOS. For this purpose, the pixel corresponding to the position of the same benchmark within the LOS displacement map was selected and the relative displacement time series was extracted. Similarly, the displacement time series relative to the whole of Sector 3 was obtained. Figure 3.10A shows the comparison made, indicating that, despite their different spatial resolutions (i.e., the T-InSAR time series is representative of a 3 m/pixel resolution, while the R-TS time series shows single-point detail), the deformation trends were coherent with external forcing.
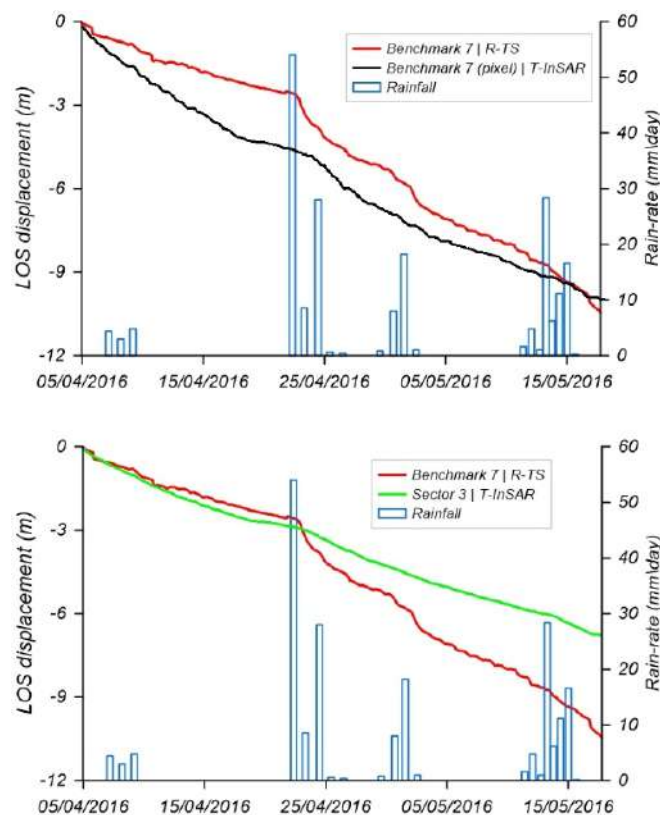
Figure 3.10. (A) *Comparison between point-based displacement time series and* (B) *point-based/area-based displacement time series.*

Although there were non-negligible intra-curve differences in terms of velocity, the cumulative displacements differed slightly and the overall trends were consistent; such a discrepancy is likely due to the intrinsic varieties in the acquisition between the technologies (T-InSAR and R-TS). It is worth noting that, because of the presence of a larger number of pixels within Sector 3, the related area time series has a smoother shape (Figure 3.10B), being a mean value of all the pixels selected.

The displacement patterns recorded with both R-TS and T-InSAR are compatible with the values observed by several authors in the literature [24,28], who applied the same technologies for different earth flow monitoring tasks. In addition, the results of the present work show a clear correlation between R-TS and T-InSAR displacement data regarding the recorded rainfall events (Figures 3.6 and 3.7), evidencing the key role of hydrologic force in these kinds of landslides [40].

T-InSAR displacement data between 21 and 22 April 2016 were also coherent with wire extensometer displacement data recorded in the same period at the site of the Pietrafitta earth flow. This instrument, used at a seismic station, was installed along the left flank in Sector 3, in the context of the experiment conducted by [62], which aimed to demonstrate that, after 4–5 h of the night closure, the landslide movement stopped and then restarted simultaneously with the road day opening. This test proved that, even in the absence of rainfall events, the vibration induced by vehicle traffic acts as a trigger event of movement when geotechnical and geomorphological settings create ideal conditions for slope failure. In this context, our study revealed that T-InSAR is able to detect the same effects induced by this process (Figure 3.11). These results demonstrate that, after data elaboration and validation, an active remote sensing system located at an observed area distance of about 800 m with a coarse spatial resolution (i.e., cross-range) allows the retrieval of a similar displacement pattern to the one recorded by a local contact sensor such as a wire-extensometer. In addition to the intrinsic differences between technologies, the temporal shift visible in the curves is mainly linked to the different spatial resolutions of the sensors used. In other words, the benchmark of the wire extensometer is representative of a single point of displacement, while T-InSAR data are representative of an area of about 10 m^2.
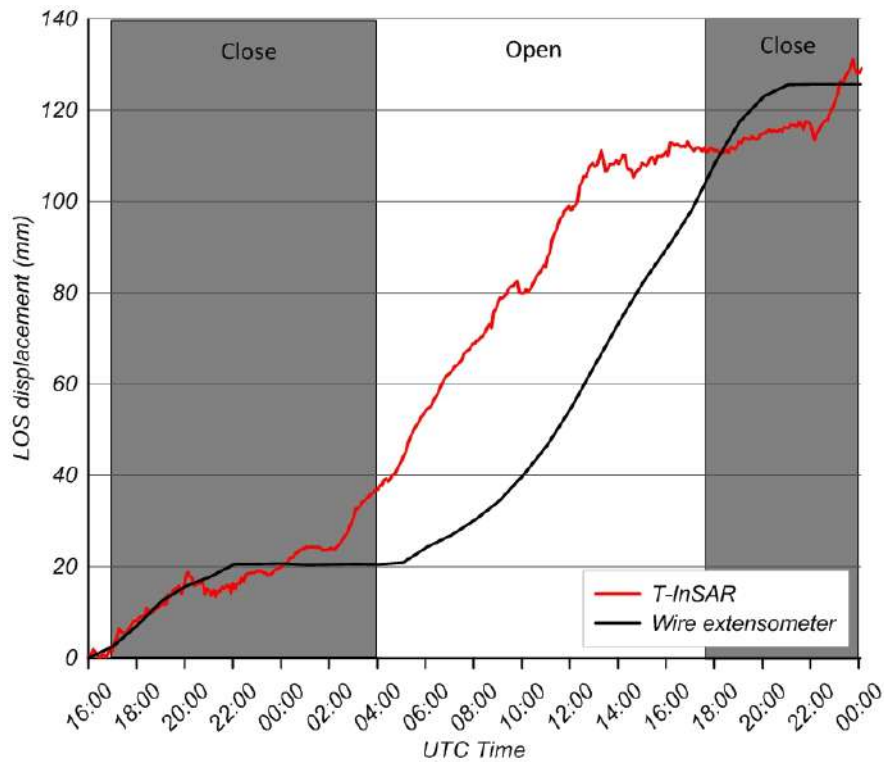
Figure 3.11. *Modified from [62]: correlation between artificial vibration generated by vehicular traffic and earth flow displacement between 16:00 (UTC +2) on 21 April 2016 and 00:00 (UTC +2) on 22 April 2016. The red line shows the displacement time series extracted from pixels corresponding to wire extensometer positions within T-InSAR LOS displacement map.*

The combination of the techniques discussed above, while allowing a comprehensive understanding of the event, did not provide a global knowledge of the process. The use of the TLS technique and Satellite DIC fit into this context and were applied to close the knowledge gap. Through the use of TLS data, it was possible to reconstruct the intensity of the process that occurred in the period of interest. In fact, TLS data, unlike T-InSAR and R-TS data, can provide 3D volumetric information that is useful for understanding material discharge and sediment pulses. Between 29 March 2016 and 27 April 2016, the volume of material involved was 852.86 m^3 (as shown in Section 4.3).

The displacement map obtained from the PhotoMonitoring analyses provided evidence that main movements were localised in Sector 2 and Sector 3 (Figure 3.8). As also reported in the literature [54,61,63], our work indicates that the displacements retrieved by this technique were underestimated, although the results are consistent in terms of the direction and location of the displacement when comparing the results obtained from T-InSAR and R-TS. The underestimation is likely due to the low geometrical resolution of RapidEye images that are not able to catch complex

geomorphological features affecting the small size of the Pietrafitta earth flow. Overall, the analysis was able to detect a maximum displacement of around 4 m. More accurate results could be achieved by overcoming the "Single-couple" approach and performing a multi-master analysis [63], using Very High Resolution (VHR) images with a Ground Sampling Distance (GSD) of 5 metres. However, our solution indicates that the DIC analysis was able to achieve a precision of around 1/10th of a pixel, in accordance with the results of [52], which produced the same value employing optical and multispectral imagery.

Despite the failure to fully detect the magnitude of the displacements that occurred, the results obtained from the PhotoMonitoring technique show some more deformations of the Pietrafitta earth flow that were not highlighted by T-InSAR and R-TS: (1) in Sector 2, an enlargement along the right flank (A in Figure 3.12) caused by the detachment of material from it, and (2) in Sector 3, an expansion zone at the right part of the toe (B in Figure 3.12), although the latter is an artefact due to the building of a drainage channel.
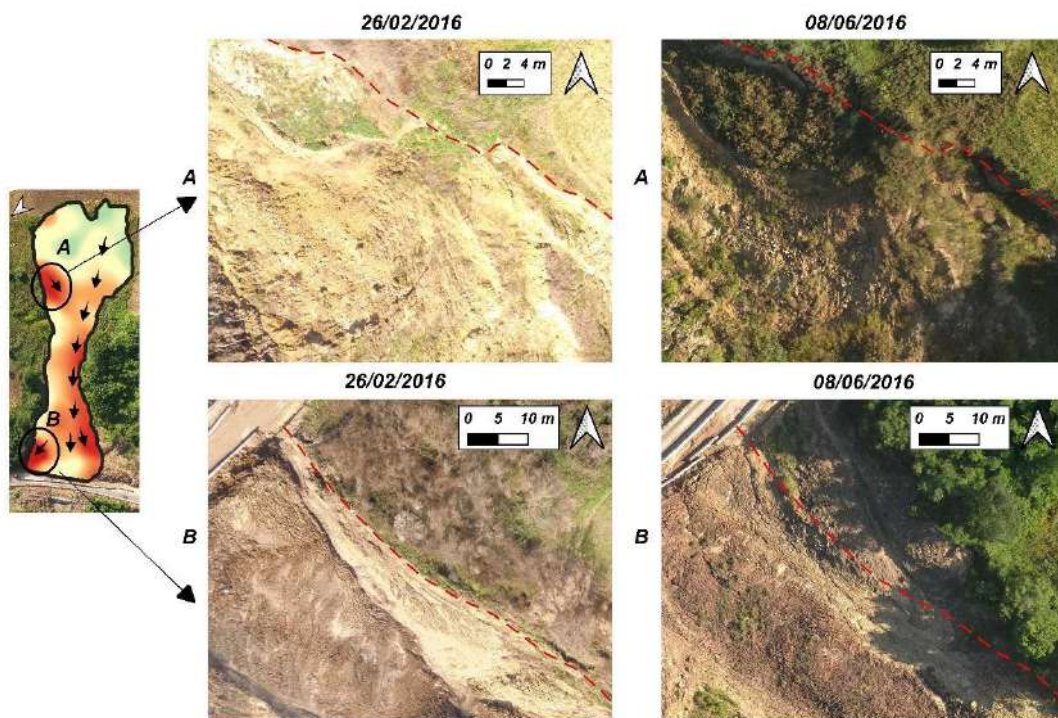
Figure 3.12. *Visual comparison of the orthophotos acquired before and after the period analysed with DIC (19 March 2016–30 April 2016) confirmed the presence of two widening zones along the right flank of the earth flow. The dashed red line represents the earth flow boundary in February 2016.*

Since there are limited examples in the literature where remote sensing has been applied for the earth flow assessment, monitoring and possible failure time prediction [12,24,28], this paper aims

to also provide the reader with a technical review of the most widely used methods in the field of engineering geology today, along with the most innovative methods which have shown the most promising results. As an example, the work carried out by Giordan et al. [24] focused on geomorphological long-term evolution (1954–2011) using aerial/satellite imagery, DEMs and topographic measurements, while Bardi et al. [29] manly focused on the role of T-InSAR during emergency monitoring.

Although, of course, the integration of technologies is often the solution to be pursued, and this should be a focus of landslide science in the next years [64], an overview of the main features of monitoring techniques applied to earth flows is provided in Table 3.6, with ratings based on the experiences of the members of this project during its conduction. Generally, it can be stated that, although T-InSAR has a high cost and involves complex deployment, it is able to reach a mm accuracy with very high temporal resolution and also allows emergency monitoring. In fact, in the present case study, the T-InSAR measurements detected a sudden acceleration of earth flow induced by an intense rainfall event (Figure 3.7C). It must be pointed out, however, that T-InSAR was only able to monitor Sector 3 with adequate accuracy along the LOS (corresponding to the earth flow toe).

Table 3.6. Overview of the main features of monitoring measurements carried out at the site of the Pietrafitta earth flow. The capability ratings for each parameter on earth flow monitoring are given in parentheses.

Techniques	Accuracy Reached	Spatial Resolution	Temporal Resolution	Range	Targets	Presumed Cost	Deployment
R-TS	mm (+)	Measurements on prisms (−)	1 h	800 m (+)	Yes (−)	€€	Complex
T-InSAR	mm (+)	8–10 m (−)	5 min (+)	800 m (+)	No (+)	€€€	Complex
TLS	cm	10 points/cm^2 (+)	Weeks	800 m (+)	No (+)	€€	Difficult
DIC	dm	5 m	Months (−)	km (+)	No (+)	€	No hardware required

R-TS measurements required the installation of prisms on the unstable slope but allowed us to extract 2D displacement measurements with a mm accuracy and adequate temporal resolution. Considering its use in earth flow processes, it is worth noting that the irregular surface deformations could cause the tilting and/or breaking of optical prisms, affecting the measurements, as happened in the present case.

TLS provides data with very high spatial resolution without using ground targets and can be effectively used to understand the amount of material mobilised using 3D volumetric information. The results from the Pietrafitta earth flow show that TLS monitoring, performed weekly, can provide useful data in terms of both vertical/horizontal deformation and the loss/gain of material for all the investigated sectors.

DIC does not require physical tools in the field and can be used with satellite data acquired several kilometres away from the unstable slope. Despite its low cost, it can be useful for observing the earth flow process as a whole. In the case of the Pietrafitta earth flow, due to the DIC results, some deformation processes were detected in areas that other techniques had failed to monitor (e.g., right flank, Figure 3.12). Overall, the algorithm used was able to detect a maximum displacement of around 4 m. Our work indicates that the displacements retrieved using this technique were underestimated.

6. Conclusions

The aims of this study were to characterise the ongoing gravitational process of the Pietrafitta earth flow and derive insights into the performance of different remote sensing techniques for the purposes of earth flow knowledge, control and emergency monitoring. Specifically, TLS, R-TS, T-InSAR and DIC technologies were applied, thus allowing us to understand the capabilities, peculiarities and limitations of the different techniques used in order to understand and monitor earth flow phenomena.

Taking into account the results achieved from each monitoring technique used, in the context of the present work, the following considerations can be made:

- The results obtained from R-TS and T-InSAR were combined and compared in order to understand the deformation behaviour at different scales. This approach made it possible to observe that, despite the different resolutions of these techniques, the deformation trends recorded remained approximately consistent, with only the presence of differences mainly related to intrinsic acquisition inequalities between the technologies. Both techniques were proven to be reliable tools for evaluating the evolution of earth flows, allowing their typical characteristics to be highlighted, such as slow, localised and persistent movements and sensitivity to rainfall events (i.e., the variation of pore water pressure), resulting in the acceleration or deceleration of displacement rates.

- Using the TLS measurements, it was possible to derive the volume of material that was mobilised during the period of maximum activity;

- The use of the DIC technique by means of satellite images made it possible to study the deformation behaviour as a whole; using this technique also allowed us to observe a deformation zone, in Sector 2, with a tendency for the landslide body to widen along the right flank. This aspect was not evidenced with the other techniques previously used.

More generally, it has been shown that, when faced with a complex landslide, the synergic use of different monitoring techniques should be considered a standard approach in order to obtain a comprehensive understanding of the processes involved [64]. However, integrated approaches based on multi-sensor data still leave unresolved areas in applied research in earth flow monitoring today. For this reason, further studies are needed to broaden the experiences reported in this field and verify the considerations made.

Within this framework, the following general points should be investigated in greater detail in future works:

- The design and use of new integrated monitoring points to be installed in the field (e.g., corner reflectors for T-InSAR equipped with optical prisms for R-TS) would make the monitoring network more efficient, providing additional insights into measurement accuracies;

- The use of orthophotos acquired from aerial platforms (e.g., UAVs) on a weekly basis would provide high-spatial- and temporal-resolution data that would constitute an excellent dataset for analysis using the DIC technique;

- The use of increasingly automated systems that make it possible to fully exploit the potential of multi-sensor monitoring should be recommended, with the help of cutting-edge techniques such as machine learning;

- The drafting of shared guidelines and standards regarding the monitoring instrumentation and techniques to be used in earth flow situations would lead to the spread of a set of best practices and better use of the monitoring solutions available today.

References

1. Revellino, P.; Grelle, G.; Donnarumma, A.; Guadagno, F.M. Structurally Controlled Earth Flows of the Benevento Province (Southern Italy). *Bull. Eng. Geol. Environ.* 2010, *69*, 487–500. https://doi.org/10.1007/s10064-010-0288-9.

2. Donnarumma, A.; Revellino, P.; Grelle, G.; Guadagno, F.M. Slope Angle as Indicator Parameter of Landslide Susceptibility in a Geologically Complex Area. In *Landslide Science and Practice: Volume 1: Landslide Inventory and Susceptibility and Hazard Zoning*; Margottini, C., Canuti, P., Sassa, K., Eds.; Springer: Berlin/Heidelberg, Germany, 2013; pp. 425–433; ISBN 978-3-642-31325-7.

3. Keefer, D.K.; Johnson, A.M. *Earth Flows: Morphology, Mobilization, and Movement*; Professional Paper; U.S. Geological Survey: 1983; Volume 1264.

4. Cruden, D.M.; Varnes, D.J. *Landslide Types and Processes*; Special Report—National Research Council; Transportation Research Board: Washington, DC, USA, 1996; pp. 36–75.

5. Hungr, O.; Evans, S.G.; Bovis, M.J.; Hutchinson, J.N. A Review of the Classification of Landslides of the Flow Type. *Environ. Eng. Geosci.* 2001, *7*, 221–238. https://doi.org/10.2113/gseegeosci.7.3.221.

6. Hutchinson, J.N.; Prior, D.B.; Stephens, N. Potentially Dangerous Surges in an Antrim Mudslide. *Q. J. Eng. Geol. Hydrogeol.* 1974, *7*, 363–376. https://doi.org/10.1144/GSL.QJEG.1974.007.04.08.

7. Handwerger, A.L.; Roering, J.J.; Schmidt, D.A. Controls on the Seasonal Deformation of Slow-Moving Landslides. *Earth Planet. Sci. Lett.* 2013, *377*, 239–247. https://doi.org/10.1016/j.epsl.2013.06.047.

8. Guerriero, L. Landslides and Infrastrucutres: The Case of the Montaguto Earth Flow in Southern Italy. *Ital. J. Eng. Geol. Environ.* 2013, 459–466. https://doi.org/10.4408/IJEGE.2013-06.B-44.

9. Revellino, P.; Guerriero, L.; Ruzza, G.; Guadagno, F.M. Defining Kinematic and Evolutive Features of Earth Flows Using Integrated Monitoring and Low-Cost Sensors. In *Understanding and Reducing Landslide Disaster Risk: Volume 3 Monitoring and Early Warning*; Casagli, N., Tofani, V., Sassa, K., Bobrowsky, P.T., Takara, K., Eds.; ICL Contribution to Landslide Disaster Risk Reduction; Springer International Publishing: Cham, Switzerland, 2021; pp. 25–40; ISBN 978-3-030-60311-3.

10. Bertello, L.; Berti, M.; Castellaro, S.; Squarzoni, G. Dynamics of an Active Earthflow Inferred From Surface Wave Monitoring. *J. Geophys. Res. Earth Surf.* 2018, *123*, 1811–1834. https://doi.org/10.1029/2017JF004233.

11. Vassallo, R.; Calcaterra, S.; D'Agostino, N.; De Rosa, J.; Di Maio, C.; Gambino, P. Long-Term Displacement Monitoring of Slow Earthflows by Inclinometers and GPS, and Wide Area Surveillance by COSMO-SkyMed Data. *Geosciences* 2020, *10*, 171. https://doi.org/10.3390/geosciences10050171.

12. Calvello, M.; Peduto, D.; Arena, L. Combined Use of Statistical and DInSAR Data Analyses to Define the State of Activity of Slow-Moving Landslides. *Landslides* 2017, *14*, 473–489. https://doi.org/10.1007/s10346-016-0722-6.

13. Di Matteo, L.; Romeo, S.; Kieffer, D.S. Rock Fall Analysis in an Alpine Area by Using a Reliable Integrated Monitoring System: Results from the Ingelsberg Slope (Salzburg Land, Austria). *Bull. Eng. Geol. Environ.* 2017, *76*, 413–420. https://doi.org/10.1007/s10064-016-0980-5.

14. Romeo, S.; Di Matteo, L.; Kieffer, D.S.; Tosi, G.; Stoppini, A.; Radicioni, F. The Use of Gigapixel Photogrammetry for the Understanding of Landslide Processes in Alpine Terrain. *Geosciences* 2019, *9*, 99. https://doi.org/10.3390/geosciences9020099.

15. Mazzanti, P. Toward Transportation Asset Management: What Is the Role of Geotechnical Monitoring? *J. Civil. Struct Health Monit.* 2017, *7*, 645–656. https://doi.org/10.1007/s13349-017-0249-0.

16. Lissak, C.; Bartsch, A.; De Michele, M.; Gomez, C.; Maquaire, O.; Raucoules, D.; Roulland, T. Remote Sensing for Assessing Landslides and Associated Hazards. *Surv. Geophys* 2020, *41*, 1391–1435. https://doi.org/10.1007/s10712-020-09609-1.

17. Mazzanti, P. Remote Monitoring of Deformation. An Overview of the Seven Methods Described in Previous GINs. *Geotech. News* 2012, *30*, 24–29.

18. Dei Cas, L.; Triglia, A.; Iadanza, C. Linee Guida per Il Monitoraggio Delle Frane. *Linee Guid. SNPA* 2021, *32*, 2021.

19. Malet, J.-P.; Maquaire, O.; Calais, E. The Use of Global Positioning System Techniques for the Continuous Monitoring of Landslides: Application to the Super-Sauze Earthflow (Alpes-de-Haute-Provence, France). *Geomorphology* 2002, *43*, 33–54. https://doi.org/10.1016/S0169-555X(01)00098-8.

20. Guerriero, L.; Guerriero, G.; Grelle, G.; Guadagno, F.M.; Revellino, P. Brief Communication: A Low-Cost Arduino®-Based Wire Extensometer for Earth Flow Monitoring. *Nat. Hazards Earth Syst. Sci.* 2017, *17*, 881–885. https://doi.org/10.5194/nhess-17-881-2017.

21. Berti, M.; Simoni, A. Reactivation of a Dormant Earthflow Documented by Field Monitoring Data; In: EGU General Assembly Conference Abstracts, 2017; p. 6331.

22. Guerriero, L.; Bertello, L.; Cardozo, N.; Berti, M.; Grelle, G.; Revellino, P. Unsteady Sediment Discharge in Earth Flows: A Case Study from the Mount Pizzuto Earth Flow, Southern Italy. *Geomorphology* 2017, *295*, 260–284. https://doi.org/10.1016/j.geomorph.2017.07.011.

23. Mantovani, F.; Pasuto, A.; Silvano, S.; Zannoni, A. Collecting Data to Define Future Hazard Scenarios of the Tessina Landslide. *Int. J. Appl. Earth Obs. Geoinf.* 2000, *2*, 33–40. https://doi.org/10.1016/S0303-2434(00)85024-2.

24. Giordan, D.; Allasia, P.; Manconi, A.; Baldo, M.; Santangelo, M.; Cardinali, M.; Corazza, A.; Albanese, V.; Lollino, G.; Guzzetti, F. Morphological and Kinematic Evolution of a Large Earthflow: The Montaguto Landslide, Southern Italy. *Geomorphology* 2013, *187*, 61–79. https://doi.org/10.1016/j.geomorph.2012.12.035.

25. Bozzano, F.; Cipriani, I.; Mazzanti, P.; Prestininzi, A. Displacement Patterns of a Landslide Affected by Human Activities: Insights from Ground-Based InSAR Monitoring. *Nat. Hazards* 2011, *59*, 1377–1396. https://doi.org/10.1007/s11069-011-9840-6.

26. Mazzanti, P.; Bozzano, F.; Cipriani, I.; Prestininzi, A. New Insights into the Temporal Prediction of Landslides by a Terrestrial SAR Interferometry Monitoring Case Study. *Landslides* 2015, *12*, 55–68. https://doi.org/10.1007/s10346-014-0469-x.

27. Pieraccini, M.; Miccinesi, L. Ground-Based Radar Interferometry: A Bibliographic Review. *Remote Sens.* 2019, *11*, 1029. https://doi.org/10.3390/rs11091029.

28. Ferrigno, F.; Gigli, G.; Fanti, R.; Intrieri, E.; Casagli, N. GB-InSAR Monitoring and Observational Method for Landslide Emergency Management: The Montaguto Earthflow (AV, Italy). *Nat. Hazards Earth Syst. Sci.* 2017, *17*, 845–860. https://doi.org/10.5194/nhess-17-845-2017.

29. Bardi, F.; Raspini, F.; Frodella, W.; Lombardi, L.; Nocentini, M.; Gigli, G.; Morelli, S.; Corsini, A.; Casagli, N. Monitoring the Rapid-Moving Reactivation of Earth Flows by Means of GB-InSAR: The April 2013 Capriglio Landslide (Northern Appennines, Italy). *Remote Sens.* 2017, *9*, 165. https://doi.org/10.3390/rs9020165.

30. Baldo, M.; Bicocchi, C.; Chiocchini, U.; Giordan, D.; Lollino, G. LIDAR Monitoring of Mass Wasting Processes: The Radicofani Landslide, Province of Siena, Central Italy. *Geomorphology* 2009, *105*, 193–201. https://doi.org/10.1016/j.geomorph.2008.09.015.

31. Clapuyt, F.; Vanacker, V.; Schlunegger, F.; Van Oost, K. Unravelling Earth Flow Dynamics with 3-D Time Series Derived from UAV-SfM Models. *Earth Surf. Dynam.* 2017, *5*, 791–806. https://doi.org/10.5194/esurf-5-791-2017.

32. Mugnai, F.; Caporossi, P.; Mazzanti, P. Exploiting Image Assisted Total Station in Digital Image Correlation (DIC) Displacement Measurements: Insights from Laboratory Experiments. *Eur. J. Remote Sens.* 2022, *55*, 115–128. https://doi.org/10.1080/22797254.2021.2025153.

33. Hermle, D.; Gaeta, M.; Krautblatter, M.; Mazzanti, P.; Keuschnig, M. Performance Testing of Optical Flow Time Series Analyses Based on a Fast, High-Alpine Landslide. *Remote Sens.* 2022, *14*, 455. https://doi.org/10.3390/rs14030455.

34. Lacroix, P.; Araujo, G.; Hollingsworth, J.; Taipe, E. Self-Entrainment Motion of a Slow-Moving Landslide Inferred From Landsat-8 Time Series. *J. Geophys. Res. Earth Surf.* 2019, *124*, 1201–1216. https://doi.org/10.1029/2018JF004920.

35. Guerriero, L.; Di Martire, D.; Calcaterra, D.; Francioni, M. Digital Image Correlation of Google Earth Images for Earth's Surface Displacement Estimation. *Remote Sens.* 2020, *12*, 3518. https://doi.org/10.3390/rs12213518.

36. Daehne, A.; Corsini, A. Kinematics of Active Earthflows Revealed by Digital Image Correlation and DEM Subtraction Techniques Applied to Multi-Temporal LiDAR Data: KINEMATICS OF ACTIVE EARTHFLOWS. *Earth Surf. Process. Landforms* 2013, *38*, 640–654. https://doi.org/10.1002/esp.3351.

37. Travelletti, J.; Oppikofer, T.; Delacourt, C. *Monitoring Landslide Displacements during a Controlled Rain Experiment Using a Long-Range Terrestrial Laser Scanning (TLS)*; Chen, J., Jiang, J., Eds.; Hans-Gerd MAAS: Beijing, China, 2008; Volume XXXVII, Part B5, p. 6.

38. Di Nocera, S.; Matano, F.; Pescatore, T.; Pinto, F.; Quarantiello, R.; Senatore, M.R.; Torre, Ma.L. Geological Scheme of the Transect Eastern Picentini-Southern Daunia Mts.: Stratigraphic Units and Tectonic Evolution of the Outer Zones of the Southern Apennines, Italy. *Boll. Soc. Geol. Ital.* 2006, *125*, 39–58.

39. Di Nocera, S.; Matano, F.; Torre, M. The "samnitic" Units Auct. (Central-Southern Apennines): Review of Current Palaegeographic and Stratigraphic Interpretations and New Hypotheses with the Introduction of the Unit of Frigento. 2002, *2002/1*, 87–102.

40. Guerriero, L.; Diodato, N.; Fiorillo, F.; Revellino, P.; Grelle, G.; Guadagno, F. Reconstruction of Long-Term Earth-Flow Activity Using a Hydro-Climatological Model. *Nat. Hazards* 2015, *77*, 1–15. https://doi.org/10.1007/s11069-014-1578-5.

41. Guerriero, L.; Revellino, P.; Mottola, A.; Grelle, G.; Sappa, G.; Guadagno, F. Multi-Temporal Mapping of the Caforchio Earth Flow, Southern Italy. *Rend. Online Della Soc. Geol. Ital.* 2015, *35*, 166–169. https://doi.org/10.3301/ROL.2015.91.

42. Guerriero, L.; Coe, J.A.; Revellino, P.; Grelle, G.; Pinto, F.; Guadagno, F.M. Influence of Slip-Surface Geometry on Earth-Flow Deformation, Montaguto Earth Flow, Southern Italy. *Geomorphology* 2014, *219*, 285–305. https://doi.org/10.1016/j.geomorph.2014.04.039.

43. Guerriero, L.; Focareta, M.; Fusco, G.; Rabuano, R.; Guadagno, F.M.; Revellino, P. Flood Hazard of Major River Segments, Benevento Province, Southern Italy. *J. Maps* 2018, *14*, 597–606. https://doi.org/10.1080/17445647.2018.1526718.

44. Revellino, P.; Guerriero, L.; Mascellaro, N.; Fiorillo, F.; Grelle, G.; Ruzza, G.; Guadagno, F. Multiple Effects of Intense Meteorological Events in the Benevento Province, Southern Italy. *Water* 2019, *11*, 1560. https://doi.org/10.3390/w11081560.

45. Castagnetti, C.; Bertacchini, E.; Corsini, A.; Capra, A. Multi-Sensors Integrated System for Landslide Monitoring: Critical Issues in System Setup and Data Management. *Eur. J. Remote Sens.* 2013, *46*, 104–124. https://doi.org/10.5721/EuJRS20134607.

46. Jaboyedoff, M.; Oppikofer, T.; Abellán, A.; Derron, M.-H.; Loye, A.; Metzger, R.; Pedrazzini, A. Use of LIDAR in Landslide Investigations: A Review. *Nat. Hazards J. Int. Soc. Prev. Mitig. Nat. Hazards* 2012, *61*, 5–28. https://doi.org/10.1007/s11069-010-9634-2.

47. Bitelli, G.; Dubbini, M.; Zanutta, A. Terrestrial Laser Scanning and Digital Photogrammetry Techniques to Monitor Landslide Bodies. *Int. Arch. Photogramm. Remote Sens. Spat. Inf. Sci.* 2004, *35*, 246–251.

48. Mazzanti, P.; Schilirò, L.; Martino, S.; Antonielli, B.; Brizi, E.; Brunetti, A.; Margottini, C.; Scarascia Mugnozza, G. The Contribution of Terrestrial Laser Scanning to the Analysis of Cliff Slope Stability in Sugano (Central Italy). *Remote Sens.* 2018, *10*, 1475. https://doi.org/10.3390/rs10091475.

49. Bozzano, F.; Esposito, C.; Mazzanti, P.; Innocca, F.; Romeo, S. Urban Engineered Slope Collapsed in Rome on February 14th, 2018: Results from Remote Sensing Monitoring. *Geosciences* 2020, *10*, 331. https://doi.org/10.3390/geosciences10090331.

50. Lague, D.; Brodu, N.; Leroux, J. Accurate 3D Comparison of Complex Topography with Terrestrial Laser Scanner: Application to the Rangitikei Canyon (N-Z). *ISPRS J. Photogramm. Remote Sens.* 2013, *82*, 10–26. https://doi.org/10.1016/j.isprsjprs.2013.04.009.

51. Yu, S.; Wen, Y.; Chen, Z.; Zhang, G.; Wang, Y.; Hao, J.; Zhang, Q. A Rapid Gradation Detection System for Earth and Stone Materials Based on Digital Image. *Adv. Civ. Eng.* 2021, *2021*, e6660301. https://doi.org/10.1155/2021/6660301.

52. Caporossi, P.; Mazzanti, P.; Bozzano, F. Digital Image Correlation (DIC) Analysis of the 3 December 2013 Montescaglioso Landslide (Basilicata, Southern Italy): Results from a Multi-Dataset Investigation. *ISPRS Int. J. Geo-Inf.* 2018, *7*, 372. https://doi.org/10.3390/ijgi7090372.

53. White, D.J.; Take, W.A.; Bolton, M.D. Soil Deformation Measurement Using Particle Image Velocimetry (PIV) and Photogrammetry. *Géotechnique* 2003, *53*, 619–631. https://doi.org/10.1680/geot.2003.53.7.619.

54. Bickel, V.T.; Manconi, A.; Amann, F. Quantitative Assessment of Digital Image Correlation Methods to Detect and Monitor Surface Displacements of Large Slope Instabilities. *Remote Sens.* 2018, *10*, 865. https://doi.org/10.3390/rs10060865.

55. Corvec, N.L.; Walter, T.R. Volcano Spreading and Fault Interaction Influenced by Rift Zone Intrusions: Insights from Analogue Experiments Analyzed with Digital Image Correlation Technique. *J. Volcanol. Geotherm. Res.* 2009, *183*, 170. https://doi.org/10.1016/j.jvolgeores.2009.02.006.

56. Kääb, A. Monitoring High-Mountain Terrain Deformation from Repeated Air- and Spaceborne Optical Data: Examples Using Digital Aerial Imagery and ASTER Data. *ISPRS J. Photogramm. Remote Sens.* 2002, *57*, 39–52. https://doi.org/10.1016/S0924-2716(02)00114-4.

57. Avouac, J.-P.; Ayoub, F.; Wei, S.; Ampuero, J.-P.; Meng, L.; Leprince, S.; Jolivet, R.; Duputel, Z.; Helmberger, D. The 2013, Mw 7.7 Balochistan Earthquake, Energetic Strike-Slip Reactivation of a Thrust Fault. *Earth Planet. Sci. Lett.* 2014, *391*, 128–134. https://doi.org/10.1016/j.epsl.2014.01.036.

58. Mugnai, F.; Cosentino, A.; Mazzanti, P.; Tucci, G. Vibration Analyses of a Gantry Structure by Mobile Phone Digital Image Correlation and Interferometric Radar. *Geomatics* 2022, *2*, 17–35. https://doi.org/10.3390/geomatics2010002.

59. Stumpf, A. Landslide Recognition and Monitoring with Remotely Sensed Data from Passive Optical Sensors; University of Strasbourg: Strasbourg, France, 2013.

60. Tong, X.; Ye, Z.; Xu, Y.; Gao, S.; Xie, H.; Du, Q.; Liu, S.; Xu, X.; Liu, S.; Luan, K.; et al. Image Registration With Fourier-Based Image Correlation: A Comprehensive Review of Developments and Applications. *IEEE J. Sel. Top. Appl. Earth Obs. Remote Sens.* 2019, *12*, 4062–4081. https://doi.org/10.1109/JSTARS.2019.2937690.

61. Dematteis, N.; Wrzesniak, A.; Allasia, P.; Bertolo, D.; Giordan, D. Integration of Robotic Total Station and Digital Image Correlation to Assess the Three-Dimensional Surface Kinematics of a Landslide. *Eng. Geol.* 2022, *303*, 106655. https://doi.org/10.1016/j.enggeo.2022.106655.

62. Guerriero, L.; Ruzza, G.; Maresca, R.; Guadagno, F.M.; Revellino, P. Clay Landslide Movement Triggered by Artificial Vibrations: New Insights from Monitoring Data. *Landslides* 2021, *18*, 2949–2957. https://doi.org/10.1007/s10346-021-01685-7.

63. Mazzanti, P.; Caporossi, P.; Muzi, R. Sliding Time Master Digital Image Correlation Analyses of CubeSat Images for Landslide Monitoring: The Rattlesnake Hills Landslide (USA). *Remote Sens.* 2020, *12*, 592. https://doi.org/10.3390/rs12040592.

64. Casagli, N.; Intrieri, E.; Tofani, V.; Gigli, G.; Raspini, F. Landslide Detection, Monitoring and Prediction with Remote-Sensing Techniques. *Nat. Rev. Earth Environ.* 2023, *4*, 51–64. https://doi.org/10.1038/s43017-022-00373-x.

Chapter 4

The Contribution of Digital Image Correlation for the Knowledge, Control, and Emergency Monitoring of Earth Flows

Authors: Davide Mazza [1-4*], Saverio Romeo [2], Antonio Cosentino [3-4], Paolo Mazzanti [3-4], Francesco Maria Guadagno[1] and Paola Revellino[1],

1   *Department of Sciences and Technologies, University of Sannio, 82100 Benevento, Italy; dmazza@unisannio.it (D.M.); guadagno@unisannio.it (F.M.G.); paola.revellino@unisannio.it (P.R.)*

2   *ISPRA—Geological Survey of Italy, Via V. Brancati 48, 00144 Roma, Italy; saverio.romeo@isprambiente.it*

3   *Earth Sciences Department, Sapienza University of Rome, Piazzale Aldo Moro 5, 00185 Rome, Italy*

4   *NHAZCA S.r.l., Via V. Bachelet 12, 00185 Rome, Italy; paolo.mazzanti@uniroma1.it*

*   *Correspondence: antonio.cosentino@uniroma1.it*

4.1 Abstract

Earth flows are complex geological processes that, when interacting with linear infrastructures, have the potential to cause significant damage. Consequently, conducting comprehensive investigations and continuous monitoring are becoming paramount in designing effective mitigation measures and ensuring sustainable risk management practices. The use of digital image correlation (DIC) algorithms for the displacement monitoring of earth flows is a relatively new and growing field with a limited number of dedicated works in the literature. Within this framework, the present paper contributes by evaluating DIC techniques at several earth flow sites. These assessments were founded upon data obtained from both low-cost and multi-platform sensors, used to assess the displacement field, pinpointing the most active sectors, and gauging their rates of movement during different kinematic phases. In this regard, the highest localized movement velocities reached in the Pietrafitta (0.01 m/day) and Grillo (0.63 m/day) earth flows experience different ongoing kinematic processes. The versatility of these techniques is notable, manifesting in the ease of installation, cost-effectiveness, and adaptability to various platforms. The proven reliability

in terms of maximum accuracy (1 pixel) and sensitivity (0.05 m) lays the foundation for the extensive use of the presented techniques. The amalgamation of these attributes positions DIC techniques as competitive, adaptable, and readily deployable tools in earth flow studies.

4.2 Introduction

Earth flows predominantly occur within clayey and structurally complex formations [1–7]. When they interact with human-made structures, they can cause substantial damage. This holds particularly true with linear infrastructures like highways, railways, and pipelines crossing inhabited hilly regions such as the Italian Apennines [8]. Implementing mitigation and stabilization measures is often challenging due to their typical rheological and mechanical behaviors and their complex kinematics [9]. In this context, investigation and monitoring activities play a pivotal role in designing effective mitigation strategies and, consequently, in sustainable risk management [10–12]. Despite this, only a few works in the literature focused on the critical evaluation of both conventional and innovative techniques for earth flow monitoring. As an example, the authors of [13] studied the geomorphological evolution of earth flow through a combination of monitoring techniques such as visual interpretation of aerial and satellite imagery, quantitative analysis of digital elevation models (DEMs), and three-dimensional topographic measurements using robotic total stations (RTSs). Also, the authors of [14] employed a Ground-Based Interferometric Synthetic Aperture Radar (GB-InSAR) for risk management associated with an earth flow reactivation. Instead, the authors of [15] compared and combined data collected during different earth flow phases that occurred in 2016 in the site of Pietrafitta using different ground-based remote sensors such as RTS, GB-InSAR, and Terrestrial Laser Scanners (TLSs), with the aim to derive insights into the performance of such techniques. In addition, the authors of [16] demonstrated the applicability of using global positioning system (GPS) techniques to determine the 3D coordinates of the moving points of an earth flow precisely.

This scarcity may stem from the need to integrate multiple sensors to monitor the various factors influencing these complex processes, along with cost issues [17]. Although imaging techniques possess considerable potential benefits, the monitoring of earth flows near linear infrastructures remains a relatively nascent and evolving field, even in common practice. In recent years, some analyses based on digital image correlation (DIC) algorithms have been successfully employed for landslide assessment and monitoring [18–30], as well as for many other applications in geosciences [31]. Applying these techniques requires careful consideration of several factors, including selecting

appropriate processing algorithms, data calibration and validation, and integrating different data types. Furthermore, interpreting DIC data requires specialized knowledge and skills in the field of engineering geology. Given the complexities involved, comprehensively studying landslides is challenging and requires accurate imaging and modeling over time [32,33]. As indicated in [34], its overarching purpose is a pivotal determinant of the success of geotechnical monitoring. Three main monitoring categories are pertinent: knowledge monitoring, control monitoringand emergency monitoring. These classifications can greatly assist in managing earth flow risk related to the presence of linear infrastructures. In all the aforementioned monitoring categories, DIC techniques are nowadays able to provide reliable data quickly, and, in specific cases, they can underpin the establishment of early warning systems (emergency monitoring) [35]. Such monitoring data can serve early warning purposes by identifying, for instance, displacement thresholds.

The overall objective of this work is to understand how modern digital image correlation (DIC) techniques can be utilized for the knowledge, control and emergency monitoring of earth flows while also conducting an assessment and comparison with more conventional monitoring techniques.

This study aims to present three examples of DIC monitoring applications on two distinct case studies, namely the Pietrafitta and Grillo earth flows, during three different timeframes. For these studies, images were acquired from three different platforms (a ground-based camera for Pietrafitta and UAV and satellite images for Grillo) during specific periods of heightened earth flow activity.

However, unlike other methodologies, DIC analysis carried out with satellite images was only used for long-term cognitive monitoring in the absence of ancillary data. The specific objectives are as follows:

- Evaluate the monitoring capabilities of the DIC technique at the Pietrafitta earth flow pilot site using low-cost ground-based sensors;

- Assess the monitoring capabilities of the DIC technique at the Grillo earth flow pilot site using sensors installed on UAV platforms;

- Perform a quantitative comparison with two classical monitoring techniques used at the pilot sites: the robotic total station survey (RTS) for Pietrafitta and the global navigation satellite system (GNSS) for Grillo. This comparison will focus particularly on displacement field assessment, identifying the most active sectors, and measuring motion rates during various phases of the earth flow.

4.3 Case study sites

This section presents the study sites characterized by the presence of slope instabilities and strategic road infrastructures. Activities were carried out at two landslide sites within the Campania Region (Italy), known as Pietrafitta and Grillo, situated in the provinces of Benevento and Avellino, respectively (Figure 1a). Both landslides can be classified as earth flows according to the well-known classification in [36], owing to their characteristic slow-moving and intermittent nature and the material involved. They mobilize clay-rich flysch formations (late Cretaceous–Miocene), which are widespread in the southern Apennines [1].
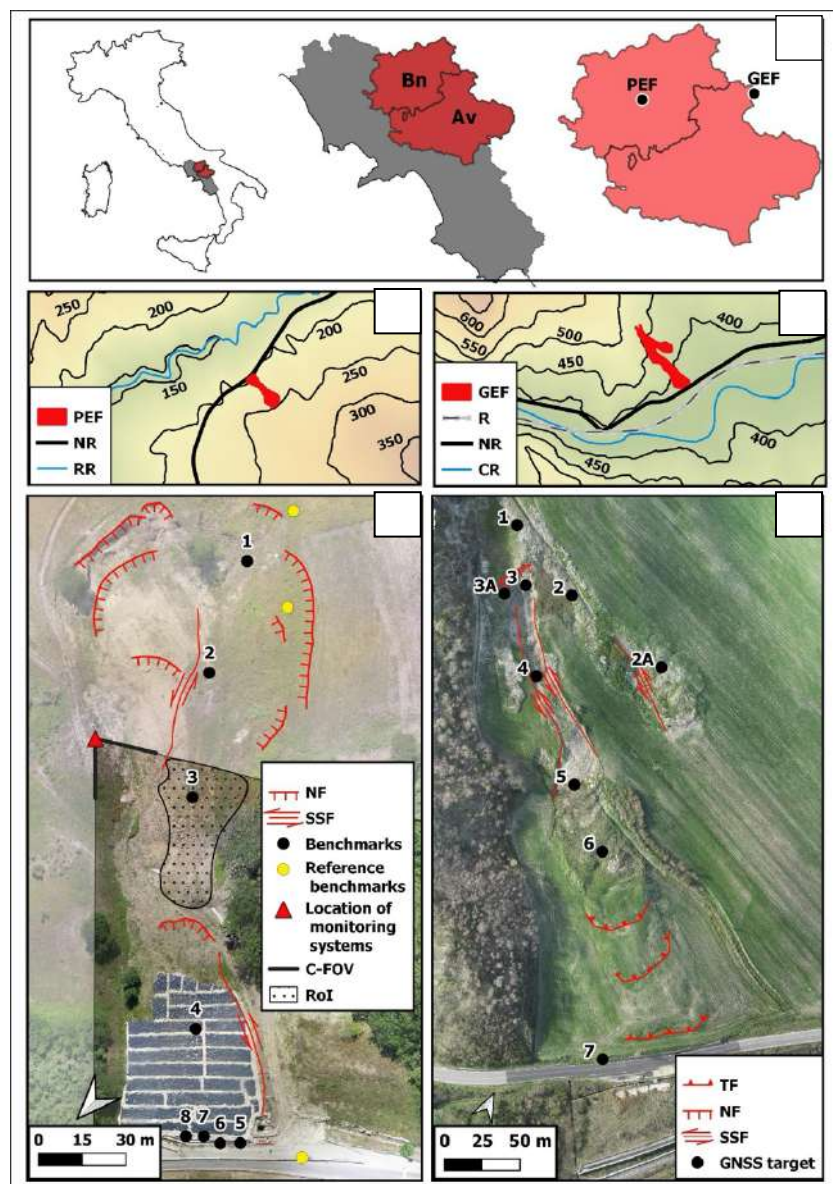
Figure 4.1. *a) General overview and location of the earth flow study site. The Pietrafitta and Grillo earth flows are shown, with their topographical setting in b) and d), and orthophotos in c) and e), respectively. PEF: Pietrafitta earth flow, GEF: Grillo earth flow, NR: national road; RR: Reventa River; R: railway; CR: Cervaro River; TF: thrust fault; NF: normal fault; SSF: strike–slip fault; C-FOV: camera field of view; RoI: region of interest.*

4.3.1 Pietrafitta Earth Flow

The *Pietrafitta* earth flow (41°13'13" N, 14°44'33" E) develops along the north-western slope of the *Torre Palazzo* hill, situated at elevations ranging from 200 to 250 m a.s.l., on the southern side of the Reventa River Valley, with an average slope angle of about 16° (Figure. 4.1 b-d). The earth flow is located within an overthrust fault zone between the *Flysch Rosso* formation (FYR) and the *Fragneto Monforte* formation (UFM). These geological sequences consist of a complex alternation of clay, sandstone, and calcareous marl levels. The entire extent of the earth flow spans approximately 250 m, with a width varying from approximately 30 m at the middle channel to around 100 m at both the source and depositional areas. Overall, it covers an area of about 10,000 m^2; the estimated thickness of the material involved is between 2 and 5 m. The volume mobilized during various reactivations events is estimated at around 300,000 m^3. Its active bulging toe has repeatedly affected a segment of the national road SS87, leading to several issues related to road asset management. The periods of greatest activity were in 2015 and 2016 which led to the complete closure of the road. From November 2016 to July 2017, some provisional works were carried out to mitigate the geomorphological risk. In particular, the earth flow toe was covered with a waterproof sheet and a drainage trench was dug at the middle of the slope. However, an intensive rainfall period- exacerbated by a rapid snow melting event- leading at the beginning of March 2018 to the earth flow reactivation affecting more than half of the slope. The rainfall period is well evidenced by rainfall data collected at the "Torrecuso" rain gauge, managed by Centro Agrometeorologico Regionale (C.A.R.) of the Campania Region, located 3 km west and at the same elevation as the *Pietrafitta* earth flow (Figure 4.2).
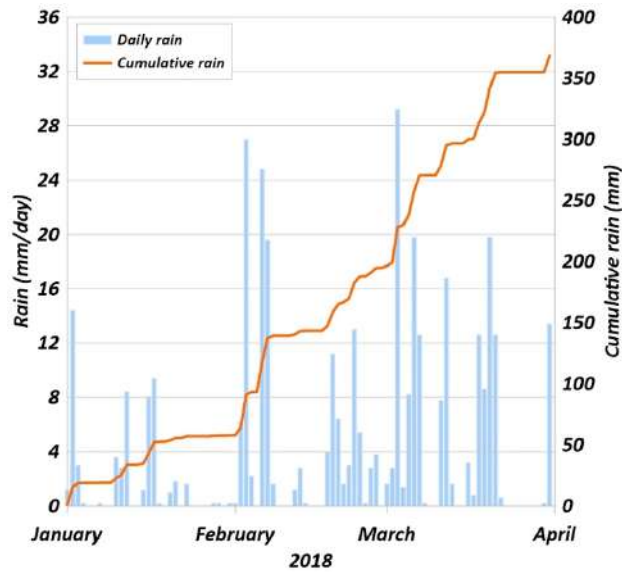
Figure 4.2. *"Torrecuso" rain gauge pluviogram.*

Pietrafitta's earth flow has been the subject of specific studies including the work [15], which aimed to study the process through remote sensing instruments and a multi-sensor approach. The work carried out by the authors of [15] took into consideration the period of activity in 2016, exploiting different monitoring systems installed along the slope and combining the results of the different technologies. Thanks to this approach, the authors were able to fully understand the deformative behaviour of earth flow in *Pietrafitta* and the work presented here has taken advantage of this knowledge to study the period of activity in March 2018.

4.3.2 Grillo Earth Flow

The *Grillo* earth flow (41°14'32"N, 15°15'51"E) is located along the southwestern slope at elevations ranging from 350 to 500 m a.s.l, on the northern side of the Cervaro River Valley (Figure 4.1 c-e), involving the *Flysch of Faeto* formation (FAE) terrain [37], which crops out with a calcareous–clayey–marly member. The *Flysch of Faeto* is highly fractured and many springs, which are typically controlled by a local permeability contrast between clayey and fractured strata, are widespread in the area, especially in the upper part of the slope [38]. The earth flow body exhibits a stream bed incision that remains wet for a significant portion of the year. Two active branches depart from the source area of the earth flow, with one of them being notably more pronounced, featuring a 130-metre-long transport zone, and a fan-shaped, bulging toe. Different from the transport and deposition zone—where thrust and strike–slip faults are dominant—the source area is characterized by the presence of normal faults (Figure 4.3). In total, the *Grillo* earth flow, covers an area of approximately 20,000 m^2

and is located in the proximity of the well-know *Montaguto* earth flow [13,38,39]. This latter earth flow has experienced multiple reactivations over the years, resulting in severe damage and disruptions to both the SS90 national road and the strategic railway line connecting *Benevento* and *Foggia* towns [38]. Similarly, the *Grillo* earth flow affects the same linear infrastructures. During the monitoring campaign, rainfall data were collected from April 2022 to June 2023 at the "Orsara di Puglia" rain gauge, managed by the local Civil Protection. Currently, the SS90 national road has been subjected to deformation due to the pressure exerted by the earth flow toe, whereas the railway line is presently safeguarded through the implementation of structural mitigation works. These measures include the construction of pile bulkheads and retaining walls (Figure 4.1e).

Figure 4.3. *The red arrows highlight the segment of the main scarp generated by the presence of a normal fault-like structure.*

4.4 Materials and Methods

This chapter presents the Remote Sensing instruments (§4.4.1) in terms of sensors and platforms used in this study as well the techniques for data processing (§4.4.2) [40].

The main tools used in the processing phases were the IRIS software (version 1.17) [20], developed by NHAZCA S.r.l., for coregistration, multi-master, single-pair DIC analysis, and generation of displacement maps and time series; the Agisoft Metashape (version 1.7.6) software for the Structure from Motion (SfM) photogrammetric processing of Unmanned Aerial System (UAS)

imagery; and the QGIS software (version 3.10.8) for Digital Surface Model (DSM) generation, computation of hillshades, and for all spatial analyses.

4.4.1 Remote Sensing Instruments and Data

In this study, monitoring instruments and available data were selected based on their functional properties to ensure efficient performance in terms of spatial, radiometric, spectral, and temporal resolution.

With reference to the *Pietrafitta* earth flow, the initial integrated monitoring system described by [15] was removed and only partially reactivated—with a different configuration—in July 2017 (Figure 4.4a). Specifically, a ground-based rugged camera (72x300mm in size) equipped with a 1/2.9" progressive CMOS low-resolution sensor (2MP) and a 3.6mm focal length was securely installed on a stable pole situated on the left flank of the earth flow (Figure 4.4b-c). Additionally, the Robotic Total Station (Topcon mod. PS-101)—previously located on the opposite slope [15]—was positioned on the right flank of the earth flow, looking at 11 reflectors strategically placed along the slope for location (Figure 4.1d). The R-TS acquired data with a minimum resolution/accuracy of 1". While the installation of these monitoring instruments—as already mentioned—occurred in July 2017, our data analysis was primarily centred on data acquired in March 2018. This timeframe coincided with the landslide reactivation. The data obtained from the RTS were compared with those derived from the DIC analysis to evaluate the reliability of the technique. We employed the well-established Pearson correlation method for this comparative analysis [41].
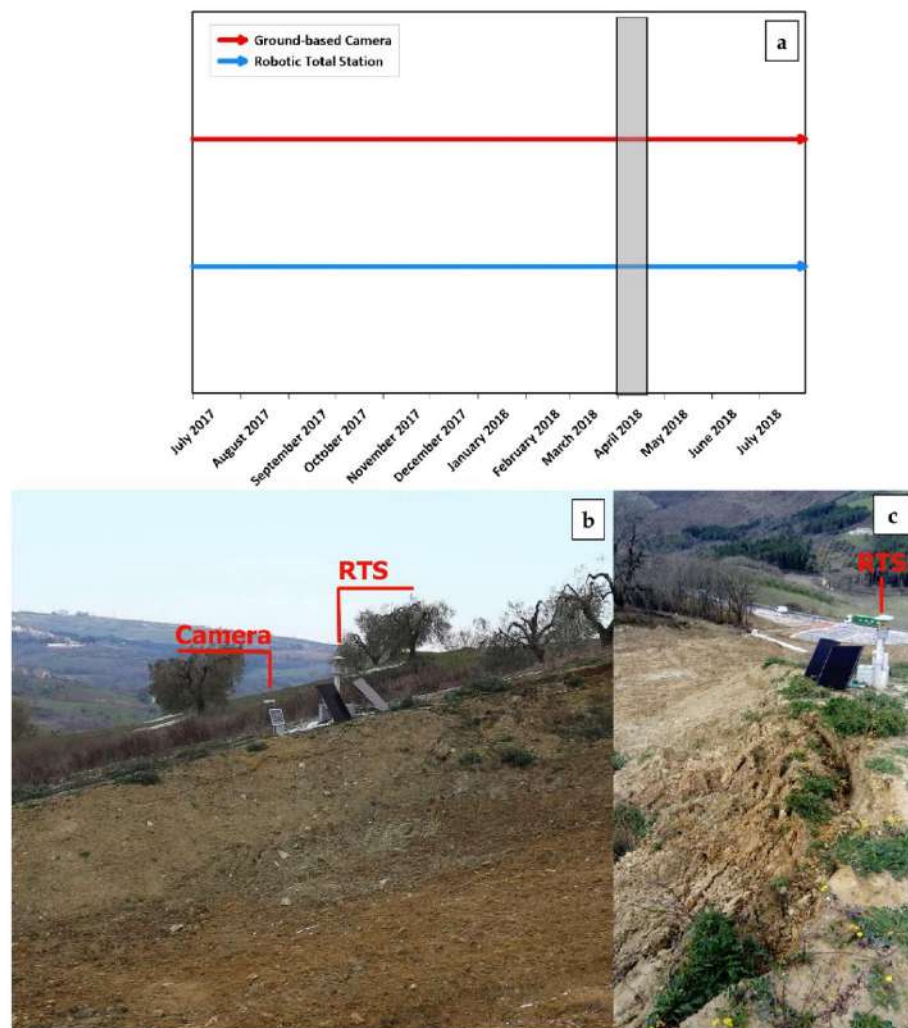
Figure 4.4. a) Timeline of the new monitoring system. The shaded grey box represents the timeframe analysed. b) Location of the ground-based camera and RTS captured from the opposite flank of the earth flow. c) Location of RTS looking downhill.

Regarding the employment of a UAS for the *Grillo* earth flow study, we used a DJI Phantom 4 coupled with a D-RTK2 mobile station. This drone was equipped with a 1-inch CMOS sensor (20 megapixels) and a 24 mm focal length. The Real-Time Kinematics (RTK) system exhibited a remarkable positioning accuracy of 2 cm + 1 part per million (ppm) in both the vertical and horizontal dimensions. For georeferencing targets and monitoring activities within the Grillo earth flow area, we employed an RTK-capable GNSS receiver (Topcon model HiPer SR) with 3.5 mm + 0.4 ppm and 3.0 mm + 0.1 ppm vertical and horizontal precision, respectively. The data were acquired during a monitoring campaign that started in April 2022 through multi-temporal UAS and GNSS acquisitions in RTK mode using self-made targets (Figure 4.5). Table 4.1 presents a synopsis of the surveys performed, offering a comprehensive summary of the acquired dataset.

Figure 4.5. *a) An operator during GNSS-RTK data collection.* **b)** *A self-made GNSS target.*

Table 4.1. *Timing of the multi-temporal UAS and GNSS surveys performed at the Grillo earth flow.*

Date	GNSS	UAS
12/04/2022		✔
03/10/2022		✔
01/12/2022	✔	✔
01/02/2023	✔	✔
22/03/2023	✔	✔
18/05/2023	✔	✔

Furthermore, with the aim of observing how the phenomenon evolved over a longer period, Google® satellite imagery was used to perform DIC analysis on the *Grillo* earth flow. A summary of the dataset is shown in Table 4.2.

Table 4.2: *Dataset for satellite DIC analysis at Grillo earth flow.*

Date	Satellite	GSD (m)
13/05/2009	GeoEye-1	0.41
15/04/2013	WorldView-1	0.47
01/11/2017	TripeSat-1	0.80
14/06/2019	WorldView-2	0.46

Table 4.3 summarizes the characteristics of the monitoring platforms from which the data for the DIC technique were acquired.

Table 4.3. *Summary of the imaging platforms used for the DIC technique.*

Platform	*Pole (ground-based*)	*UAS*	*Satellite*
Sensor	1/2.9" CMOS (2MP)	1" CMOS (20MP)	various (depending on constellation)
Scenario	*Pietrafitta* earth flow	*Grillo* earth flow	*Grillo* earth flow
Geometric resolution	10-63 cm	3 cm	30-100 cm
Radiometric resolution	10-bit	12-bit	various
Spectral resolution	low (RGB)	low (RGB)	low (RGB)
Temporal resolution	days–hours	months	years

4.4.2 Imaging techniques for data processing

For each study site, separate processing chains were created for the DIC techniques. To enhance clarity, these processing chains have been categorized into three main stages: Pre-processing, Processing, and Post-processing (Figure 4.6). The analyses were carried out for a 2D monitoring of the slope surface; therefore, no volumetric studies were carried out because they were not in line with the objective of the work.

	Ground-based camera imagery (Pietrafitta earth flow)	UAS imagery (Grillo earth flow)	Google Satellite imagery (Grillo earth flow)
Pre-processing	Images coregistration ⇩ Average GSD computation	SfM Photogrammetric elaboration ⇩ DSMs generation ⇩ Hillshades computation ⇩ Hillshades coregistration	Images containing GCPs export ⇩ Images geoferencing using GCPs coordinates ⇩ Images coregistration
Processing	Multi-master DIC analysis: PC algorithm ⇩ Displacement map	Multi-master DIC analysis: PC algorithm ⇩ Displacement map	Multi-master DIC analysis: NCC algorithm ⇩ Displacement map
Post-Processing	Time series extraction from displacement map ⇩ DIC and R-TS time series comparison and validation	Time series extraction from displacement map ⇩ DIC and GNSS time series comparison and validation	Time series extraction from displacement map

Figure 4.6. General workflow for the instruments used.

The analyses performed with the dataset obtained from the ground-based camera (for the *Pietrafitta* earth flow) and those performed with the UAV dataset (for the *Grillo* earth flow) were then quantitatively compared with the data obtained with other monitoring tools (RTS and GNSS, respectively). For the *Grillo* earth flow, in addition to the mentioned methods of analysis, it was necessary to use a dataset of satellite images with for long-term cognitive monitoring, which was previously performed for the *Pietrafitta* earth flow [15]. These DIC analyses using satellite images were used for a qualitative purpose and the results were not quantitatively compared with the other techniques.

a) Analysis at the Pietrafitta landslide

For the *Pietrafitta* earth flow, we commenced by co-registering the data acquired from the ground-based rugged camera. This co-registration process was undertaken as an initial step in the pre-processing stage. Subsequently, we computed the Ground Sampling Distance (GSD), which represents the distance, measured on the ground, between two adjacent pixel centres (*Pre-processing*). The determination of GSD holds pivotal importance as it serves as a key parameter to be considered before starting any monitoring activities. The GSD is calculated by taking into account the distance from the area of interest to the camera, along with the specific camera specifications such as image and sensor widths, as well as the focal length. To clarify, it is worth noting that a larger GSD corresponds to a reduced spatial resolution within the captured image, resulting in diminished visibility of finer details.

In this scenario, an average GSD value was determined, factoring in the distance arising from the camera's non-perpendicular alignment relative to the Line of Sight (LoS) and this configuration can significantly distort the pixel size. Unfortunately, in this case, the value of the angle of incidence was omitted from the GSD calculation due to obvious measurement problems. To solve this problem and correct the GSD value, identifiable points of known sizes within the image were used as benchmarks.

To generate a displacement map, a multi-master analysis based on the DIC algorithm was carried out. DIC is an optical numerical measurement technique that provides 2D surface deformation data through the comparison of co-registered digital images collected at different time points [42,43]. Displacement maps can be generated either by comparing a single pair of images taken before and after the deformation event (single analysis approach) or by utilizing an image stack of the same area (multi-master approach). The latter approach allows for the extrapolation of displacement time series for each selected pixel. The displacement analysis, performed to retrieve the movements that occurred at the *Pietrafitta* earth flow, relies on the Phase Correlation (PC) algorithm proposed in [44].

The PC algorithm is based on a frequency domain data representation, computed through fast Fourier transforms (FTs) employing a moving window. It leverages the FT translation property, wherein a spatial domain shift between two images manifests as phase differences in the frequency domain [15]. In Equation (1), the functions $F(u,v)$ and $G(u,v)$ represent the respective FTs of $f(x,y)$ and $g(x,y)$, which we assume to be two image functions. The notation F−1 signifies the inverse FT.

$$PC=F-1\{F(u,v)*G(u,v)|F(u,v)*G(u,v)|\}= F-1\{exp(-i(u\Delta x+v\Delta y))\} \qquad (1)$$

It is worth noting that three different displacement analyses, designated as *A*, *B*, and *C,* were performed for this case study using the PC algorithm. The primary objective was to evaluate variations in the accuracy of image analysis in response to different temporal resolutions. In this regard, different moving windows sizes were used, and different approaches were tested as detailed in Table 4.4.

Table 4.4. Analysis performed for the Pietrafitta case study. Time span covered by analysis B and C refers to a single day (21 March 2018). Time is expressed as UTC +1. MM: multi-master analysis; SA: single analysis.

	Analysis		
	A	B	C
Time span covered	07.03.2018 – 31.03.2018	08:47 – 17:18	13:02 – 14:06
Images processed	25	8	2
Temporal resolution	1 day	1 hour	1 hour
Approach	MM	MM	SA
Window size	64 pixel	8 pixel	8 pixel

Considering the camera FOV, after the co-registration stage, a region of interest (RoI) was selected (Figure 1e) and the analysis was started (*Processing*). This was also to avoid the possible noise that could interfere with the analyses due to the presence of dense vegetation on the sides of the slope.

Harnessing the intrinsic capability of DIC to quantitatively measure deformations that occurred between two or more sequentially acquired images, captured at different times, we systematically extrapolated displacement time series for select deforming pixels, in order to assess their evolution over time (*Post-processing*). The verification and validation of these time series were conducted with regard to the available ancillary data, primarily derived from the RTS.

b) Analysis at the Grillo landslide

With regard to the utilization of Unmanned Aerial Systems (UASs) in the monitoring of the Grillo earth flow, we used the acquired aerial images to conduct photogrammetric processing through the well-known SfM technique [45]. The application of SfM photogrammetry to UAS imagery represents an emerging methodology that ensures high spatial resolution and flexible surveying periodicity, both of which are fundamental elements in earth flow monitoring [46–48]. Furthermore, UAS photogrammetry facilitates the mapping of remote and impervious areas [46,49,50].

Subsequently, 3D topographic models were generated and accurately georeferenced, enabling the derivation of DSMs and consequently, the production of hillshades at a resolution of 20 cm\pixel for each UAS campaign (*Pre-processing*).

Following this stage, a multi-master analysis, employing the PC algorithm, was used to generate a displacement map. This approach is similar to the methodology utilized for the Pietrafitta earth flow (Processing). In this case, a window size of 32 pixels was employed for the analysis.

Similarly, we extrapolated displacement time series for specific deforming pixels to evaluate their temporal evolution (*Post-processing*). As described above, these time series were compared and validated with the available ancillary data (GNSS receiver, Table 4.1).

Moreover, Google® satellite imagery between 2009 and 2019 was exploited for image analysis. Firstly, we exclusively selected and exported images that contained well-known Ground Control Points (GCPs). Subsequently, these images were georeferenced using the coordinates of the reference points themselves (Pre-Processing). Furthermore, the selected images were co-registered to facilitate the customary multi-master analysis utilizing the Normalized Cross Correlation (NCC) algorithm for the generation of the displacement map (Processing). Unlike the previously introduced PC algorithm, it is worth noting that the NCC operates directly within the spatial domain of the data [51]. For each pixel of the master image, a Square Template Window (STW) is defined, and various parameters such as the number of pixels, mean, and standard deviation are computed. Simultaneously, the search template, which shares the same size as the STW, is also moved within a defined search radius around each pixel of the secondary image, with similar parameters computed for this template. An iterative computation of the NCC value then allows us to identify the optimal correspondence correlation surface. Mathematically, the NCC is defined as follows:

$$NCC = \frac{1}{n} \sum_{x,y} \frac{1}{\sigma_f \sigma_t} \left(f(x,y) - \mu_f \right) \left(t(x,y) - \mu_t \right) \qquad (2)$$

where f and t are the primary and secondary images, respectively; n is the number of pixels in each template; μ is the mean; and σ is the standard deviation.

In addition, in this case, the displacement time series from pixels were also extrapolated (*Post-processing*).

4.5 Results

In this section, we present the main outcomes obtained in both temporal (e.g., displacement time series) and spatial terms (e.g., displacement maps). Furthermore, whenever feasible, we conducted comparisons among different datasets originating from the diverse monitoring instruments to validate the strength and direction of the linear relationship between the two quantitative variables, utilizing the Pearson Correlation Coefficient (r) [9].

4.5.1 Image analysis acquired by ground-based camera (Pietrafitta landslide)

Due to the presence of a pole-mounted camera, initially intended solely for visual inspection purposes, along with its optimal configuration in terms of distance and perspective, we were able to generate detailed displacement maps and time series. Specifically, this setup enabled us to detect the main direction of displacement of the geomorphological process, which aligns approximately with the line of the maximum slope gradient and quantify its rate.

Figure 4.7 shows the displacement map resulting from the image analysis *A* (in Table 4.4) with a daily image capture frequency. It should be noted that the earth flow involves a considerable section of the slope with velocities that are notably higher in the inner part of the earth flow body and decreasing towards the edge and toe of the earth flow, closer to the road infrastructure. To validate displacement rates, we deployed a Robotic Total Station on the right flank of the earth flow looking at 11 reflectors placed along the slope. For this analysis, only reflector No. 3 was considered as it was located within the area covered by the visual beam (see Figure 1d for location). The comparison of data shows a high correlation in terms of direction (positive) and strength (strong), with a Pearson Coefficient of r = 0.91 (chart in Figure 4.7). Importantly, the p-value is less than 0.05, confirming the statistical significance of the correlation between these two variables. Moreover, the chart in Figure 4.7 also compares the cumulative displacement of the monitoring point, with rainfall data collected at the "Torrecuso" rain gauge. The acceleration trend dues to the rainy events of 11-22 March 2018 (84.4 mm) is well evident.
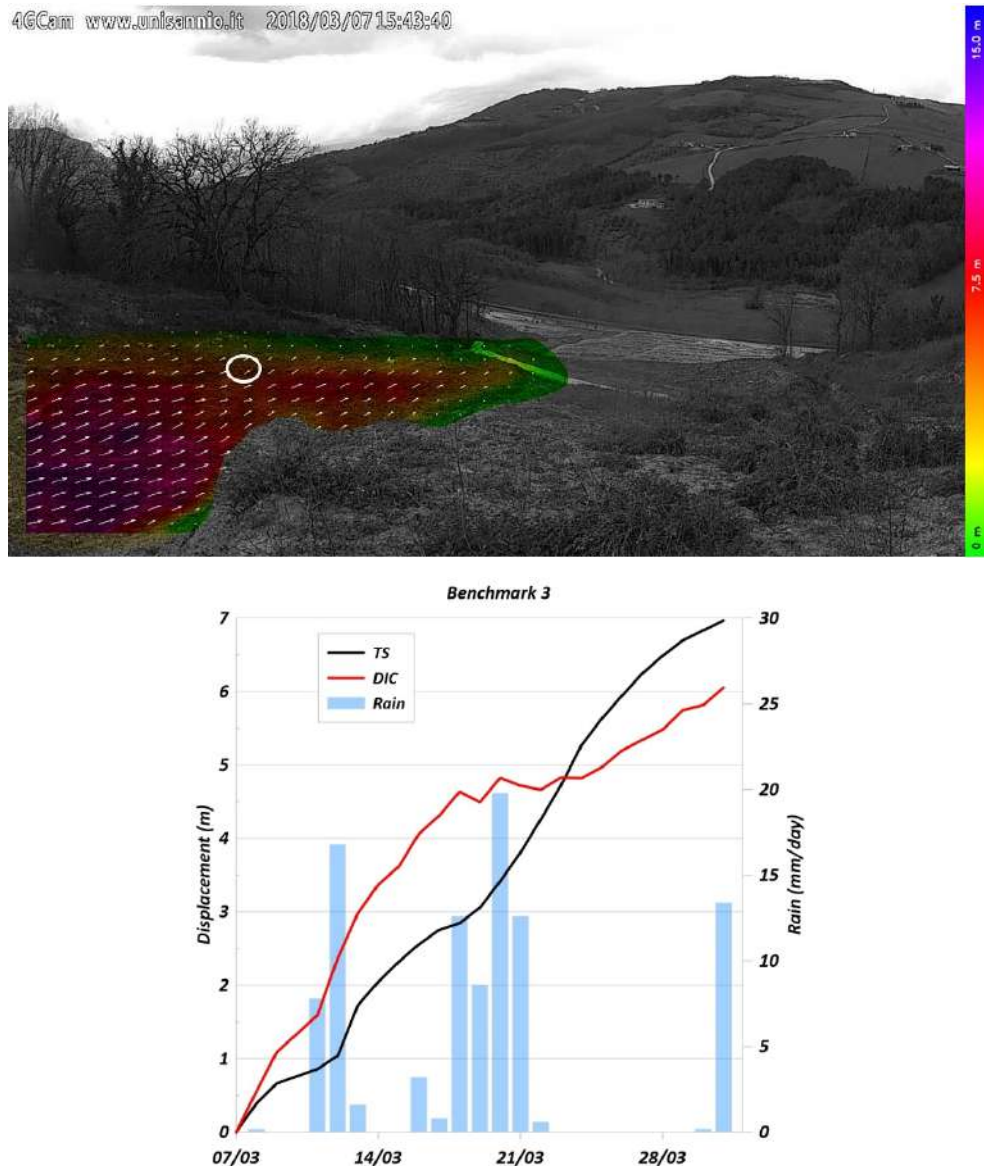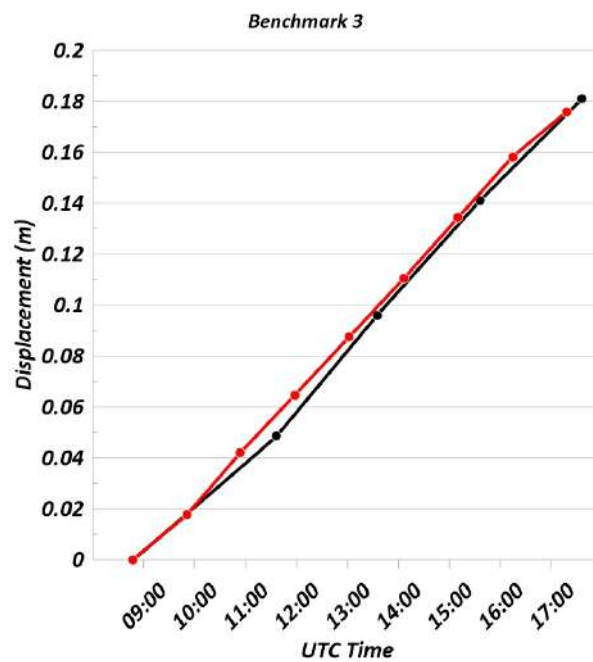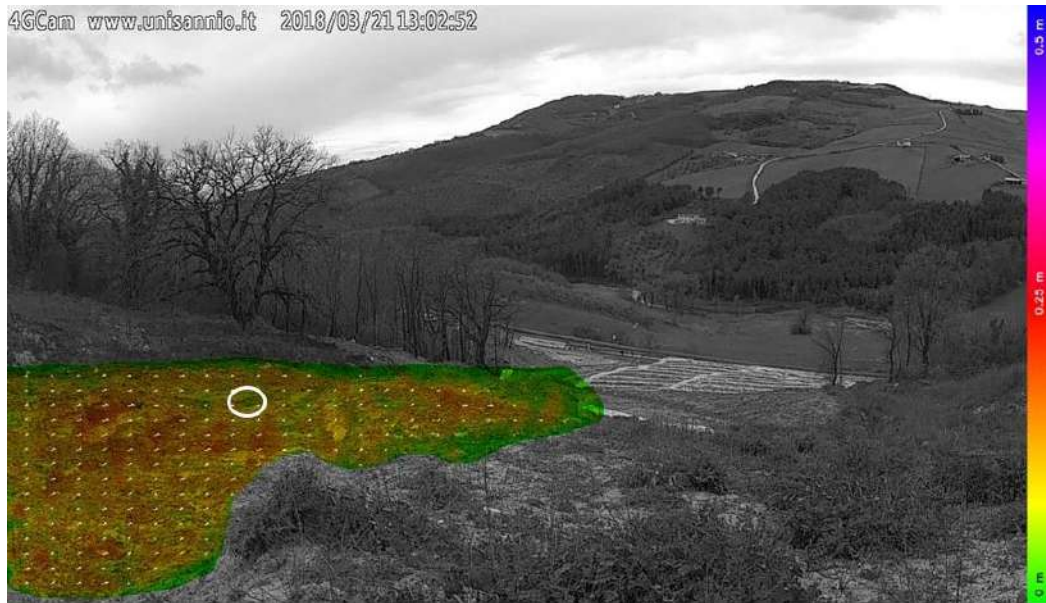
Figure 4.7. Displacement map from image analysis (labelled A in Table 4.4) with a daily image frequency. The white circle represents the area of interest around reflector 3. The chart below shows the correlation among displacement time series derived from DIC analysis, Total Station reflector No. 3 and rainfall data.

We used hourly images to investigate the velocity rates achieved during periods characterized by high earth flow activity. As shown in Figure 4.8, on March 21st, 2018, the earth flow exhibited a displacement of 18 cm in approximately 8.5 h, maintaining a constant velocity (R^2 = 0,99) of about 2 cm/h (i.e., *moderate velocity* according to [52]). Again, the displacement measurements were confirmed by comparisons with reflector (No. 3) sightings made by RTS. Additionally, Figure 4.9, displaying the displacement map obtained through a single analysis approach (utilizing two images captured between 13:00 and 14:00), demonstrates the analysis's remarkable sensitivity, capable of measuring approximately 5 cm of displacement within 1 h. This result aligns with RTS data, specifically

referencing benchmark 3, which underscores that the maximum displacement velocity on March 21, 2018, was reached between 13:00 and 14:00.

Figure 4.8. *Displacement map from multi-master analysis (labelled B in Table 4) with an hourly image frequency. The white circle represents the area of interest around reflector 3. The chart below shows the correlation between displacement time series derived from DIC analysis (in red) and Total Station reflector No. 3 (in black).*
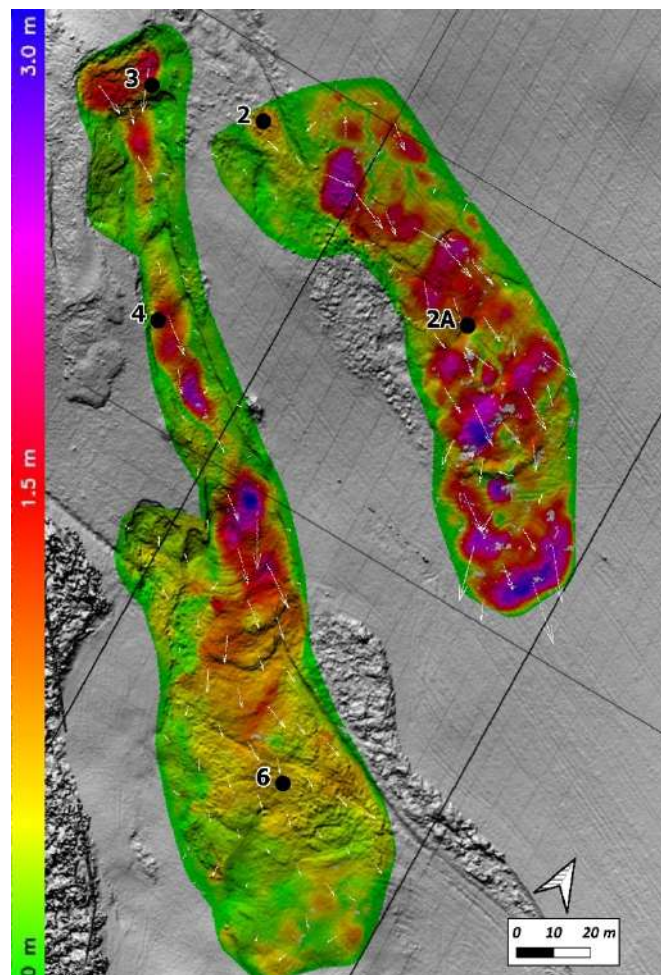
Figure 4.9. Displacement map obtained through single analysis approach (labelled C in Table 4.4). The white circle represents the area of interest around reflector 3.

4.5.2 Image analysis acquired by UAS camera (Grillo landslide)

For the Grillo earth flow, an image analysis was carried out using accurate and georeferenced imagery generated through several UAS photogrammetric surveys. In contrast to the *Pietrafitta* earth flow, the displacements observed in this case are presented from a top-down perspective (zenithal view). Also, in this case study, the DIC techniques used enabled the identification of the main displacement direction of the earth flow process and the localization of its most active areas. The results show a heterogeneous displacement pattern characterized by localized reactivations occurring along two main directions (Figure 4.10). Additionally, these movements exhibited a "step-like" kinematic, potentially indicative of impulsive responses to rainfall events. This trend was confirmed by the available rainfall data collected from April 2022 to June 2023 at the "Orsara di Puglia" rain gauge, managed by the Protezione Civile (Centro Funzionale Decentrato, C.F.D.) of the Puglia Region, located about 2 km east and at the same elevation as the *Grillo* earth flow (Figure 4.11). Although the distance is not negligible, it is considered to be acceptable given the unique availability of the instrument and the gentle terrain catchments of the area [53]. In addition, for the type of analysis performed, even small cumulate changes would be irrelevant.

Furthermore, a reliability assessment of the measurements was carried out considering GNSS data for the targets placed on the ground (Figure 4.11). Since not all targets were placed and surveyed simultaneously with the UAS surveys, the reliability analysis was restricted to three specific targets

(No. 2, No. 3, and No. 4). Although the sample size was limited (n=4), the comparison shows a robust positive correlation in terms of direction (positive) and strength (strong) with a Pearson Coefficient r = 0.99 for each of the targets. Given that the p-value is less than 0.05, we can conclude that the correlation between these two variables holds statistical significance. The GNSS analysis for target No. 2a is not present because, having been installed on 23 March, it was no longer found on 23 May, probably due to surface modifications caused by the landslide process under consideration (no data available). Regarding target No. 6, it is probable that the reference area experienced its maximum displacement before the installation of the target itself. In fact, the latest GNSS measurements validate the trend recorded through DIC, with comparable absolute displacements. Overall, the accuracy of the DIC analysis ranged from 0.2 to more than 1 m, namely from 1 pixel to more than 5 pixels.

Figure 4.10. *Displacement map obtained from UAS hillshade DIC analysis. The numbered black dots represent the position of the GNSS targets.*
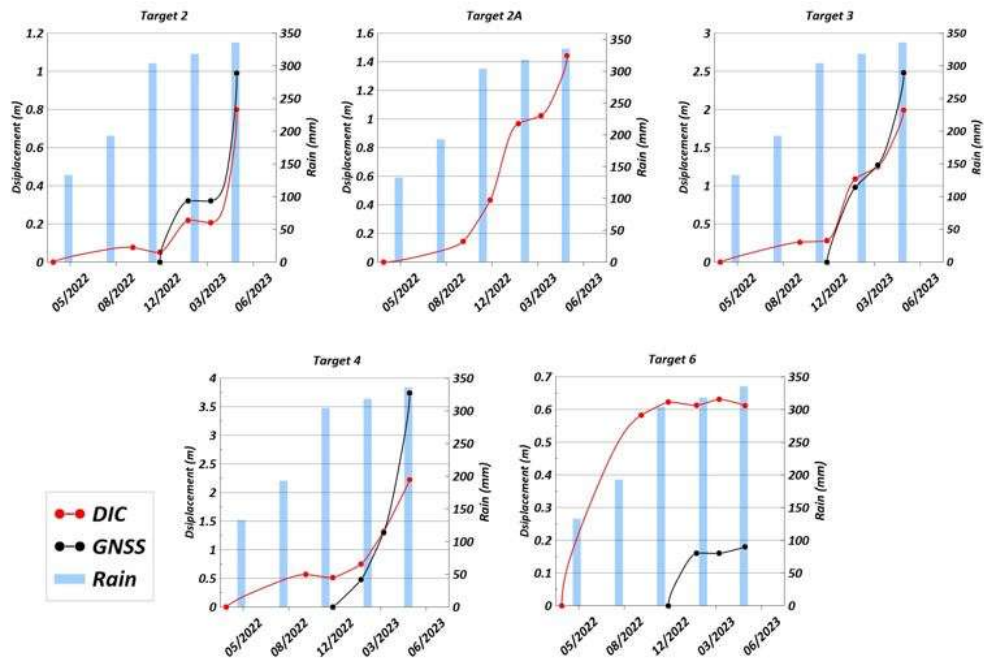
Figure 4.11. Time series from DIC and GNSS analyses using UAS imagery of Grillo earth flow. Each shaded blue vertical bar represents the rain fall in three months from April 2022 to June 2023.

4.5.3 Image analysis acquired by satellite camera (Grillo landslide)

A further analysis was conducted using optical Google® satellite imagery for the *Grillo* earth flow. As previously mentioned with regard to UAS imagery, the displacements detected are presented in an overhead perspective (zenithal view.). The employed DIC techniques provided sufficient detail to discern the main direction of movement in the geomorphological process and identify the most active areas (Figure 4.12). The results confirmed the heterogeneous displacement pattern observed earlier using UAS imagery, with localized unstable areas along two primary directions. The displacement observed at the source area (Area of Interest) can be attributed to a retrogressive kinematic process (Figure 4.12). This can be currently witnessed by the presence of grabens, scarps, and back-tilted surfaces mainly linked to normal fault-like structures in the source area. These extensive kinematic elements cause an upstream widening of the earth flow resulting in a movement inverse to the "natural direction" (i.e., downstream) in the DIC analysis.
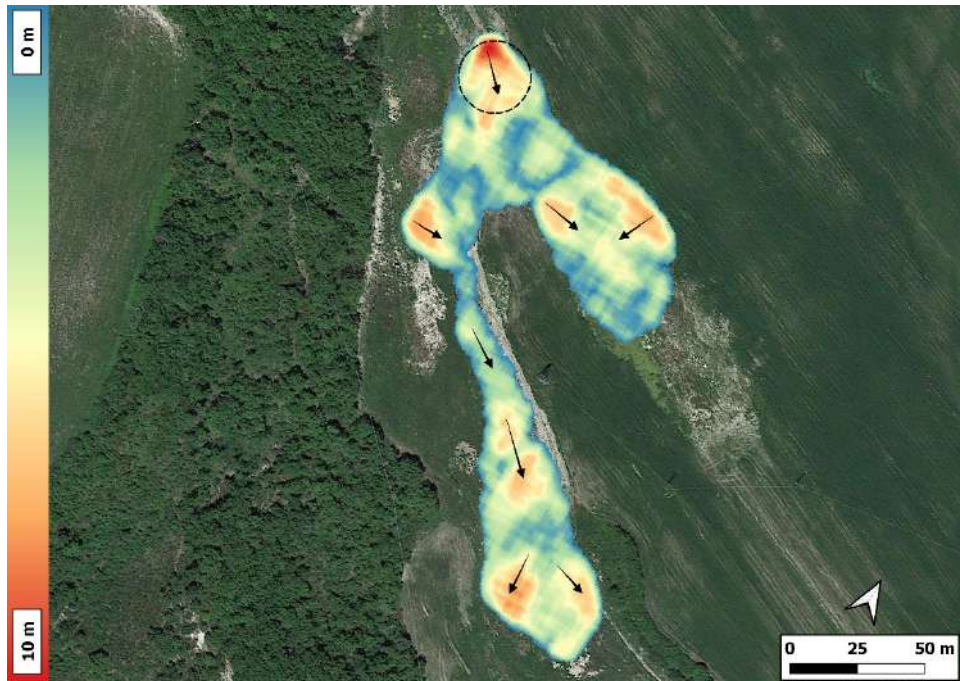
Figure 4.12. *Displacement map from an image analysis using satellite imagery of the Grillo earth flow. The black circle represents the area of interest. The arrows represent the main displacement directions.*

4.6 Discussion

The results presented above appear promising for all configurations adopted (e.g., the various platforms), but their potential and limitations still warrant further investigation. Nevertheless, the utilization of DIC techniques is steadily gaining popularity as the method for data acquisition and processing. The necessary setup is often cost-effective and straightforward to install, enabling the acquisition of substantial amounts of data across diverse environments with minimal efforts. With regard to the Pietrafitta earth flow, due to the optimal configuration in terms of distance and perspective of the pole-mounted camera, we were able to generate detailed displacement maps and time series. This allowed us to discern the main displacement direction of the geomorphological process—approximately aligned with the maximum slope gradient—and to quantify its rate. Furthermore, when comparing the displacement rates with the data obtained from reflectors sighted by an independent RTS, we observed a close correlation in terms of both direction (positive) and strength (strong). However, it is important to note that this comparison was made on the horizontal component measured by the RTS, which is the component most perpendicular to the image plane. This choice was made to ensure maximum comparability. This aspect is of particular significance in imaging since post-processing still requires complex steps, including georeferencing, georectification, and feature tracking. These steps are necessary to transform oblique images into meaningful data for quantitative analysis (e.g., velocity rates). In this regard, several attempts have been made, and today, there are some free and open-source applications available to overcome these obstacles [54,55]. Furthermore, looking ahead to future monitoring campaigns, particular attention must be paid to achieving the optimal geometric configuration for measuring the intended movement while also keeping factors such as the angle of incidence and position of the camera in relation to the monitoring target under control. However, this is not always possible and there are cases where the distance between the object and the sensor, as well as its GSD, may increase or may not be in the optimal configuration. In these cases, it may be advantageous to use higher-resolution cameras, such as gigapixel or depth cameras [56].

In reference to the Grillo earth flow, which was analyzed using images acquired by a UAS, a critical aspect lies in the precise determination of the image capture point due to the utilization of an aerial platform. This specific configuration granted us a comprehensive, bird's-eye view of the entire earth flow kinematics. In the author's perspective, when dealing with landslides of this type, specifically earth flows, this vantage point represents the optimal approach for generating a

comprehensive map of the unstable sectors and their respective displacements. Regarding the timing of these acquisitions, there are two factors to consider: (a)the extreme versatility of the acquisition technique (survey through a drone) permits us to adjust—increasing or decreasing—the frequency of data collection in accordance with the evolving state of the geomorphological process; (b)the necessity for a well-trained team and physical accessibility to the investigation site can influence the planning and execution of these acquisitions. The incorporation of ground-based targets for georeferencing significantly facilitated data processing and analysis while enhancing their overall reliability. However, even in the absence of georeferenced data, UAS surveys, when coupled with DIC processing, still enable us to initiate the mapping and monitoring of earth flows, even when other sources of information and control monitoring are unavailable. The analysis of satellite imagery of the Grillo earth flow provided us with a general understanding of the evolution of the geomorphological process over the past decade, thereby facilitating knowledge monitoring. Although the absence of ancillary data from conventional monitoring techniques did not allow a quantitative assessment of the displacement values, our analysis confirmed the potentiality to derive surface displacement data from Google® Earth images [57], especially for a knowledge monitoring of an earth flow. This application could be utilized to obtain very high geometric resolution (i.e., GSD) satellite imagery easily [58]; however, when conducting DIC analyses for processes characterized by high seasonality, especially those occurring within relatively vegetated areas, it is advisable to avoid using optical images, be they satellite based or otherwise. This is because changes in vegetation can introduce a multitude of processing errors. In such cases, it is recommended to employ hillshade products instead.

Moreover, the results and interpretation of monitoring activities carried out at the two study sites allowed us to observe the typical earth flow activity: slow localized movements (e.g., Grillo earth flow) and surging events (e.g., Pietrafitta earth flow) [52].

The key role of the hydrologic forcing on earth flow movement velocity was demonstrated at the Pietrafitta study site: the intensive rainfall period of January–March 2018 and the snow melting that occurred at the end of February 2018, increasing the pore-water pressure causing a fluidization of the earth flow material and resulting in a surge event. In this phase, the highest localized movement velocity reached was about 0.63 m/day. This value is consistent with other earth flow surge speeds in the literature [38,59]. Meanwhile, the distribution of the displacement and average velocity observed along the longitudinal axis of the right branch of the Grillo earth flow proved the importance of the basal slip-surface geometry [60] on earth flow activity, expressed as the relationship between

morphological structures and velocity distributions. Indeed, as observed in Figure 4.10, the highest
displacement rates were measured where the flow movement was bounded by normal and strike–
slip faults, whereas the lowest velocities were measured where thrust faults were present (Figure
4.1e). As reported in [60], extensional and compression structures could be associated with risers and
treads, respectively, in the basal slip surface.

To contextualize the contribution of our study and, therefore, of DIC techniques within
geotechnical monitoring, with a specific focus on monitoring earth flows facing linear infrastructures,
Figure 4.13 shows the application domains of the monitoring techniques used in this study and
presented using the classification proposed in [34]. Considering the three main monitoring categories
proposed, namely knowledge, control, and emergency monitoring, and drawing insights from our
practical field experiences (indicated by colored dots in Figure 4.13), the utilization of the DIC has
been generalized (represented by colored areas in Figure 4.13) based on the specific platform used
and its general purpose.
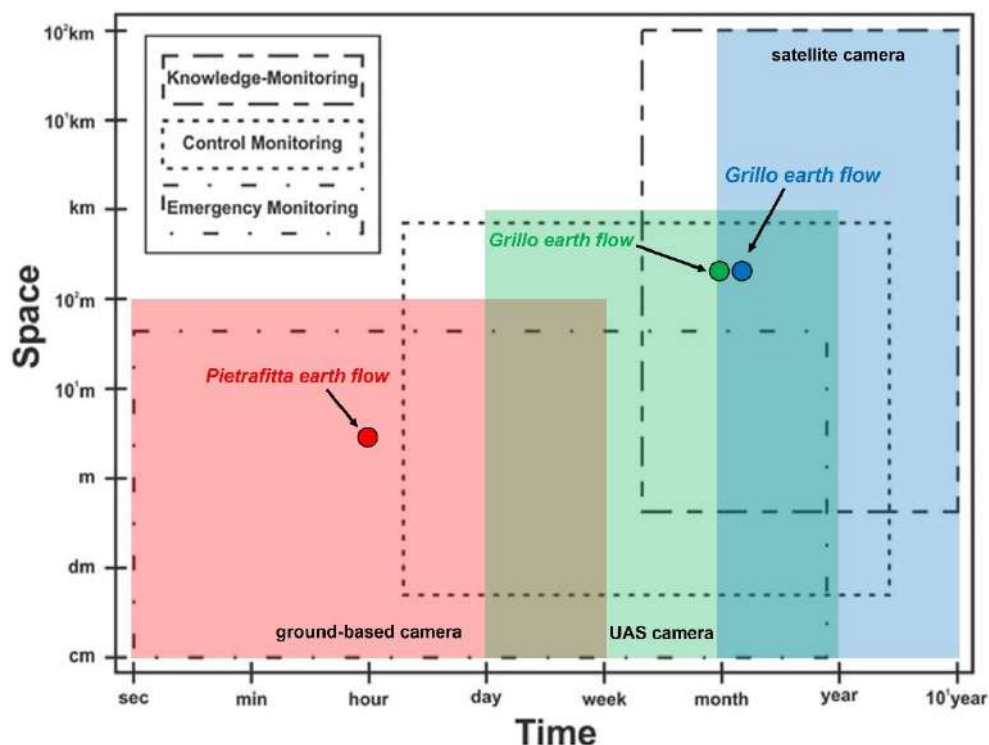
Figure 4.13. *Usage domains of the presented monitoring techniques on a space–time chart based on the used platforms (red: ground-based camera; green: UAS camera; blue: satellite camera). The boxes indicate the different types of geotechnical monitoring: knowledge, control, and emergency monitoring (modified from [34]).*

For example, ground-based cameras, such as the one used in the *Pietrafitta* earth flow,
demonstrated great potential in emergency and, partially, control monitoring. Cameras mounted on
drones (UASs), as in the case of the *Grillo* earth flow, give a great advantage, especially for control

monitoring. Satellite images, such as those employed for the *Grillo* earth flow, seem to be crucial for knowledge monitoring.

4.6 Conclusions

The present study has examined the use of digital image correlation (DIC) for the displacement monitoring of earth flows by presenting the outcomes from the evaluation and comparison of distinctive techniques for three different study sites in the Pietrafitta and Grillo earth flows. Based on the results presented in this study and considering the main potentialities of the DIC techniques that have emerged from this research, the following general considerations can be made:

- The spatially continuous coverage, given by the DIC technique, affords the opportunity to perform monitoring with clear, practical advantages. Indeed, this approach enables us to (i) comprehensively cover large areas, thereby avoiding the risk of underestimating geomorphological processes; (ii) increase the statistical robustness of the acquired data; and (iii) identify the most active sectors and their rates of movement. These aspects are particularly relevant when monitoring complex kinematic phenomena like earth flows.

- The versatility of DIC, in terms of the facility of the installation of sensors, cost-effectiveness, and compatibility with various platforms, makes this technique a competitive, adaptable, and ready-to-use solution. This versatility holds significant importance in the field of geotechnical asset management (GAM).

- The proven reliability in terms of both accuracy (e.g., high correlation with RTS; r = 0.91) and sensitivity (ability to measure approximately 5 cm of displacement within 1 h) lays the foundation for extensive use of the DIC techniques presented so far. Furthermore, through future developments, e.g., involving the automation of analyses, the DIC could easily be implemented as a technique underlying early warning systems (EWS).

In the view and opinion of the authors, the most appropriate way to quantitatively monitor earth flows in the case of control monitoring is to use the DIC from UAS data and through hillshades for several reasons: (i) they are not subject to variations in vegetation; (ii) due to the high resolution, it is possible to also identify localized displacements without running the risk of ambiguity; and (iii) low cost of realization. For continuous and emergency monitoring, the most effective way to

quantitatively monitor the earth flow is to use low-cost ground-based cameras that maintain a good cost–benefit ratio.

Although it has been shown that the techniques used, with their different configurations and acquisition platforms, can be immediately exploited for the above-mentioned purposes, their actual benefit will only materialize once some of the main limitations, which also emerged in our work, have been addressed. For example, with regard to ground-based cameras, great care should be paid to achieving the optimal geometric configuration for measuring the intended movement while also maintaining the angle of incidence and position of the camera in relation to the targets.

Finally, from our perspective, the revised rating presented in Figure 13 and a focus on imaging (DIC) could be very useful for the risk management of earth flows in the presence of linear infrastructures.

References

1. Revellino, P.; Grelle, G.; Donnarumma, A.; Guadagno, F.M. Structurally Controlled Earth Flows of the Benevento Province (Southern Italy). Bull. Eng. Geol. Environ. 2010, 69, 487–500.

2. Bertello, L.; Berti, M.; Castellaro, S.; Squarzoni, G. Dynamics of an Active Earthflow Inferred from SurfaceWave Monitoring. J. Geophys. Res. Earth Surf. 2018, 123, 1811–1834.

3. Malet, J.-P.; Laigle, D.; Remaître, A.; Maquaire, O. Triggering Conditions and Mobility of Debris Flows Associated to Complex Earthflows. Geomorphology 2005, 66, 215–235.

4. Baum, R.L.; Savage, W.Z.; Wasowski, J. Mechanics of Earth Flows. In Proceedings of the International Workshop on Occurrence and Mechanisms of Flows in Natural Slopes and Earthfills, Sorrento, Italy, 14–16 May 2003; 2003; p. 8.

5. Di Crescenzo, G.; Santo, A. Debris Slides–Rapid Earth Flows in the Carbonate Massifs of the Campania Region (Southern Italy): Morphological and Morphometric Data for Evaluating Triggering Susceptibility. Geomorphology 2005, 66, 255–276.

6. Bovis, M.J.; Jones, P. Holocene History of Earthflow Mass Movements in South-Central British Columbia: The Influence of Hydroclimatic Changes. Can. J. Earth Sci. 1992, 29, 1746–1755.

7. Mulas, M.; Ciccarese, G.; Truffelli, G.; Corsini, A. Integration of Digital Image Correlation of Sentinel-2 Data and Continuous GNSS for Long-Term Slope Movements Monitoring in Moderately Rapid Landslides. Remote Sens. 2020, 12, 2605.

8. Quinn, P.E.; Hutchinson, D.J.; Diederichs, M.S.; Rowe, R.K. Regional-Scale Landslide Susceptibility Mapping Using the Weights of Evidence Method: An Example Applied to Linear Infrastructure. Can. Geotech. J. 2010, 47, 905–927.

9. Picarelli, L.; Russo, C. Remarks on the Mechanics of Slow Active Landslides and the Interaction with Man-Made Works. In Landslides: Evaluation and Stabilization; A. A. Balkema: Leiden, The Netherlands, 2004; pp. 1141–1176.

10. Di Maio, C.; Vassallo, R.; Scaringi, G.; Scaringi, G.; Pontolillo, D.M.; Grimaldi, G.M. Monitoring and analysis of an earthflow in tectonized clay shales and study of a remedial intervention by KCl wells. Riv. Ital. Geotec. 2017, 51, 48–63.

11. Hungr, O.; Fell, R.; Couture, R.; Eberhardt, E. Landslide Risk Management; CRC Press: Boca Raton, FL, USA, 2005; ISBN 978-1-4398-3371-1.

12. Scaioni, M. (Ed.) Modern Technologies for Landslide Monitoring and Prediction; Springer: Berlin/Heidelberg, Germany, 2015; ISBN 978-3-662-45930-0.

13. Giordan, D.; Allasia, P.; Manconi, A.; Baldo, M.; Santangelo, M.; Cardinali, M.; Corazza, A.; Albanese, V.; Lollino, G.; Guzzetti, F. Morphological and Kinematic Evolution of a Large Earthflow: The Montaguto Landslide, Southern Italy. Geomorphology 2013,187, 61–79.

14. Bardi, F.; Raspini, F.; Frodella, W.; Lombardi, L.; Nocentini, M.; Gigli, G.; Morelli, S.; Corsini, A.; Casagli, N. Monitoring the Rapid-Moving Reactivation of Earth Flows by Means of GB-InSAR: The April 2013 Capriglio Landslide (Northern Appennines,Italy). Remote Sens. 2017, 9, 165.

15. Mazza, D.; Cosentino, A.; Romeo, S.; Mazzanti, P.; Guadagno, F.M.; Revellino, P. Remote Sensing Monitoring of the Pietrafitta Earth Flows in Southern Italy: An Integrated Approach Based on Multi-Sensor Data. Remote Sens. 2023, 15, 1138.

16. Malet, J.-P.; Maquaire, O.; Calais, E. The Use of Global Positioning System Techniques for the Continuous Monitoring of Landslides: Application to the Super-Sauze Earthflow (Alpes-de-Haute-Provence, France). Geomorphology 2002, 43, 33–54.

17. Castagnetti, C.; Bertacchini, E.; Corsini, A.; Capra, A. Multi-Sensors Integrated System for Landslide Monitoring: Critical Issues in System Setup and Data Management. Eur. J. Remote Sens. 2013, 46, 104–124.

18. Hermle, D.; Gaeta, M.; Krautblatter, M.; Mazzanti, P.; Keuschnig, M. Performance Testing of Optical Flow Time Series AnalysesBased on a Fast, High-Alpine Landslide. Remote Sens. 2022, 14, 455.

19. Bickel, V.T.; Manconi, A.; Amann, F. Quantitative Assessment of Digital Image Correlation Methods to Detect and Monitor Surface Displacements of Large Slope Instabilities. Remote Sens. 2018, 10, 865.

20. Mazzanti, P.; Caporossi, P.; Muzi, R. Sliding Time Master Digital Image Correlation Analyses of CubeSat Images for Landslide Monitoring: The Rattlesnake Hills Landslide (USA). Remote Sens. 2020, 12, 592.

21. Hermle, D.; Keuschnig, M.; Krautblatter, M. Potential of Multisensor Assessment Using Digital Image Correlation for Landslide Detection and Monitoring; Copernicus Meetings. 2020.

22. Lacroix, P.; Araujo, G.; Hollingsworth, J.; Taipe, E. Self-Entrainment Motion of a Slow-Moving Landslide Inferred from Landsat-8 Time Series. J. Geophys. Res. Earth Surf. 2019, 124, 1201–1216.

23. Daehne, A.; Corsini, A. Kinematics of Active Earthflows Revealed by Digital Image Correlation and DEM Subtraction Techniques Applied to Multi-Temporal LiDAR Data: Kinematics of Active Earthflows. Earth Surf. Processes Landf. 2013, 38, 640–654.

24. Travelletti, J.; Oppikofer, T.; Delacourt, C. Monitoring Landslide Displacements during a Controlled Rain Experiment Using a Long-Range Terrestrial Laser Scanning (TLS); Chen, J., Jiang, J., Eds.; Hans-Gerd MAAS: Beijing, China, 2008; Volume XXXVII, p. 6.

25. Tondo, M.; Mulas, M.; Ciccarese, G.; Marcato, G.; Bossi, G.; Tonidandel, D.; Mair, V.; Corsini, A. Detecting Recent Dynamics in Large-Scale Landslides via the Digital Image Correlation of Airborne Optic and LiDAR Datasets: Test Sites in South Tyrol (Italy). Remote Sens. 2023, 15, 2971.

26. Travelletti, J.; Delacourt, C.; Allemand, P.; Malet, J.-P.; Schmittbuhl, J.; Toussaint, R.; Bastard, M. Correlation of Multi-Temporal Ground-Based Optical Images for Landslide Monitoring: Application, Potential and Limitations. ISPRS J. Photogramm. Remote Sens. 2012, 70, 39–55.

27. Travelletti, J.; Malet, J.-P.; Delacourt, C. Image-Based Correlation of Laser Scanning Point Cloud Time Series for Landslide Monitoring. Int. J. Appl. Earth Obs. Geoinf. 2014, 32, 1–18.

28. Stumpf, A.; Malet, J.-P.; Delacourt, C. Correlation of Satellite Image Time-Series for the Detection and Monitoring of Slow-Moving Landslides. Remote Sens. Environ. 2017, 189, 40–55.

29. Motta, M.; Gabrieli, F.; Corsini, A.; Manzi, V.; Ronchetti, F.; Cola, S. Landslide Displacement Monitoring from Multi-Temporal Terrestrial Digital Images: Case of the Valoria Landslide Site. In Landslide Science and Practice: Volume 2: Early Warning, Instrumentation and Monitoring; Margottini, C., Canuti, P., Sassa, K., Eds.; Springer: Berlin/Heidelberg, Germany, 2013; pp. 73–78. ISBN 978-3-642-31445-2.

30. Travelletti, J.; Delacourt, C.; Malet, J.-P.; Allemand, P.; Schmittbuhl, J.; Toussaint, R. Performance of Image Correlation Techniques for Landslide Displacement Monitoring. In Landslide Science and Practice: Volume 2: Early Warning, Instrumentation and Monitoring; Margottini, C., Canuti, P., Sassa, K., Eds.; Springer: Berlin/Heidelberg, Germany, 2013; pp. 217–226. ISBN 978-3-642-31445-2.

31. Dematteis, N.; Giordan, D. Comparison of Digital Image Correlation Methods and the Impact of Noise in Geoscience Applications.Remote Sens. 2021, 13, 327.

32. Corominas, J.; Van Westen, C.; Frattini, P.; Cascini, L.; Malet, J.-P.; Fotopoulou, S.; Catani, F.; Van Den Eeckhaut, M.; Mavrouli, O.; Agliardi, F.; et al. Recommendations for the Quantitative Analysis of Landslide Risk. Bull. Eng. Geol. Environ. 2013, 73, 209–263.

33. Chowdhury, R.; Flentje, P. Role of Slope Reliability Analysis in Landslide Risk Management. Bull. Eng. Geol. Environ. 2003, 62, 41–46.

34. Mazzanti, P. Toward Transportation Asset Management: What Is the Role of Geotechnical Monitoring? J. Civ. Struct. Health Monit. 2017, 7, 645–656.

35. Whiteley, J.S.;Watlet, A.; Kendall, J.M.; Chambers, J.E. Brief Communication: The Role of Geophysical Imaging in Local LandslideEarly Warning Systems. Nat. Hazards Earth Syst. Sci. 2021, 21, 3863–3871.

36. Hungr, O.; Leroueil, S.; Picarelli, L. The Varnes Classification of Landslide Types, an Update. Landslides 2014, 11, 167–194.

37. Pinto, F.; Guerriero, L.; Revellino, P.; Grelle, G.; Senatore, M.R.; Guadagno, F.M. Structural and Lithostratigraphic Controls of Earth-Flow Evolution, Montaguto Earth Flow, Southern Italy. J. Geol. Soc. 2016, 173, 649–665.

38. Guerriero, L.; Revellino, P.; Grelle, G.; Fiorillo, F.; Guadagno, F. Landslides and Infrastructures: The Case of the Montaguto Earth Flow in Southern Italy. Ital. J. Eng. Geol. Environ. 2013, 2013, 459–466.

39. Ferrigno, F.; Gigli, G.; Fanti, R.; Intrieri, E.; Casagli, N. GB-InSAR Monitoring and Observational Method for Landslide Emergency Management: The Montaguto Earthflow (AV, Italy). Nat. Hazards Earth Syst. Sci. 2017, 17, 845–860.

40. Casagli, N.; Intrieri, E.; Tofani, V.; Gigli, G.; Raspini, F. Landslide Detection, Monitoring and Prediction with Remote-Sensing Techniques. Nat. Rev. Earth Environ. 2023, 4, 51–64.

41. Pearson's Correlation Coefficient. In Encyclopedia of Public Health; Kirch,W. (Ed.) Springer: Dordrecht, The Netherlands, 2008; pp. 1090–1091, ISBN 978-1-4020-5613-0.

42. Caporossi, P.; Mazzanti, P.; Bozzano, F. Digital Image Correlation (DIC) Analysis of the 3 December 2013 Montescaglioso Landslide (Basilicata, Southern Italy): Results from a Multi-Dataset Investigation. ISPRS Int. J. Geo-Inf. 2018, 7, 372.

43. Pan, B.; Xie, H.;Wang, Z.; Qian, K.;Wang, Z. Study on Subset Size Selection in Digital Image Correlation for Speckle Patterns. Opt. Express 2008, 16, 7037.

44. Tong, X.; Ye, Z.; Xu, Y.; Gao, S.; Xie, H.; Du, Q.; Liu, S.; Xu, X.; Liu, S.; Luan, K.; et al. Image Registration with Fourier-Based Image Correlation: A Comprehensive Review of Developments and Applications. IEEE J. Sel. Top. Appl. Earth Obs. Remote Sens. 2019, 12, 4062–4081.

45. Carrivick, J.; Smith, M.; Quincey, D. Structure from Motion in the Geosciences;Wiley, Blackwell: Chichester, UK; Ames, IA, USA, 2016; ISBN 978-1-118-89584-9.

46. Mugnai, F.; Masiero, A.; Angelini, R.; Cortesi, I. High-Resolution Monitoring of Landslides with UAS Photogrammetry and Digital Image Correlation. Eur. J. Remote Sens. 2023, 56, 2216361. [CrossRef]

47. Angeli, M.-G.; Pasuto, A.; Silvano, S. A Critical Review of Landslide Monitoring Experiences. Eng. Geol. 2000, 55, 133–147.

48. Mucchi, L.; Jayousi, S.; Martinelli, A.; Caputo, S.; Intrieri, E.; Gigli, G.; Gracchi, T.; Mugnai, F.; Favalli, M.; Fornaciai, A.; et al. A Flexible Wireless Sensor Network Based on Ultra-Wide Band Technology for Ground Instability Monitoring. Sensors 2018,18, 2948.

49. Lindner, G.; Schraml, K.; Mansberger, R.; Hübl, J. UAV Monitoring and Documentation of a Large Landslide. Appl. Geomat. 2016, 8, 1–11.

50. Sestras, P.; Bilasco, S.; Rosca, S.; Dudic, B.; Hysa, A.; Spalevi´c, V. Geodetic and UAV Monitoring in the Sustainable Management of Shallow Landslides and Erosion of a Susceptible Urban Environment. Remote Sens. 2021, 13, 385.

51. Lewis, J.P. Fast Template Matching. In Proceedings of the Vision Interface 95, Canadian Image Processing and Pattern Recognition Society, Quebec City, QC, Canada, 15–19 May 1995; pp. 120–123.

52. Cruden, D.M.; Varnes, D.J. Landslide Types and Processes; Special Report National Research Council Transportation Research; Board Transportation Research Board, National Academy of Sciences: Washington, DC, USA, 1996; Volume 247, pp. 36–75.

53. Gariano, S.L.; Sarkar, R.; Dikshit, A.; Dorji, K.; Brunetti, M.T.; Peruccacci, S.; Melillo, M. Automatic Calculation of Rainfall Thresholds for Landslide Occurrence in Chukha Dzongkhag, Bhutan. Bull. Eng. Geol. Environ. 2019, 78, 4325–4332.

54. Messerli, A.; Grinsted, A. Image Georectification and Feature Tracking Toolbox: ImGRAFT. Geosci. Instrum. Methods Data Syst. 2015, 4, 23–34.

55. How, P.; Hulton, N.R.J.; Buie, L.; Benn, D.I. PyTrx: A Python-Based Monoscopic Terrestrial Photogrammetry Toolset for Glaciology. Front. Earth Sci. 2020, 8, 21.

56. Romeo, S.; Cosentino, A.; Giani, F.; Mastrantoni, G.; Mazzanti, P. Combining Ground Based Remote Sensing Tools for Rockfalls Assessment and Monitoring: The Poggio Baldi Landslide Natural Laboratory. Sensors 2021, 21, 2632.

57. Guerriero, L.; Di Martire, D.; Calcaterra, D.; Francioni, M. Digital Image Correlation of Google Earth Images for Earth's Surface Displacement Estimation. Remote Sens. 2020, 12, 3518.

58. Stumpf, A.; Malet, J.-P.; Allemand, P.; Ulrich, P. Surface Reconstruction and Landslide Displacement Measurements with PléiadesSatellite Images. ISPRS J. Photogramm. Remote Sens. 2014, 95, 1–12.

59. Keefer, D.K.; Johnson, A.M. Earth Flows: Morphology, Mobilization, and Movement; Professional Paper; U.S. Geological Survey:Washington, DC, USA, 1983; Volume 1264.

60. Guerriero, L.; Coe, J.A.; Revellino, P.; Grelle, G.; Pinto, F.; Guadagno, F.M. Influence of Slip-Surface Geometry on Earth-Flow Deformation, Montaguto Earth Flow, Southern Italy. Geomorphology 2014, 219, 285–305.

Chapter 5

Optical and Thermal Image Processing for monitoring rainfall triggered shallow landslides: insights from analogue laboratory experiments

Authors: Antonio Cosentino [1,4], Gian Marco Marmoni [1*], Matteo Fiorucci [2], Paolo Mazzanti [1,3,4], Gabriele Scarascia Mugnozza [1], Esposito Carlo [1,4]

[1] *Department of Earth Sciences - Sapienza University of Rome and CERI Research Centre for Geological Risks. P.le Aldo Moro 5, 00185, Rome, Italy*

[2] *Department of Civil and Mechanical Engineering, University of Cassino and Southern Lazio, Via G. Di Bi-asio 43, 03043 Cassino (FR), Italy.*

[3] *Nhazca S.r.l., - Start UP "Sapienza" University of Rome, via V. Bachelet n.12, 00185 Rome, Italy*

[4] *ntelligEarth S.r.l., - Start UP "Sapienza" University of Rome, via V. Bachelet n.12, 00185 Rome, Italy*

* *Correspondence: gianmarco.marmoni@uniroma1.it;*

Keywords: Image Processing; Infrared Thermography; Change Detection; Digital Image Correlation; shallow landslides; Remote Sensing; PhotoMonitoring

5.1 Abstract

This study explores the innovative use of Digital Image Processing (DIP) techniques, also named PhotoMonitoring, to the monitoring the triggering condition of shallow landslide. The approach, based on the combination of Optical and Infrared Thermographic imaging (IRT), is applied to a laboratory-scaled slope, reconstructed in a flume test apparatus. Three experiments were conducted to replicate rainfall-induced shallow landslide, applying Change Detection and Digital Image Correlation analysis to both optical and thermal images. The method combines IRT's ability to measure ground surface temperature changes with DIP's capacity to track movement and displacement. Results showed the high reliability of the displacement time-series obtained through IRT-DIP with respect to the reference Optical-DIP. IRT-DIP technique also detect anomaly signals two minutes before the landslide occurrence that can be regarded as a possible failure precursor. The

study testifies to the potential of PhotoMonitoring as a remote sensing technique, demonstrating the ability of DIP to capture the dynamics of shallow landslides, as well as the advantages of Optical-IRT combinations to follow slope deformation processes during night-time. This approach, if scaled to real scenarios, could contribute to a better understanding of the behaviour of landslides, improving strategies for landslide monitoring and thus promoting more effective Early Warning Systems (EWS).

5.2 Introduction

The ability to detect early evidence of incipient slope instabilities from contact and remote monitoring is one of the main challenges for engineering geologist and geotechnical engineers. Landslide monitoring is the most cost-effective way to minimise the direct [1] and indirect [2] consequences of landslides [3,4]. Their mitigation passes through the understanding of their predisposing, preparatory and triggering factors [5] and the ability to monitor their evolution in advance with respect to their characteristic deformative behaviour.

Given the large number of landslides, the full monitorability of landslide result as an optimistic mirage, as well as only some of the broad spectrum of failure mechanisms can be adequately monitored for early warning purposes [4]. In this sense, the use of alternative and cost-effective solutions for landslides monitoring is crucial, especially for areal distributed scenarios of ground failures, like the one posed by prolonged intense rainfall events or impulsive episodes. This type of landslide are mainly shallow and featured by reduced volumes, however are often causes of extensive damage to infrastructure and human casualties in many mountainous regions of the world [6].

In situ monitoring techniques are generally not suitable for wide area monitoring, while Remote-sensing techniques (RSTs) offer a systematic and synoptic view of the ground surface at various scales [7].

In this sense, RST fit the requirements for a proper monitoring for some typical hazard scenarios, especially in terms of kinematic features and extent of the areas of interest, where several and concomitant shallow landslides clustered within small catchment (e.g., rainfall-induced landslide scenarios). The latter can be nowadays detected and monitored thanks to the rapid growth and development of technologies and computational resources and algorithms [3,8]. Despite this, cost-effective, distributed ground-based monitoring solutions, integrative with aerial or satellite ones, must be taken into account to maximize the monitoring potential and the ability to collect reliable

information on slope processes. For this reason, the use of less expensive tools for a long-term monitoring activity is a strategy that the scientific community is pursuing in order to increase the likelihood of effectively monitoring any potential activation.

In recent years, Digital Image Processing (DIP), also called PhtoMonitoring, has gained traction in various engineering geology applications, evidenced by a growing in literature [9–12]. DIP is characterised by its adaptability, particularly in contrast to resource-intensive in-situ methods. Advancements in camera technology and customized algorithms have made DIP techniques like Digital Image Correlation (DIC) and Change Detection (CD) increasingly appealing [13,14]. DIP offers the chance to extract data from images captured at different times and from different types of platform, allowing quantitative assessments of changes and movements within a scene [11]. These techniques produce displacement field maps (DIC) and change field maps (CD) with an accuracy that is linked to the image resolutions (spatial, temporal and radiometric).

Another RST that has experienced a large number of applications in various fields of engineering geology in recent years is InfraRed Thermography (IRT) imagery. The adaptability and skills of this method allow the use which has been tried and tested in recent years, for volcanic surveillance [15,16], geothermal [17–19], archaeological [20], and civil engineering [21,22]. Growing are the applications for engineering geological purposes, spanning from in-situ laboratory tests [23,24], sinkhole detection [25], or large-scale monitoring of rock slope instabilities (e.g., [24,26–33]) but the application of IRT for quantitative monitoring of rain-triggered shallow landslide is rarely in the literature [32].

The primary aim of this research is to evaluate the utility of Digital Image Processing (DIP) techniques, specifically when applied to infrared thermography (IRT-DIP) data, in the context of rain-triggered shallow landslides. While the use of IRT-DIP has been emerging in laboratory settings, primarily for assessing jointed rock behaviour under concentrated load [34], its application to shallow landslides triggered by rainfall and the detection of early subsidence or precursor signals is an area that remains relatively unexplored in the existing literature.

To investigate this novel approach, three laboratory-scale experiments were conducted using a flume test apparatus, replicating an analogue model of a rain-induced earth slope failure. Given the intricate nature of this subject and the multitude of variables involved, we sought to replicate and monitor rain-triggered shallow landslides using a combination of contact and remote sensing techniques within a controlled laboratory environment. This experimental configuration allowed us to recreate the landslide process under controlled conditions, including specific physical parameters,

slope geometry, dimensions, and trigger intensity [35,36]. The application, and this experimental setup, allows combining the capability of IRT imaging, which can be used to measure the relative difference in land surface temperature (LST) [37], with the ability to obtain displacement and velocity information, together with changes maps offered by DIP techniques.

The specific objectives are as follows:

- To assess the reliability, potential, and capabilities of Optical and IRT-DIP techniques as an innovative method for monitoring shallow landslides triggered by rainfall, using RGB optical images extracted from digital videos and InfraRed thermal images.

- To study the deformative behaviour of shallow landslides, reproducing it in the laboratory using flume test analogic apparatus,

- To deepen the understanding of the behaviour of earth slopes involved in shallow landslide processes, identifying potential precursors of slope failures.

5.3 Materials and Methods

To test the suitability of DIP techniques for detecting incipient failures for shallow landslides mechanism and analyse potential precursor signals of an incipient instability, a suite of laboratory experiments was conducted using a flume test apparatus able to reproduce triggering conditions of earth landslides under scaled conditions [38].

5.3.1 Descriptions of experimental Set-Up

The experimental set-up is composed of a rectangular sloping flume apparatus 100 cm long, 60 cm wide, and 20 cm high, filled with a granular soil mixture collected from the Cinque Terre field laboratory [39]. Both sides of the metallic framework were made of thick plexiglass to allow the visual observation of the wetting and triggering processes along the lateral soil section. To ensure basal friction between the soil particles and the base of the flume apparatus and avoid generalized displacement of the filling material, a rough plastic panel was applied. A stiff permeable barrier was fixed in front of the soil to contain it after the failure (Figure 5.1).

The soil material used for the experiments was composed of silty gravel (GM according to the Unified Soil Classification System-USCS), i.e., composed of more than 50 % of gravel with a range of

11 %- 25 % of silty fine (ML according to Casagrande Plasticity Chart) and reconstituted at the site density according to the in-situ natural bulk density, equal to 14.6 ± 1.05 kN/m3. The granular soil mixture has been posed on a squared box by overlaying four compacted layers 4 cm thick parallel to the flume base. Given the fixed rectangular geometry, the soil weight required to fill that volume was calculated considering also the fixed initial water content. Finally, a wedge-shaped slope was created in the termination of the material. Three different tests were conducted with soil initial water content (w0) of 9 % (T1), 14 % (T2) and 16 % (T3). Soil water content was imposed before placing the soil into the flume, by wetting a specific quantity of oven-dried soil with the amount of water needed to reach the desired initial water content value. After, the soil was set into the flume and the water content was checked by sampling the soil at different points.To artificially reproduce the rainfall process, two sprinklers consisting of individual nozzles were placed at a height of 3 m from the flume, at a distance such that the free surface was evenly wetted, and the raindrop size and impact energy distribution was consistent with the scale of the experiment. To ensure the correct functioning of the system, the supplied water pressure has been kept constant at 3.2 bar, resulting in a steady rainfall input of approximately 1mm/min.
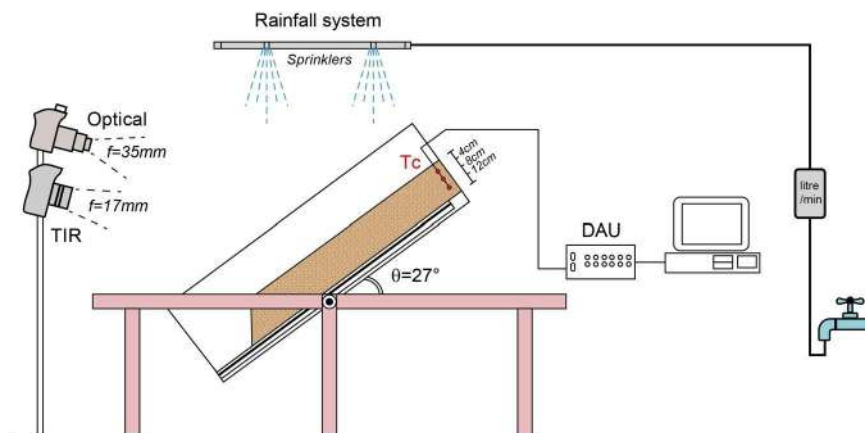
Figure 5.1. *Above) Sketch of the equipment for monitoring slope instability phenomena; Below) different stages of preparation of the for the flume test equipment.*

5.3.2. Description of sensors

During experiments, a video camera was used to monitor the time occurrence and location of failure initiation, while concurrent thermographic acquisitions were carried out every 30 sec to frame surface temperature evolution during the artificial rainfall event. For this work, a Canon PowerShot SX730 HS and a FLIR T840 model, IRT imaging camera were used, both installed on a fixed tripod at 2.40 meters from the flume. The two cameras were installed at the front of the experimental channel, to have the same viewpoint. The characteristics of the cameras are shown in Table 5.1 below.

Table 5.1. a) *technical specifications of the FLIR Thermal Camera; **b**) Technical specifications of the Optical camera.*

a)

Monitoring Tool	Specifications	
	IR Resolution:	464 x 348 (161,472 pixels)
	Accuracy:	±2°C (±3.6°F) or ±2% of reading
	Thermal Sensitivity/NETD:	<30 mK at 30°C (42° lens)
FLIR T840	Object Temperature Range:	-20°C to 1500°C (-4°F to 2732°F)
	Spectral Range:	7.5- 14.0 µm
	Lens:	24°

b)

Monitoring Tool	Specifications	
	Sensor Type:	1/2.3 CMOS
	Sensor Resolution:	20 Mpx
	Focal Length:	4.3 – 172.0 mm
	Zoom:	Optical 40x
Canon PowerShot SX730 HS	Movies Resolution:	(Full HD) 1920 x 1080, 59.94 / 29.97 fps (HD) 1280 x 720, 29.97 fps (L) 640 x 480, 29.97 fps

An infrared thermal camera typically consists of an optical system, a detector, and a signal processor. The principle of InfraRed Thermography (IRT) relies on the acquisition of energy reflected by an object in the InfraRed band of the electromagnetic spectrum, and on the conversion of such energy in temperature according to the Stephan-Boltzmann "black-body" law, given a specific emissivity [40]. The phenomenon is known as "thermal radiation," which can be detected from a distance and used to measure the radiant temperature of the analysed environment [41]. In the electromagnetic spectrum, infrared (IR) occupies a position between visible light and microwaves. The infrared band extends from approximately 430 MHz (with a wavelength of about 0.7 µm) to 300 GHz (with a wavelength of about 103 µm). This band can be divided into several sub-bands: near-infrared (with wavelengths between 0.7 and 1 µm), short-wave infrared (between 1 and 3 µm), mid-wave infrared (between 3 and 5 µm), and long-wave infrared (between 8 and 14 µm). Unlike visible light, infrared wavelengths are longer, making this radiation generally invisible to the human eye. However, it can be detected using specifically designed sensors, such as infrared thermal cameras. In a thermal image, a false-colour scale is used to represent the temperature of each pixel. The temperature of each pixel is based on the infrared radiance detected in the area under consideration. Different temperature values are then mapped to different colours, creating a visual representation of the thermal profile of the object under examination.

The emissivity value of soil was evaluated a priori adopting a standard reference method with the use of reference material with a known emissivity (ISO 18434-1). Reflected apparent temperature was realised using a reflector method, according to the ISO standard, availing of aluminium foil and setting an emissivity equal to one and a distance between the camera and the monitored object to zero.

The use of video footage to acquire high sampling rate optical data and study very rapid processes with a PhotoMonitoring approach has shown encouraging results in some applications for the dynamic study of structures [42]. This application could also be used to study processes such as rainfall triggering landslides. In this work, the same principle shown by [42]was used, i.e. recording a video from a fixed position in order to acquire high-frequency optical data during experimental flume tests.

Video recording during the analogue laboratory tests was performed using a Canon PowerShot SX730 HS camera, mounted on a tripod at 2.40 metres from the flume test as shown in figure 5.1. The video camera was programmed to acquire an image at a frequency of 30 Hz, that is 30 frames per

second and in Full HD resolution (1920 x 1080). The characteristics of the video camera are shown in Table 5.1.

5.3.3. Remote Sensing Technique (RTS)

5.3.3.1. Principles of PhotoMonitoring

PhotoMonitoring is an innovative monitoring solution that utilizes advanced digital image processing algorithms to harness the extensive utilization of optical/multispectral, hyperspectral, and radar sensors on a global scale [12]. By employing digital image processing techniques, PhotoMonitoring enables the extraction of considerable change information (Change Detection) and or analysis of displacement of target object in two (or more) pictures (Digital Image Correlation) (Figure 5.2).
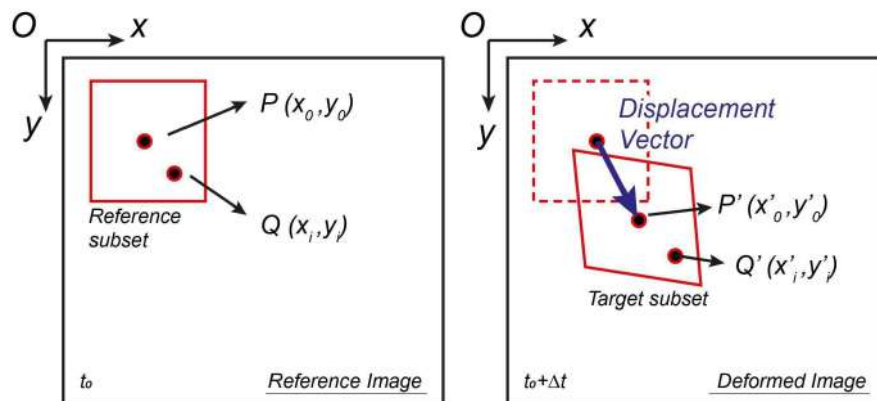
Figure 5.2 *A conceptual scheme illustrating the process of digital image correlation analysis (DIC) is presented. This analysis involves comparing two images of the same scenario, one as a Reference image and the other one as a Deformed image, captured at two distinct time points, denoted as t0 and t0+Δt, respectively (with Δt determined based on the temporal resolution needed to monitor the event). The result is a displacement vector map within a predefined region of interest.*

The versatility and abilities of this method have proven to be particularly advantageous in the identification and monitoring of landslides, especially when compared to traditional *in-situ* techniques that can be costly and time-consuming in terms of manpower and installation. Advancements in camera technology, along with optical sensing and image processing algorithms, have made technologies like Digital Image Processing (DIP) highly appealing [13].

Digital Image Correlation (DIC) is an optical-numerical measurement technique capable of providing full-field 2D surface displacements or deformations in a direction normal to the Line of Sight. The accuracy of the displacement field maps obtained from DIC algorithms depends on the

spatial and temporal resolution of the dataset. DIC involves registering two or more images of the same scene and extracting displacement fields to determine the best match. Deformations are calculated by comparing and processing co-registered digital images of the object's surface before and after the deformation event [43]. Theoretically, DIC displacement measurements can achieve sub-pixel accuracy of approximately 1/50th of a pixel [44] under optimal conditions. However, challenges related to image orientation, co-registration, topographical distortion, instrumental and atmospheric noise, temporal and spatial decorrelations, and co-registration errors may limit the attainment of these accuracy values [11,45]. In many cases, DIC enables displacement and deformation measurements without the need for installing sensors or reflectors on the object, making it a fully remote measurement system [46]. However, a random speckle pattern on the object's surface is a fundamental requirement for obtaining a unique solution in the correlation process [11].

The here presented analysis was performed using IRIS software, developed by NHAZCA S.r.l., a start-up of the 'Sapienza' University of Rome, which enables Change Detection (CD) and Digital Image Correlation (DIC), using various algorithms from the relevant literature and new algorithms developed specifically for this purpose.

The Change Detection method employed in the software utilizes the Structural Similarity Index Method (SSIM), a perception-based model. SSIM considers image degradation as a change in the perception of structural information, incorporating factors such as luminance masking and contrast masking.

Below is the equation found in the literature of the SSIM.

$$SSIM\,(x,y) = [l(x,y)]^{\alpha} \cdot [c(x,y)]^{\beta} \cdot [s(x,y)]^{\gamma}$$

Here, l is the luminance (used to compare the brightness between two images), c is the contrast (used to differ the ranges between the brightest and darkest region of two images) and s is the structure (used to compare the local luminance pattern between two images to find the similarity and dissimilarity of the images) and α, β and γ are the positive constants [47]. The algorithm will return an index that express the images similarity, i.e., in which a value of '0' will indicate a total change between the master and slave image, while a value of '1' will be associated with areas where no change between the two analysed images was identified.

The term "structural information" highlights the strong interdependence and spatial proximity of pixels, providing important visual object information within the image domain. In image quality assessment, SSIM is one of the widely used techniques, but there are other methods such as MSE,

UIQI, PSNR, HVS and FSIM; these methods estimate perceived quality by measuring the similarity between the original image and the secondary image [47]. As noted by [48], SSIM showed great potential for use in change monitoring due to the good quality and accuracy of the results.

The CD method implemented in the software uses the Structural Similarity Index (SSIM) algorithm to assess image quality based on a reference image. It operates on a local scale, iteratively assessing image similarity within small subsets of pixels (window size), allowing automatic identification of regions where changes have occurred. In this research, the analysis was conducted using a moving window size of 32 pixels. The IRIS software used for this work returns a raster map with an SSIM value for each pixel. The map is associated with a colour bar that varies from 'green', which is associated with the SSIM value '1' (no change identified between the two images), to 'blue', which is associated with the SSIM value '0' (total change between the two images).

The displacement analysis method implemented in the IRIS software, on the other hand, involves different types of algorithms that exploit different analysis techniques (feature tracking, phase correlation and Optical Flow algorithm). Displacement maps can be created through a single pair of images (single analysis approach) or through a stack of images depicting the same area (multi-Master approach) [12]. In this second case, the use of a stack of images instead of a single pair allows an advanced application of the DIC technique (multiple-pairwise image matching correlation (MPIC) or Multi-master analysis). This approach involves the use of a sliding master that is compared with a user-selected redundancy with the rest of the images in the stack. This processing makes it possible to obtain for each pixel the time series of the displacement along the N-S and E-W directions and the correlation coefficient (i.e. an estimate of the "quality of the cross-correlation"), with an increase in the signal-to-noise ratio (Figure 5.3) [9,49,50].
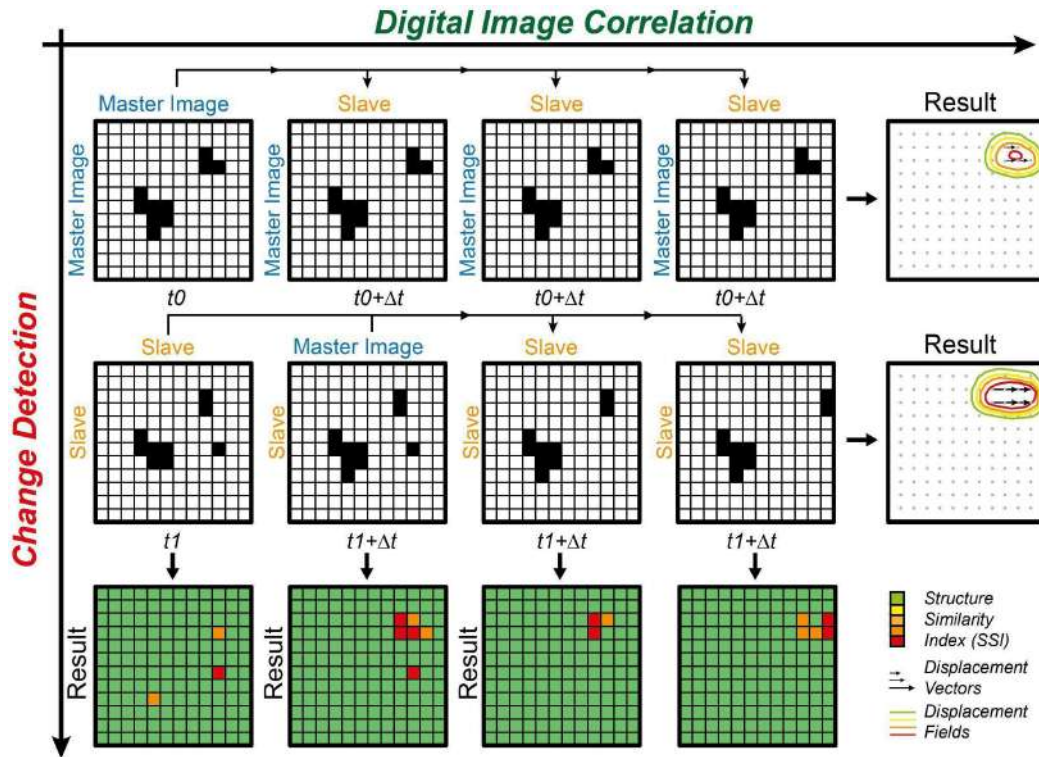
Figure 5.3. Conceptual depiction of Digital Image Correlation (DIC) and Change Detection (CD) Analysis applied to a series of images acquired at different time points. The Change Detection Analysis approach is portrayed vertically, enabling the observation of variations between the image at time t0 (Master) and the one at time t1 (Slave) step by step. This analysis, executed redundantly and sequentially, traces the evolution of changes over time. Meanwhile, the Digital Image Correlation approach is represented horizontally and, when iteratively applied to each image in the stack (where each image progressively becomes the Master), yields a cumulative displacement of the objects present. The outcomes are presented through maps of the Structural Similarity Index (SSI) or displacement fields.

The analysis in this case was conducted using the GEFolkie algorithm, which is a specific implementation of the Optical Flow algorithm [51]. The latter reconstruct the distribution of apparent velocity of brightness patterns in an image, allowing the derivation of relative motion of objects with respect to the observer's plane. Consequently, optical flow can provide valuable information about the spatial arrangement of observed objects and the speed at which such arrangement changes [52]. In detail, the GEFolkie algorithm is based on moving-window methods, of the Lucas-Kanade type, which employs an iterative, multi-resolution approach, following a pyramid strategy that allows the estimation and identification of large and small displacements [53].

The equation of the GeFolkie algorithm used is shown below:

$$J(u; x) = \sum_{x' \in S} \omega(x' - x)(f_1(I_1(x')) - f_2(I_2(x' + u(x))))^2$$

where ω defines a local window of radius r and size *(2r + 1) × (2r +1)*, thus $\omega(x)=1$ *iff* $|x|_\infty \leq r$ and 0 else; f_1 is a function applied to the master image I_1, and f_2 is a function applied to the slave image I_2. These functions f_1 and f_2 are designed to project the images in a space where f_1 (I_1) and f_2 (I_2) are similar enough to validate the brightness constancy model [53].

5.3.3.2. Data processing

Figure 5.4 illustrates the flow chart showing the steps performed from data acquisition to data processing carried out for the monitoring of rainfall-triggered landslide failures here reproduced in the laboratory and studied with the integrated monitoring system previously described.
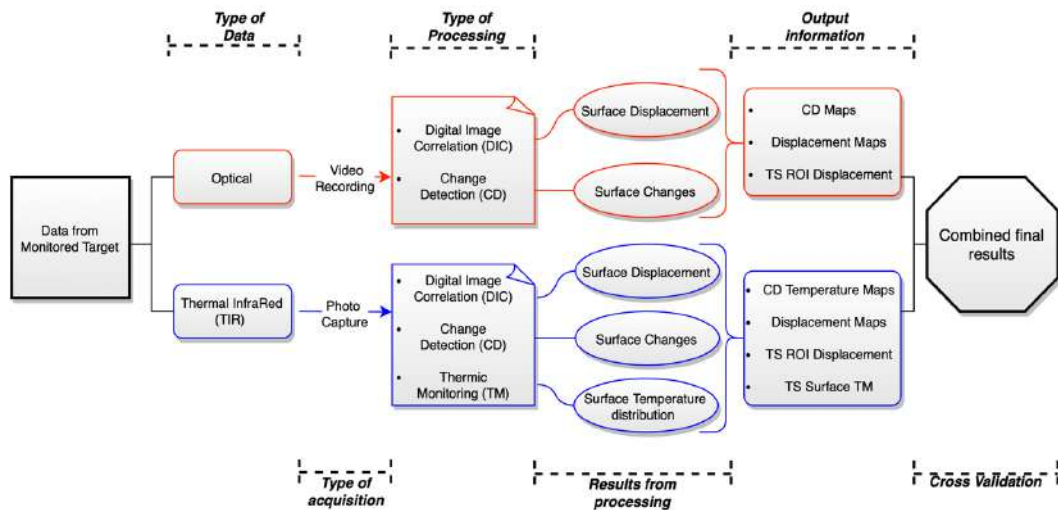
Figure 5.4. *Flow chart of the experimental procedure with summary of the data analysed and processing performed.*

sampling rate of 30 Fps. IRT images were taken at regular intervals of 30 seconds from when the test began. The contact sensors (Soil Temperature), instead recorded continuously throughout the test.

The optical data were pre-processed, extrapolating from each video the frames over the first 20 minutes, encompassing the occurrence of slope failure in the flume, then sub-sampling one frame every 10 seconds, i.e., 1 frame every 300, as described in Table 5.2.

Table 5.2. *Frames extrapolated from each video of the 3 experimental flume tests performed.*

Experiment	Execution date	Video duration	Frame*	Subsampling (1/300) **
1	01/06/2022	29:59	36000	120
2	19/07/2022	23:45	36000	120
3	02/09/2022	23:44	36000	120

* Number of frames extrapolated for the first 20 minutes of video

** Subsampled at a rate of 1 frame every 10 seconds.

IRT images were pre-processed directly using the proprietary Research-IR Max FLIR® Software. Colour palettes were standardised and extrapolated in JPEG-Rad format, in order to retain the radiance information. The IRT images used are different for each experiment, as can be seen in Table 5.3, in relation to the time and mode of break-up of the three experiments.

Table 5.3. Number of IRT images used and analysed for each experiment.

Experiment	Execution date	Number IRT images
1	01/06/2022	150
2	19/07/2022	120
3	02/09/2022	76

For both datasets, DIC and CD analyses were performed using the IRIS® software. IRT images were also processed directly on the proprietary FLIR® software to extrapolate the surface temperature changes during the test. From these analyses performed on both datasets, displacement and change maps were extrapolated for the entire duration of the experiments.

The final combination and cross-validation step were conducted by comparing the results obtained from CD and DIC, using both the Optical and IRT datasets. Specifically, for the DIC, a time series was extracted from both datasets on a specific Region of Interest (ROI 1) and then a time series was also extracted for a smaller ROI 2 located at the fracture enucleation area. The time series of ROI 1, one from the optical data and the other one from the IRT data, were quantitatively compared by

calculating the Pearson Correlation Coefficient. This was performed iteratively on all three laboratory tests in order to ensure adequate statistical representativeness.

The Pearson correlation coefficient is a statistical measure that indicates the strength and direction of the linear relationship between two variables. Its value can range from -1 to +1, where maximum positive or minimum negative values express positive correlation, i.e., the two-time series are perfectly linearly and positively correlated or a perfect anticorrelation. A value of 0 indicates no linear correlation between the two-time series.

Through this approach, it was possible to assess the similarity between the two measurement techniques and the confidence of the displacement analyses conducted on the IRT images compared to those performed on the Optical images. Contact deformation monitoring devices are not available to retrieve ground truth. In addition, the displacement measurements were subjected to advanced validation by direct comparison with measurements performed directly in the laboratory. All displacement maps were returned in millimetres by calculating the Ground Sampling Distance (GSD), i.e., the distance between two consecutive pixel centres measured on the ground. The higher the GSD value of the image, the lower the spatial resolution of the image and the less detail is visible. In this case, IRT images have a GSD of 2.3 mm and Optical images have a GSD value of 1.8 mm.

5.4. Results

The laboratory experiments were performed with three different initial water contents (w_0) and showed different behaviour and times to failure. The characteristics of the three experiments are shown below in Table 5.4.

Table 5.4. Number of IRT images used and analysed for each experiment. The time-to-failure is expressed as hh:mm:ss from the beginning of the test in which the failure occurs in the model.

Experiment	Execution date	Initial Water Content (w_0)	Time to Failure [HH:MM:SS]
1	01/06/2022	9.86%	00:29:30
2	19/07/2022	14.65%	00:11:30
3	02/09/2022	15.51%	00:12:90

In general, all the tests exhibited a similar behaviour. Indeed, in each case, an initial stable phase was followed by an incipient slope movement, which was subsequently accompanied by the appearance of fractures on the surface of the earthen slope shortly before generalized failure.

This paper only presents and discusses the results of experiment No. 2 from 19/07/2022, which was used as a reference for the occurrence of failures. The discussion section includes an evaluation of all three experiments.

5.4.1. Results from optical camera

As previously described, 3600 frames were extracted from the video. To make the analysis process quicker, a sub-sampling was employed capturing one frame every 10 seconds (equivalent to 1 frame every 300 seconds). The result was a set of 120 frames to be analysed that made it possible to reconstruct the time evolution of the laboratory test (Figure 5.5). It was observed that the first surface fractures occur approximately 10:30 minutes after the start of the experiment. Based on the observed evidence, a specific ROI 1 was selected to extract a displacement Time Series (TS) and highlighted in Figure 5.5. These selected images from ROI 1 were imported into the IRIS software and analysed following the previously described methods.

Optical-CD analyses performed on the optical images' frames allowed us to observe how the surface of the slope changes during the experiments by comparing the previous frame with the subsequent frame (sequential frame-by-frame analysis every 10 seconds). This enabled us to study when and where changes in the slope surface occur due to the initiation of landslide phenomena. The results revealed that the surface showed consistent evidence of activity, and then from minute 10:30 onwards, the formation of first surface fractures and after the beginning of the slope failure. As depicted in Figure 5.5, the slope surface reproduced in the laboratory experiment displayed evidence of changes in the lower left portion of the image, the active and moving portion. The failure occurred at minute 11:30, and after the CD analysis (at minute 16:00) showed the distributed failure phase, with the formation of fracture in the upper portion of the slope previously unaffected by the failure, as well as the development of a longitudinal fracture from left to right in the test flume. Such linear fracture is representative of a translational deformation (and failure) mechanism, that well reproduced the infinite slope conditions. Despite the general translational mechanism, a single and coherent rotational surface occurred in the slope toe.
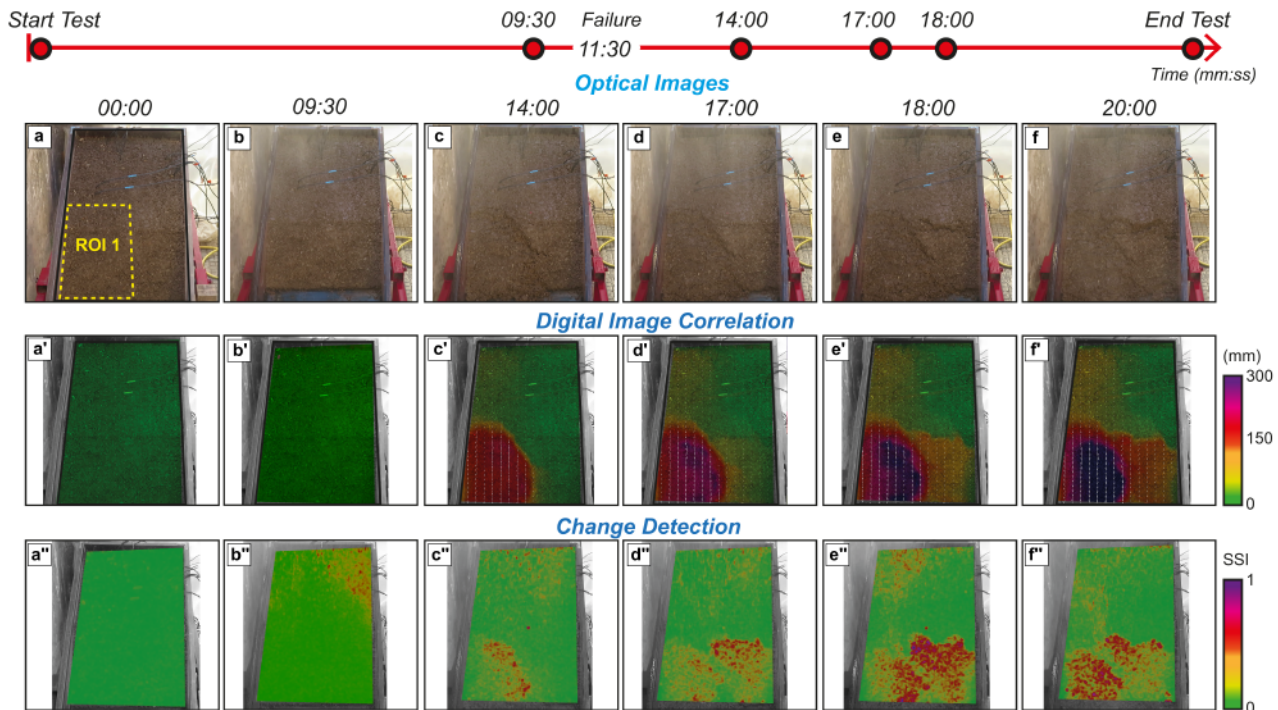
Figure 5.5. *The image illustrates the chronological progression of the experiment, spanning from its initiation to its conclusion, and it includes the outcomes derived from the analyses carried out on the optical dataset. Each column corresponds to a specific moment, depicting the condition of the slope, alongside the corresponding CD and DIC results, at various time intervals following the experiment's commencement (0 minutes (a), 9 minutes and 30 seconds (b), 14 minutes (c), 17 minutes (d), 18 minutes (e), 20 minutes (f))*

Optical-DIC analysis allowed us to obtain a quantitative representation of the process evolution, as depicted in Figure 5.5. In the lower left part was observed a displacement of about 35 mm and a formation of first surface fractures after 10:30 minutes from the start of the experiment. In the same area the failure was observed after 11:30 minutes from the beginning and with a cumulated displacement of about 70 mm. The Optical-DIC results, presented in Figure 5.5, demonstrate a gradual backward of the landslide process after 14 minutes, accompanied by a displacement of approximately other 145 mm in the lower portion. This backward movement is also evident in the Optical-CD analyses, which reveal the formation of perimeter fractures in the upper part of the ground slope. Gradual movement in the upper section of the test flume is observable, reaching 40 mm after 18 minutes from the start of the experiment. In addition to the retrogressive style, it is worth to note that the fracture also affects the right side, exhibiting a significant displacement of approximately 150 mm towards the end of the experiment. After 20 minutes from the start of the experiment, Optical-DIC analysis observed a maximum displacement of approximately 320 mm in the lower section of the test flume (Maximum displacement highlighted in purple in Figure 5.5). As observed from Figure 5.5, there is a significant spatial overlap between the results of Optical-

CD and Optical-DIC. In fact, both analyses highlight the bottom-left area as the region undergoing incipient deformation and then fractures.

Thanks to the Optical-DIC analysis performed on the dataset comprising 120 images, it was possible to obtain a temporal displacement series for each pixel within the analysed area (figure 5.5a). Within the ROI 1, a temporally averaged series was extracted, enabling the reconstruction of the temporal evolution of the process for that specific area and facilitating the observation of the displacement value in millimetres throughout the entire duration of the test. As depicted in Figure 5.6, the time series exhibits an initial phase of apparent stability lasting until 9:00 minutes. From that point onwards, a rapid velocity change is observed, indicating a phase of incipient slope movement followed by the formation of first surface fractures (10:30 minute) and the failure of the experimentally simulated slope (11:30 minute). From the beginning of the incipient slope movement until the distributed failure (from 9.00 minute to the end of the test), two distinct behaviours occur: an initial phase with a velocity of 0.82 mm/s, followed by a phase with a velocity of 0.35 mm/s. This observation indicates that the process tends to decelerate slightly, possibly due to a decrease in the slope angle.
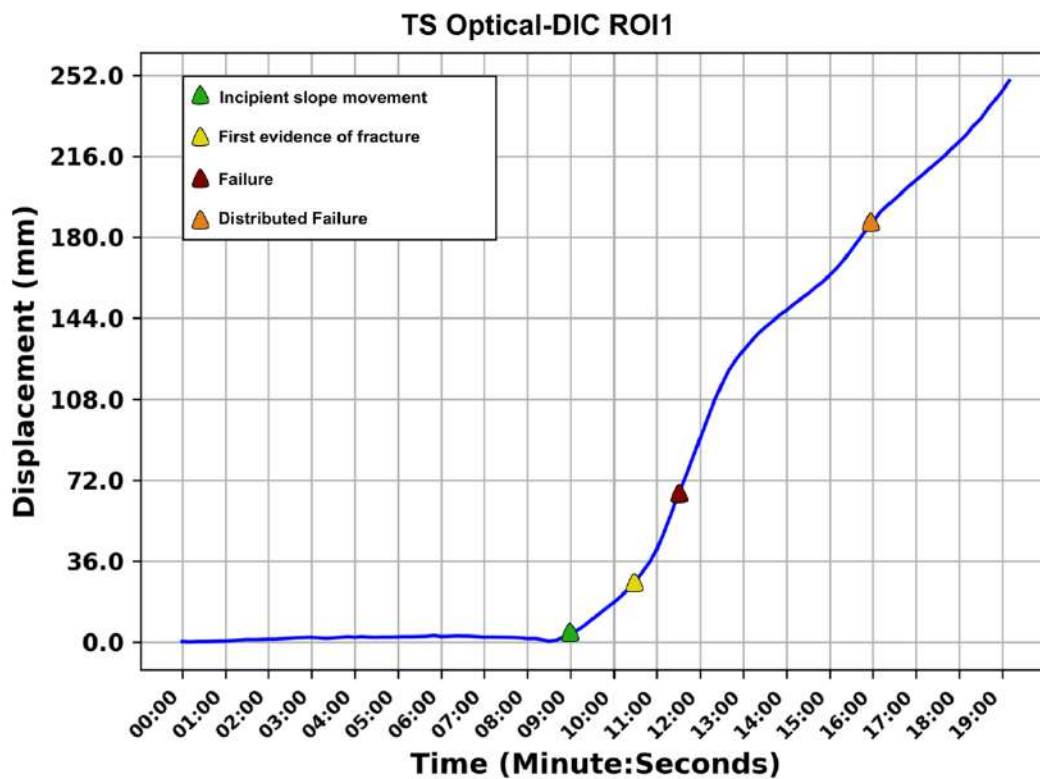

Figure 5.6. Time series acquired from the optical dataset and extracted from the ROI 1, illustrating the temporal evolution of the experiment with an initial phase of stability followed by a phase of incipient slope movement (green point), fracturing (yellow point), failure (red point) and distributed failure phase (orange point).

5.4.2. Results from IRT sensor

Using IRT images acquired at regular intervals of 30 seconds, the same DIC and CD analyses performed on the optical images were conducted as described in the Materials and Methods section. The temporal evolution of the laboratory test was thus observed through a sequence of 40 IRT images, as highlighted in Figure 5.7. The results of the IRT-CD analyses allowed for the observation of changes in the slope related to variations in surface temperature caused by the pluviation, surficial wetting and initiation of the landslide phenomenon. Analyses were performed, as mentioned above, by comparing the previous IRT image with the next one (sequential image-by-image analysis every 30 seconds).

The results of the IRT-CD analysis, as shown in Figure 5.7, identified changes occurring in specific portions of the slope surface, consistent with the area where slope failure occurred. The changes detected by the IRT-CD analysis, represented by the red areas with an SSIM value below 0.5, can be associated with zones that exhibit alterations on the surface of the slope, linked to the presence of positive thermal anomalies caused by the opening of longitudinal fractures (a phenomenon also observed in the corresponding optical images). As reported in Figure 5.7, after 10:30 from the beginning of the test, during the formation of first surface fractures, positive thermal anomalies (higher temperature than the surrounding area) start to appear in the lower left portion of the flume test. The failure occurred at 11:30 minute after the beginning of experiment and by the 14:00 minute, the scattered anomalies observed tend to coalesce, clearly indicating the fracture delimiting the portion of the slope where maximum displacement occurs, and a section of the slope detaches. As the laboratory test progresses, after 17 minutes from the start, the IRT-CD analyses reveal the presence of longitudinal anomalies from left to right, associated with fractures affecting the entire lower part of the slope.
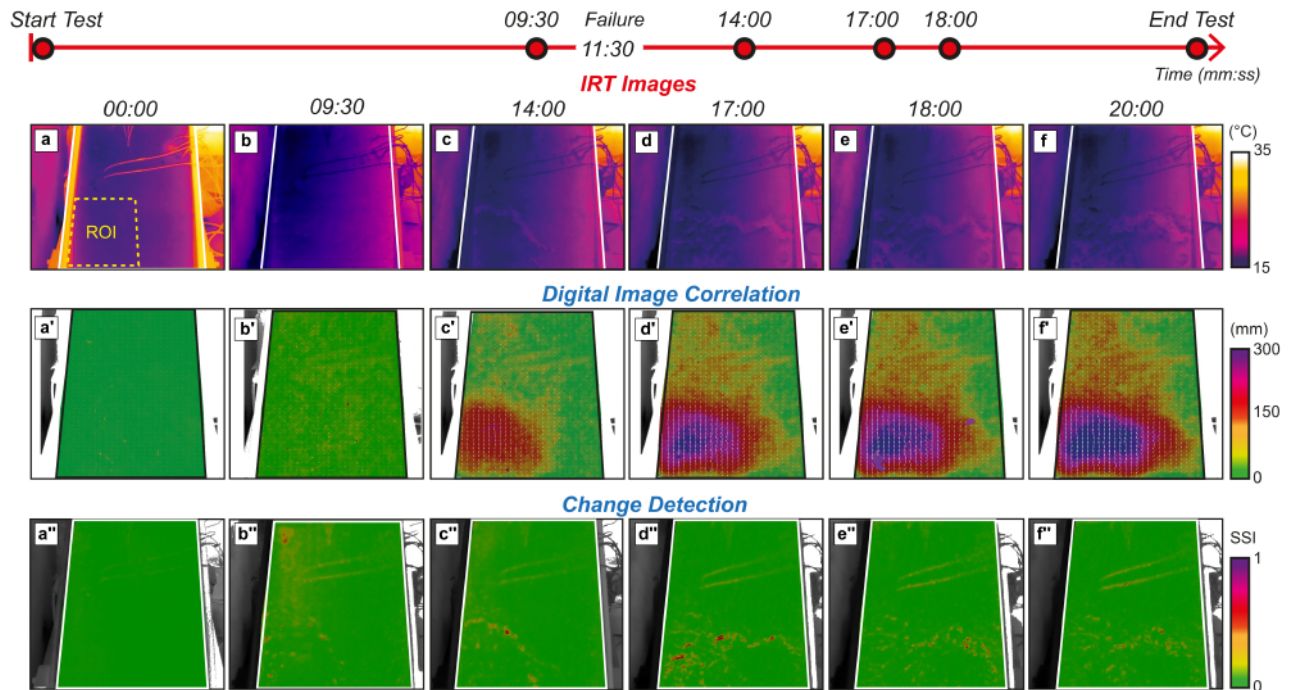
Figure 5.7. *The image illustrates the chronological progression of the experiment, spanning from its initiation to its conclusion, and it includes the outcomes derived from the analyses carried out on the optical dataset. Each column corresponds to a specific moment, depicting the condition of the slope, alongside the corresponding CD and DIC results, at various time intervals following the experiment's commencement (0 minutes (**a**), 9 minutes and 30 seconds (**b**), 14 minutes (**c**), 17 minutes (**d**), 18 minutes (**e**), 20 minutes (**f**))*

The IRT-DIC analysis was conducted to obtain a quantitative representation of the process evolution using IRT images. The analysis clearly reveals the formation of a fracture zone with a progressive displacement in the lower left portion of the flume (Figure 5.7). As indicated by the IRT-DIC results, after 14 minutes from the beginning of the test, the formation of an active area in the lower left part becomes evident, with a measured displacement of approximately 140 mm. Starting from minute 17, a progressive widening of the deformation front is observed, exhibiting a retrogressive trend. In fact, it can be observed that the upper left part of the slope suffers a displacement of approximately 35 mm.

Additionally, after 18 minutes from the start of the test, it is evident that the fracture also involves the right side of the slope, displaying a significant widening of the deformation zone. After 20 minutes from the start of the experiment, through IRT-DIC analysis, a maximum displacement of approximately 320 mm was observed in the lower part of the flume test (Maximum displacement highlighted in purple in Figure 5.7).

The IRT-DIC analyses performed on the dataset of 40 IRT images allowed for obtaining a displacement time series for each pixel within the analysis area. For the ROI 1, a temporally averaged displacement series was extracted to reconstruct the temporal evolution of the process for that

specific area, thereby observing the displacement values in mm throughout the entire duration of the test. Figure 5.8 displays the temporal series of the ROI 1 obtained from the IRT images. It is clearly visible that the time series exhibits, although not perfectly centred around zero, an apparent stability phase of the area for up to 9 minutes from the start of the test. From that point onwards, a rapid change in the gradient is observed, indicating a phase of incipient slope movement followed by the formation of first surface fractures (10:30 minute) and the failure of the material under progressive saturation (11:30 minute). From the beginning of the slope movement until the distributed failure (from 9.00 minute to the end of the test), displays two different trends: a first part with a velocity of 0.50 mm/s and a subsequent part with a velocity of 0.28 mm/s. This indicates that the process tends to slightly slow down due to the probable decrease in the slope angle, and the achievement of a new dynamic equilibrium, as similarly observed by Optical-DIC (Figure 5.6).
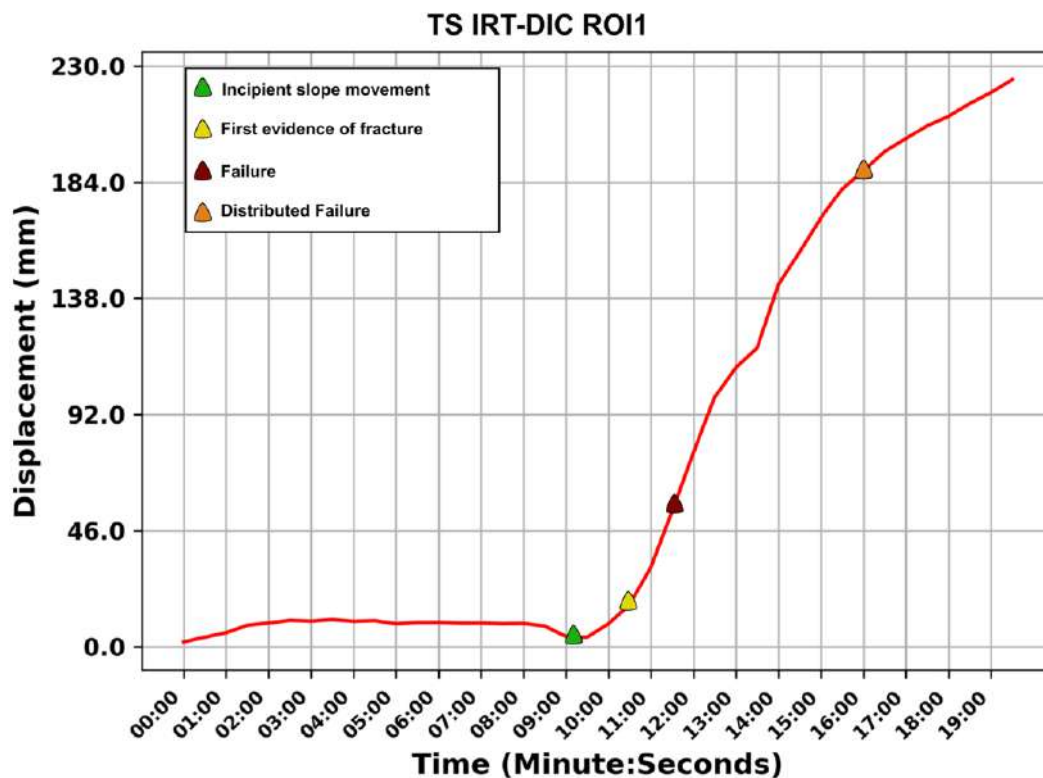
Figure 5.8. *Time series acquired from the IRT Images and extracted from the ROI, illustrating the temporal evolution of the experiment with an initial phase of stability followed by a phase of incipient slope movement (green point), fracturing (yellow point), failure (red point) and distributed failure phase (orange point).*

5.5 Discussion

The performed DIC analyses allowed to study the shallow landslide replicated in the laboratory and quantitatively reconstruct the evolutionary process leading to failure, with a precision that is capable to reach resolution lower that the 1/50 of the pixel size [54] and relevant accuracy [55].

Furthermore, the laboratory experiment facilitated the acquisition of measurable and comparable data, ensuring the repeatability and adaptability of the proposed workflow. Indeed, as demonstrated by [35,40], the utilization of the laboratory analogue model has emerged as an extremely effective means to comprehensively explore and understand the behaviour of slopes involved in landslide dynamics. This approach has proven essential for evaluating new monitoring methods, allowing for the control of variables influencing such phenomena, including precipitation, temperature, and soil mechanics.

The obtained results from DIC and CD analyses conducted on the Optical and IRT images acquired during the execution of flume test experiments were compared. As reported in Figure 5.5 and Figure 5.7, the results qualitatively show the same deformation trend and magnitude of cumulative displacement, which reflected in a similar failure mechanism: with a fracture nucleating in the bottom-left portion of the flume after 10:30 minutes from the beginning of the test, which then evolves with a retrogressive and roto-translational failure.

For a quantitative comparison, as shown in Figure 5.6 and Figure 5.8, the two time series were extracted from the DIC displacement analyses for the same ROI 1, one obtained from Optical data and the other from IRT data. Subsequently, these two time-series were quantitatively compared using a Pearson Correlation Coefficient.

As reported in Figure 5.9, the IRT and optical DIC time series exhibit a high correlation with a coefficient of 0.75, indicating a strong correspondence among the series and the suitability of the two techniques. Approximately 9 minutes after the start of the test, a significant incipient slope movement phase can be observed, followed by the appearance of the first fracture and the subsequent failure of the slope. Both time series are characterised, from 9:00 minutes onwards, by two different slope angles, the first one constant up to 14:00 minutes (speed of approx. 0.82 mm/s), which subsequently changes, indicating a tendency to decelerate due to the reduction of the slope (speed of approx. 0.35 mm/s).

To study the quantitative difference between the two time-series, the Mean Absolute Percentage Error (MAPE) was calculated, which expresses the average percentage error. This value

was calculated without considering the initial part (0 min. - 9:00 min.). In this stage, there is an overestimation error of displacement in the IRT-DIC analysis. In fact, the displacement in this stability phase is not perfectly zero. Consequently, throughout this initial part, the IRT time series (in red) consistently appears above the Optical time series (blue line in Figure 5.9). This is due to the surface temperature change that occurred following the opening of the rain irrigators in the initial phase of the test, which are sensitive to IRT images but not to Optical ones. From the analysis of the second part of the time series, it is evident that the DIC analyses conducted with IRT images tend to underestimate the displacement by approximately 3.6% compared to the DIC analyses performed with Optical images (considered as a benchmark and validated by the displacement measured in the laboratory). In this case it is possible to see how the Optical-DIC is slightly more precise and accurate than the IRT-DIC, in fact it is able to better discern the beginning of the phase of Incipient slope movement. It must be considered, however, that the techniques of Optical-DIC are more used in the literature and therefore more evolved from a computational point of view [56].
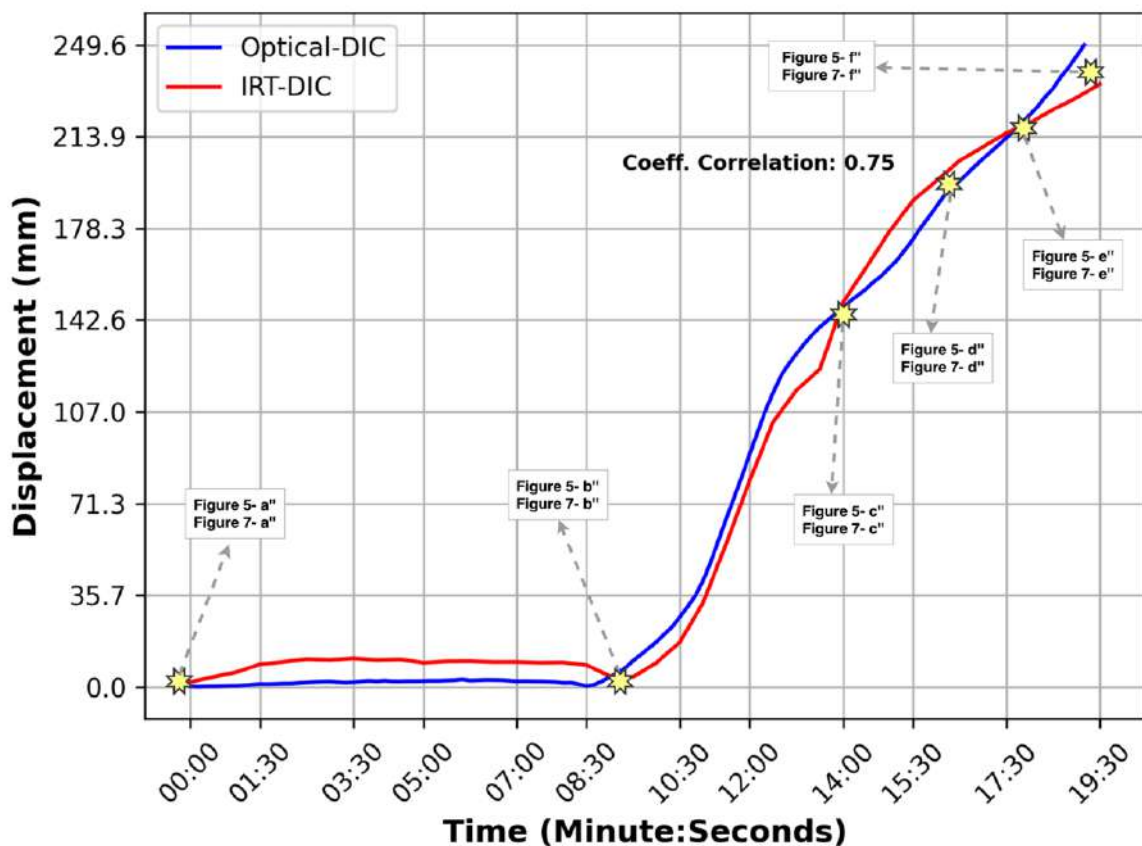
Figure 5.9. Quantitative comparison between the Time Series obtained from DIC-Optical analyses (in blue colour) and the Time Series obtained from IRT-DIC analyses (in red colour) for the ROI area. The figure indicates the corresponding images present in the results chapter.

The correlation analysis conducted on DIC results reported for Experiment No. 2 were also carried out for the other laboratory experiments. Specifically, the time series obtained from DIC analyses conducted with optical data were compared with the time series obtained from DIC analyses conducted with thermal data for the same Region of Interest (ROI). The correlation index values for all three experiments are presented in Table 5.5 below.

Table 5.5. Summary of the correlation coefficient obtained from the other laboratory tests comparing the time series obtained from DIC-Optics and IRT-DIC for the same ROI.

Experiment	Date	Coeff. Correlation TS
1	01/06/2022	0.71
2	19/07/2022	0.75
3	02/09/2022	0.69

The correlation coefficient values highlight an excellent correspondence between the time series obtained with optical images and those obtained with thermal images over the three experiments. This result confirms that through the IRT-DIC analyses it is possible to quantitatively reconstruct the deformation process induced in the flume introducing a small underestimate but enabling the monitoring the soil surface temperature evolution during and after the rainfalls and following the deformation process up to failure. In addition, IRT-DIC analyses could allow 24h monitoring in contrast to those of Optical-DIC, which are not applicable for example during the night, making the technique suitable for continuous monitoring and can also be used in an Early Warning system after more in-depth studies.

The Change Detection analyses, on the other hand, were used to compare step-by-step changes occurring on the surface of the earth slope, investigating any signs of incipient failure. As the results show (Figure 5.5 and Figure 5.7), the surface of the slope did not undergo any noticeable changes until after the first fracture had appeared (10:30 minutes). The results obtained from the Optical-CD clearly show an area with low SSIM values (red area in Figure 5.5), representative of the large portion where significant surface changes occur due to the deformation affecting the lower left portion (Figure 5.5 b"- c"- d"- e"- f").

In contrast to Optical-CD, the results obtained from IRT-CD allow the observation of numerous small changes (with low SSIM values) that resulting from the appearance of positive thermal anomalies on the surface. These thermal anomalies, clearly visible, are attributable to the enucleation

of the fractures. For this difference, IRT-CD analysis was better suited and effective than Optical-CD for a more detailed examination of the fracture geometry and their growth over time (Figure 5.7 b"-c"- d"- e"- f").

The presence of this specific positive thermal anomalies on the surface is primarily due to the thermal difference produced between the surface, cooled by the presence of infiltrating water, and the deeper soil, which is affected with a temporal delay by the cooling effect of water. These thermal contrasts begin to be seen from the formation of the first surface fractures (10:30 minutes), when the fracturing slowly exposes the deepest soil. This is further confirmed by comparing the surface temperature to the temperature measured using the thermocouples located at depths of 4, 6, and 12 cm below the surface (Figure 5.10). From the analysis of Figure 5.10, an important drop of approximately 2 degrees °C in surface temperature is clearly observed around 2 minutes after the start of the test.

Through the results of IRT-CD, it was possible to accurately reconstruct the fracture geometry due to the emergence of thermal anomalies. To achieve this, a detailed study of the occurrence of these positive thermal anomalies was conducted, correlating the IRT-CD results with the time series obtained through IRT-DIC. This allowed for an understanding of the deformation state of the test in the moment when surface thermal anomalies related to the fracture phase appeared. As shown in Figure 5.9, the appearance of surface thermal anomalies occurs after the incipient slope movement phase, approximately 10:30 minutes after the start of the test.

However, thanks to the detailed analysis and the correlation between IRT-CD and IRT-DIC results, small and localized positive thermal anomalies were observed at 9:30 minutes from the start of the test, as depicted in Figure 5.7b". These small anomalies, identified exclusively through IRT-CD results and not visible to the naked eye or through Optical-CD, appear in the lower left portion of the slope before the appearance of surface fractures. In fact, as the test progressed, these anomalies evolved to form the first fracture and the subsequent collapse of the slope into the soil (Figure 5.7b-5.7b'-5.7b") (Figure 5.10).
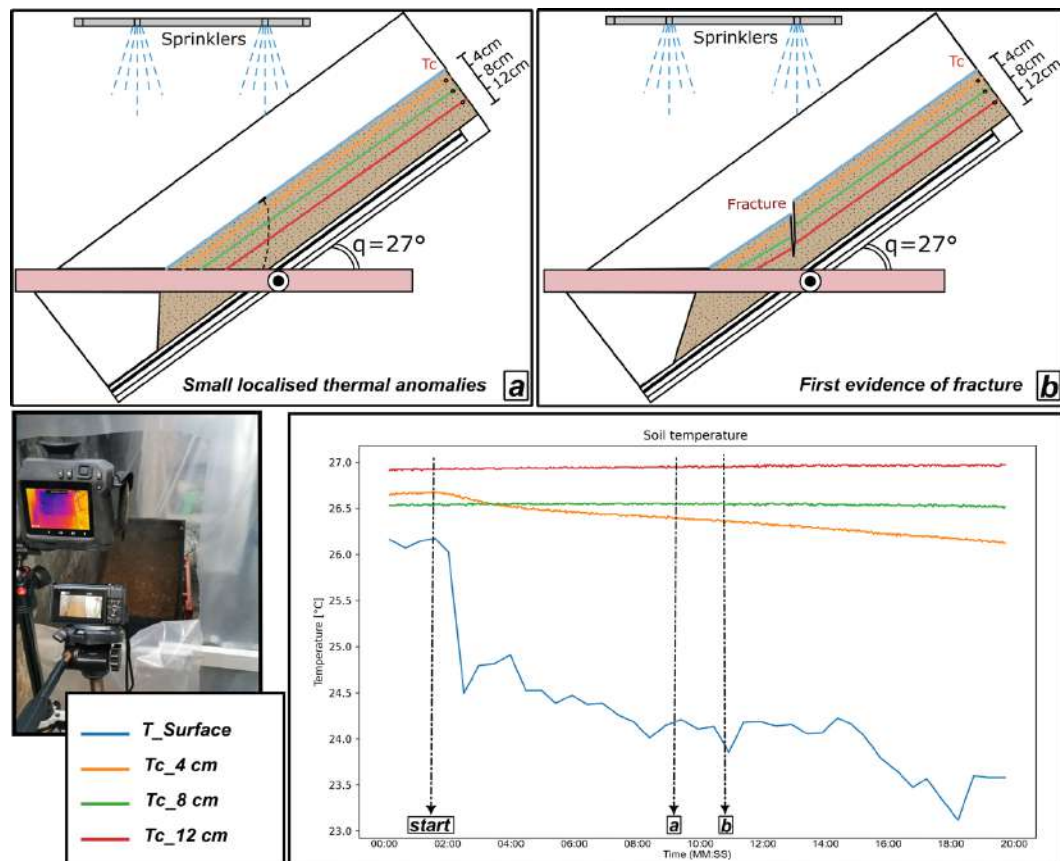
Figure 5.10. Descriptive sketch of the surface fracturing that occurred during the experiment is presented in the image. The analysis of the thermal images reveals positive anomalies due to the exposure of the deeper soil, which is warmer than the surface soil cooled by the infiltrated water. To confirm this, it can be observed from the temperature time series shown in the figure that at 10:30 minutes (when the first fracture appears), there is a temperature differential of approximately 2°C between the surface and the deeper soil.

To understand the origin of the thermal anomalies observed before the fracture, which were not caused by the thermal difference produced between the surface and the deeper soil, a more detailed time series was extracted. This time series was obtained from the IRT-DIC analysis within ROI 2, located within ROI 1, in the portion where these thermal anomalies were registered. The primary aim was to determine if these thermal anomalies were caused by a small displacement that opening the fracture, or if they were caused by drainage-induced settling effect before the first fracture appeared. To better understand the origin of these pre-failure thermal anomalies, the results of IRT-CD and IRT-DIC were compared (Figure 5.11).
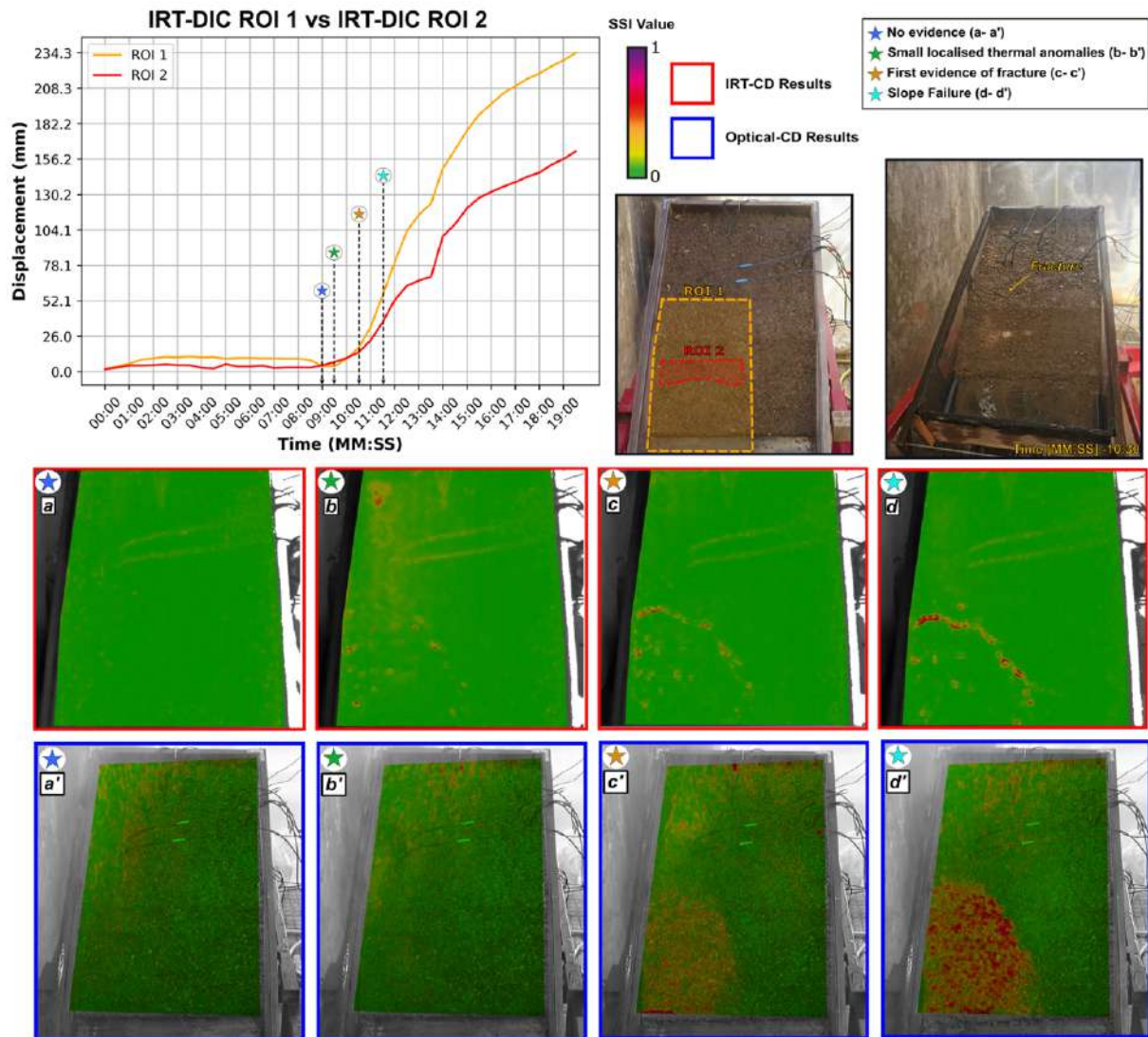
Figure 5.11. *Result of IRT-DIC with a time series extracted from ROI 2 and ROI 1 combined with IRT-CD results and Optical-CD. This combination allowed us to observe how thermal anomalies appeared at 9:30 minutes from the start of the test (image with green star), preceding the appearance of the first fracture occurring at minute 10:30 (image with orange star). It is noteworthy how the small thermal anomalies observed pre-fracture evolve until the failure (image with blue star).*

As is clearly observed in Figure 5.11, the surface thermal anomalies occur a 2 minute before the slope failure, which is preceded by the formation of a surface fracture. It is evident that the area in which the thermal anomalies are observed at 9:30 minutes corresponds to the sector in which a continuous fracture has developed (Fig. 5.11c), as these thermal anomalies progressively coalesce into a main fracture that allows roto-translational sliding at the foot of the slope.

Considering what has been observed, it is therefore assumed that the appearance of these thermal anomalies is linked to a slight pre-fracture settlement and internal slope drainage, which is not visible to the naked eye and in the visible bands.

This occurs in response to the infiltration effect of water from the rainfall system and consequent development of a saturated water front migrating downward (e.g., [35,39]). In fact,

recent reports [57–59] have concluded that, for rainfall-induced translational slides in terrains of homogeneous soil, the sliding failure can be categorized as occurring in two major phases: the infiltration phase and the saturation phase. In the infiltration phase, rainwater infiltrates causing the advance of the wetting zone. If the failure takes place in this phase, the failure plane can occur at specific depth depending on slope angle, rainfall intensity, and soil mechanical parameters and matrix suction conditions. The saturation phase takes place during the rising of the water table, which initially occurs after rainwater reaches the impermeable interface [60]. If failure occurs in the infiltration phase, precursor signs may occur relatively close to the final stages of landslide triggering and therefore conventional instruments are not suitable to identify [61]. On the other hand, if failure occurs during the saturation phase the failure plane occurs only at the impermeable interface and with instrument like Soil deformation sensors at high frequency, installed in subsurface, it possible to investigate the precursors signals [62].

The approach tested in this work, i.e., the combined use of IRT-CD and IRT-DIC, turns out to be able to reconstruct the landslide process by extrapolating time series, and also to identify thermal anomalies (Figure 11 b) directly relatable to the specific failure mechanism can be registered in advance (before the fracture nucleation and slope failure).

However, further studies and tests are needed to extend this application to real-world scenarios where geometric and triggering conditions are not controlled and cause-effect relationships unclear. The major potential of this methodology resides in the versatility of the sensors used for the analysis, which allow for a wide range of flexibility in real-world applications. This includes the possibility of using IRT sensors with different, focal length and spatial and temporal resolutions and/or in combination with optical cameras with higher geometric resolution, offering higher measurement sensitivity. The here reported findings, if scaled up for real-life monitoring applications, could create a low-cost Photomonitoring technique capable of operating both in day and night that could also be integrated into a more complete monitoring system able to provide near real-time information in a broader spectral band.

5.6 Conclusion

In this study, we present an integrated approach to monitor shallow landslides triggered by rainfall, employing Digital Image Processing (DIP) techniques by availing of Optical and InfraRed

Thermography (IRT) data. Two principal methods of image analysis have been adopted: Digital Image Correlation (DIC) and Change Detection (CD). While these techniques are more frequently used with Optical data, the use of IRT data for monitoring shallow landslides is a relatively new and promising research application. The adopted approach, applied at the scale of a laboratory experiment, enabled us to accurately reconstruct the entire landslide process throughout its stages of stability, incipient slope movement, and slope failure.

We use in this work DIC and CD analysis with the advantages offered by infrared thermography, capturing and integrating data on displacement, velocity (IRT-DIC), and surface temperature changes (IRT-CD), as well as performing the same analysis using the Optical dataset (Optical-DIC and Optical-CD).

IRT-DIC analyses shown a high reliability and accuracy in defining the pattern and magnitude of slope displacement, highlighting the same deformation phases observed in the Optical-DIC analysis. Cross-correlation among IRT-DIC and Optical- DIC derived time series results in good correlation coefficient for all the test conducted. Notably, both IRT-DIC and Optical-DIC analysis results showed the presence of an incipient slope movement phase about two and a half minutes before the slop failure and without the presence of any type of surface evidence. In addition, the combination of the IRT-CD and IRT-DIC results showed the presence of anomalies in the Structure Similarity Index value, given by slight thermal anomalies about one minute before the slop failure and without the presence of surface evidence of fracture.

Our results, in particular the identification of the incipient slope movement phase and the small thermal anomalies, can be considered potential precursor signs of slope failure, providing convincing evidence of the reliability of digital image processing (DIP) with the combination of Optical and Thermal data.

More generally, the considerations are that this methodology has proven its reliability on a laboratory scale, promising for potential real-scale applications. Informative potential of the obtained results can be remarkable, especially when scaled and transferred to real scenarios for Early Warning purposes, where the delay between precursors signal and failure can be large. Application of DIP on thermal data, unlike optical images, improve the ability to collect data even during the night-time, which is very useful for an Early Warning System.

The Optical and IRT-DIP techniques introduced in this study represent a tool for monitoring the deformation processes associated with shallow landslides. Despite the full scalability of this approach to natural processes requires further investigation, the obtained results represent a

promising example of integrated monitoring functional for defining appropriate and cost-effective strategies for shallow landslide risk mitigation and safety improvement in vulnerable areas.

References

1. Haque, U.; Blum, P.; Da Silva, P.F.; Andersen, P.; Pilz, J.; Chalov, S.R.; Malet, J.-P.; Auflič, M.J.; Andres, N.; Poyiadji, E.; et al. Fatal Landslides in Europe. *Landslides* 2016, *13*, 1545–1554, doi:10.1007/s10346-016-0689-3.

2. Klose, M.; Maurischat, P.; Damm, B. Landslide Impacts in Germany: A Historical and Socioeconomic Perspective. *Landslides* 2016, *13*, 183–199, doi:10.1007/s10346-015-0643-9.

3. Casagli, N.; Intrieri, E.; Tofani, V.; Gigli, G.; Raspini, F. Landslide Detection, Monitoring and Prediction with Remote-Sensing Techniques. *Nat Rev Earth Environ* 2023, *4*, 51–64, doi:10.1038/s43017-022-00373-x.

4. Canuti, P.; Casagli, N.; Ermini, L.; Fanti, R.; Farina, P. Landslide Activity as a Geoindicator in Italy: Significance and New Perspectives from Remote Sensing.

5. Gunzburger, Y.; Merrien-Soukatchoff, V.; Guglielmi, Y. Influence of Daily Surface Temperature Fluctuations on Rock Slope Stability: Case Study of the Rochers de Valabres Slope (France). *International Journal of Rock Mechanics and Mining Sciences* 2005, *42*, 331–349, doi:10.1016/j.ijrmms.2004.11.003.

6. Dai, F.C.; Lee, C.F.; Ngai, Y.Y. Landslide Risk Assessment and Management: An Overview. *Engineering Geology* 2002.

7. Remote Sensing Techniques for Landslide Studies and Hazard Zonation in Europe.Pdf.

8. Chae, B.-G.; Park, H.-J.; Catani, F.; Simoni, A.; Berti, M. Landslide Prediction, Monitoring and Early Warning: A Concise Review of State-of-the-Art. *Geosci J* 2017, *21*, 1033–1070, doi:10.1007/s12303-017-0034-4.

9. Mazzanti, P.; Caporossi, P.; Muzi, R. Sliding Time Master Digital Image Correlation Analyses of CubeSat Images for Landslide Monitoring: The Rattlesnake Hills Landslide (USA). *Remote Sensing* 2020, *12*, 592, doi:10.3390/rs12040592.

10. Guerriero, L.; Di Martire, D.; Calcaterra, D.; Francioni, M. Digital Image Correlation of Google Earth Images for Earth's Surface Displacement Estimation. *Remote Sensing* 2020, *12*, 3518, doi:10.3390/rs12213518.

11. Caporossi, P.; Mazzanti, P.; Bozzano, F. Digital Image Correlation (DIC) Analysis of the 3 December 2013 Montescaglioso Landslide (Basilicata, Southern Italy): Results from a Multi-Dataset Investigation. *IJGI* 2018, *7*, 372, doi:10.3390/ijgi7090372.

12. Mazza, D.; Cosentino, A.; Romeo, S.; Mazzanti, P.; Guadagno, F.M.; Revellino, P. Remote Sensing Monitoring of the Pietrafitta Earth Flows in Southern Italy: An Integrated Approach Based on Multi-Sensor Data. *Remote Sensing* 2023, *15*, 1138, doi:10.3390/rs15041138.

13. Oats, R.C.; Dai, Q.; Head, M. Digital Image Correlation Advances in Structural Evaluation Applications: A Review. *Pract. Period. Struct. Des. Constr.* 2022, *27*, 03122007, doi:10.1061/(ASCE)SC.1943-5576.0000725.

14. Mugnai, F.; Caporossi, P.; Mazzanti, P. Exploiting Image Assisted Total Station in Digital Image Correlation (DIC) Displacement Measurements: Insights from Laboratory Experiments. *European Journal of Remote Sensing* 2022, *55*, 115–128, doi:10.1080/22797254.2021.2025153.

15. Spampinato, L.; Calvari, S.; Oppenheimer, C.; Boschi, E. Volcano Surveillance Using Infrared Cameras. *Earth-Science Reviews* 2011, *106*, 63–91, doi:10.1016/j.earscirev.2011.01.003.

16. Calvari, S.; Spampinato, L.; Lodato, L.; Harris, A.J.L.; Patrick, M.R.; Dehn, J.; Burton, M.R.; Andronico, D. Chronology and Complex Volcanic Processes during the 2002–2003 Flank Eruption at Stromboli Volcano (Italy) Reconstructed from Direct Observations and Surveys with a Handheld Thermal Camera. *J. Geophys. Res.* 2005, *110*, 2004JB003129, doi:10.1029/2004JB003129.

17. Schöpa, A.; Pantaleo, M.; Walter, T.R. Scale-Dependent Location of Hydrothermal Vents: Stress Field Models and Infrared Field Observations on the Fossa Cone, Vulcano Island, Italy. *Journal of Volcanology and Geothermal Research* 2011, *203*, 133–145, doi:10.1016/j.jvolgeores.2011.03.008.

18. Furukawa, Y. Infrared Thermography of the Fumarole Area in the Active Crater of the Aso Volcano, Japan, Using a Consumer Digital Camera. *Journal of Asian Earth Sciences* 2010, *38*, 283–288, doi:10.1016/j.jseaes.2010.02.001.

19. Stevenson, J.A.; Varley, N. Fumarole Monitoring with a Handheld Infrared Camera: Volcán de Colima, Mexico, 2006–2007. *Journal of Volcanology and Geothermal Research* 2008, *177*, 911–924, doi:10.1016/j.jvolgeores.2008.07.003.

20. Pappalardo, G.; Mineo, S.; Caliò, D.; Bognandi, A. Evaluation of Natural Stone Weathering in Heritage Building by Infrared Thermography. *Heritage* 2022, *5*, 2594–2614, doi:10.3390/heritage5030135.

21. Grinzato, E.; Bison, P.G.; Marinetti, S. Monitoring of Ancient Buildings by the Thermal Method. *Journal of Cultural Heritage* 2002, *3*, 21–29, doi:10.1016/S1296-2074(02)01159-7.

22. Lucchi, E. Applications of the Infrared Thermography in the Energy Audit of Buildings: A Review. *Renewable and Sustainable Energy Reviews* 2018, *82*, 3077–3090, doi:10.1016/j.rser.2017.10.031.

23. Mineo, S.; Pappalardo, G. The Use of Infrared Thermography for Porosity Assessment of Intact Rock. *Rock Mech Rock Eng* 2016, *49*, 3027–3039, doi:10.1007/s00603-016-0992-2.

24. Mineo, S.; Pappalardo, G.; Rapisarda, F.; Cubito, A.; Di Maria, G. Integrated Geostructural, Seismic and Infrared Thermography Surveys for the Study of an Unstable Rock Slope in the Peloritani Chain (NE Sicily). *Engineering Geology* 2015, *195*, 225–235, doi:10.1016/j.enggeo.2015.06.010.

25. Lee, E.J.; Shin, S.Y.; Ko, B.C.; Chang, C. Early Sinkhole Detection Using a Drone-Based Thermal Camera and Image Processing. *Infrared Physics & Technology* 2016, *78*, 223–232, doi:10.1016/j.infrared.2016.08.009.

26. Baroň, I.; Bečkovský, D.; Míča, L. Application of Infrared Thermography for Mapping Open Fractures in Deep-Seated Rockslides and Unstable Cliffs. *Landslides* 2014, *11*, 15–27, doi:10.1007/s10346-012-0367-z.

27. Teza, G.; Marcato, G.; Castelli, E.; Galgaro, A. IRTROCK: A MATLAB Toolbox for Contactless Recognition of Surface and Shallow Weakness of a Rock Cliff by Infrared Thermography. *Computers & Geosciences* 2012, *45*, 109–118, doi:10.1016/j.cageo.2011.10.022.

28. Martino, S.; Mazzanti, P. Integrating Geomechanical Surveys and Remote Sensing for Sea Cliff Slope Stability Analysis: The Mt. Pucci Case Study (Italy). *Nat. Hazards Earth Syst. Sci.* 2014, *14*, 831–848, doi:10.5194/nhess-14-831-2014.

29. Grechi, G.; Fiorucci, M.; Marmoni, G.M.; Martino, S. 3D Thermal Monitoring of Jointed Rock Masses through Infrared Thermography and Photogrammetry. *Remote Sensing* 2021, *13*, 957, doi:10.3390/rs13050957.

30. Guerin, A.; Jaboyedoff, M.; Collins, B.D.; Stock, G.M.; Derron, M.-H.; Abellán, A.; Matasci, B. Remote Thermal Detection of Exfoliation Sheet Deformation. *Landslides* 2021, *18*, 865–879, doi:10.1007/s10346-020-01524-1.

31. Loiotine, L.; Andriani, G.F.; Derron, M.-H.; Parise, M.; Jaboyedoff, M. Evaluation of InfraRed Thermography Supported by UAV and Field Surveys for Rock Mass Characterization in Complex Settings. *Geosciences* 2022, *12*, 116, doi:10.3390/geosciences12030116.

32. Vivaldi, V.; Bordoni, M.; Mineo, S.; Crozi, M.; Pappalardo, G.; Meisina, C. Airborne Combined Photogrammetry—Infrared Thermography Applied to Landslide Remote Monitoring. *Landslides* 2023, *20*, 297–313, doi:10.1007/s10346-022-01970-z.

33. Massi, A.; Ortolani, M.; Vitulano, D.; Bruni, V.; Mazzanti, P. Enhancing the Thermal Images of the Upper Scarp of the Poggio Baldi Landslide (Italy) by Physical Modeling and Image Analysis. *Remote Sensing* 2023, *15*, 907, doi:10.3390/rs15040907.

34. Yang, H.; Liu, B.; Karekal, S. Experimental Investigation on Infrared Radiation Features of Fracturing Process in Jointed Rock under Concentrated Load. *International Journal of Rock Mechanics and Mining Sciences* 2021, *139*, 104619, doi:10.1016/j.ijrmms.2021.104619.

35. Schilirò, L.; Poueme Djueyep, G.; Esposito, C.; Scarascia Mugnozza, G. The Role of Initial Soil Conditions in Shallow Landslide Triggering: Insights from Physically Based Approaches. *Geofluids* 2019, *2019*, 1–14, doi:10.1155/2019/2453786.

36. Lourenço, S.D.N.; Sassa, K.; Fukuoka, H. Failure Process and Hydrologic Response of a Two Layer Physical Model: Implications for Rainfall-Induced Landslides. *Geomorphology* 2006, *73*, 115–130, doi:10.1016/j.geomorph.2005.06.004.

37. Scaioni, M.; Longoni, L.; Melillo, V.; Papini, M. Remote Sensing for Landslide Investigations: An Overview of Recent Achievements and Perspectives. *Remote Sensing* 2014, *6*, 9600–9652, doi:10.3390/rs6109600.

38. Montrasio, L.; Schilirò, L.; Terrone, A. Physical and Numerical Modelling of Shallow Landslides. *Landslides* 2016, *13*, 873–883, doi:10.1007/s10346-015-0642-x.

39. Schilirò, L.; Marmoni, G.M.; Fiorucci, M.; Pecci, M.; Mugnozza, G.S. Preliminary Insights from Hydrological Field Monitoring for the Evaluation of Landslide Triggering Conditions over Large Areas. *Nat Hazards* 2023, doi:10.1007/s11069-023-06064-0.

40. Ma, J.; Niu, X.; Liu, X.; Wang, Y.; Wen, T.; Zhang, J. Thermal Infrared Imagery Integrated with Terrestrial Laser Scanning and Particle Tracking Velocimetry for Characterization of Landslide Model Failure. *Sensors* 2019, *20*, 219, doi:10.3390/s20010219.

41. Frodella, W.; Gigli, G.; Morelli, S.; Lombardi, L.; Casagli, N. Landslide Mapping and Characterization through Infrared Thermography (IRT): Suggestions for a Methodological Approach from Some Case Studies. *Remote Sensing* 2017, *9*, 1281, doi:10.3390/rs9121281.

42. Mugnai, F.; Cosentino, A.; Mazzanti, P.; Tucci, G. Vibration Analyses of a Gantry Structure by Mobile Phone Digital Image Correlation and Interferometric Radar. *Geomatics* 2021, *2*, 17–35, doi:10.3390/geomatics2010002.

43. Pan, B.; Xie, H.; Wang, Z.; Qian, K.; Wang, Z. Study on Subset Size Selection in Digital Image Correlation for Speckle Patterns. *Opt. Express* 2008, *16*, 7037, doi:10.1364/OE.16.007037.

44. Stumpf, A. Landslide Recognition and Monitoring with Remotely Sensed Data from Passive Optical Sensors.

45. Leprince, S.; Berthier, E.; Ayoub, F.; Delacourt, C.; Avouac, J.-P. Monitoring Earth Surface Dynamics With Optical Imagery. *Eos Trans. AGU* 2008, *89*, 1–2, doi:10.1029/2008EO010001.

46. Mazzanti, P. Toward Transportation Asset Management: What Is the Role of Geotechnical Monitoring? *J Civil Struct Health Monit* 2017, *7*, 645–656, doi:10.1007/s13349-017-0249-0.

47. Sara, U.; Akter, M.; Uddin, M.S. Image Quality Assessment through FSIM, SSIM, MSE and PSNR—A Comparative Study. *JCC* 2019, *07*, 8–18, doi:10.4236/jcc.2019.73002.

48. Kim, D.; Balasubramaniam, A.S.; Gratchev, I.; Kim, S.-R.; Chang, S.-H. Application of Image Quality Assessment for Rockfall Investigation.

49. Stumpf, A.; Malet, J.-P.; Delacourt, C. Correlation of Satellite Image Time-Series for the Detection and Monitoring of Slow-Moving Landslides. *Remote Sensing of Environment* 2017, *189*, 40–55, doi:10.1016/j.rse.2016.11.007.

50. Lacroix, P.; Araujo, G.; Hollingsworth, J.; Taipe, E. Self-Entrainment Motion of a Slow-Moving Landslide Inferred From Landsat-8 Time Series. *J. Geophys. Res. Earth Surf.* 2019, *124*, 1201–1216, doi:10.1029/2018JF004920.

51. Plyer, A.; Le Besnerais, G.; Champagnat, F. Massively Parallel Lucas Kanade Optical Flow for Real-Time Video Processing Applications. *J Real-Time Image Proc* 2016, *11*, 713–730, doi:10.1007/s11554-014-0423-0.

52. Optical_Flow_Estimation_An_Error_Analysis_of_Gradient-Based_Methods_with_Local_Optimization.Pdf.

53. Brigot, G.; Colin-Koeniguer, E.; Plyer, A.; Janez, F. Adaptation and Evaluation of an Optical Flow Method Applied to Coregistration of Forest Remote Sensing Images. *IEEE J. Sel. Top. Appl. Earth Observations Remote Sensing* 2016, *9*, 2923–2939, doi:10.1109/JSTARS.2016.2578362.

54. Debella-Gilo, M.; Kääb, A. Sub-Pixel Precision Image Matching for Measuring Surface Displacements on Mass Movements Using Normalized Cross-Correlation. *Remote Sensing of Environment* 2011, *115*, 130–142, doi:10.1016/j.rse.2010.08.012.

55. Bickel, V.; Manconi, A.; Amann, F. Quantitative Assessment of Digital Image Correlation Methods to Detect and Monitor Surface Displacements of Large Slope Instabilities. *Remote Sensing* 2018, *10*, 865, doi:10.3390/rs10060865.

56. Singleton, A.; Li, Z.; Hoey, T.; Muller, J.-P. Evaluating Sub-Pixel Offset Techniques as an Alternative to D-InSAR for Monitoring Episodic Landslide Movements in Vegetated Terrain. *Remote Sensing of Environment* 2014, *147*, 133–144, doi:10.1016/j.rse.2014.03.003.

57. Li, W.C.; Lee, L.M.; Cai, H.; Li, H.J.; Dai, F.C.; Wang, M.L. Combined Roles of Saturated Permeability and Rainfall Characteristics on Surficial Failure of Homogeneous Soil Slope. *Engineering Geology* 2013, *153*, 105–113, doi:10.1016/j.enggeo.2012.11.017.

58. Yubonchit, S.; Chinkulkijniwat, A.; Horpibulsuk, S.; Jothityangkoon, C.; Arulrajah, A.; Suddeepong, A. Influence Factors Involving Rainfall-Induced Shallow Slope Failure: Numerical Study. *Int. J. Geomech.* 2017, *17*, 04016158, doi:10.1061/(ASCE)GM.1943-5622.0000865.

59. Naidu, S.; Sajinkumar, K.S.; Oommen, T.; Anuja, V.J.; Samuel, R.A.; Muraleedharan, C. Early Warning System for Shallow Landslides Using Rainfall Threshold and Slope Stability Analysis. *Geoscience Frontiers* 2018, *9*, 1871–1882, doi:10.1016/j.gsf.2017.10.008.

60. Chinkulkijniwat, A.; Tirametatiparat, T.; Supotayan, C.; Yubonchit, S.; Horpibulsuk, S.; Salee, R.; Voottipruex, P. Stability Characteristics of Shallow Landslide Triggered by Rainfall. *J. Mt. Sci.* 2019, *16*, 2171–2183, doi:10.1007/s11629-019-5523-7.

61. Askarinejad, A.; Akca, D.; Springman, S.M. Precursors of Instability in a Natural Slope Due to Rainfall: A Full-Scale Experiment. *Landslides* 2018, *15*, 1745–1759, doi:10.1007/s10346-018-0994-0.

62. Askarinejad, A.; Springman, S.M. A Novel Technique to Monitor Subsurface Movements of Landslides. *Can. Geotech. J.* 2018, *55*, 620–630, doi:10.1139/cgj-2016-0338.

Chapter 6

Conclusion

This last chapter is structured to offer a synoptic overview of the results obtained in the previous four papers, answer to research questions presented in the introduction and highlight the implications and future prospects of this doctoral research. These four papers offer an in-depth examination of the opportunities offered by the innovative, non-intrusive PhotoMonitoring (PM) technique, also known as Digital Image Processing (DIP) and highlight the fundamental importance of both understanding the rapid landslide processes like Rockfall or slow but impulsive processes like Earth Flow and mitigation of the risks.

6.1 Summary of Main Results

The thesis begins with the paper in Chapter 2 "Combining Ground Based Remote Sensing Tools for Rockfalls Assessment and Monitoring: The Poggio Baldi Landslide Natural Laboratory", in which a complete exposition of the remote sensing systems used to monitor the phenomena of rockfall in the Poggio Baldi natural laboratory is made. The work shows the results obtained by different remote sensing systems (HYDRA-G ArcSAR; Gigapan robotic systems equipped with DSLR cameras and DUO Smart Noise Monitor) during a three-day continuous monitoring operation. The HYDRA-G ArcSAR technique provided the displacement of debris accumulated both on the escarpment and the sandstone layers after detachment. While the integration of acoustic measurements and Gigapixel 2D-CD, resulted in a very effective integrated monitoring method to improve the dating and characterization- in terms of source zones, dimensions and lithology- of the events of rockfall.

The obvious consideration that emerged from the work is that the Gigapixel images, combined with the PM analysis, provided a unique view of the deformations before the rockfall and the escarpment state of activity.

Therefore, rapid processes such as rockfalls can be carefully monitored through a low-cost non-invasive technique such as PM, which in this case showed a greater sensitivity than other techniques. In addition, the use of very high-resolution images for the PM application allows us to obtain some information (identification of small isolated rockfall events and/or observation

deformations before rockfall) not achievable with more conventional techniques but essential for the rockfall risk assessment.

The following Chapter 3 "Remote Sensing Monitoring of the Pietrafitta Earth Flow in Southern Italy: An Integrated Approach Based on Multi-Sensor Data", discusses the case study of the Pietrafitta Earth Flow in Benevento province. This chapter aims to combine and critically evaluate different remote sensing techniques (T-InSAR; R-TS; TLS and DIC) for the monitoring and understanding of slow but impulsive processes such as Earth Flows and specifically to assess how PM technology, using satellite images, can be integrated with information obtained from other techniques. The results show a high capacity of the most common techniques (T-InSAR; R-TS and TLS) to evaluate the constant evolution of Earth Flows, allowing to highlight of slow and localized movements sensitive to rainfall events.

On the other hand, the use of the DIC technique through satellite images has allowed monitoring at a lower detailed scale and this allows to study of the overall deformative behaviour. This application highlighted some areas of the body of landslide in expansion and a retrogressive style, aspects that had not been highlighted with other techniques previously used.

The consideration that emerges from these results is that the PM technique, using satellite images, is very valid to improve the understanding of slow but impulsive processes such as Earth Flow and allows to close the knowledge gaps of other monitoring tools. Moreover, by using high-performance algorithms, it is possible to use the medium-low resolution and open-source satellite images to observe movements smaller than the pixel size (usually you can get to displacements of 1/10 Pixel size). The PM technique from satellite images is, therefore, a perfect method of analysis if the goal is to conduct a Knowledge-Monitoring also because it allows for investigation of the landslide event over a very wide time frame (satellite images acquired in the last 20 years). On the other hand, the same technique could currently have some gaps in the case of Emergency-Monitoring due to a weekly revisit time of the most common satellites.

In Chapter 4, "The Contribution of Digital Image Correlation for the Knowledge, Control, and Emergency Monitoring of Earth Flows" the discussion of Chapter 3 was expanded. in effect, the objective of this chapter is to understand how modern digital image correlation techniques (DIC) can be used for different types of monitoring (knowledge, Control and Emergency Monitoring) of Earth Flows, also carrying out an assessment and comparison with more conventional monitoring techniques. In detail, analyses were carried out in two different pilot sites where optical data acquired

from two different platforms were used (ground-based camera for Pieterafitta Earth Flow; UAV data for Grillo Earth-Flow) and compared respectively with RTS and GNSS data. The results show a high reliability and sensitivity of the DIC technique applied to both case studies. On the other hand it resulting that in the case of periodic knowledge- Monitoring the best way to quantitatively monitoring the Earth Flow with PM techniques is definitely to use the UAS data, with the hillshade for several reasons (they are not subject to changes in vegetation; it is possible thanks to the high resolution to identify also localized displacements without running the risk of ambiguity; low cost of realization; possibility to control also the volumetric variation). Instead, for continuous and emergency monitoring, however, the best way to quantitatively monitoring the Earth Flow with PM techniques is definitely to use low-cost ground based cameras that maintain, as noted, a good cost-benefit ratio and can be used as surveillance or as Early Warning Systems (EWS) through a continuous analysis process.

The topic highlighted in this chapter is that PM analyses can be used in different ways and can be useful in obtaining a large amount of information compared to the different monitoring purposes (knowledge, control and emergency). In addition, even using low-cost and low-resolution sensors, the PM technique maintains an excellent level of reliability and ensures a significant impact on the scientific understanding of slow but impulsive landslide processes such as Earth Flow. This consideration is especially useful for professional purposes because it shows how the PM technique if used correctly, can be an excellent tool to be used for Geotechnical Asset Management (GAM) and landslide risk assessment.

Finally, Chapter 5 "Optical and Thermal Image Processing for monitoring rainfall triggered shallow landslides: insights from analogue laboratory experiments" aims to evaluate the utility of combining IRT imaging, which is used to measure the relative difference in Land Surface Temperature (LST), with the analysis on the change and displacement offered by Digital Image Processing (DIP) techniques, in the context of shallow landslides triggered by rainfall. This goal has been pursued through some experiments on a laboratory scale in which flume test equipment has been used, replicating an analogue model of failure of a shallow landslide failure triggered by rainfall. The experiments were monitored through sensors installed on the ground, video shooting and the acquisition of periodic images from a Thermal Camera. The results obtained highlight that the application of this methodology for the study of the Shallow landslide triggered by rainfall has a huge potential, especially for the detection of a precursor signals failure (IRT-DIP). In detail, Digital Image

Correlation (DIC) analyses performed on both IRT thermal images and optical images indicated the presence of an incipient slope movement phase about 1 minute before surface fracturing became apparent. In addition, by combining the results obtained with DIC analysis and Change Detection (CD) analysis on thermal IRT images, it was possible to clearly observe the presence of positive thermal anomalies 1 minute before the appearance of the first fracture on the surface, and 2 minutes before slope failure.

What emerges from this chapter is that the versatility of the PM technique makes it possible to test different, even experimental, approaches that involve the use of new analysis procedures even using input data not derived from optical images. In contrast to optical images, thermal images can provide information even at night, making this technique ideal for Early Warning Systems (EWS) applications. This allows optimisation and increases the potential of PM for monitoring slow but impulsive processes such as shallow landslides, which act at slope scale.

Therefore, even slow but impulsive processes such as shallow landslides can be carefully monitored through a low-cost and non-invasive technique such as PM, which in this experimental application showed greater sensitivity in observing precursor signals of slope failure. The consideration is that the potential of this innovative approach is considerable, especially when adapted to real scenarios, where the delay between the precursors and the failure could be used for Early Warning purposes.

Together, these four chapters show the high potential of the PM technique when used in various settings (real or experimental), for various objectives (knowledge monitoring, control, and emergency), and when using various data acquisition platforms (satellite, UAV, and ground-based) with the goal of monitoring rapid or slow but impulsive processes like Rockfall, Earth Flow and Shallow Landslide.

6.2 Answer to the Research Questions

The results summarized in the previous paragraph are in line with the general objectives of the research and have made it possible to answer specific Research Questions.

I. *Can non-invasive monitoring techniques that utilize digital image processing, such as Digital Image Correlation (DIC) and Change Detection (CD), contribute to the monitoring of rapid landslides such as Rockfall and slow but impulsive processes such as Earth Flow?*

- Yes, this doctoral thesis has provided concrete evidence that non-invasive remote sensing techniques such as DIC (see Chapters 3, 4 and 5) and CD (see Chapter 2 and Chapter 5) can significantly contribute to the monitoring of rapid landslides such as Rockfall and slow but impulsive processes such as Earth Flow.

II. *What additional information can PhotoMonitoring techniques provide compared to more conventional monitoring methods?*

- The correct application of PhotoMonitoring (PM) techniques can, as shown in Chapters 2, 3, and 4, boost our understanding of rapid or slow but impulsive landslide processes and provide more information than conventional methods. They can occasionally be used instead of other monitoring approaches (see Chapters 2 and 4) or in addition to them (see Chapter 3). It has been demonstrated in the thesis work that these techniques typically provide high versatility, significant spatial coverage, and good measurement sensitivity.

III. *How accurate and reliable are measurements obtained through PhotoMonitoring techniques, including their ability to detect and quantify movement with high precision and sensitivity?*

- This work's DIC analyses have shown that accurate measurements with good precision, sensitivity, and reliability can be obtained using PhotoMonitoring techniques (see chapters 3, 4, and 5). These properties are frequently influenced by the quality of the input data (geometric resolution, illumination, field of view, etc.), and under normal conditions, displacements of 1/10 of a pixel can be detected.

IV. *What are the main limitations of PhotoMonitoring techniques, and how may they be overcome to improve digital image analysis techniques?*

- The primary factor contributing to the limitations of PhotoMonitoring techniques is the use of passive sensors (such as optical sensors) as a data acquisition tool. In fact, the analyses become ineffective in bad weather (snow or fog), with rapid fluctuations in brightness (the appearance of shadows), and/or when there isn't a sufficient artificial or natural "speckle pattern". These limitations can be overcome

by using images collected by other sensors or by improving analysis and pre-processing algorithms (see Chapter 5).

V. *How can the understanding of shallow landslides be improved using thermal infrared data, analysed with PhotoMonitoring techniques?*

The use of thermal data contributes significantly to understanding the shallow landslide processes. In fact, it is possible to study the evolution of the process in various weather conditions as well as measure the variation of surface temperature at the same time by analysing thermal infrared images using PhotoMonitoring techniques. Additionally, it has been observed that using thermal images to perform Digital Image Correlation and Change Detection analysis allows for to measurement of the displacement of the slope and to identify some thermal anomalies that occur before the slope failure (see chapter 5).

VI. *Could DIC and CD techniques contribute to the development of early warning systems (EWS) for landslides?*

- Yes, DIC and CD techniques can be used to create Early Warning Stems (EWS) for landslides. In fact, they provide quick data analysis, excellent scalability to various site-specific conditions, and good accuracy (see Chapters 2 and 4). Additionally, by combining DIC and CD with multispectral data, such as thermal infrared data, and by resolving a few technical issues (such as night visibility), early warning signals have even been identified at the laboratory scale (see Chapter 5).

VII. *Can PhotoMonitoring techniques be used to mitigate the risk of landslides and help to manage high-risk areas in a safe and sustainable way?*

- Yes, as demonstrated by the results of this doctoral thesis, the characteristics of sensitivity, precision, and adaptability make PhotoMonitoring techniques particularly suitable for the mitigation of the risk of landslides. However, there are still limits that prevent these approaches from being used to their full potential (see Chapters 3, 4, and 5). Despite this, digital image processing continues to be a practical, non-intrusive, and manageable solution; that are all essential elements for safe and sustainable monitoring.

6.3 Broader Implications and Future Prospective

The work done in this PhD programme has centred on the innovative application of the PhotoMonitoring (PM) technique for the monitoring of rapid or slow but impulsive geological phenomena, including rock falls, Earth Flows, and Shallow landslides. The broad implications in the field of engineering geology are significant, and the final results demonstrate many kinds of consequences for scientific and practical application.

For instance, the PM solution's adaptability enables it to satisfy a variety of needs and scenarios, such as emergency knowledge, control, and monitoring. The last type of monitoring is crucial because it offers the opportunity to develop Early Warning Systems for geological hazards while maintaining a reasonable level of measurement sensitivity. Due to exceptional adaptability, in addition to the capability of using data from various sources, such as Satellites, Unmanned Aerial Vehicles (UAVs), Ground Sensors, and Mobile Sensors, makes PM suitable for use in a wide range of real-world application fields, including experimental settings and natural environments.

The more significant aspect still may be the cost-effectiveness and non-intrusiveness of PM, which presents a practical and user-friendly alternative to more expensive conventional monitoring techniques. This is important because it enables the development of cost-effective monitoring strategies for high-risk geological regions that are difficult for users and technical staff to access. All these implications highlight that the use of the PM technique can make the monitoring more widespread on the territory, expanding and improving the control of the environment and helping us to better understand the natural processes and the Landslide risk assessment.

All of this extraordinary potential is also connected to the statistics related to the optical sensor market. The optical sensor market has grown significantly in recent years, achieving an estimated value of $1.93 billion in 2021. Projections indicate that by 2030, this sector may grow to a value of $7.02 billion, with total CMOS image sensor shipments increasing from 6.7 billion units in 2020 to approximately 13.5 billion units in 2025. This significant evolution is due to several key factors. In the first place, the continuous technological progress of optical sensors has made it possible to use them even in extremely adverse environments and in sectors that are constantly evolving and innovating. The amazing thing is that by 2023, it is estimated that an average of 4.7 billion photos will be taken per day worldwide, an incredible total of 1.81 trillion images per year. This high flexibility has contributed to significant market growth, especially given the exponential increase in the use of

mobile devices for photography. Currently, 92.5% of photos are taken with smartphones, while only 7% are captured with traditional cameras or other platforms.

The potential of the PhotoMonitoring techniques discussed in this doctoral thesis, combined with the increasing use of smartphones, would produce an enormous quantity of data, and transform a typical object like a smartphone into an effective monitoring tool (Figure 6.1).
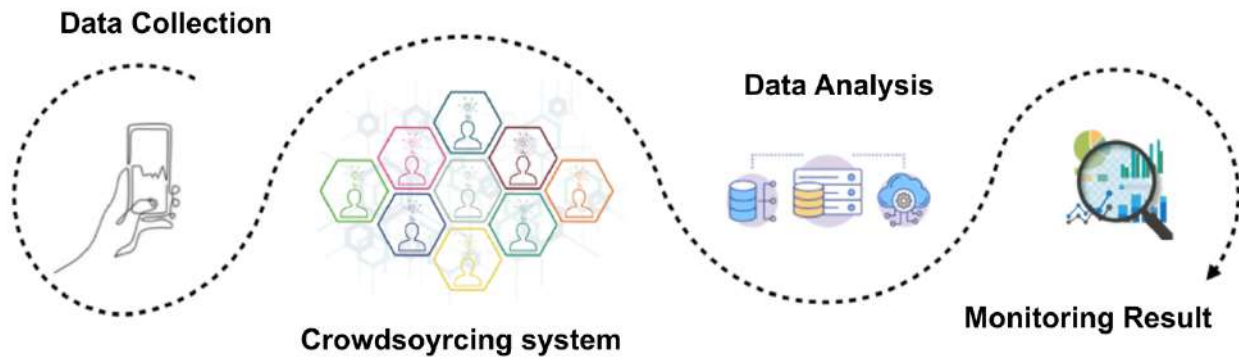
Figure 6.1. Example of an approach for using the smartphone as a data collection tool.

In July 2023, "IntelligEarth," a Sapienza start-up of the Department of Earth Sciences for the university's third mission activities, was founded with this vision and based on the considerations that emerged from this PhD work.

Despite their significant potential, image analysis approaches still have several limitations, as this thesis study showed (e.g., image shadows, visibility at night, poor visibility due to bad weather, geometric distortion, the presence of vegetation, etc.). Exploring PhotoMonitoring's potential will open up new opportunities for advancements in geological engineering and natural risk management. In fact, it is simple to believe that several limitations will be overcome in the near future by working on improving the procedures of analysis (use of artificial intelligence) and the methods of data collecting (use of multiple spectral bands).

Appendix

Appendix A: PhD Candidate contribution to each paper

This appendix provides a detailed overview of the specific contributions made by the PhD candidate to each paper included in the thesis.

CHAPTER 2

Title of the Paper: *Combining Ground Based Remote Sensing Tools for Rockfalls Assessment and Monitoring: The Poggio Baldi Landslide Natural Laboratory.*

Authors: *Davide Mazza, Antonio Cosentino, Saverio Romeo, Paolo Mazzanti, Francesco M. Guadagno and Paola Revellino*

Citation: *Romeo, S.; Cosentino, A.; Giani, F.; Mastrantoni, G.; Mazzanti, P. Combining Ground Based Remote Sensing Tools for Rockfalls Assessment and Monitoring: The Poggio Baldi Landslide Natural Laboratory. Sensors 2021, 21, 2632.*

PhD Candidate's Contribution:

- *Research Design*: The PhD Candidate was one of the individuals responsible for developing the initial hypothesis and designing the methodology for data collection and analysis.
- *Data Collection*: The PhD Candidate led the fieldwork to data collect, including coordination with other authors.
- *Data Analysis*: The PhD Candidate conducted the Optical data analysis using QGIS software and compared the results with other monitoring techniques used in that specific application.
- *Writing*: The PhD Candidate drafted more chapters in the initial manuscript and significantly contributed to revisions based on feedback from co-authors.
- *Other Contributions*: The PhD Candidate personally organized field activities and specialized in the use of gigapixel images for identifying very small rockfalls.

Author Contributions:

Conceptualization, S.R., G.M., P.M and A.C.; methodology, S.R., G.M. and A.C.; formal analysis, G.M., A.C., and F.G.; investigation, S.R., G.M., A.C., and F.G.; data curation, G.M., A.C., and F.G.; writing—original draft preparation, S.R., G.M., A.C.; writing—review and editing, G.M., S.R., P.M.; supervision, P.M. All authors have read and agreed to the published version of the manuscript.

CHAPTER 3

Title of the Paper: *Remote Sensing Monitoring of the Pietrafitta Earth Flows in Southern Italy: An Integrated Approach Based on Multi-Sensor Data.*

Authors: *Saverio Romeo, Antonio Cosentino, Francesco Giani, Giandomenico Mastrantoni and Paolo Mazzanti.*

Citation: *Mazza, D.; Cosentino, A.; Romeo, S.; Mazzanti, P.; Guadagno, F.M.; Revellino, P. Remote Sensing Monitoring of the Pietrafitta Earth Flows in Southern Italy: An Integrated Approach Based on Multi-Sensor Data. Remote Sens. 2023, 15, 1138.*

PhD Candidate's Contribution:

- *Research Design*: The PhD Candidate was involved in developing the initial hypothesis and designing the methodology for data analysis.
- *Data Collection*: The PhD Candidate assisted the first author in the formal data research phase.
- *Data Analysis*: The PhD Candidate led the formal analysis phase, leveraging extensive experience with the IRIS software utilized for the analyses.
- *Writing*: The PhD Candidate drafted more chapters in the initial manuscript and significantly contributed to revisions based on feedback from co-authors.
- *Other Contributions*: The PhD Candidate provided training to the other authors' team on optical analysis techniques using IRIS Software, specifically focusing on the Phase Correlation (PC) algorithm.

Author Contributions

Conceptualization, D.M., P.M., A.C. and P.R.; methodology, P.M., A.C. and D.M.; formal analysis, D.M., A.C.; investigation, D.M.; resources, D.M. and P.R.; data curation, D.M.; writing—original draft preparation, D.M., A.C. and S.R.; writing—review and editing, P.M., S.R., F.M.G. and P.R.; supervision, P.M. and P.R.; project administration, P.R. and F.M.G.; funding acquisition, P.R. and F.M.G. All authors have read and agreed to the published version of the manuscript.

CHAPTER 4

Title of the Paper: *The Contribution of Digital Image Correlation for the Knowledge, Control, and Emergency Monitoring of Earth Flows.*

Authors: *Davide Mazza, Saverio Romeo, Antonio Cosentino, Paolo Mazzanti, Francesco Maria Guadagno and Paola Revellino.*

Citation: *Mazza, D.; Romeo, S.; Cosentino, A.; Mazzanti, P.; Guadagno, F.M.; Revellino, P. The Contribution of Digital Image Correlation for the Knowledge, Control and Emergency Monitoring of Earth Flows. Geosciences 2023, 13, 364.*

PhD Candidate's Contribution:

- *Research Design*: The PhD Candidate was involved in developing the methodology for data analysis.
- *Data Collection*: The PhD Candidate assisted the first author in the formal data research phase.
- *Data Analysis*: The PhD Candidate supervised during the formal analysis phase, leveraging extensive experience with the IRIS software utilized for the analyses.
- *Writing*: The PhD Candidate made very significant contributions during the review and revision phase.
- *Other Contributions*: The PhD Candidate provided training to the other authors' team on new optical analysis techniques using IRIS Software, specifically focusing on the NCC Algorithms. Specifically, leveraging significant expertise in analysis techniques, the candidate supported the team in understanding the most effective optical remote

sensing platforms for various monitoring objectives (Knowledge, Control, and Emergency Monitoring).

Author Contributions

Conceptualization, D.M. and S.R.; methodology, D.M., S.R. and A.C.; formal analysis, D.M.; investigation, D.M.; resources, A.C. and P.M.; writing—original draft preparation, D.M. and S.R.; writing—review and editing, D.M., S.R., A.C., P.M. and P.R.; supervision, F.M.G. and P.R. All authors have read and agreed to the published version of the manuscript.

CHAPTER 5

Title of the Paper: *Optical and Thermal Image Processing for monitoring rainfall triggered shallow landslides: insights from analogue laboratory experiments.*

Authors: *Antonio Cosentino, Gian Marco Marmoni, Matteo Fiorucci, Paolo Mazzanti, Gabriele Scarascia Mugnozza, Esposito Carlo.*

Citation: *Cosentino, A.; Marmoni, G.M.; Fiorucci, M.; Mazzanti, P.; Scarascia Mugnozza, G.; Esposito, C. Optical and Thermal Image Processing for Monitoring Rainfall Triggered Shallow Landslides: Insights from Analogue Laboratory Experiments. Remote Sens. 2023, 15, 5577.*

PhD Candidate's Contribution:

- *Research Design*: The initial hypothesis and the methodology for the data analysis were developed by the PhD candidate.
- *Data Collection*: The PhD Candidate led the fieldwork to collect the data, coordinating with other authors.
- *Data Analysis*: The PhD Candidate conducted Optical and Thermal data analysis using IRIS software and compared the results using Python and GIS software.
- *Writing*: The PhD Candidate drafted the initial manuscript and significantly contributed to revisions based on feedback from co-authors.
- *Other Contributions*: The PhD Candidate supported the developers of IRIS in implementing technical improvements derived from the analyses and provided training to the other authors' team on new optical analysis techniques (Optical Flow Algorithms).

Author Contributions

Acknowledgements

Desidero esprimere la mia sincera gratitudine a tutte le persone che hanno contribuito al completamento di questo percorso.

Innanzitutto, desidero ringraziare i miei Tutor, il Prof. Paolo Mazzanti ed il Prof. Carlo Esposito, per la guida preziosa ed il costante sostegno lungo tutto il percorso.

Un sentito ringraziamento va anche a Nhazca per avermi dato questa opportunità ed aver creduto in me. La collaborazione in Azienda non solo ha arricchito il mio percorso accademico, ma ha anche offerto preziose opportunità di applicare le mie conoscenze in un contesto pratico e di interagire con professionisti di spicco nel campo.

Ai miei genitori e alla mia famiglia, desidero dedicare un profondo ringraziamento per il loro costante sostegno, incoraggiamento e amore incondizionato.

Un ringraziamento speciale va alla mia amata Francesca per la sua pazienza, comprensione e supporto incondizionato, così come voglio ringraziare tutta la sua splendida famiglia.

Infine, desidero ringraziare i miei stimati colleghi per il loro supporto, la collaborazione e le stimolanti discussioni che hanno arricchito questi anni.

A tutti voi, grazie di cuore per aver condiviso con me questo straordinario percorso.

Antonio